Charge Collection in Irradiated Silicon-Detectors

A Study of the Operation Conditions of Silicon Sensors in the ATLAS Pixel Detector

Olaf Krasel

Charge Collection in Irradiated Silicon-Detectors

A Study of the Operation Conditions of

Silicon Sensors in the ATLAS Pixel Detector

Dissertation
zur Erlangung des akademischen Grades
eines Doktors der Naturwissenschaften
der Abteilung Physik
an der Universität Dortmund

vorgelegt von
Dipl.-Phys. Olaf Krasel
aus Bad Laasphe

Erstgutachter:	Prof. Dr. C. Gößling, Universität Dortmund
Zweitgutachter:	PD Dr. Dr. W. Rhode, Universität Wuppertal
Tag der mündlichen Prüfung:	29. Juli 2004

Contents

Chapter 1

Introduction

PARTICLE physics aims at a deep understanding of the microscopic structure of matter. It searches for the fundamental building blocks of the world – the elementary particles. Particle physics also investigates the forces between these particles. Today's knowledge is summarised in the so called *standard model*. In this description matter consists of quarks and leptons, which interact via three fundamental forces. In nature exists gravity as a fourth force which is up to now not included in the standard model.
Nowadays large particle accelerators are used to bring particles to high energies and collide them. The *Large Hadron Collider* (LHC) is a circular collider being built at CERN[1] near Geneva/Switzerland. It is designed to accelerate protons to energies of up to 7 TeV with a luminosity of $10^{34}\,\mathrm{cm}^2/\mathrm{s}$. Therefore it enables the exploration of rare and high-energetic processes which are not accessible up to now.
In order to observe the collisions between the protons several experiments are being built, one of them is ATLAS[2]. The ATLAS experiment's detector has an onion-like design which is typical for colliding beam experiments. It can be divided roughly into three parts: the innermost part is the Inner Detector which measures the tracks of charged particles emerging from the interaction point. Around the tracking system the calorimeter is situated. Its purpose is to determine the particles' energies. The outermost system is the muon spectrometer which measures tracks of muons. ATLAS is equipped with two magnet systems whose fields bend the particles' tracks and enable thereby measurements of the momentum of the particles. A toroidal magnet system surrounds the whole ATLAS detector. Additionally, the Inner Detector is built within a solenoidal magnet.
The University of Dortmund takes part in the development and construction of the Pixel Detector which is the innermost component of the Inner Detector. This sub-detector is the closest one to the interaction point and gives tracking information at three spatial points for traversing particles in the pseudo-rapidity range

[1] **C**onseil **E**uropéen pour la **R**echerche **N**ucléaire
[2] **A** **T**oroidal **L**HC **A**pparatus

$|\eta| \leq 2.5$. The investigated particle physics demands a good spatial resolution and a high granularity due to the high track density. The pixel detector's sensors are fabricated from silicon and have pixels of the size $50\,\mu\text{m} \times 400\,\mu\text{m}$.
Pixel sensors require a two-dimensional connection technique to the read-out electronics. This is realised by small solder balls—so-called bump-bonds—between each pixel cell and the corresponding electronic read-out channel. The small size of the pixels and their high density are a demanding challenge which is far ahead from the industrial standard for this technique.
The proximity to the interaction point leads to a heavy radiation load of up to 10^{15} 1- MeV-$\text{n}_{\text{eq}}/\,\text{cm}^2$ within ten years of operation. If an extension of LHC towards higher luminosities (Super-LHC) is realised the fluences will increase even by a factor 10. In order to cope with these requirements for radiation hardness a radiation hard design of the pixel sensor and oxygenated silicon material are being used.

Will ATLAS be successful in answering the open questions of particle physics? This question has to be answered during the development of this large experiment. The general design of the ATLAS detector has been proven to be suitable for particle physics research by Monte Carlo studies [AT99].
But it has to be proven that the individual components of this complex experiment can fulfill the demands set upon them as well. The scope of this work is to test some aspects of the appropriateness of the pixel module design. It is restricted to two topics: a very specialised part of this work is spent on the design of test structures which can be used to check the quality of bump-bond connection technique between the sensor and the FE electronics. The quality of these connection is crucial for the long-term operability of the modules which cannot be replaced due to the difficult access conditions to the pixel detector.
The second and much larger part of this work investigates the charge collection properties of silicon sensors. The questions which have to be answered for the sensor can be summarised in the question for the collected charge during the years of data taking. The charge collection efficiency of the sensors is affected by the harsh radiation field in which the detector has to work.
The answer to this problem is found by laboratory measurements of basic detector parameters with irradiated samples. Knowledge about the fluence dependence of these parameters is of general interest for all fields which work with silicon detectors in strong radiation fields. The prediction of the charge collection efficiency for the ATLAS pixel sensors is done by using these measurement results as input for simulation studies.
The measurements necessary to obtain the required parameters are done on proton- and neutron-irradiated pad-detectors. Several measurement techniques are applied for these measurements: samples are characterised before and after irradiation by measurements of the current-voltage and capacitance-voltage characteristics. But the central focus of this work lies on measurements with the *transient current technique* (TCT). This method delivers time-resolved measurements of signal-currents

of detectors. The detector signals are caused by drifting charges which have been injected by laser illumination. Due to the short duration of these pulses (5–20 ns) the technique is quite ambitious in point of accurate measurement of fast signals with rise times below 1 ns. From the TCT-measurements it is possible to derive informations on trapping times and electric field configuration.
After having done the measurements their results are used for simulations. In a first step the behaviour of irradiated pad-detectors with respect to pulse-shape and charge collection efficiency is simulated and compared to the measurements in order to verify the applied simulation techniques. In a second step the properties of pixelated detectors are simulated in order to obtain predictions for the later operation of the ATLAS Pixel Detectors.
This work aims on the derivations of these predictions since they are crucial for the design and the operation of the detector. On the one hand comparisons between the predictions from simulation and the real detector behaviour which will be done during the operation will serve as a check for arising problems. On the other hand the simulation will have to be developed further in order to take into account the actual history of operation and new results from the research on radiation hard detectors.

This thesis is split into six parts. Part I introduces into the application of silicon sensors in particle physics experiments of the LHC generation. The physics under investigation in the ATLAS experiment will be shortly summarised in chapter 2 together with a coarse overview of the ATLAS detector and a more detailed one of the pixel detector and its operation environment. Finally, the requirements for this sub-detector and the consequences for this work will be summarised. Chapter 3 covers basic knowledge of semiconductor physics and applies it to explain the functionality of semiconductor detectors. It also treats the energy deposition mechanisms of different particles traversing matter. This chapter is completed by a description of the signal formation process in silicon-detectors. The consequences of radiation damage to silicon detectors are explained in chapter 4. The changes of the crystal structure which are caused by non-ionising energy loss are explained on a microscopic level and their consequences for macroscopic detector parameters are described.
With part II the report on development, measurements and simulations done for this thesis begins. Chapter 5 treats the development of test structures designed for tests concerning connections between pixel sensors and read-out electronics.
Part III is dedicated to the characterisation of pad-detectors. Chapter 6 contains the description of experimental and analysis techniques used for this work. It also describes the design of the pad-detectors used for this work and the facilities in which they were irradiated. Further items are the measurement and analysis techniques for capacitance-voltage and current-voltage characteristics. The chapter is finished by the description of the transient current technique (TCT). The results of CV- and TCT-measurements are given in chapters 7 and 8, respectively. These chapters also include the analysis of the data and some first conclusions.

It is followed by part IV on simulation studies. This part starts with chapter 9 describing the simulation tools developed for this work. Chapter 10 shows the application of the simulation tools for pad-detectors. By comparing simulation and measurement the reliability of the simulation software is tested and its systematic error is estimated. In the next chapter the simulation tools are used to predict the properties of pixel detectors operated in the ATLAS environment.
In part V the measurement and simulation results are summarised and the conclusions are drawn and discussed.
Part VI contains additional material: app. A contains compilations of physical constants, material properties of silicon and a list of abbreviations. App. B contains additional material on the determination of the depletion voltage. The last app. C features additional data from TCT measurements.

Part I

Silicon Detectors in High Energy Physics Experiments

Chapter 2

The ATLAS Pixel Detector

2.1 LHC Physics

2.1.1 The Standard Model of Particle Physics

Today's knowledge of the fundamental particles and their interactions is summarised in the *standard model* of particle physics [Pe91][Po97]. According to this model all matter is built from fermions, i.e. particles with spin $\frac{1}{2}$. These fermions can be divided into *quarks* and *leptons*. Both kinds of particles exist in three generations as it can be seen in Table 2.1.
The particles of the first generation form the stable matter. Most of the second and third generations' particles are heavy and instable. Henceforth they decay into particles of the first generation. Only the neutrinos from the second and third generation do not decay but are subject to so-called neutrino-oscillations. This effect includes also the electron neutrino from the first generation.
The existence of a fourth generation of particles can be ruled out up to very high limits on the mass by measurements of the decay width of the Z^0 boson. The particle listing in Table 2.1 is completed by anti-particles having the same properties but opposite electric charge.
Quarks can be divided into *light* and *heavy* quarks according to their mass. The first group consists of the u and d having masses of $\approx 300\,\mathrm{MeV}/c^2$ and the s having a mass of $\approx 450\,\mathrm{MeV}/c^2$. The remaining quarks have much higher masses: $1.0 - 1.6\,\mathrm{GeV}/c^2$ for the c, $4.1 - 4.5\,\mathrm{GeV}/c^2$ for the b and $168 - 192\,\mathrm{GeV}/c^2$ for the heaviest one, the t[1].

[1]The quark masses given here are constituent masses.

	1st generation	2nd generation	3rd generation	el. charge
quarks	up (u)	charm (c)	top (t)	$+2/3$
	down (d)	strange (s)	bottom (b)	$-1/3$
leptons	e-neutrino (ν_e)	μ-neutrino (ν_μ)	τ-neutrino (ν_τ)	0
	electron (e)	muon (μ)	tau (τ)	-1

Table 2.1: Fermionic building blocks of matter.

Interaction	couples to	exchange particle	Mass [GeV/c^2]
strong	colour	8 gluons (g)	0
electromagnetic	el. charge	photon (γ)	0
weak	weak charge	$W^{\pm}$, Z^0	$\approx 10^2$
gravitational	mass	graviton G	0

Table 2.2: Interactions and their exchange bosons. g, γ, $W^{\pm}$ and Z^0 have spin 1, the graviton G has spin 2.

These particles interact by three different forces with each other: quarks and leptons are both subject to *electromagnetic* and *weak interaction*, quarks interact additionally by *strong interactions*. Within the standard model interactions between particles are described by the exchange of *bosons* which are particles with even numbered spin (see Table 2.2). A further force is *gravitation*. However, since its coupling to the elementary particles is very weak compared to the three other forces it can be neglected in particle physics. The gravitation is not described within the standard model.
The interactions couple to specific properties of the fundamental fermions:

Gravitation The Gravitation couples with the mass of the particles and has infinite range. The corresponding boson is the *graviton* which has not been observed up to now.

Electromagnetic Force The electromagnetic force is transmitted by the photon which couples to the electric charge of particles. Except for the neutral neutrinos all particles in Table 2.1 are subject this force. It is described by *quantum electrodynamics* (QED).

Weak Force The weak force acts on all fermions of the standard model. It is carried by the charged W^+ and W^- and the neutral Z^0. These particles have a rather large mass contrary to the exchange particle of the electromagnetic force. This mass limits the range of the weak interaction.

Electromagnetic and weak force have been described in a unified way by Glashow, Weinberg and Salam in the *electroweak theory*. According to this description they originate from the same phenomenon.

Strong Force The strong force couples to the *colour charge* of quarks while leptons do not interact strongly. The strong force is transmitted by gluons which carry colour charge, too. Thus these bosons can also couple to other gluons.

A characteristic property of the strong force is the *confinement*: the force between two strongly bound quarks grows with their distance. If the field between them contains enough energy it is used to produce new particles. Thus quarks do not exist as free particles but only in bound states of at least two quarks.

Compound particles which are subject to the strong force are called *hadrons*. The strong force is described by *quantum chromodynamics*.

2.1.2 Beyond the Standard Model

Although the formulation of the standard model was a great success of particle physics there are many open questions, e.g. the standard model does not include gravitation and does not explain the masses of its particles. Also a unified description of the electroweak and strong forces in a *Grand Unified Theory* (GUT) is desirable.
Further points of present and future research in particle physics are [AT99]:

Search for the Higgs Theoretically the masses of particles can be explained by symmetry-breaking of the so-called Higgs field. The corresponding particle would be the Higgs-boson which has not been observed up to now.

Supersymmetry A further research topic is the test of different supersymmetric models which introduce for each up to now known particle a supersymmetric partner. These models deliver unified theories.

CP-violation A new generation of experiments with high event rates enable investigations of the CP-violation in B-mesons.

Precision measurements Such experiments can also deliver precise measurements of the top quark mass and the W bosons.

New Particles Increased collision energy and statistics enable the search for new particles which are unknown up to now due to their high mass or low production probability. Examples are a further quark and lepton generation, new gauge bosons and compound states consisting of several quarks.

Heavy Ions The research in the field of heavy ion physics will also benefit from future experiments: ATLAS will allow further investigations of the equation of state of nuclear matter. Further interesting points are quark-gluon plasma (deconfinement) and jet-quenching.

All of these research topics will be addressed by the ATLAS experiment which is described in the following sections.

2.2 The Large Hadron Collider

The *Large Hadron Collider* (LHC) is a new collider which is being built at CERN near the Swiss town Geneva [Go02]. It will accelerate protons to an energy of 7 TeV. Unlike other colliders like LEP[2] or Tevatron it brings particles with the same sign of electric charge to collision. Therefore, it consists of two storage rings

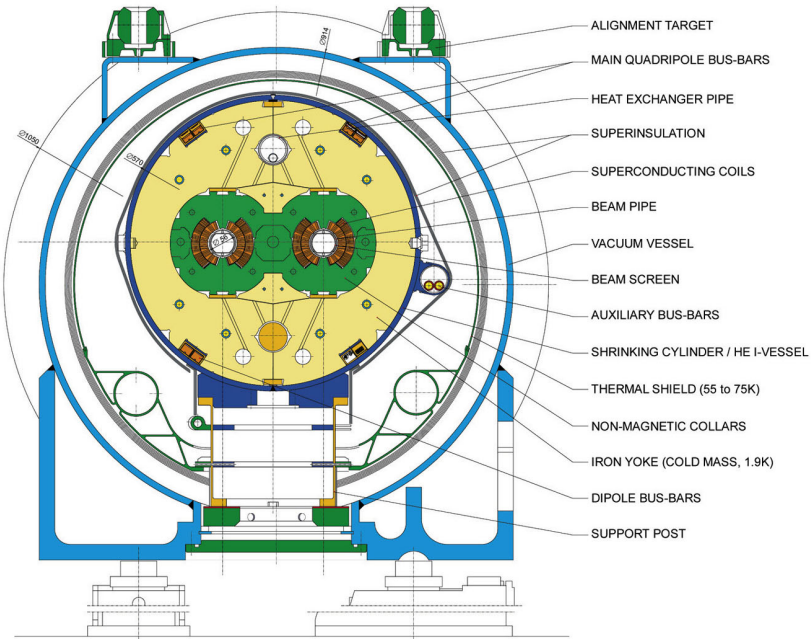

Fig. 2.1: Cross-section of the Large Hadron Collider showing its two separate storage rings in a common housing.

built close to each other as shown in the drawing in Fig. 2.1. Alternatively, the acceleration of heavy ions will be possible: for heavy ion physics LHC will provide lead beams with an energy of 2.76 TeV per nucleon. Collisions between particles from the two beams will occur at four points. The collision rate will be 40 MHz and the intended design luminosity is $10^{34}\,\mathrm{cm^2 s^{-1}}$ for pp-collisions.
Four experiments will be built at the collision points, the two multi-purpose experiments CMS[3] and ATLAS[4], the heavy-ion experiment ALICE[5] and an experiment dedicated to b-physics named LHCb. It is intended to operate the experiments for ten years and to take data on 100 days per year. An overview over the LHC and its experimental areas can be seen in Fig. 2.2.

2.3 The ATLAS Experiment

2.3.1 Overview

The ATLAS experiment is designed as multi-purpose experiment to cover all fields of interest in future particle physics research. It is built by a collaboration consisting of 1 800 scientists from 150 institutes.

[2] **L**arge **E**lectron **P**ositron Collider
[3] **C**ompact **M**uon **S**olenoid
[4] **A** **T**oroidal **LHC** **A**pparatu**S**
[5] **A** **L**arge **I**on **C**ollider **E**xperiment

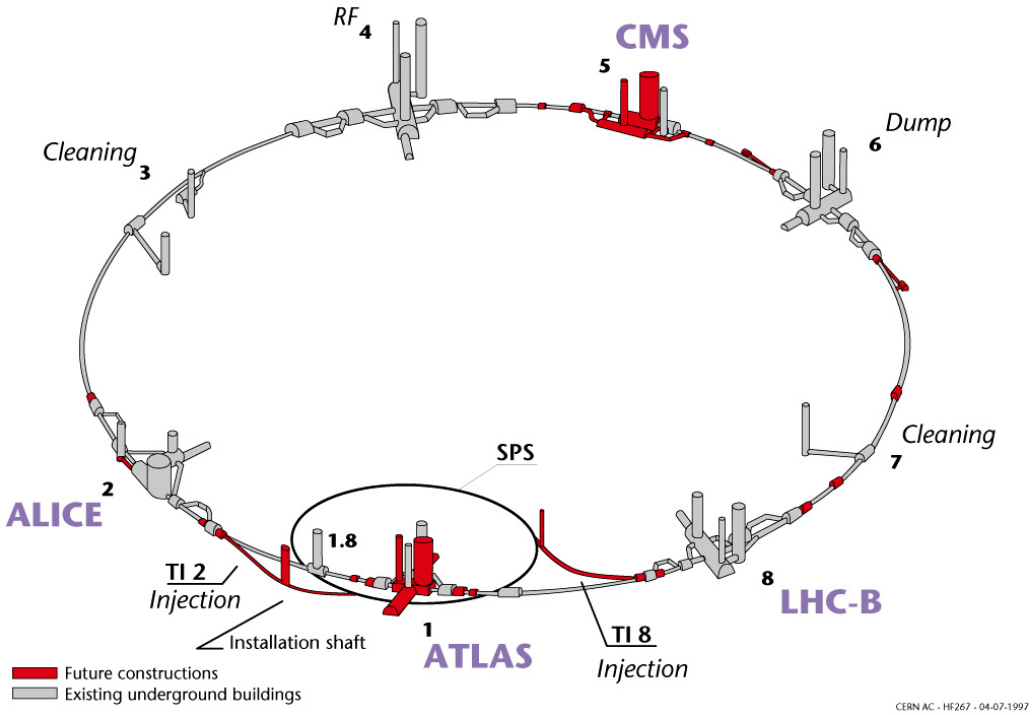

Fig. 2.2: Layout of the LHC tunnel and its experimental areas.

Fig. 2.3 shows an overview of the experiment. Like most other collider experiments it is built in an onion-like fashion consisting of several layers (subdetectors) enclosing each other. Each of the subdetectors is dedicated to a specific purpose. The innermost system is the Inner Detector. Its task is the space-resolved measurement of charged particles emerging from the collisions at the interaction point. In order to measure the momentum of particles the Inner Detector has a solenoidal magnet system which bends the particle tracks. The energies of the particles are measured by the calorimeters which enclose the Inner Detector. The outermost subdetector system is a large muon spectrometer which measures the momentum of muons that penetrate all subdetectors. It is equipped with a toroidal magnet system. The following sections give some more details about the subdetector systems.

2.3.2 Muon Spectrometer

The momentum of muons which have penetrated all other detector parts are measured by the muon spectrometer. Fig. 2.4 shows the layout of the muon spectrometer. Its working principle is based on the deflection of charged particles in magnetic fields. These fields are provided by large superconducting air-core toroid magnets. The muon spectrometer covers the pseudorapidity range $|\eta| \leq 2.7$.

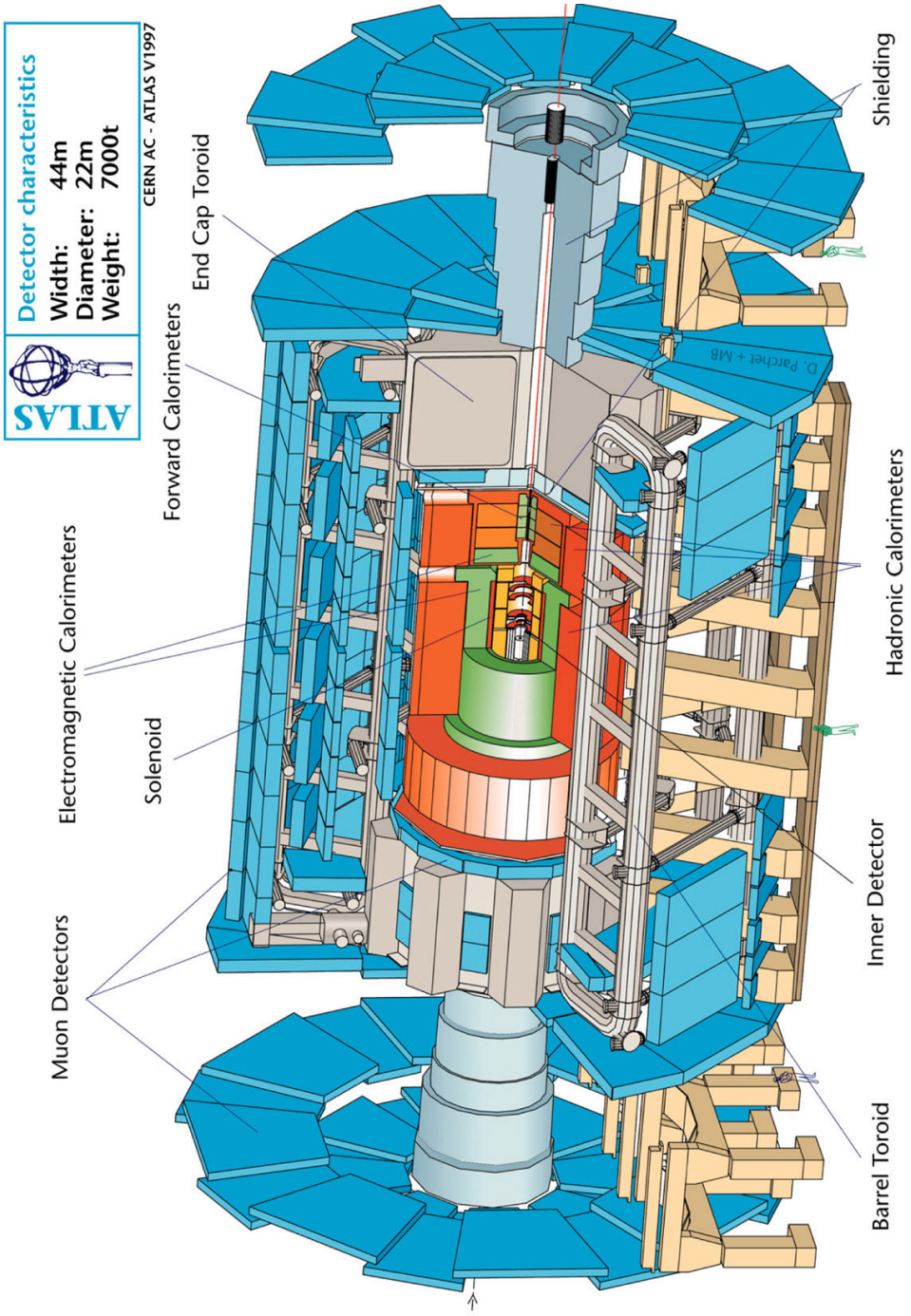

Fig. 2.3: Overall layout of the ATLAS Detector [AT99].

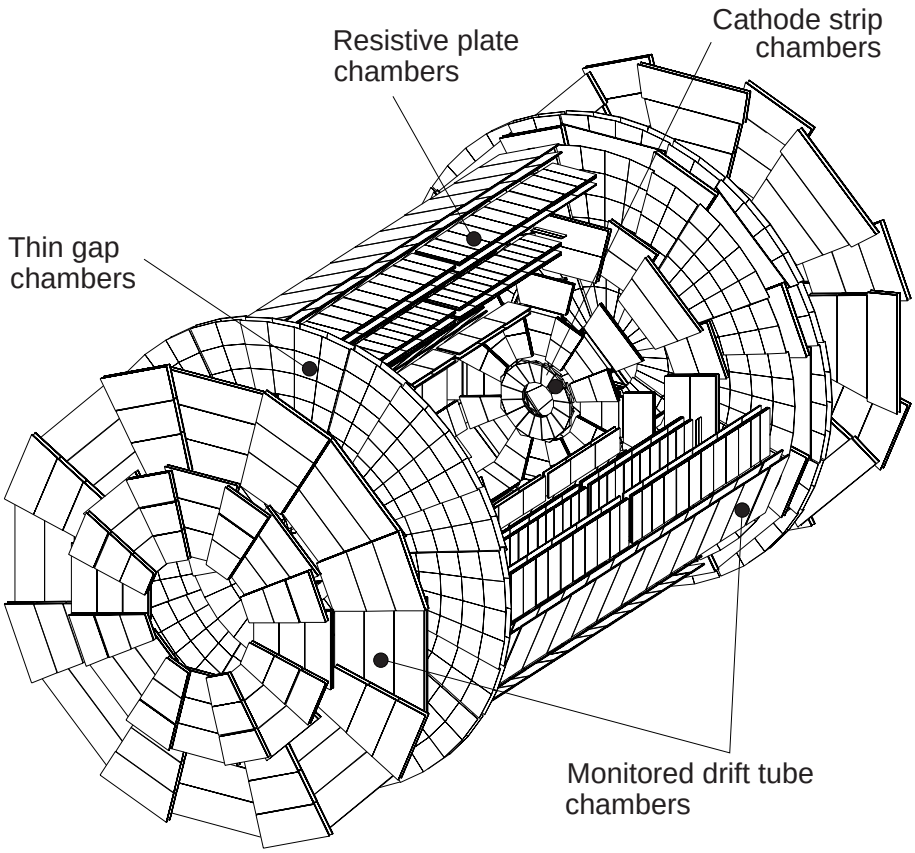

Fig. 2.4: Three-dimensional view of the muon spectrometer instrumentation indicating the areas covered by the four different chamber technologies. [AT99].

It consists of a barrel part having three layers and end-caps having also three layers of detectors. Precision measurements of the coordinates are done by monitored drift tubes (MDTs) and cathode strip chambers (CSCs). The choice of MDTs or CSC depends on the demands from rate and background condition of the installation position.
MDTs and CSCs are completed by a trigger system consisting of resistive plate chambers (RPCs) and thin gap chambers (TGCs). These trigger chambers serve three purposes: they provide the bunch crossing information with a sufficient time resolution, the trigger system uses their signals and they measure the second coordinate in a direction being perpendicular to that measured by the precision chambers.

2.3.3 Calorimeters

Energies of particles are determined by the ATLAS calorimetry system which is split into an electromagnetic calorimeter, a hadronic barrel calorimeter, hadronic end-cap calorimeters and forward calorimeters, see Fig. 2.5.

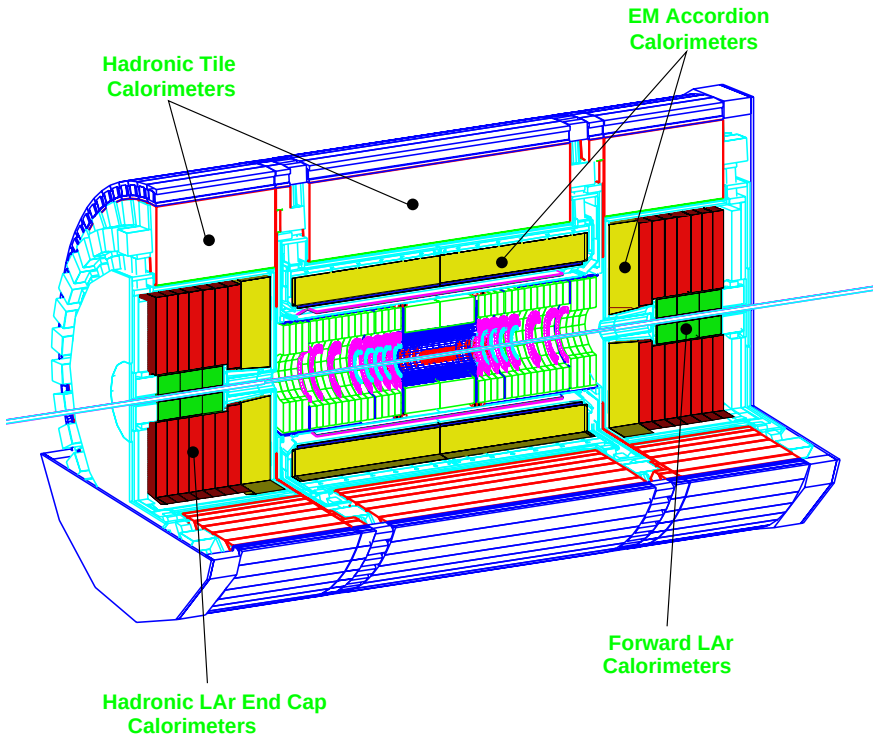

Fig. 2.5: Three-dimensional cutaway view of the ATLAS calorimeters [AT99].

The electromagnetic calorimeter is a lead/liquid-argon detector. Its barrel part is contained in a barrel cryostat which surrounds the Inner Detector and houses also the solenoid magnet. This magnet supplies a 2 T strong magnetic field for the Inner Detector. The electromagnetic calorimeter has a thickness of > 24 radiation lengths in the barrel part and > 26 radiation lengths in the end-caps.
The hadronic calorimeter is used for the energy measurement of hadronic showers which are not contained in the electromagnetic calorimeter. The hadronic barrel calorimeter consists of three cylindrical parts and is based on a sampling technique with plastic scintillator plates (tiles) embedded in an iron absorber. In the high-irradiation region towards high rapidities the liquid-argon (LAr) technique is used because of its superior radiation hardness for all calorimeters. The thickness of the hadronic calorimeter corresponds to 11 interaction lengths at $\eta = 0$.

2.3.4 Inner Detector

The particles which have been measured by the calorimeters have to be tracked back to the interaction point. The bending of the particles' tracks has to be measured as well in order to determine the momenta. This demand is fulfilled by the Inner Detector which is the subdetector being closest to the interaction point (IP) [AT97].

Due to the high number of collisions per bunch crossing (see Fig. 2.6), high multiplicities in the events and the detector's close proximity to the IP, a high granularity and fast readout are necessary. Especially B-physics, b-quark tagging and other tasks require highly precise tracking and a good secondary vertex detection.

A further consequence of the close proximity to the interaction point is an extremely high radiation load. The innermost parts are designed to be still operable for fluences equivalent to $1 \cdot 10^{15}$ 1-MeV-n/cm^2 and ionisation doses of 500 kGy.

A further requirement is to use as few material as possible for the detector in order to reduce nuclear interactions and multiple scattering within the detector material since otherwise the performance of the whole ATLAS detector would suffer.

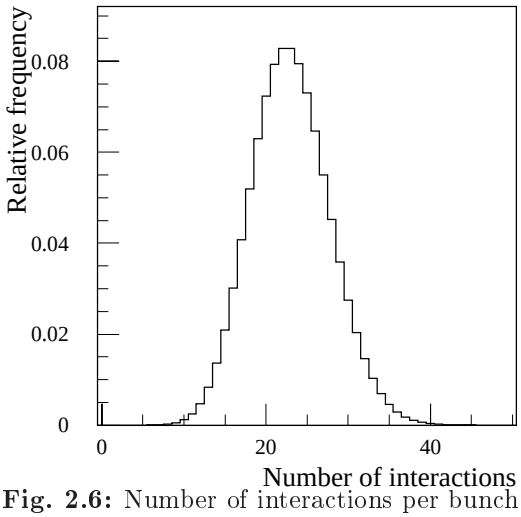

Fig. 2.6: Number of interactions per bunch crossing at full luminosity [AT97].

Fig. 2.7 shows a schematic drawing of the Inner Detector. The Inner Detector consists of three subsystems: closest to the interaction point the pixel detector is situated. Due to its relevance for this work it will be described separately in sec. 2.4. The pixel detector is enclosed by the Semiconductor Tracker (SCT) and the Transition Radiation Tracker (TRT). Fig. 2.8 shows the hits in the tracking system (projected on the r-ϕ-plane) from a simulated $H \rightarrow \mu^+\mu^-e^+e^-$

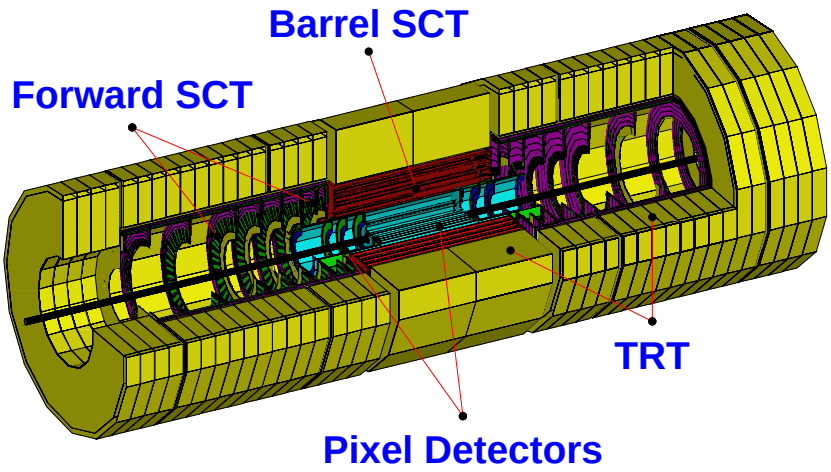

Fig. 2.7: View of the Inner Detector. It consists from inside to outside of the Pixel Detector, the Semiconductor Tracker (SCT) and the Transition Radiation Tracker (TRT).

event and underlying background events. This picture demonstrates the high number of tracks that have to be separated.

The SCT is designed to provide four precision measurements per track in the intermediate radial range. It is built from silicon strip detectors having a total area of 61 m^2 with 6.2 millions readout channels. The spatial resolution is 16 μm in r-ϕ-plane and 580 μm in z-direction. The detector can distinguish tracks which are separated by more than 200 μm.

The mechanical structure of the SCT has four complete barrels mounted at radii of 30.0 cm, 37.3 cm, 44.7 cm and 52.0 cm. Additionally, it has nine wheels with up to three rings of modules in each direction.

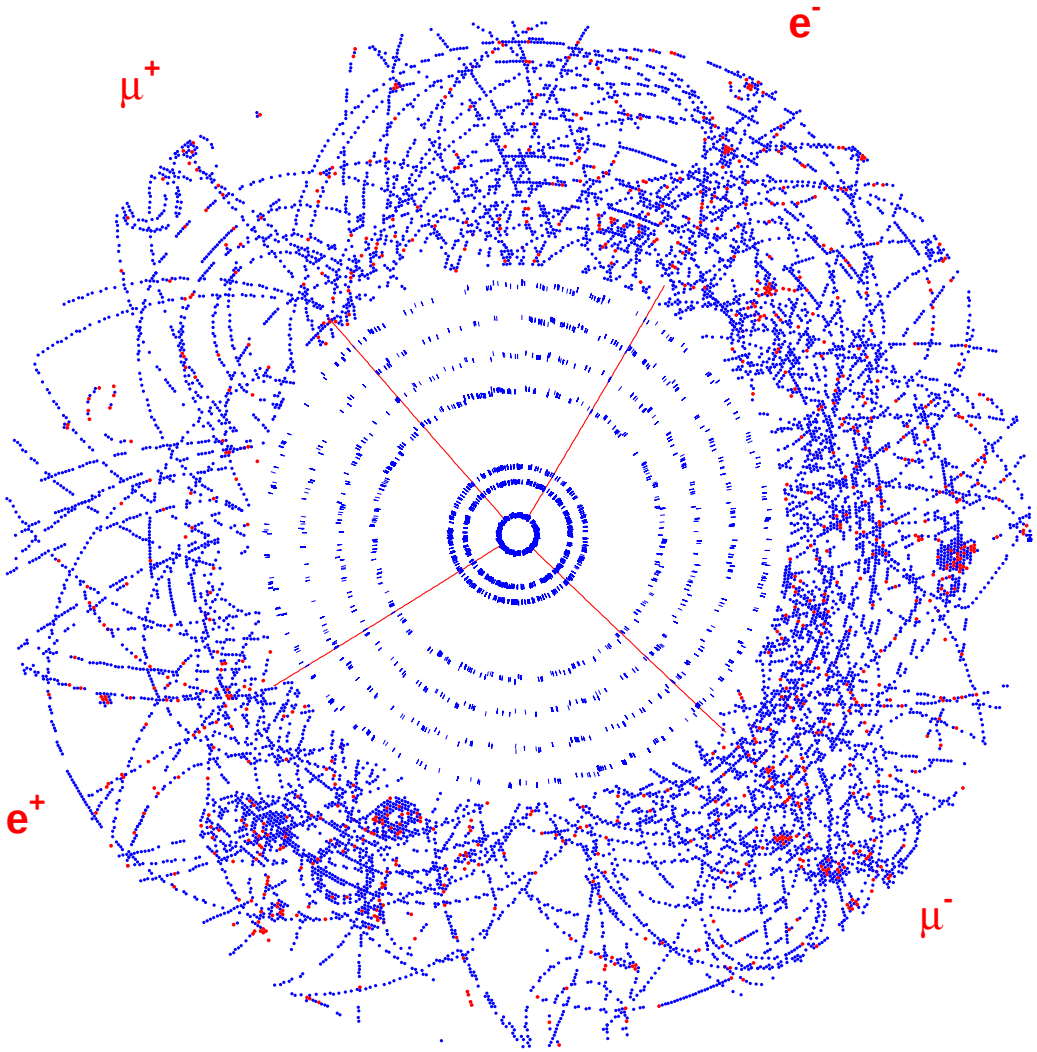

Fig. 2.8: Projection of tracks from a simulated $H \to \mu^+\mu^- e^+ e^-$ event ($m_H = 130\,\mathrm{GeV}$) on the r-ϕ-plane in the barrel part of the Inner Detector [AT97].

The Transition Radiation Tracker (TRT) is built from straw detectors consisting of 4 mm thick aluminium tubes with a sense wire. With the help of a radiator between the straws it can distinguish electrons from other charged particles by detecting transition radiation photons: due to the transition radiation the signal from fast electrons is significantly higher than that from other particles leading to a good background rejection.

2.4 Pixel Detector

2.4.1 Physics Requirements

The ATLAS Pixel Detector is designed to provide robust pattern recognition together with excellent vertexing capacities [AT97]. It measures a minimum of three space points for tracks in the pseudorapidity-range of $|\eta| < 2.5$.
The physics requirements demand a b-tagging efficiency of 50% with a rejection factor of about 100 against light-quark jets. This is necessary for the detection of Higgs and SUSY signals at low and high luminosity runs of LHC. Additionally studies of the decays of B-hadrons are of great interest. These studies include the search for CP-violation, mixing angles, rare B-decays and B-hadron spectroscopy. Therefore, the detection of leptons and hadrons with low transverse momentum in combination with a good vertex resolution is of great importance. Detection of secondary vertices and the impact parameter resolution depend on the pixel point resolutions and on the material thickness traversed by the particles.
The development work of the pixel detector is aimed at point resolutions of $\sigma_{r\phi} = 12\,\mu$m and $\sigma_z = 60\,\mu$m assuming a binary read-out scheme.

2.4.2 Overall Layout

For this innermost part of the ATLAS tracking system silicon detectors have been chosen due to their short read-out time. R&D work which has been performed over the last years by the RD2-collaboration [RD2], the ATLAS Pixel Collaboration and the RD48-collaboration [RD48], has also proven that the radiation hardness of this material is simply the best even for the harsh radiation environment of the ATLAS Pixel Detector. Pixelisation of the sensors provides the necessary granularity to work in the high track-density environment with sufficient position resolution and occupancy.
The ATLAS Pixel Detector will consist of 1744 modules. A *module* has an active size of 16.4 mm by 60.8 mm and provides 47 232 pixels. Most of the pixels have a size of $50 \times 400\ \mu\text{m}^2$.
The modules are arranged in three barrel layers and three discs on each side (see Fig. 2.9). They form a 1.4 m long and 0.5 m thick cylinder. The three barrel layers have radial positions of 5.05 cm, 8.85 cm and 12.25 cm. They are built from 22, 38 and 52 staves, respectively. The staves are rotated by 20° in azimuth. Each stave is composed of 13 modules. The disks are positioned at $z = 49.5$ cm, 58.0 cm and

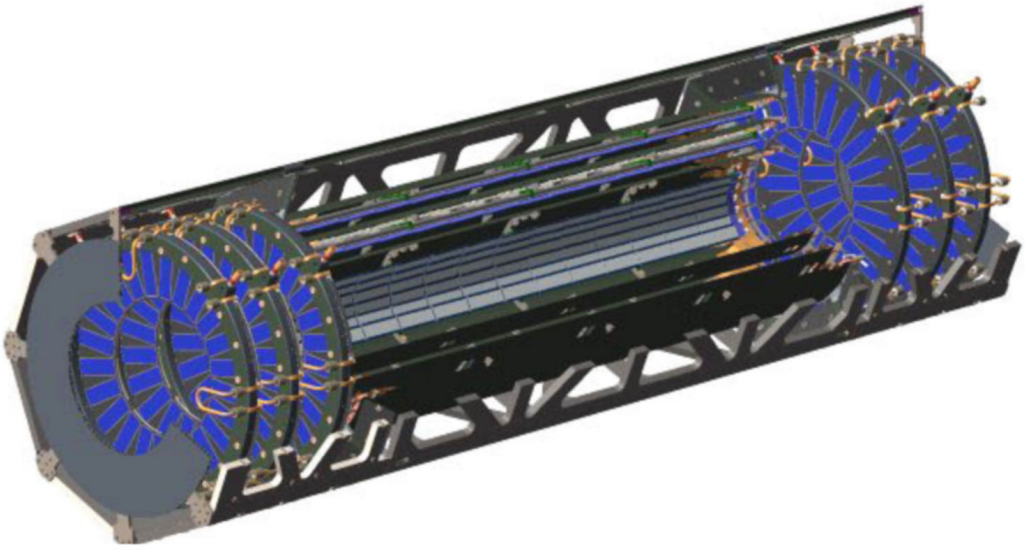

Fig. 2.9: Perspective view of ATLAS Pixel Detector consisting of three barrel layers and six discs mounted in a supporting frame.

65.0 cm. They are made from 8 sectors having 6 modules each, which are identical to those of the barrel.

2.4.3 Radiation Environment

Due to its position close to the interaction point the ATLAS pixel detector has to operate in a harsh radiation environment. Simulations with a model detector were used to predict the radiation field [AT98]. DTUJET code [Bo94] was used to generate minimum bias particles and the transport of particles through the detector material was simulated with the FLUKA transport code [Fa94]. Table 2.3 contains the radiation loads for the barrel layers of the ATLAS pixel detector as given in [AT98]. The radiation load of the discs is comparable to that of Layer 2. However, the distances to the beam axis as given in Table 2.3 are not up-to-date since the layout of the detector has been changed in the meantime. But

element	r [cm]	z [cm]	annual fluence [$10^{13}\,\mathrm{cm}^{-2}$]	total fluence [$10^{14}\,\mathrm{cm}^{-2}$]
B-layer (5 yrs)	4.3	0	34.8	10.44
Layer 1	10.1	0	8.3	6.64
Layer 2	13.2	0	5.0	4.0

Table 2.3: Maximum annual fluences at a luminosity of $10^{34}\,\mathrm{cm}^{-2}\mathrm{s}^{-1}$ and total fluences over 10 years (B-layer 5 years) for the pixel detector. The numbers are given for the old positions, see text for details.

these values will be used later in chapter 11 to obtain numbers for the radiation load at the actual positions. The charged fractions of the particle flux are 85% for the B-layer and 70% for Layer 1 (at the old positions).

2.4.4 Module Design

The modules consist of the rectangular sensor tile, 16 front-end (FE) electronic chips and the *Module Control Chip* (MCC). The FE chips are flip-chipped to the n-side of the sensor. The sensor's p-side is covered by a flex-hybrid carrying the module control chip (MCC) and further electronic parts. Supply with several voltages (for sensor biasing and electronics powering) and connection with the data acquisition system (DAQ) is made via the so-called *pig-tail*. Fig. 2.10 shows a drawing and a photograph of a pixel module.

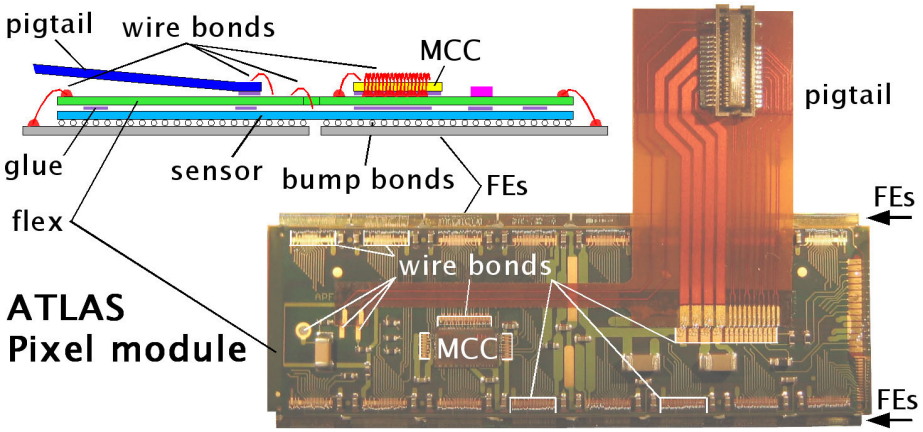

Fig. 2.10: Layout and photograph of pixel module [Do04].

FE chips have 2 880 read-out cells each of them containing an amplifier and an analog-to-digital converter. The amount of charge is described by the time over threshold (TOT) being the time the amplifier output stays above a certain (selectable) threshold. Furthermore, each FE pixel contains a small memory and functionality to change settings like thresholds. The data from the pixel cells are piped to the end-of-column logic at the edge of the chip.
The FE chips are connected via bump-bonds to the pixel sensor so that each of the pixels is connected to one read-out cell, see Fig. 2.11. By this connection the n-side of the pixel-sensor is grounded and read-out. The high-voltage is brought to the p-side of the sensor by a contact from the flex-hybrid.
The module control chip controls and reads out the FE chips. It processes the data and sends them over the pig-tail to the DAQ.

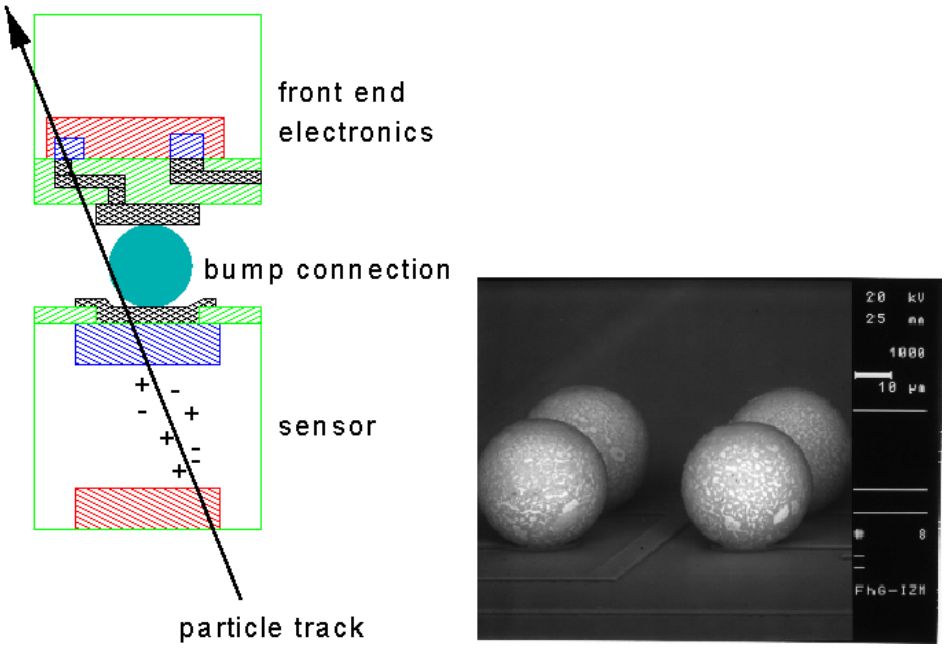

Fig. 2.11: Schematic drawing of the connection technique between pixel cell and corresponding front-end electronic by bump-bonding.

2.4.5 Sensor Design

The sensors are produced on n-type substrate silicon wafers. The first production step is the growth of an silicon oxide layer on both sides. On the n-side this oxide is opened by etching for the n-implantations. After the implantation the wafer is covered by a nitride layer and an aluminium layer. The whole wafer is protected by a passivation layer which is only opened for electric contacts.

The sensor is segmented in 47 232 pixel cells which are arranged in rows and columns (columns numbered along long side of pixels). One FE chip reads out the pixel cells of 18 columns and 164 rows. A normal pixel cell has a size of $50\,\mu\text{m} \times 400\,\mu\text{m}$. Since connections between sensor and electronic cannot be made between the edges of two neighbouring FE chips the pixels of the two outermost columns in every FE region are *long pixels* i.e. they have dimensions of $50\,\mu\text{m} \times 600\,\mu\text{m}$. The same problems exists for the other side of a FE region. Therefore, the uppermost 4 rows of a FE region consist of *ganged pixels*: their pixels are connected by metal-lines with other pixels from lower rows and read-out by the same FE chip cell. The resulting ambiguity of the track position must be resolved later in the event analysis. By this method the 47 232 pixels of a sensor tile are connected to 46 080 read-out channels of a module.

For the ATLAS Pixel Detector a sensor design with n^+ (highly n-doped) pixels on n-substrate has been chosen. The other side of the wafer is highly p-doped (see

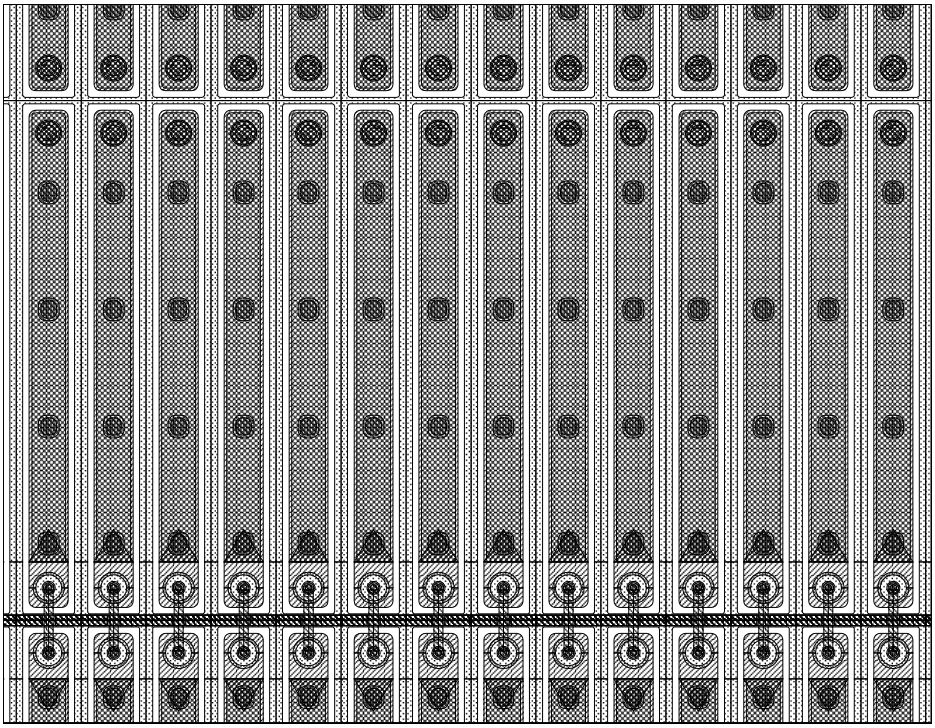

Fig. 2.12: Section from sensor with pixel cell array. Dark shaded areas are the n-implantations. The four small dark circles are openings in the nitride which enable the electric connection between n-implantation and metal layer. The uppermost circle in a pixel is bump-pad which used for electric contact to the FE electronics. At the lower edge one can see the bias grid which runs through every second column of pixels. Every pixel is surrounded by an opening of the nitride layer in order to moderate the p-spray dose.

chapter 3 for explanation of working principle of semiconductor detectors). Before the sensor has been irradiated above type-inversion (see chapter 4) the depletion zone grows from the p-side towards the n-side. Due to its low depletion voltage before irradiation the volume of the sensor can be fully depleted and thus it has its maximum sensitivity for particles. After type-inversion the depletion zone starts to grow from the n-side. Therefore, the pixelated side of the sensor is always at the depletion zone even if not the whole sensor is depleted which will be the case after irradiation with high fluences.

Fig. 2.12 shows the layout of an array of pixel cells (n-side of wafer). Each pixel has an n^+-implantation having a size of $30\,\mu\text{m} \cdot 380\,\mu\text{m}$. The implantation is covered by a metal strip. Openings in the oxide provide electrical contact between implantation and metal. The uppermost "circle" on a pixel cell as shown in Fig. 2.12 is an passivation opening. It serves as bump-bond pad. The bump-bonds are built-up on it and provide the electrical connection to the pixel n-side.

In order to suppress cross-talk between pixels they have to be electrically isolated against each other. This is done with the so-called *p-spray* technique where a low

dose p-implantation is done over the complete wafer-surface without a mask. In the n-implantation the p-spray is overcompensated by the much higher concentration of n-dopants. In order to avoid field maxima at the rims of the n-implantations the p-spray has been *moderated* by openings in the nitride layer. Moderating leads to lower p-spray concentrations at the rims of the n-implantations. These openings can be seen in Fig. 2.12 as the atoll-like structure around and between the pixels. Normally pixels are electrically connected via their bump-pad. An additional possibility is the *bias-grid* which can be seen in Fig. 2.13. It provides contact to all pixels via punch-through contacts. The bias-grid can be used to contact all pixels during quality assurance measurements before module production. During the operation it ensures that pixels with failing bump-bond connections are not floating but have a potential that is only a few volts lower (the punch-through voltage) than that of the neighbouring pixels. This ensures a better homogenity of the electric field even in the case of missing bump-bonds. A more detailed description of the sensor design can be found in [AT98] and [Hü01].

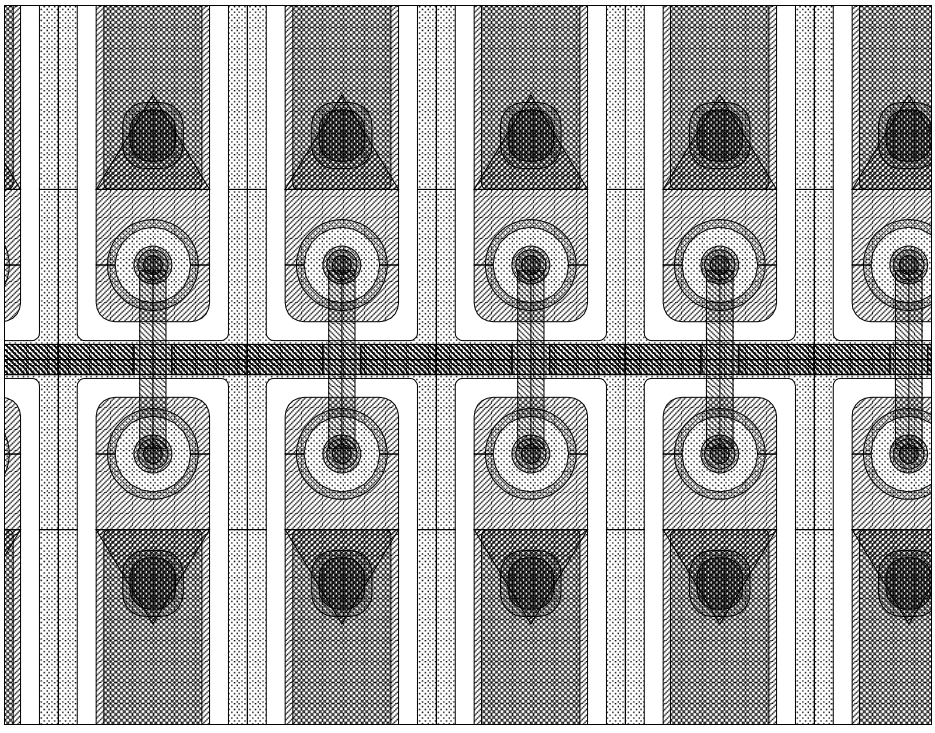

Fig. 2.13: Magnification from Fig. 2.12 showing the structure of the bias grid and the punch-through contact.

Chapter 3

Silicon Semiconductor Detectors

IN this chapter the basic properties of semiconductor detectors made from silicon will be introduced. After describing the mechanisms of energy deposition by ionising particles it will be explained how this deposited energy is detected in a semiconductor device and transformed to a measurable signal. Within this chapter only the properties of non-irradiated devices will be discussed. The effects of irradiation to detectors will be covered in chapter 4. Values for constants and material properties can be found in Tables A.1 and A.2 in app. A (p. 231).

3.1 Ionising Energy Deposition in Silicon

3.1.1 Charge Deposition

Ionising radiation being absorbed by a silicon crystal leads to free charge-carriers. As it will be described later these free charge-carriers can be used to form a measurable signal. The creation of free charge-carriers by ionisation and excitation is a reversible process which does not damage the crystal. Non-ionising energy loss (NIEL) that leads to permanent damage will be treated in chapter 4. The mechanisms for energy deposition depend on the kind of impinging particles. Therefore, also the distribution of deposited energy along the path of the particle depends on the kind of particle. In the following section the charge depositions mechanisms for several kinds of particles will be introduced.

3.1.2 Photons

This section focuses mainly on photons with wavelengths in the visible and infrared region as can be obtained from a laser: these relatively low energetic photons are absorbed due to the photo effect. More energetic photons which deposit energy also by compton scattering and pair-production are not considered here.

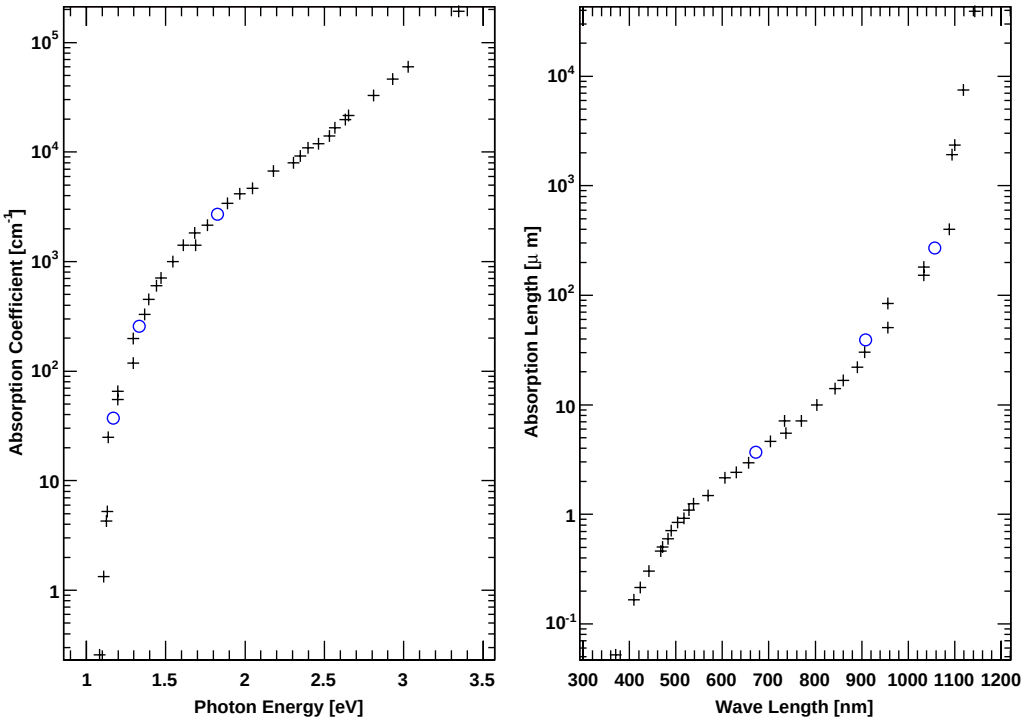

Fig. 3.1: Absorption coefficient vs. photon energy and absorption length vs. wavelength. The data (+) are taken from [Da55] ($T = 300\,\mathrm{K}$). The wavelengths of the lasers used for this work are marked with ∘ (interpolations of the data).

Because of the complete absorption of photons by photo effect and a constant absorption probability per length the beam intensity $I(x)$ drops exponentially:

$$I(x) = I_0\, e^{-\mu x}\ . \tag{3.1}$$

I_0 is the original intensity of the beam given as energy per area, x is the traversed material thickness and μ the absorption coefficient. This coefficient depends strongly on the wavelength of the laser light. Data on this dependence are displayed in Fig. 3.1. Table 3.1 gives the absorption lengths for some typical laser wavelengths which have been considered in the preparation phase of this work.
The exponential attenuation of the laser beam leads to a charge deposition profile which is exponential as well. The energy deposited up to a depth x in the device is given by

$$E(x) = A \cdot \int_0^x I_0\, e^{-\mu x}\, dx = A \cdot \frac{I_0}{\mu}\left(1 - e^{-\mu x}\right) \tag{3.2}$$

where A is the illuminated surface area.

λ [nm]	E_{phot} [eV]	$1/\mu$ [μm]
672	1.85	3.7
908	1.37	39.1
1057	1.17	270

Table 3.1: Wavelengths and photon energies E_{phot} of the lasers used for this work. The absorption lengths $1/\mu$ are taken from the data in Fig. 3.1.

3.1.3 α-Particles

α-particles traversing matter lose their kinetic energy by ionisation and excitation. Their differential energy loss along their path is described by the Bethe-Bloch formula for heavy particles [Gr93]:

$$-\frac{dE}{dx} = 4\pi N_0 r_e^2 m_0 c^2 z^2 \frac{Z}{A}\frac{1}{\beta^2}\left[\ln\left(\frac{2m_e c^2\gamma^2\beta^2}{I}\right) - \beta^2 - \frac{\delta}{2}\right] \tag{3.3}$$

The constants used are:

z	–	charge of particle in units of elementary charge
Z, A	–	atomic number and mass of the absorber
m_0	–	electron mass
r_e	–	classical electron radius
N_0	–	Avogadro's number
I	–	ionisation constant, property of the absorbing material, $I \approx 16\, Z^{0.9}$ eV
δ	–	parameter for description of density effect

α-particles are stopped in silicon after a relatively short track due to their high charge $z = 2$. As an example α-particles from a ^{241}Am-source are considered: this isotope emits particles with kinetic energies of 5.486 MeV and 5.443 MeV [KN95]. The mean penetration depth (i.e. the depth after which the particles are stopped) of these particles in silicon is $(28.06 \pm 0.31)\,\mu$m. This number is obtained from simulations done with the SRIM software[1]. The centre of gravity of the deposited charge is at $(16.3 \pm 8.0)\,\mu$m. The distributions of deposited energy and penetration depth are shown in Fig. 3.2.

3.1.4 MIPs/β-Particles

Particles whose energy is in the region of the minimum of differential energy loss as described by the Bethe-Bloch formula are called *minimum ionising particles*

[1] SRIM is a Monte Carlo simulation which can calculate the energy deposition of ions in matter. A description can be found in [Zi85].

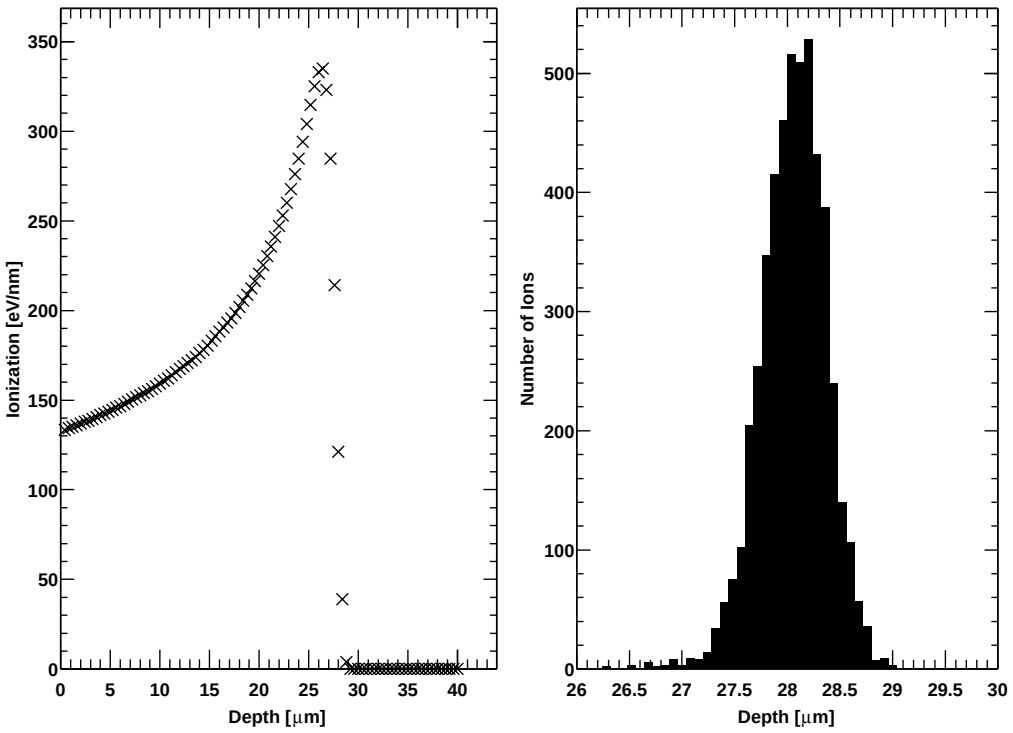

Fig. 3.2: Distribution of deposited energy (left, clearly seeable Bragg peak) and penetration depth (right) for α-particles with an energy of 5.486 MeV in silicon. The results are obtained from SRIM simulations of 5 000 single particles.

(mips). They lose only little energy per length and thus they deposit their energy—different from laser and α-particles—uniformly along the track. During operation the ATLAS pixel detector has to detect mips. The differential energy loss in silicon is [Lu99]

$$\left.\frac{dE}{dx}\right|_{\text{min}} = 3.8 \text{ MeV/cm}\,. \tag{3.4}$$

The Bethe-Bloch formula describes only the *mean* energy loss $\Delta\overline{E}$ per length. The fluctuation around $\Delta\overline{E}$ is described by the Landau distribution. It is relatively complicated to fit this function to measured data because it is given by the Laplace transform of the function s^s. A simpler approach is given by the Moyal approximation to the Landau distribution [Gr93, Bo98]:

$$L(\lambda) = \frac{1}{\sqrt{2\pi}} \cdot \exp\left(-\frac{1}{2}\left(\lambda + e^{-\lambda}\right)\right) \tag{3.5}$$

with

$$\lambda(\Delta E) = \frac{\Delta E - \Delta E_{\text{mp}}}{\xi}\,. \tag{3.6}$$

λ is the normalised deviation of the deposited energy ΔE from the most probable energy loss ΔE_{mp}. The normalisation factor ξ is proportional to the thickness d of the absorber and has the dimension of an energy:

$$\xi = 2\pi N_0 r_e^2 m_e c^2 z^2 \frac{Z}{A}\frac{1}{\beta^2}\rho d = \kappa \rho d\,. \tag{3.7}$$

The most probable energy loss ΔE_{mp} is different from the mean energy loss $\Delta\overline{E}$ because the Landau distribution is asymmetric. It has a long tail towards high energy losses which is caused by single high energy transfers to electrons (δ-electrons).
In order to make laboratory measurements with particles penetrating the whole detector radiation from an ^{90}Sr source can be used to inject charges. This isotope makes a β-decay in ^{90}Y. The maximum energy of the emitted electron is 0.5 MeV. ^{90}Y converts into the stable ^{90}Zr by a further β-decay with a maximum energy of 2.3 MeV. The half-lifes of the two subsequent decays are 28.64 a and 64.1 h [KN95]. The source used for this work was several years old, so it can be considered as being in the radioactive balance. Therefore, the emitted radiation originates to equal parts from both decays.

3.2 pn-Junction

3.2.1 Intrinsic Semiconductors

In intrinsic semiconductors the number of impurities is small compared to the number of thermally generated (free) electrons and holes. The electric properties of semiconductors can be explained by the band theory [Lu99]: in this model the energetically possible electron states lie either in the valence band or in the energetically higher conduction band (see Fig. 3.3). The highest energy of the valence band is denoted by E_V, the lower edge of the conduction band is E_C. The range between these two bands is called *band gap*. Its width $E_G = E_C - E_V$ is 1.12 eV for silicon. The band gap is a zone which is energetically forbidden for electrons. At low temperatures all states of the valence band are occupied while

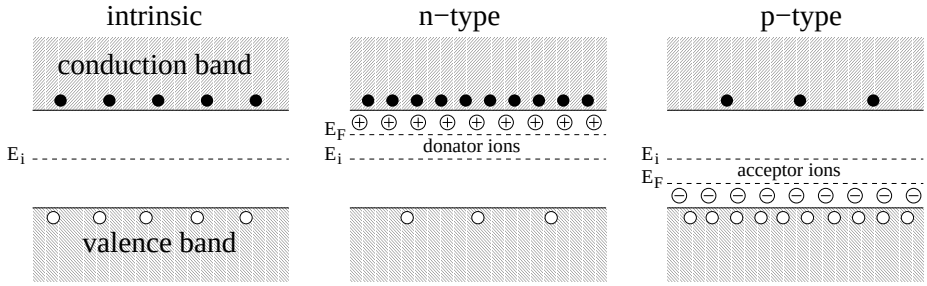

Fig. 3.3: Energy band structure of semiconductors. On the left hand side intrinsic semiconductor, in the middle extrinsic semiconductor of n-type with donators and on the right hand side p-type with acceptors.

the conduction band is empty. In this condition the conductivity of the crystal is zero. At elevated temperatures the conduction band becomes partly occupied by electrons from the valence band. After going up to the conduction band the electrons leave behind an unoccupied state in the valence band (a so-called *hole*) which can be considered as a positive charge-carrier. Both types of charge-carriers contribute now to the conductivity of the semiconductor which is increasing with temperature.
The occupation probability of an electronic state with energy E at temperature T is described by the Fermi-Dirac statistics:

$$F(E) = \frac{1}{1 + \exp\left(\frac{E-E_F}{kT}\right)} . \tag{3.8}$$

The Fermi energy E_F is the energy with the occupation probability $\frac{1}{2}$, k is Boltzmann's constant. For E_F being not too close to the edges of conduction or valence band the expression in eq. (3.8) can be approximated by

$$F_e(E) \approx e^{-\frac{E-E_F}{kT}} \qquad \text{and} \tag{3.9}$$

$$F_h(E) = 1 - F(E) \approx e^{-\frac{E_F-E}{kT}} . \tag{3.10}$$

for electrons (index e) and holes (index h), respectively. Typically, this approximation is valid as E_F normally is situated close to the middle of the band gap.
The density of states for electrons with kinetic energy E_{kin} is

$$N(E_{\text{kin}})dE_{\text{kin}} = 4\pi \left(\frac{2m_{\text{eff}}}{h^2}\right)^{\frac{3}{2}} E_{\text{kin}}^{\frac{1}{2}} dE_{\text{kin}} . \tag{3.11}$$

For the mass of the charge-carriers the effective masses m_{eff} have to be used (m_e for electrons, m_h for holes). The kinetic energy is measured from the band edges, i.e. for electrons from the lower edge of the conduction band upwards and for holes from the upper edge of the valence band downwards.
The density n_e of free electrons is given by the integral over the product of density of states N and occupation probability F_e for electrons:

$$n_e = 2\left(\frac{2\pi m_e kT}{h^2}\right)^{\frac{3}{2}} e^{-\frac{E_C-E_F}{kT}} = N_C e^{-\frac{E_C-E_F}{kT}} . \tag{3.12}$$

The integration interval is the conduction band. For holes the integration yields correspondingly

$$n_h = 2\left(\frac{2\pi m_h kT}{h^2}\right)^{\frac{3}{2}} e^{-\frac{E_F-E_V}{kT}} = N_V e^{-\frac{E_F-E_V}{kT}} . \tag{3.13}$$

N_C and N_V are the effective densities of states in the conduction and valence band, respectively. The product

$$n_e \cdot n_h = N_C N_V e^{-\frac{E_C-E_V}{kT}} = N_C N_V e^{-\frac{E_G}{kT}} \tag{3.14}$$

is independent of the Fermi energy E_F. It depends only on the magnitude of the band gap E_G. The Fermi level for intrinsic semiconductors E_i can be derived from the condition that the number of holes equals the number of electrons: $n_e = n_h = n_i$. Thus it is

$$n_i = \sqrt{N_C N_V} e^{-\frac{E_C - E_V}{2kT}} = \sqrt{N_C N_V} e^{-\frac{E_G}{2kT}} \tag{3.15}$$

for the intrinsic charge-carrier density n_i. Furthermore, the Fermi level of the intrinsic semiconductor is given by

$$E_i = \frac{E_C + E_V}{2} + \frac{3kT}{4} \ln \frac{m_h}{m_e} \,. \tag{3.16}$$

E_F is close to the middle of the band gap, the deviation results from the difference in the effective masses of electrons and holes. The intrinsic level E_i defined by this is also important for extrinsic semiconductors which are treated in the following course of the discussion. With the introduction of the intrinsic charge-carrier density n_i eqs. (3.12) and (3.13) can be rewritten as

$$n_e = n_i \, e^{\frac{E_F - E_i}{kT}} \quad \text{and} \quad n_h = n_i \, e^{\frac{E_i - E_F}{kT}} \text{ , respectively.} \tag{3.17}$$

3.2.2 Extrinsic Semiconductors

Extrinsic semiconductors can be obtained by adding small amounts of impurities during fabrication of the semiconductor device. This can either happen during crystal growth for the whole crystal or later when processing of the surface is done by implantation of impurity atoms. The process of intended addition of impurities is called *doping*. As an element of the IVth main group silicon has four electrons in its outer shell. In a crystal it forms covalent bonds with four neighbours leading a tetraedric crystal structure (diamond lattice). Dopant atoms have either one electron more (*donors*, elements of the Vth main group) or one electron less (*acceptors*, IIIrd main group) in their outer shell. Those impurities act as dopants as they are still integrated into the crystal structure like Si atoms with four covalent bonds to their neighbours. Therefore, the donors lose their additional electron which can move freely in the crystal. Analogously, the acceptors gather an electron to form four covalent bonds. By these processes the dopant atoms remain as fixed *space-charges* in the crystal. Donors contribute positively, acceptors contribute negatively to the space-charge density. The doping with donors is called *n-doping* while introduction of acceptors is called *p-doping*.
n-doping introduces additional states with energy level E_D into the band gap close to the conduction band edge (see Fig. 3.3). Even at low temperatures electrons from these states can be excited and get into the conduction band. Phosphorus ($E_C - E_D = 0.045\,\text{eV}$) and arsenic ($E_C - E_D = 0.054\,\text{eV}$) can be used as donors. Correspondingly, acceptors constitute energy levels E_A close to the valence band edge. They can take electrons out of the valence band leading to creation of free holes. p-doping can be done e.g. by introduction of boron ($E_A - E_V = 0.045\,\text{eV}$).

These additional levels correspond to a shift of the Fermi level. In the case of n-doping E_F moves towards the conduction band while p-doping lowers E_F towards the valence band.
The value of E_F in n-doped material can be derived up to high doping concentrations from eq. (3.12) by setting the electron concentration in the conduction band equal to the donor concentration. Thus

$$E_C - E_F = kT \ln \frac{N_C}{N_D} . \tag{3.18}$$

Analogously, the according expression for p-doping can be derived from eq. (3.13):

$$E_F - E_V = kT \ln \frac{N_V}{N_A} . \tag{3.19}$$

Electrons in an n-type semiconductor are called *majority charge-carriers*. The still — but much smaller in number — existing holes are named *minority charge-carriers*. In the case of a p-type semiconductor holes and electrons are named analogously.

3.2.3 Charge-Carrier Transport

Movable charge-carriers in a semiconductor can be considered as free particles whose kinetic energy is $\frac{3}{2}kT$. Their mean velocity is in the order of 10^7 cm/s. They interact with imperfections of the lattice which are caused by lattice vibrations, crystal defects and impurities. The mean free path is about 10^{-5} cm and the mean free time is $\tau_f \approx 10^{-12}$ s. This thermal movement causes on average no displacement.
In an electric field the charge-carriers start to drift. The drift velocities $v_{\mathrm{dr},e}$ and $v_{\mathrm{dr},h}$ of electrons and holes depend on the field strength and the effective masses m_e and m_h:

$$\vec{v}_{\mathrm{dr},e} = -\frac{e_0 \cdot \tau_f}{m_e}\vec{E} = -\mu_e \vec{E} , \tag{3.20}$$

$$\vec{v}_{\mathrm{dr},h} = \frac{e_0 \cdot \tau_f}{m_h}\vec{E} = \mu_h \vec{E} . \tag{3.21}$$

In these equations the *mobilities* μ_e and μ_h are introduced. Charge-carriers can also be transported by diffusion. Diffusion is caused by an inhomogeneous distribution of charge. Therefore, it is proportional to the gradient of charge-carrier density:

$$\vec{F}_e = -D_e \cdot \vec{\nabla} n_e , \tag{3.22}$$

$$\vec{F}_h = -D_h \cdot \vec{\nabla} n_h . \tag{3.23}$$

$\vec{F}_e$ and $\vec{F}_h$ are the fluxes of electrons and holes. The magnitude of diffusion is governed by the diffusion constants D_e and D_h. The current densities of charge-carriers are the combination of drift and diffusion, therefore

$$\vec{J}_e = e_0 \mu_e n_e \vec{E} + e_0 D_e \vec{\nabla} n_e \quad \text{and} \tag{3.24}$$

$$\vec{J}_h = e_0 \mu_h n_h \vec{E} + e_0 D_h \vec{\nabla} n_h . \tag{3.25}$$

Mobilities and diffusion constants are related to each other by the Einstein equations:

$$D_e = \frac{kT}{e_0}\mu_e \quad \text{and} \quad D_h = \frac{kT}{e_0}\mu_h \,. \tag{3.26}$$

3.2.4 pn-Junction

A pn-junction consists of the direct connection of a p-type with an n-type semiconductor (see Fig. 3.4). Connecting them leads to diffusion of charge-carriers due to different concentrations of charge-carriers in the two regions. Electrons move from the n-side to the p-side and recombine there with holes. Analogously, holes move into the opposite direction. Due to recombination free charge-carriers vanish and leave behind the charged dopant atoms as fixed space charges. The region without free charge-carriers is called *space charge region* (SCR).

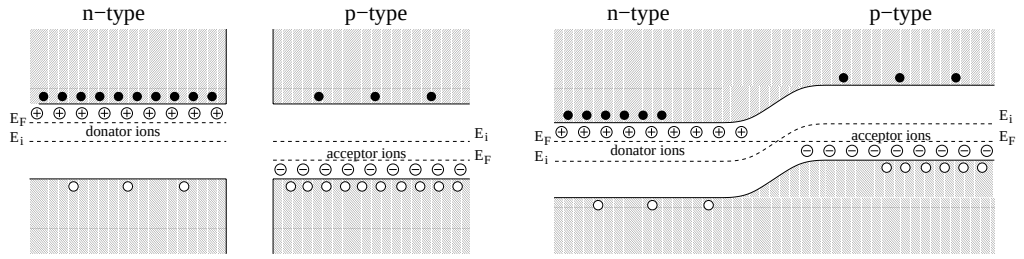

Fig. 3.4: Band structure of a pn-junction. Left side shows the two semiconductors before contacting them, right side after connecting.

The space charges cause an electric field which makes charge-carriers drift in the opposite direction of the diffusion. The space charge region grows until an equilibrium between drift and diffusion is reached. This effect limits the depth of the space charge region.

A pn-junction is described in the band theory by a bending of the bands: the energy levels in the p-zone are raised by $e_0 V_{\mathrm{bi}}$ where V_{bi} is the so-called *built-in voltage*. This voltage is not caused by an externally applied voltage. The magnitude of the band bending can be determined considering the condition that the Fermi levels have to line up.

The built-in voltage V_{bi} is derived from the difference of the intrinsic levels in the neutral n- and p-zones. The concentrations of the majority charge-carriers in the n-type semiconductor $n_{e,n}$ and the majority concentration in the p-type region $n_{e,h}$ result from (3.17):

$$\left.\begin{aligned} n_{e,n}{=}N_D{=}n_i\, e^{\frac{E_F - E_i^n}{kT}} \\ n_{h,p}{=}N_A{=}n_i\, e^{\frac{E_i^p - E_F}{kT}} \end{aligned}\right\} \Rightarrow N_A \cdot N_D = n_i^2\, e^{\frac{E_i^p - E_i^n}{kT}} \tag{3.27}$$

with N_D being the donor concentration in the n-type region and N_A being the acceptor concentration in the p-type region. For the desired built-in voltage V_{bi} follows

$$V_{\mathrm{bi}} = \frac{1}{e_0}(E_i^p - E_i^n) = \frac{kT}{e_0} \ln \frac{N_A N_D}{n_i^2} \,. \tag{3.28}$$

In order to calculate the depth of the space charge region an abrupt change from n- to p-type at the junction is considered. As the electric field has to vanish at the borders of the space charge region the total charge within the SCR has to be zero:

$$N_D \, d_n = N_A \, d_p \,. \tag{3.29}$$

d_n and d_p are the depths of the space charge region in the n-region and the p-region, respectively. The electric field strength at the junction can be calculated with Gauss' law as integral over the charge density ρ:

$$\int\limits_{\partial V} \vec{E} \cdot \, d\vec{a} = \frac{1}{\varepsilon \varepsilon_0} \int\limits_{V} \rho \, dV \,. \tag{3.30}$$

A coordinate system is introduced for the following calculations as indicated in Fig. 3.5: the x-axis runs perpendicular through the plane of the pn-junction. The junction is at $x = 0$, positive x run towards the n-zone.
The volume V which is used for integration is a cuboid with cross-section A. A is parallel to the plane of the junction and the depth of the volume is x. One of the two sides being perpendicular to the x-direction is in the space-charge region. The opposite side is far enough away, so the field vanishes at that point. For reasons of symmetry all field lines are perpendicular to the plane of the pn-junction. With $dV = A \cdot dx$ and $\rho = e_0 N_D$

$$E(x) \cdot A = \frac{1}{\varepsilon \varepsilon_0} \int\limits_{0}^{x} e_0 N_D A \, dx \tag{3.31}$$

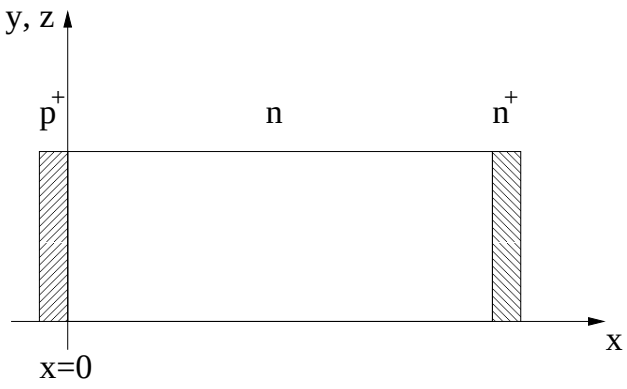

Fig. 3.5: The coordinate system which is used for calculations.

follows from eq. (3.30). Therefore, solving the integral in eq. (3.31) for the interval $0 \leq x \leq d_n$ yields the field strength at the pn-junction ($x = 0$) as

$$E_{\max} = \frac{1}{\varepsilon\varepsilon_0} e_0 N_D d_n = \frac{1}{\varepsilon\varepsilon_0} e_0 N_A d_p \,. \tag{3.32}$$

The field strength drops from this maximum to zero at the border of space-charge region. So the voltage drops in the n- and p-region are

$$V_n = \frac{E_{\max} d_n}{2} = \frac{1}{\varepsilon\varepsilon_0} \frac{e_0 N_D d_n^2}{2} = \frac{1}{\varepsilon\varepsilon_0} \frac{e_0 N_A d_p d_n}{2} \quad \text{and} \tag{3.33}$$

$$V_p = \frac{E_{\max} d_p}{2} = \frac{1}{\varepsilon\varepsilon_0} \frac{e_0 N_A d_p^2}{2} = \frac{1}{\varepsilon\varepsilon_0} \frac{e_0 N_D d_p d_n}{2} \,. \tag{3.34}$$

If the voltage across the pn-junction $V_n + V_p$ is set equal to the built-in voltage V_{bi} one obtains for the depth of the space charge region $d = d_n + d_p$

$$d = \sqrt{\frac{2\varepsilon\varepsilon_0 (N_A + N_D)}{e_0 N_A N_D} V_{\mathrm{bi}}} \tag{3.35}$$

and for the maximum field strength at the pn-junction

$$E_{\max} = \frac{1}{\varepsilon\varepsilon_0} e_0 N_D d_n = \sqrt{\frac{2e_0}{\varepsilon\varepsilon_0} \frac{N_A N_D}{N_A + N_D} V_{\mathrm{bi}}} \,. \tag{3.36}$$

For Si-detector the case of strong asymmetric doping is important. In many detectors a highly doped p-layer ("p^+") is put on an only lowly doped n-type bulk. In this case ($N_A \gg N_D$) the depth and the maximum field strength can be approximated by

$$d \approx \sqrt{\frac{2\varepsilon\varepsilon_0}{e_0 N_D} V_{\mathrm{bi}}} \qquad \text{and} \tag{3.37}$$

$$E_{\max} \approx \sqrt{\frac{2e_0}{\varepsilon\varepsilon_0} N_D V_{\mathrm{bi}}} \,. \tag{3.38}$$

3.2.5 pn-Junction with Externally Applied Voltage

A device with an externally applied voltage across the pn-junction is no longer in thermal equilibrium. Thus the equations derived up to this point are now valid only in an approximative way.
With an externally applied voltage $V_{\mathrm{bias}} > 0$ (*forward bias*) the voltage across the pn-junction drops to $V_{\mathrm{bi}} - V_{\mathrm{bias}}$. Consequently the depth of the space charge region shrinks to

$$d = \sqrt{\frac{2\varepsilon\varepsilon_0 (N_A + N_D)}{e_0 N_A N_D} (V_{\mathrm{bi}} - V_{\mathrm{bias}})} \tag{3.39}$$

$$\approx \sqrt{\frac{2\varepsilon\varepsilon_0}{e_0 N_D} (V_{\mathrm{bi}} - V_{\mathrm{bias}})} \,. \tag{3.40}$$

Eq. (3.40) holds for the case of a strongly asymmetric p^+-on-n doping. Contrarily, the application of a negative bias voltage (*reverse bias*) leads to a growth of the space charge region. By such a measure the space charge region — also called *depletion zone* — can be extended over the whole thickness of the device. The minimum bias voltage which is necessary to achieve this is called *depletion voltage* V_{dep}. For an asymmetric doped p^+-on-n diode with thickness d the depletion voltage is

$$V_{\mathrm{dep}} = \frac{e_0 N_D}{\varepsilon\varepsilon_0}\frac{d^2}{2}\,. \tag{3.41}$$

The depletion voltage is normally much higher than the built-in voltage, so that the latter can be neglected. Therefore, the thickness of the depletion zone is proportional to the square root of the applied bias voltage as can be derived from eq. (3.39).
For later applications it is important to know the field strength $E(x)$ in a fully depleted detector. $E(x)$ consists of two components:

$$E(x) = E_D(x) + E_0(x)\,. \tag{3.42}$$

$E_D(x)$ is the field which is caused by the space charges. It can be calculated with Gauss' law. For integration the same volume as above is used:

$$\int\limits_{\partial V} \vec{E}_D(x)\cdot d\vec{a} = \frac{1}{\varepsilon\varepsilon_0}\int\limits_V \rho\, dV \tag{3.43}$$

$$[E_D(0) - E_D(x)]\cdot A = \frac{1}{\varepsilon\varepsilon_0} e_0 N_D A x \tag{3.44}$$

$$E_D(x) = E_D(0) - \frac{1}{\varepsilon\varepsilon_0} e_0 N_D x\,. \tag{3.45}$$

$E_D(0)$ is the maximum of the field strength at the pn-junction which has already been calculated in eq. (3.32). From this it follows

$$E_D(x) = \frac{1}{\varepsilon\varepsilon_0} e_0 N_D (d_n - x)\,. \tag{3.46}$$

Together with eq. (3.41) this expression can be rewritten for fully depleted pn-junctions of thickness d as

$$E_D(x) = \frac{2V_{\mathrm{dep}}}{d}\left(1 - \frac{x}{d}\right)\,. \tag{3.47}$$

The previous equation describes the field due to the space charges. If V_{bias} exceeds V_{dep}, an additional component $E_0(x) = E_0 = \text{const.}$ must be added. This contribution must be constant because no further charges are introduced into the detector volume. In order to derive E_0 it is assumed that the p-side ($x = 0$) has

the potential $\varphi = 0$. The n-side is set to the potential $\varphi(x = d) = V_{\text{bias}}$. For the electric potential follows:

$$\varphi(x) = \int_0^x E(x')\,dx' = \int_0^x E_D(x') + E_0(x')\,dx' \tag{3.48}$$

$$= \int_0^x \frac{2V_{\text{dep}}}{d}\left(1 - \frac{x'}{d}\right) + E_0\,dx' \tag{3.49}$$

$$= \frac{2V_{\text{dep}}}{d}\left(x - \frac{x^2}{2d}\right) + E_0\,x\,. \tag{3.50}$$

Taking into account the boundary conditions it follows

$$\varphi(x = d) = V_{\text{dep}} + E_0\,d \stackrel{!}{=} V_{\text{bias}} \tag{3.51}$$

$$\Rightarrow E_0 = \frac{V_{\text{bias}} - V_{\text{dep}}}{d} \tag{3.52}$$

Therefore, the total electric field strength in a fully depleted detector is:

$$\begin{aligned} E(x) &= E_0 + E_D(x) \quad \text{with} \\ E_0 &= \frac{V_{\text{bias}} - V_{\text{dep}}}{d} \quad \text{and} \\ E_D(x) &= \frac{2V_{\text{dep}}}{d}\left(1 - \frac{x}{d}\right)\,. \end{aligned} \tag{3.53}$$

Analogously, one can derive $E(x)$ for a partially depleted detector which is depleted to a thickness $d_n < d$. d_n can be written as (cf. 3.41)

$$d_n = d \cdot \sqrt{\frac{V_{\text{bias}}}{V_{\text{dep}}}}\,. \tag{3.54}$$

for $V_{\text{bias}} < V_{\text{dep}}$. From eq. (3.46) follows for the field in a partially depleted detector

$$E(x) = \frac{2V_{\text{dep}}}{d_n}\left(1 - \frac{x}{d_n}\right) \tag{3.55}$$

$$= \frac{2V_{\text{dep}}}{d}\left(\sqrt{\frac{V_{\text{bias}}}{V_{\text{dep}}}} - \frac{x}{d}\right) \tag{3.56}$$

for $0 \le x \le d_n$. For $d_n < x \le d$ the field strength is zero.

3.2.6 Capacitance-Voltage-Characteristic

The capacitance-voltage characteristic (CV-characteristic) is important for the characterisation and quality control of detectors. Its theoretical derivation given here is again valid only for an asymmetric pn-junction. d denotes the depth of

the depletion zone and the neutral n-zone has zero potential. In order to derive the CV-characteristic a displacement of the border of the depletion zone from x to $x+dx$ is considered. By this displacement the surface charge density is reduced by $e_0 N_D\, dx$. The electric field strength changes by $\frac{e_0 N_D\, dx}{\varepsilon\varepsilon_0}$ and the external voltage by $x\frac{e_0 N_D dx}{\varepsilon\varepsilon_0}$. Executing the integration from $x = 0$ to $x = d$ it follows

$$Q_p = -\int_0^d e_0 N_D(x)\, dx \quad \text{and} \tag{3.57}$$

$$\psi_p = \int_0^d \frac{e_0 N_D(x)}{\varepsilon\varepsilon_0} x\, dx\,. \tag{3.58}$$

The potential difference ψ_p is the difference between externally applied voltage V_{bias} and built-in voltage V_{bi} (eq. (3.28)). The measured capacitance of the diode is

$$C = \frac{\partial Q_p}{\partial V} = \frac{\partial Q_p/\partial d}{\partial V/\partial d} \quad \text{with} \tag{3.59}$$

$$\frac{\partial Q_p}{\partial d} = -e_0 N_D(d) \quad \text{and} \tag{3.60}$$

$$\frac{\partial V}{\partial d} = \frac{-\partial\psi_p}{\partial d} + \frac{\partial V_{\text{bi}}}{\partial d} = -\frac{e_0 N_D(d)}{\varepsilon\varepsilon_0} d + \frac{kT}{e_0}\frac{1}{N_D(d)}\frac{\partial N_D(d)}{\partial d}\,. \tag{3.61}$$

This yields for the inverse capacitance

$$\frac{1}{C} = \frac{d}{\varepsilon\varepsilon_0} - \frac{1}{e_0 N_D(d)}\frac{\partial V_{\text{bi}}}{\partial d} = \frac{d}{\varepsilon\varepsilon_0} - \frac{kT}{e_0}\frac{1}{e_0 N_D^2}\frac{\partial N_D}{\partial d} \approx \frac{d}{\varepsilon\varepsilon_0} \quad . \tag{3.62}$$

The second term can be neglected for reverse bias. Thus the depletion depth d is

$$d = \frac{\varepsilon\varepsilon_0}{C}\,. \tag{3.63}$$

As it will be described later in chapter 4 irradiation introduces additional defects making the relation between d and capacitance more complicated. But nevertheless, the capacitance is still roughly proportional to the inverse thickness of the space-charge region.

3.3 Particle Detection

3.3.1 Creation of Free Charge-Carriers

Ionising energy loss (see sec. 3.1) leads to creation of electron-hole-pairs in the detector. Due to the small band gap ($E_G \approx 1.12\,\text{eV}$) a large quantity of free carriers is produced. The mean energy necessary to create one pair is $\approx 3.6\,\text{eV}$ for silicon [Lu99]. For instance, a mip that traverses 250 μm of silicon creates $\approx 26\,400$ pairs (cf. eq. (3.4)).
The injected charge-carrier pairs have to be separated by an electric field because otherwise they would recombine rather quickly. In the electric field the electrons

and holes drift towards their respective target electrodes. It is an important fact that only the depleted zone of the detector is sensitive for particle detection. The rest of the material—except for a small zone at the border of the depletion from where carriers can diffuse into the depletion zone—is insensitive to particles because holes and electrons recombine quickly if they are not separated by an electric field. In order to achieve a good charge collection efficiency and thereby strong signal it is important to deplete the detector as much as possible.
In the following discussion always an asymmetric pn-junction is considered. A p^+-doped layer is fabricated on top of an n-bulk. On the opposite side the surface is n^+-doped in order to get a good ohmic contact to the bulk. Both highly doped sides of the device are contacted by metal electrodes.

3.3.2 Mobility and Charge Collection Time

The mobilities μ_e and μ_h have already been defined in eqs. (3.20) and (3.21) on p. 30. A closer examination of the mobilities reveals a strong dependence on the field strength and the temperature. Thus the mobilities are considered as functions of this quantities in the following discussion.
The charge collection time t_c is the time which a charge-carrier needs to drift from its starting point x_0 to its target electrode:

$$t_c = \int_{x_0}^{x_z} \frac{1}{v_{\mathrm{dr}}(x)}\, dx = \int_{x_0}^{x_z} \frac{1}{\mu(E(x))E(x)}\, dx\,. \tag{3.64}$$

$v_{\mathrm{dr}}(x) = \mu(E(x))E(x)$ is the drift velocity which depends implicitly on the spatial variable x.

3.3.3 Signal Formation

The free charge-carriers start to drift towards their respective target electrodes after the passage of a particle. The signal currents at the electrodes rise as soon as a charge-carrier is moving in the detector. This effect can be explained in a simple way by the induction of charges on the electrodes and the concept of mirror charges. A more elaborate description is the Ramo theorem [Ra39]. This theorem states that the induced charge dQ is proportional to the drifting charge q:

$$dQ = q\,\vec{E}_{\mathrm{R}}(\vec{r}) \cdot \vec{v}_{\mathrm{dr}}(\vec{r})\, dt\,. \tag{3.65}$$

$\vec{E}_{\mathrm{R}}$ is the so-called *Ramo field*, which describes the electrostatic coupling of the drifting charge to the electrode. In order to derive eq. (3.65) a point-charge with charge q is considered in the presence of a number of grounded conductors. For one of these conductors, say C_1, the induced current is desired. The point-charge is thought to be surrounded by a tiny equipotential sphere S. Φ is the electrostatic potential in the region between the conductors. It must satisfy the Laplace equation:

$$\Delta\Phi = 0 \tag{3.66}$$

As the conductors are grounded Φ is zero at their positions, Φ_q shall be the potential of the tiny sphere around the charge. Then Gauss's law states

$$-\int\limits_{\partial S} \vec{\nabla}\Phi \cdot d\vec{a} = \frac{1}{\varepsilon\varepsilon_0} q\,. \tag{3.67}$$

Now another configuration is considered: The charge is removed, conductor C_1 is raised to unit potential ($\Phi|_{C_1} = 1$) and all other conductors are still grounded. The potential for this configuration is Φ', again fulfilling $\Delta\Phi' = 0$ in the space between the conductors, including the position where the electron was situated before. The new potential of this point is Φ'_q.
Now a volume R is considered which is bounded by the conductors and the tiny sphere S. Green's theorem states for the potentials in R

$$\int\limits_R \left(\Phi'\Delta\Phi - \Phi\Delta\Phi'\right)\, dV = -\int\limits_{\partial R} \left(\Phi'\vec{\nabla}\Phi - \Phi\vec{\nabla}\Phi'\right) \cdot d\vec{a}\,. \tag{3.68}$$

The left-hand side of this equation is zero ($\Delta\Phi = 0$ and $\Delta\Phi' = 0$). The right-hand side can be divided into three contributions:

1. Integral over the surfaces of the conductors except C_1: This contribution is zero because both potentials are zero at these points (grounded conductors).

2. Integral over C_1: This reduces to

$$-\int\limits_{\partial C_1} \vec{\nabla}\Phi \cdot d\vec{a}\,, \tag{3.69}$$

   for $\Phi' = 1$ and $\Phi = 0$.

3. Integral over S: this yields

$$-\Phi'_q \int\limits_{\partial S} \vec{\nabla}\Phi \cdot d\vec{a} + \Phi_q \int\limits_{\partial S} \vec{\nabla}\Phi' \cdot d\vec{a}\,. \tag{3.70}$$

The second integral in eq. (3.70) is zero because it is the negative enclosed charge (Gauss' law). But this charge is zero because the electron has been removed for the second configuration. Finally, we obtain

$$0 = -\int\limits_{\partial C_1} \vec{\nabla}\Phi \cdot d\vec{a} - \Phi'_q \int\limits_{\partial S} \vec{\nabla}\Phi \cdot d\vec{a} \tag{3.71}$$

$$= \frac{1}{\varepsilon\varepsilon_0}\, Q_{C_1} + \frac{1}{\varepsilon\varepsilon_0}\, q\Phi'_q\,. \tag{3.72}$$

Q_{C_1} is the charge on C_1. This can be solved to

$$Q_{C_1} = -q\Phi'_q \tag{3.73}$$

$$i(t) = \frac{dQ_{C_1}}{dt} = -q\frac{d\Phi'_q}{dt} = -q\left(\vec{\nabla}\Phi'_q \cdot \frac{d\vec{r}}{dt}\right) \tag{3.74}$$

where $\vec{r}$ is the position of the charge. With $\vec{v}_{\mathrm{dr}} = d\vec{r}/dt$ and $\vec{\nabla}\Phi'_q = -\vec{E}_{\mathrm{R}}$ follows eq. (3.65).
The previous calculations can be summarised as follows: in order to compute the induced currents it is necessary to calculate the Ramo potential Φ'_q, which shall from now on be denoted by Φ_{R}. It is obtained by considering all electrodes set to zero potential except for the electrode on which the induced current is to be calculated. This electrode is set to unit potential. The problem can now be solved analogously to an electrostatic problem with boundary conditions. The Ramo potential has to fulfill the conditions:

$$\Delta\Phi_{\mathrm{R}} = 0 \quad \text{between the electrodes,} \tag{3.75}$$

$$\Phi_{\mathrm{R}} = 1 \quad \text{on the electrode where the signal is measured and} \tag{3.76}$$

$$\Phi_{\mathrm{R}} = 0 \quad \text{on all other electrodes.} \tag{3.77}$$

The Ramo field is obtained from Φ_{R} by

$$\vec{E}_{\mathrm{R}} = -\vec{\nabla}\Phi_{\mathrm{R}}\,. \tag{3.78}$$

In the case of a planar diode with thickness d (which is considered as being infinite in the y and z direction, thus edge effects can be neglected) the solution is simply

$$\Phi_{\mathrm{R}} = -\frac{x}{d} \quad \Rightarrow \quad \vec{E}_{\mathrm{R}} = \frac{1}{d}\vec{e}_x\,. \tag{3.79}$$

Considering more difficult configurations of the electrodes the problem can be solved numerically (see chapter 9).
For the understanding of the later described measurements it is important that the magnitude of the induced current is proportional to the amount of drifting charge and its velocity. In the case of constant charge q (or if the time dependent charge $q(t)$ is known) the drift velocity can be derived from measurements of the signal current. This is especially easy in the case of a planar diode because there the Ramo field is constant.

3.3.4 Charge Trapping

A part of the drifting charge can be trapped by crystal defects acting as *trapping centres*. As a consequence they stop to move and do not contribute to the signal as long as they are trapped. They maybe reemitted from the trapping centre after a while but if this *detrapping* takes too long compared to the integration time of the read-out electronics they are lost for the signal. The mechanism of trapping itself and the dependence on acquired fluence will be covered more thoroughly in

sec. 4.2.3 (p. 54). In the current section only the consequences for the measured signals will be discussed.
The probability that a moving charge is trapped is proportional to the covered distance dl. Therefore the number N of charge-carriers drops according to

$$dN = -N\frac{1}{\lambda_{\text{eff}}}dl\,. \tag{3.80}$$

The inverse factor of proportionality λ_{eff} is the *effective trapping length*. If the thermal velocity v_{th} is large compared to the drift velocity v_{dr} the covered distance depends almost exclusively on the thermal velocity and the time:

$$v_{\text{th}} \gg v_{\text{dr}} \Rightarrow dl = v_{\text{th}}\,dt\,. \tag{3.81}$$

In order to check this assumption the thermal velocities have to be compared to the drift velocities for different temperatures and electric field strengths. The kinetic energy due to the thermal motion of electrons and holes is [Sz85]

$$\frac{1}{2}\,m_{e,h}v_{\text{th}}^2 = \frac{3}{2}\,k_{\text{B}}T\,. \tag{3.82}$$

The values for $m_{e,h}$ can be found in Table A.2. Using the approximation eq. (3.81) eq. (3.80) can be rewritten as

$$dN = -N\frac{1}{\tau_{\text{eff}}}dt \quad \text{mit} \quad \tau_{\text{eff}} = \frac{\lambda_{\text{eff}}}{v_{\text{th}}}\,, \tag{3.83}$$

i.e. the amount of trapped charge per unit time is independent from the drift velocity.

3.3.5 Signal Current

Solving the differential equation (3.83) yields the charge $q(t)$ which remains from the initially injected charge q_0 after the time t:

$$q(t) = qN_0\,e^{-t/\tau_{\text{eff}}} = q_0\,e^{-t/\tau_{\text{eff}}}\,. \tag{3.84}$$

The expression for the signal current in a planar diode is obtained by using this equation together with eqs. (3.79) and (3.65):

$$\begin{aligned} i(t) = \frac{dQ}{dt} &= \frac{q_0}{d}\,e^{-t/\tau_{\text{eff}}}\,v_{\text{dr}}(t) \\ &= i_0(t)\,e^{-t/\tau_{\text{eff}}} \end{aligned} \tag{3.85}$$

with $i_0(t)$ being the signal current without charge trapping. For a detector with a different configuration of electrodes this expression becomes more complicated due to a more complex Ramo potential.

3.3.6 Close-to-Surface Charge Injection

An important application of the mechanism of signal formation as described by the Ramo theorem is the close-to-surface charge injection. If a laser is used that penetrates only a few micro-meter into the silicon, one type of charge-carriers is injected close to its target electrode while the other type has to drift through the whole detector. By using a short-time laser pulse a cloud of charge-carriers is drifting through the detector (see Fig. 3.6).

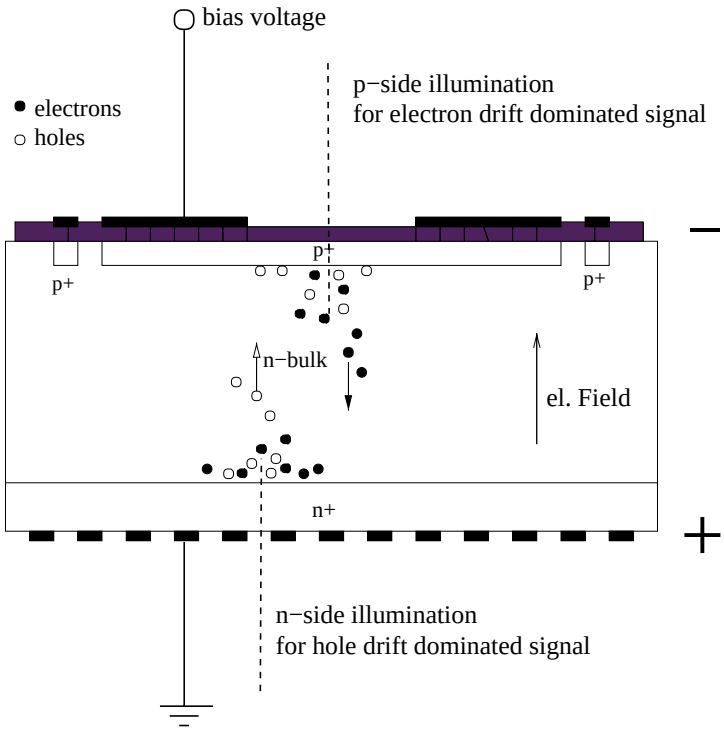

Fig. 3.6: Close-to-surface injection of charge-carriers. One charge-carrier type is produced close to its target electrode while the other type has to drift through the whole detector. Figure is taken from [Rj03].

The signal current is proportional to the amount of drifting charge and drift velocity as described by eq. (3.85). As one charge-carrier type is produced close to its target electrode and therefore has a short drift distance it contributes only negligibly to the signal. In practice the signal is too short to be measured by the electronics and the total signal is dominated by the charge-carriers drifting through the detector. This effect can be utilised to measure the properties of electrons and holes separately: p-side illumination results in an electron dominated signal, illumination of the n-side gives hole dominated signals. Fig. 6.11 (p. 91)

shows the different signal currents as measured after p- and n-side illumination. Having a constant amount of drifting charge a mapping of drift velocity vs. time is obtained. With a known dependence of velocity on electric field this could be converted into a field map. Vice versa, with a known field configuration it would be possible to measure the drift velocities of the charge-carriers.

Chapter 4

Radiation Damage

THIS chapter discusses the consequences of non-ionising energy loss by particles in silicon detectors. In the first section a short introduction to the microscopic damage mechanisms is given. The second section treats more detailed the fluence dependence and annealing for several macroscopic detector parameters.

4.1 Microscopic Damages

4.1.1 Bulk Damage

Particles that pass through the silicon crystal transfer energy to it by different mechanisms. As already described in sec. 3.1, a part of the energy is transferred by ionisation and excitation after interactions with the atomic shells. These reversible processes are used to detect particles and cause no permanent damage. Alongside these effects, energy can also be deposited by non-ionising interactions with the lattice atoms. In these processes three mechanisms are important: silicon atoms can be removed from their lattice position after having been hit by a particle. This brings an interstitial atom and a vacancy in the lattice into existence (see Fig. 4.1). Interactions between radiation and the nuclei of the lattice atoms can lead to nuclear transmutations. If the first hit atom has received enough kinetic energy it can cause further crystal defects until it is stopped. This often leads to defect clusters. Fig. 4.1 shows some further possible point defects. Defect clusters are a large number of such point defects close together, so they act different from isolated point defects.

It requires a transferred energy of at least 15 eV to remove a silicon atom from its lattice position. The minimum energy depends on the direction of the recoil with respect to the lattice. With a transferred energy of 25 eV the probability is $\frac{1}{2}$ that the atom is removed from the lattice [Lu99]. Such an atom is called *primary knock-on atom* (PKA).

The probability to produce a PKA depends on the kind and the energy of the impinging particle. Electrically neutral particles like neutrons scatter elastically on the nucleus via strong interactions. Charged particles like protons and pions

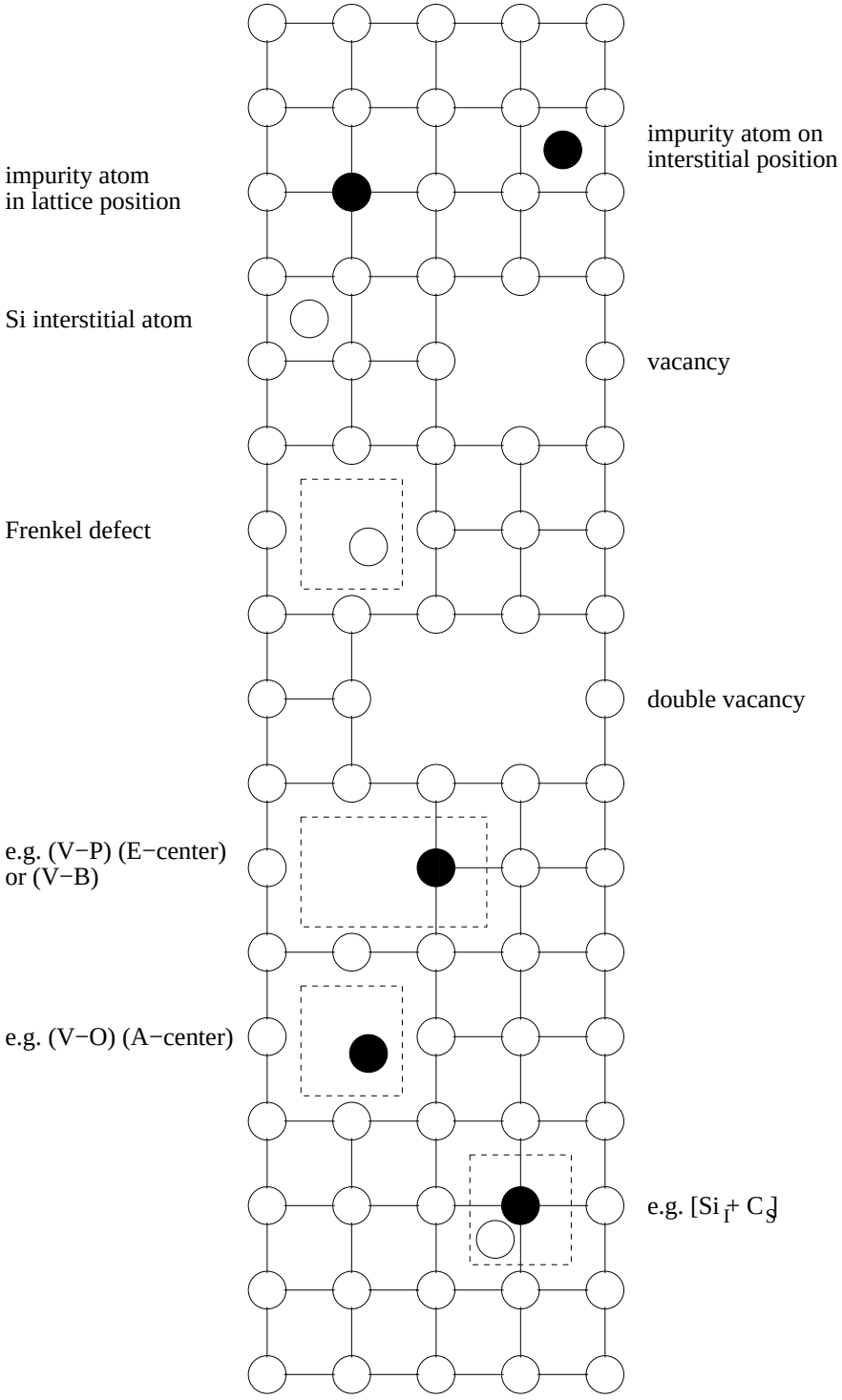

Fig. 4.1: Schematic picture of point defects in a silicon crystal using a two-dimensional representation. In reality the lattice has a three-dimensional tetrahedric structure [Wu92].

can additionally interact electromagnetically. Values for the necessary minimum energy of different particles can be found in Table 4.1.
The effects of different kinds of irradiation with the same fluence vary strongly. Therefore, it is useful to normalise the damage effects to a "standard irradiation". This is possible because only the interaction with the first hit atom depends on the kind of the impinging radiation. All further damages are caused by the PKA. Since energy that is deposited by ionisation causes no enduring damages the *non-ionising energy loss* (NIEL) is the decisive variable. This so-called *NIEL-hypothesis* is valid as long as the defects consist of point-defects and defect-clusters. For instance, electron irradiation cannot described by this hypothesis since electrons cause no defect-clusters.
The NIEL of different particles is normalised to that of neutrons with a kinetic energy of 1 MeV. In the following the *equivalent fluence* is given in $n_{\mathrm{eq}}/\,\mathrm{cm}^2$:

$$1\ n_{\mathrm{eq}}/\mathrm{cm}^2 = 1 \text{ neutron with } 1\,\mathrm{MeV} \text{ kinetic energy per } \mathrm{cm}^2. \tag{4.1}$$

For an irradiation causing a fluence Φ_{irr} (e.g. of protons with a certain energy) the corresponding equivalent fluence Φ_{eq} is obtained by multiplying Φ_{irr} with the so-called *hardness factor*:

$$\Phi_{\mathrm{eq}} = \kappa \cdot \Phi_{\mathrm{irr}}\,. \tag{4.2}$$

The hardness factors κ are specific for every particle and depend also on their kinetic energy. They are obtained by measuring the additional leakage current of the device due to the irradiation with Φ_{irr} (see end of this section and sec. 4.2.2) with Φ_{irr} and comparing it to the leakage current of a diode that has been irradiated with 1-MeV-neutrons.
At room temperature the primary defects—Si-interstitials and vacancies—are mobile. Hence the damaged crystal can *anneal*, that means the atoms return to their lattice positions as well as combine with other defects to new defect types. This

Radiation	electrons	protons	neutrons	Si^+
Interaction	Coulomb scattering	Coulomb and nuclear scattering	nuclear scattering	Coulomb scattering
T_{max}[eV]	155	133 700	133 900	1 000 000
T_{m}[eV]	46	210	50 000	265
E_{min}[eV]				
point defect	260 000	190	190	25
defect cluster	4 600 000	15 000	15 000	2 000

Table 4.1: Properties of different radiations. T_{max} is the maximum recoil energy which can be transferred, T_{m} is the mean transferred recoil energy for particles with a kinetic energy of 1 MeV. E_{min} is the minimum particle energy to create a point defect or defect cluster. The table is taken from [Lu99].

can happen with a defect that is originating from crystal growth, e.g. with a doping atom. For instance, a vacancy can build an E-centre together with a phosphorus atom. Another example is the A-centre, which consists of an oxygen atom on an interstitial position together with a vacancy. The beforehand electrically neutral oxygen atom becomes an acceptor that can trap electrons. The primary defect can also interact with another defect produced by irradiation. An example is the divacancy which consists of two neighbouring vacancies.
The electrical properties of all these possible defects are complex and effect macroscopic parameters which are crucial for detector operation:

- Donors and acceptors can be induced or made inactive by irradiation. These effects alter the effective doping concentration of the crystal leading to a change of the depletion voltage V_{dep} according to eq. (3.41).
- Defects can act as generation and recombination centres, i.e. they can emit and catch electrons and holes. Alternating emission of electrons and holes in the space charge region leads to increased reverse-bias current (*leakage current*).
- Irradiation can produce *trapping centres*. They trap drifting electrons and holes in the space charge region. If the trapped charge-carriers are released (*detrapped*) after times longer than the integration time of the read-out electronics they are lost for the signal.
- Defects can act as *deep levels*, which are donor- or acceptor-like states deep in the band-gap. These states can be occupied by holes or electrons and by this change their charge-state. Their occupation probability depends on the densities of free electrons and holes from the leakage current which are not homogeneous throughout the crystal. Therefore, also the contribution from occupied deep level states to the space-charge varies throughout the substrate. This leads to a *distortion of the field configuration* which is no longer a linearly increasing one.

4.1.2 Surface Damage

Although in the bulk only the non-ionising energy loss causes damages, the surface properties of the crystal can as well be changed permanently by ionisation. The surface of the silicon crystal is characterised by the abrupt termination of the periodic lattice structure. Thus in the surface region Si atoms have no covalent bonds to neighbouring ones. These so-called *dangling bonds* make these atoms chemically and electrically highly active. In order to overcome this problem the surface of the wafer is passivated by a silicon oxide film which is thermally grown. This prevents also impurities from diffusing into the highly pure silicon bulk. However, the Si/SiO_2 interface hosts electronic states whose number and properties are altered by ionising irradiation. Further explaination of the surface properties can be found in [Wü01].

These interface states lead to an increased reverse bias current after irradiation which adds to the leakage current which is caused by defects in the bulk. However, the magnitude of this *surface current* depends on the structure of the surface and thus it can be controlled by the chosen sensor design. Since it is proportional to the ratio of unimplanted area to complete sensor area it is negligible compared to the bulk leakage current for pad-detectors as they are used in this work. Furthermore, it also has been shown that in the ATLAS pixel sensor with the radiation hard design this effect will not endanger the detector operation [Wü01].

4.2 Radiation Effects on Macroscopic Properties

4.2.1 Depletion Voltage

Effective Doping Concentration

Irradiation leads to removal of donors and introduction of acceptors. For a more useful description of the doping concentration the *effective doping concentration* N_{eff} is used instead of N_D and N_A:

$$N_{\text{eff}} = N_{\text{D}} - N_{\text{A}} \,. \tag{4.3}$$

Eq. (3.41) is rewritten to

$$V_{\text{dep}} = \frac{e_0 |N_{\text{eff}}|}{\varepsilon\varepsilon_0} \frac{d^2}{2} \,. \tag{4.4}$$

The following discussion covers only detectors having a bulk made from n-doped silicon. In such material the donor removal and acceptor introduction lead after a certain fluence—which is determined by the initial doping concentration—to a *space charge sign inversion* (SCSI), i.e. the bulk is converted from n-type to p-type and N_{eff} changes its sign.
SCSI also leads to a changed field configuration in irradiated detectors. Since after conversion the bulk is p-type, the space charge region grows from the n-side towards the p-side of the detector. Therefore, the field maximum is now on the n-side and eq. (3.53) has to be modified to:

$$\begin{aligned} E(x) &= E_0 + E_D(x) \quad \text{with} \\ E_0 &= \frac{V_{\text{bias}} - V_{\text{dep}}}{d} \quad \text{and} \\ E_D(x) &= \frac{2V_{\text{dep}}}{d} \cdot \frac{x}{d} \,. \end{aligned} \tag{4.5}$$

Eq. (3.56) has to be modified accordingly. The change ΔN_{eff} of N_{eff} from the original doping concentration $N_{\text{eff},0}$ is given by

$$\Delta N_{\text{eff}}(\Phi_{\text{eq}}, t(T_a)) = N_{\text{eff},0} - N_{\text{eff}}(\Phi_{\text{eq}}, t(T_a)) \,. \tag{4.6}$$

This equation considers alongside the fluence dependence the dependence on time to describe annealing effects as well. The annealing leads to a change of detector

properties even after the irradiation has finished since some of the defects are mobile. The expression $t = t(T_a)$ takes into regard the fact that the speed of annealing depends on the annealing temperature T_a since the mobility of defects grows with temperature.

Annealing Effects

According to the *Hamburg model* [RD48b] the change of N_{eff} can be split into three components:

$$\Delta N_{\text{eff}}(\Phi_{\text{eq}}, t(T_a)) = N_{\text{a}}(\Phi_{\text{eq}}, t(T_a)) + N_{\text{c}}(\Phi_{\text{eq}}) + N_{\text{y}}(\Phi_{\text{eq}}, t(T_a)) \,. \tag{4.7}$$

This split up considers the different behaviour with time of the individual contributions to ΔN_{eff}:

- N_{a} anneals on a short time-scale and decreases with time. Therefore, it is called *short-term annealing* or *beneficial annealing*. The latter name is chosen because short-term annealing increases N_{eff}. This leads to a lower depletion voltage and consequently better detector properties for converted material where N_{eff} is negative.

- N_{c} is a stable damage which depends only on the acquired fluence and does not change with time.

- N_{y} describes the *anti-annealing* or *reverse-annealing* since this effects counteracts the beneficial annealing on a long time-scale and leads to an increase of the depletion voltage after long annealing times in converted material. Considering the relevant long time-scales it is also called *long-term annealing*.

The RD48 collaboration [RD48] performed studies on these effects. They revealed a dependence of the radiation damage on the oxygen concentration $[\text{O}_i]$ in the detector material: silicon with a higher $[\text{O}_i]$ (so-called *DOFZ material*[1]) has a more advantageous characteristic of the depletion voltage. The oxygenation of the bulk material is done by heating the wafers after oxide growth to 1150°C for 24 h. Thereby oxygen atoms diffuse from the oxide layer on the surface into the crystal.
The introduction rate of stable acceptors g_c (see below) after proton irradiation is in DOFZ material a factor 3.5 lower than for not oxygenated (standard) material. A further improvement when using DOFZ is the saturation of the reverse annealing amplitude towards high fluences. Therefore, the depletion voltage after long annealing times is lower in oxygenated silicon compared to non-oxygenated material. A dependence on the initial specific resistance is due to the complete donor removal not oberservable. Neutron irradiation of DOFZ material leads to the

[1] **D**iffusion **O**xygenated **F**loat **Z**one, "float zone" denotes the production process of the wafer.

same introduction rate for stable acceptors as in standard silicon and the reverse annealing shows also no dependence on the oxygen concentration [RD48b].
Thus the effect of the oxygenation is different wether the particles are charged or neutral. This can be explained by the following consideration: neutrons interact via the strong force with the lattice atoms. The strong force can transfer large energies to the PKAs. Protons interact additionally to the strong force by the electromagnetic force. The electromagnetic force leads to smaller energy transfers and therefore proton-irradiated material has a larger fraction of point-defects compared to neutron-irradiated silicon. Point-defects can be inactivated by the oxygen while in defect-clusters the defect-concentration is too high to be compensated. Since the depletion voltage is sensitive on the point-defect concentration a difference for proton- and neutron-irradiation is visible.

The following paragraphs give more detailed descriptions of the components of ΔN_{eff}.

Short Term Annealing

Beneficial annealing increases N_{eff}. This leads for detectors before type conversion —which have a positive N_{eff}—to an increase of the depletion voltage while the depletion voltage of type converted detectors with a negative N_{eff} is decreased. On a microscopic scale this is usually explained by an annealing of acceptors.
N_{a} is mathematically described by a sum of exponentials of the form $e^{-t/\tau_{a,i}}$ but after some time N_{a} is dominated by the contribution with the largest time constant. Contributions with shorter time constants can be neglected for the problems treated in this work. Therefore, N_{a} can be written as

$$N_{\mathrm{a}} = g_a \, \Phi_{\mathrm{eq}} \, e^{-t/\tau_a} \, . \tag{4.8}$$

The introduction rate g_a does not depend on the used detector material and its mean value for DOFZ material is [RD48b][2]

$$g_a = 1.4 \cdot 10^{-2} \, \mathrm{cm}^{-1} \, . \tag{4.9}$$

The temperature dependence of τ_a is parameterised by [Mo99][3]

$$\frac{1}{\tau_a} = k_a = k_{0a} \cdot \exp\left(-\frac{E_{aa}}{k_{\mathrm{B}} T_a}\right) \, . \tag{4.10}$$

[2]Although g_a is physically independent from the oxygen concentration the experimentally determined numbers depend on the sample because all parameters of ΔN_{eff} are won by a fit to the annealing curve (depletion voltage vs. annealing time). Since other parameters—especially the reverse annealing behaviour—depend on the oxygen concentration one obtains also a slight dependence of g_a on $[\mathrm{O}_i]$.

[3]For the parameterisation of ΔN_{eff} results of two works were combined: As a source for data on DOFZ material [RD48b] is used. However, these studies did not include an inquiry of the temperature dependence of annealing times. Data for the temperature dependence are taken from [Mo99] and were measured with standard material. Comparable studies with DOFZ material have not been made up to now but differences to standard material are not expected.

The values for the activation energy E_{aa} and the frequency factor k_{0a} are

$$E_{aa} = (1.09 \pm 0.03)\,\mathrm{eV} \quad \text{und} \tag{4.11}$$
$$k_{0a} = 2.4^{+1.2}_{-0.8} \cdot 10^{13}\,\mathrm{s}^{-1}\,. \tag{4.12}$$

Stable Damage

The stable damage has two components: A donor removal that depends exponentially on the fluence with an amplitude N_{c0} and on the other side an acceptor introduction which is proportional to the fluence with a factor g_c:

$$N_c = N_{c0}\,(1 - \exp(-c\,\Phi_{\mathrm{eq}})) + g_c\,\Phi_{\mathrm{eq}}\,. \tag{4.13}$$

Only a specific fraction $N_{c0}/N_{\mathrm{eff},0}$ of the initially existing donors is removed by irradiation. The amplitude N_{c0} of the donor removal depends for neutron irradiation on the effective doping concentration $N_{\mathrm{eff},0}$ and the oxygen concentration $[\mathrm{O}_i]$:

$$N_{c0,n} = N_{\mathrm{eff},0} \cdot 0.8 \cdot \exp\left(-[\mathrm{O}_i]/\left(4.3 \cdot 10^{17}\,\mathrm{cm}^{-3}\right)\right)\,. \tag{4.14}$$

Proton irradiation removes the donors completely:

$$N_{c0,p} = N_{\mathrm{eff},0}\,. \tag{4.15}$$

The different behaviour under irradiation with protons and neutrons suggests the existence of two different kinds of donors: in a model using such a consideration protons can remove both types while neutron can remove only one type of donors. This consideration will be important in the later described model which is used for simulation studies (chapters 9 and 11). The remaining parameters in eq. (4.13) have the values

$$c = 0.109/N_{\mathrm{eff},0} \tag{4.16}$$
$$g_c = \begin{cases} 2.0 \cdot 10^{-2}\,\mathrm{cm}^{-1} & \text{for neutrons} \\ 5.3 \cdot 10^{-3}\,\mathrm{cm}^{-1} & \text{for protons} \end{cases}\,. \tag{4.17}$$

Reverse Annealing

Reverse annealing leads to a further decrease of N_{eff} after long annealing times. It can be parameterised by[4]

$$N_y = N_{y0} \cdot (1 - \exp(-t/\tau_y)) \ . \tag{4.18}$$

For standard silicon N_{y0} is proportional to the fluence and has a constant introduction rate g_y which depends only on the kind of radiation. However, in DOFZ silicon its behaviour depends on the irradiation particle type: under neutron irradiation the introduction rate is still a constant number:

$$N_{y0,n} = g_{y,n} \cdot \Phi_{\text{eq}} \quad \text{with} \quad g_{y,n} = 4.80 \cdot 10^{-2}\,\text{cm}^{-1} \ . \tag{4.19}$$

For proton irradiation a saturation can be observed [Mo99]:

$$N_{y0,p} = g_{y,p} \cdot \phi_0 \,(1 - \exp(-\Phi_{\text{eq},p}/\phi_0)) \qquad \text{with} \tag{4.20}$$

$$g_{y,p} = 7.40 \cdot 10^{-2}\,\text{cm}^{-1} \qquad \text{and} \tag{4.21}$$

$$\phi_0 = 2.1 \cdot 10^{14}\, n_{\text{eq}}/\,\text{cm}^2 \ . \tag{4.22}$$

The temperature dependence of the annealing time constant is decribed analogously to that of the beneficial annealing [Mo99]:

$$\frac{1}{\tau_y} = k_y = k_{0y} \exp\left(-\tfrac{E_{yy}}{k_{\text{B}} T_a}\right) \qquad \text{with} \tag{4.23}$$

$$k_{0y} = 7.4 \cdot 10^{14}\,\text{sec}^{-1} \qquad \text{and} \tag{4.24}$$

$$E_{yy} = 1.325\,\text{eV} \ . \tag{4.25}$$

All values for the parameters in DOFZ silicon are given in Table 4.2. This table contains also the numbers for standard silicon as a comparison.

Consequences for Detector Operation

During operation of the ATLAS experiment the applied bias voltage of the sensors shall always be above the depletion voltage ("overdepleted operation"). The bias voltage is to be set 50 V above the depletion voltage but never less than 150 V.

[4] In some of the literature also a parameterisation of the form

$$\left[1 - \frac{1}{1 + t/\tau_y}\right]$$

is given [Mo99, RD48b]. This ansatz describes a 2nd order process. However, a 2nd order process can be ruled out by investigations of the dependence of the annealing time constants on the fluence [Mo99]. Nevertheless, the data of depletion voltage after long annealing times ($t > \approx 50$ h at 60°C) are betterly described by a 2nd order process. The exponential parameterisation which is used here and corresponds to a 1st order process deviates from the description with a 2nd order process only marginally for short annealing times but is much more practical for simulations (cf. chapter 9).

	DOFZ silicon		standard silicon	
	neutrons	protons	neutrons	protons
g_a	$1.4 \cdot 10^{-2}\,\mathrm{cm}^{-1}$	$1.4 \cdot 10^{-2}\,\mathrm{cm}^{-1}$	$1.8 \cdot 10^{-2}\,\mathrm{cm}^{-1}$	$1.8 \cdot 10^{-2}\,\mathrm{cm}^{-1}$
$\tau_a(20^\circ\mathrm{C})$	70 h	70 h	55 h	55 h
g_c	$2.0 \cdot 10^{-2}\,\mathrm{cm}^{-1}$	$5.3 \cdot 10^{-3}\,\mathrm{cm}^{-1}$	$1.5 \cdot 10^{-2}\,\mathrm{cm}^{-1}$	$1.9 \cdot 10^{-2}\,\mathrm{cm}^{-1}$
$N_{c0}/N_{\mathrm{eff},0}$	0.45	1.0	0.70	0.70
g_y	$4.8 \cdot 10^{-2}\,\mathrm{cm}^{-1}$	$2.3 \cdot 10^{-2}\,\mathrm{cm}^{-1}$	$5.2 \cdot 10^{-2}\,\mathrm{cm}^{-1}$	$6.6 \cdot 10^{-2}\,\mathrm{cm}^{-1}$
$\tau_y(20^\circ\mathrm{C})$	800 d	950 d	480 d	480 d

Table 4.2: Damage parameter for DOFZ and standard silicon. The data are taken from [RD48b].

Technical limitations of the cabling and power supplies restrict the maximum applicable bias voltage to 600 V. In order to operate also highly irradiated sensors effectively the annealing behaviour of them has to be considered. The depletion voltage can be kept low by influencing the annealing by an elaborate temperature control:

- Interim warm-ups will have a positive effect since they accelerate the beneficial annealing and lower thereby the depletion voltage. Such warm-ups will already happen during necessary interruptions of the detector operation for maintenance.
- Reverse annealing deteriorates the sensors' properties. This can be limited by avoiding to extend the length of warm-up periods beyond the minimum in the annealing curve and keep the detector always as cold as possible.
- The main contribution to radiation damage comes from the constant part of ΔN_{eff}. This contribution cannot be influenced by temperature control but solely by choosing DOFZ silicon as sensor material.

In chapter 11 the effects of different temperature profiles on the evolution of the depletion voltage will by inquired with the help of simulations.

4.2.2 Leakage Current

Fluence Dependence

Radiation induced defects act as generation and recombination centres and increase the reverse-bias leakage current by alternating emission of electrons and holes. Previous inquiries of this aspect of radiation damage showed no dependence on the chosen detector material, DOFZ and standard material show the same behaviour.
The leakage current I_{leak} of a device is proportional to the acquired equivalent fluence Φ_{eq} and the depleted volume V:

$$I_{\mathrm{leak}} = \alpha \cdot \Phi_{\mathrm{eq}} \cdot V\,. \tag{4.26}$$

Annealing Effects

The annealing behaviour is independent from the used detector material. $\alpha(t)$ can be parameterised in the following way [Mo99]:

$$\alpha(t) = \alpha_I \cdot \exp\left(-\frac{t}{\tau_I}\right) + \alpha_0 - \beta \cdot \ln(t/t_0)\,. \tag{4.27}$$

t_0 is set to 1 min. The factor α_I for the rapidly annealing part which is parameterised by an exponential function has the value

$$\alpha_I = (1.23 \pm 0.06) \cdot 10^{-17}\,\mathrm{A/cm}\,. \tag{4.28}$$

The dependence on the temperature is described by

$$\frac{1}{\tau_I} = k_{0I} \cdot \exp\left(-\frac{E_I}{k_\mathrm{B} T_a}\right) \tag{4.29}$$

with the parameter values

$$k_{0I} = 1.2^{+5.3}_{-1.0} \cdot 10^{13}\,\mathrm{s}^{-1} \quad \text{and} \tag{4.30}$$

$$E_I = (1.11 \pm 0.05)\,\mathrm{eV}\,. \tag{4.31}$$

At room temperature τ_I is ≈ 10 d. The parameters of the logarithmic part in eq. (4.27) have the values

$$\beta = (3.07 \pm 0.18) \cdot 10^{-18}\,\mathrm{A/cm} \quad \text{and} \tag{4.32}$$

$$\alpha_0 = -(8.9 \pm 1.3) \cdot 10^{-17}\,\mathrm{A/cm} + (4.6 \pm 0.4) \cdot 10^{-14}\,\mathrm{AK/cm} \cdot \frac{1}{T_a}\,. \tag{4.33}$$

α_0 exhibits a temperature dependence which is in this form only valid for a constant annealing temperature T_a. This is obstructive for simulations with varying T_a as it will be in the later operation. With the help of some assumptions [Mo99] the time axis may be scaled according to

$$\Theta(T_a) = \exp\left[-\frac{E_I^*}{k_\mathrm{B}}\left(\frac{1}{T_a} - \frac{1}{T_\mathrm{ref}}\right)\right]\,. \tag{4.34}$$

The time at annealing temperature T_a is scaled to the time at a reference temperature T_ref. Eq. (4.27) is changed to

$$\alpha(t) = \alpha_I \cdot \exp\left(-\frac{t}{\tau_I}\right) + \alpha_0^* - \beta \cdot \ln\left(\Theta(T_a) t/t_0\right)\,. \tag{4.35}$$

As value for α_0^* it has to be taken the value which is measured at T_ref and not the value calculated with eq. (4.33). The latter results from a fit to data measured at several temperatures. In this work the data measured at an annealing temperature of 21°C in [Mo99] are used as reference point since this temperature comes closest

to the operation temperature of ATLAS. The data set used for calculations of leakage currents are:

$$\alpha_I = 1.23 \cdot 10^{-17}\,\mathrm{A/cm} \tag{4.36}$$
$$\alpha_0^* = 7.07 \cdot 10^{-17}\,\mathrm{A/cm} \tag{4.37}$$
$$\beta = 3.29 \cdot 10^{-18}\,\mathrm{A/cm} \tag{4.38}$$
$$E_I^* = 1.30\,\mathrm{eV} \tag{4.39}$$

The values given here are only valid for the range

$$1 \cdot 10^{-17}\,\mathrm{A/cm} < \alpha < 6 \cdot 10^{-17}\,\mathrm{A/cm}\,. \tag{4.40}$$

Consequences for Detector Operation

Since the leakage current shows a simpler annealing behaviour—no reverse annealing as in the case of N_{eff}—the consequences for detector operation are much simpler: warm-up periods lead *always* to an improvement of the detector properties.
The most important impact of leakage current characteristics on detector operation conditions results from the strong temperature dependence of the current. The current at a temperature T is obtained from a reference measurement at a temperature T_{ref} as

$$I(T) = I(T_{\mathrm{ref}}) \cdot \left(\frac{T}{T_{\mathrm{ref}}}\right)^2 \exp\left(-\frac{E_G}{2k_{\mathrm{B}}}\left(\frac{1}{T} - \frac{1}{T_{\mathrm{ref}}}\right)\right)\,. \tag{4.41}$$

Therefore, it is very important to keep the sensor cooled during operation. The leakage current is strongly suppressed and thus also the noise is reduced. As a rule of thumb, the leakage current is cut in half for every temperature drop of 8°C.

4.2.3 Charge Collection Deficiency

Charge trapping is caused by radiation induced defects which catch drifting charges and stop their movement. With the approximation (3.81) the trapping probability can be written as

$$\frac{1}{\tau_{\mathrm{eff}}} = \sum_i N_i(1 - P_i)\,\sigma_i\,v_{\mathrm{th}}\,, \tag{4.42}$$

where N_i is the concentration of the trapping centre i, P_i its occupation probability and σ_i the carrier capture cross-section. In first order the fluence dependence of N_i can be written as

$$N_i = g_i\,\Phi_{\mathrm{eq}}\,f_i(t) \tag{4.43}$$

with g_i as introduction rate, the equivalent fluence Φ_{eq} and $f_i(t)$ describing the annealing with time. This description neglects second order effects like reactions

between defects which are neglectable for the investigated fluence range. With this model $1/\tau_{\text{eff}}$ can be parameterised as

$$\frac{1}{\tau_{\text{eff}}} = \gamma \cdot \Phi_{\text{eq}} \,. \tag{4.44}$$

The factor of proportionality γ between fluence and trapping probability is of the form

$$\gamma = \sum_i g_i \, f_i(t) \, (1 - P_i) \, \sigma_i \, v_{\text{th}} \,. \tag{4.45}$$

In a general description P_i and σ_i should be regarded as temperature dependent, the latter also as velocity dependent.

4.2.4 Field Distortion by Deep Level States

In highly irradiated sensors the occurence of a double peak configuration of the electric field is observed [Er95][Me99]. This configuration leads to two field maxima at the contacts with a minimum in between which is in contrast to the theoretical expectation derived previously from a homogeneous doping concentration. Thus it hints to an inhomogeneous space charge distribution which also changes its sign from one side of the sensor to the other. Ref. [Er02] proposes a model to explain this field configuration. For application within this work this model is modified by replacing some of the approximations made in [Er02] by the exact expressions. The following paragraphs describe the model as it is used in this work. In all equations the equilibrium state is considered.
Since the current generation rate G is the same throughout the detector, also the leakage current density is independent from x:

$$\mathrm{j}_{\text{leak}} = G \cdot d \,. \tag{4.46}$$

However, the electron and hole components of j_{leak} depend linearly on x,

$$j_e = Gx \,, \tag{4.47}$$
$$j_h = G(d - x) \,. \tag{4.48}$$

These dependences can be derived from the continuity equations and boundary conditions:

$$\vec{\nabla} j_e = G \tag{4.49}$$
$$j_e = 0 \text{ at p-side } (x = 0) \tag{4.50}$$
$$\vec{\nabla} j_h = G \tag{4.51}$$
$$j_h = 0 \text{ at n-side } (x = d) \,. \tag{4.52}$$

Plots of total current density and its electron and hole components are shown in Fig. 4.2(b) for a detector having been irradiated with $\Phi_{\text{eq}} = 2.04 \cdot 10^{14} \, n_{\text{eq}}/\,\text{cm}^2$.

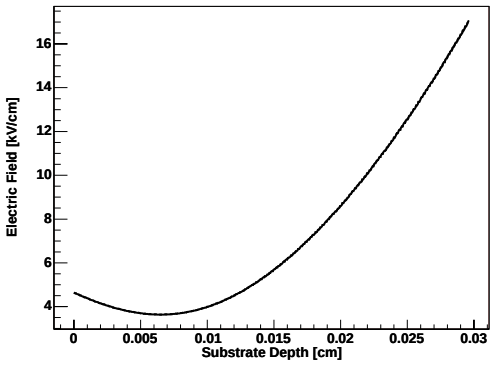

(a) Electric Field

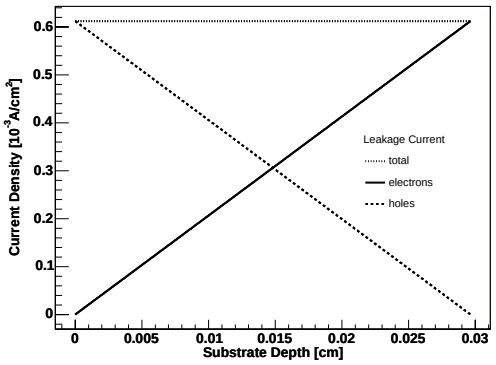

(b) Components of leakage current density

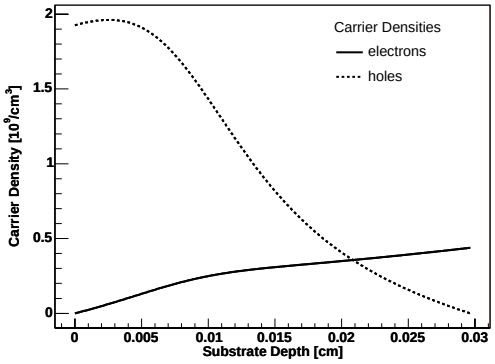

(c) Carrier Densities

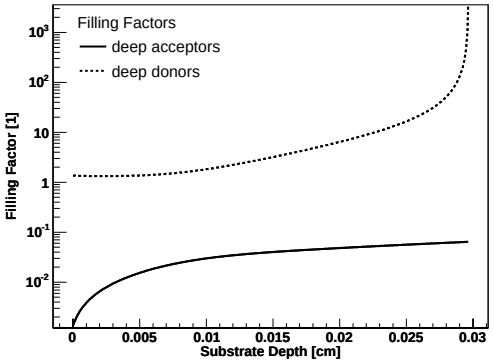

(d) Filling Factors

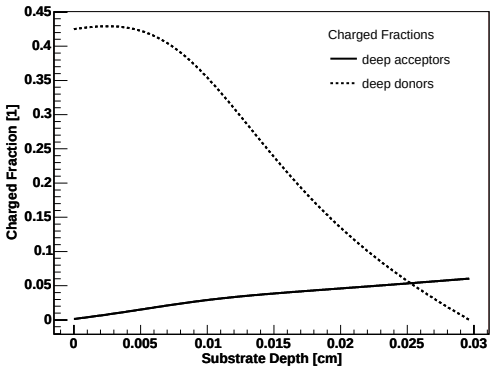

(e) Charged Fractions

Parameters:

- diode thickness 0.0297 cm
- V_{dep}=120 V, V_{bias}=220 V
- current rate $G = 2.07 \cdot 10^{-02} A/\,\mathrm{cm}^3$ at 0°C
- deep acceptor: $E_t = E_C - 0.52\,\mathrm{eV}$, $\sigma_e = 10^{-15}\,\mathrm{cm}^2$, $\sigma_h = 10^{-15}\,\mathrm{cm}^2$, $N_{\mathrm{DA}} = 9.95 \cdot 10^{13}/\,\mathrm{cm}^3$
- deep donor: $E_t = E_V + 0.53\,\mathrm{eV}$, $\sigma_e = 10^{-15}\,\mathrm{cm}^2$, $\sigma_h = 3 \cdot 10^{-14}\,\mathrm{cm}^2$, $N_{\mathrm{DD}} = 7.2 \cdot 10^{12}/\,\mathrm{cm}^3$

Fig. 4.2: Application of deep level model to a pad-detector irradiated with $\Phi_{\mathrm{eq}} = 2.04 \cdot 10^{14}\, n_{\mathrm{eq}}/\,\mathrm{cm}^2$. From the electric field (a) and the leakage current density (b) follows the concentration of free charge-carriers (c). Deep levels are charged according to (d) and (e). More details can be found in the text.

The resulting densities of free carriers are

$$n_e(x) = \frac{j_e(x)}{e_0\, v_{\mathrm{dr},e}(E(x))} \tag{4.53}$$

$$n_h(x) = \frac{j_h(x)}{e_0\, v_{\mathrm{dr},h}(E(x))}\,, \tag{4.54}$$

which are inhomogeneous due to the dependence of the drift velocities on electric field strength. Fig. 4.2(c) shows $n_{e,h}(x)$ plotted vs. substrate depth x. The displayed numbers were calculated with the electric field shown in Fig. 4.2(a). (This field is the result a calculation based on this model, more technical details of the calculation can be found in chapter 9.) These free carriers can be trapped in deep level states, changing their charge state. The occupation probability of these states depends on the density of free carriers. Thus it is also inhomogeneous and leads to accumulation of more negative charge towards the n-side and more positive charge at the p-side. This can lead to a change of the space charge sign and results for that case in a double-peak field configuration.
In order to derive a numerical model for calculations the excess carrier generation rates U_e and U_h are considered. $U_{e,h}$ are the differences between generation rates $G_{e,h}$ and recombination rates $R_{e,h}$:

$$U_e = G_e - R_e\,, \tag{4.55}$$

$$U_h = G_h - R_h\,. \tag{4.56}$$

At the moment only one type of deep level defects is considered. The generation rate for electrons is proportional to the density of trapped electrons n_t and the emission rate ε_e:

$$G_e = n_t\, \varepsilon_e\,. \tag{4.57}$$

G_h is proportional to the density of unoccupied traps $N_t - n_t$ with N_t being the total density of traps:

$$G_h = (N_t - n_t)\, \varepsilon_h\,. \tag{4.58}$$

The emission rates are given by

$$\varepsilon_e = v_{\mathrm{th},e}\sigma_e N_C \exp\left(-\frac{E_C - E_t}{kT}\right) \quad \text{and} \tag{4.59}$$

$$\varepsilon_h = v_{\mathrm{th},h}\sigma_h N_V \exp\left(-\frac{E_t - E_V}{kT}\right)\,. \tag{4.60}$$

N_C and N_V are the effective densities of states in the conduction and valence band as given by eqs. (3.12) and (3.13), respectively. $E_C - E_t$ and $E_t - E_V$ are the activation energies for carrier transitions between the deep level with energy E_t and the conduction and valence band.

The recombination rates depend on N_t, n_t, $n_{e,h}(x)$ and the capture rates $c_{e,h}$ by

$$R_e = (N_t - n_t)\, c_e\, n_e(x) \quad \text{and} \tag{4.61}$$

$$R_h = n_t\, c_h\, n_h(x)\,. \tag{4.62}$$

The capture rates are the products of thermal velocities $v_{\mathrm{th},e,h}$ and the capture cross-sections $\sigma_{e,h}$:

$$c_e = v_{\mathrm{th},e} \cdot \sigma_e\,, \tag{4.63}$$

$$c_h = v_{\mathrm{th},h} \cdot \sigma_h\,. \tag{4.64}$$

Under the condition that the excess carrier generation rates for holes and electrons must be equal in thermal equilibrium ($U_e = U_h$) for the filling factor F (see Fig. 4.2(d)) follows

$$F = \frac{n_t}{N_t - n_t} \tag{4.65}$$

$$= \frac{c_e\, n_e + v_{th,h}\sigma_h N_V \exp(-(E_t - E_V)/kT)}{c_h\, n_h + v_{th,e}\sigma_e N_C \exp(-(E_C - E_t)/kT)}\,. \tag{4.66}$$

Usually a trap is called "occupied" if it is in the more negative state. Therefore occupied deep donors are electrically neutral and positive if unoccupied. Analogously, deep acceptors are negative in the occupied state and neutral in the unoccupied case. So the *charged* fractions of acceptors and donors are (see Fig. 4.2(e))

$$F^- = \frac{F}{1+F} \quad \text{for acceptors} \quad \text{and} \tag{4.67}$$

$$F^+ = \frac{1}{1+F} \quad \text{for donors.} \tag{4.68}$$

In case of the existence of several types of deep level defects this calculation has to be done for all types. The space charge density is calculated as the sum over all contributions:

$$N_{\mathrm{eff}}(x) = N_{\mathrm{sh}} + \sum_i F_i^+(x) N_{\mathrm{DD},i} - \sum_i F_i^-(x) N_{\mathrm{DA},i}\,. \tag{4.69}$$

$N_{\mathrm{DD},i}$ and $N_{\mathrm{DA},i}$ are the densities for deep donors and deep acceptors, respectively. N_{sh} is the contribution of shallow levels (including the sign of the space charge, i.e. $N_{\mathrm{sh}} < 0$ for p-type material) which are completely ionised in the depletion zone.
In the later analysis the model is simplified to have only one deep donor and one deep acceptor. In that case the effective doping concentration is given by

$$N_{\mathrm{eff}}(x) = N_{\mathrm{sh}} + F^+(x) N_{\mathrm{DD}} - F^-(x) N_{\mathrm{DA}}\,. \tag{4.70}$$

A compilation of properties of known deep levels can be found in [Er02]. The electric field can be derived from $N_{\mathrm{eff}}(x)$ by using Gauss's law.

The difficulty of the derivation of the electric field by using this model is that the electric field distribution is already needed to calculate the drift velocities which are needed for determination of the carrier densities and the charged fractions which are in turn used to calculate $E(x)$. Therefore, an iterative procedure is useful where the drift velocities are calculated with an ansatz for $E(x)$ and the resulting $E(x)$ is used as input for a further iteration. (The electric field in Fig. 4.2(a) has been calculated by this method.)

Part II

Development of Pixel Modules

Chapter 5

Bump Bond Testing

THE reliability of the bump bond connections is a crucial point for a good quality and long-life performance of the modules for the ATLAS pixel detector. Therefore, their quality has to be checked already during the development of the modules. In order to enable simple tests and reduce costs so-called dummy modules have been designed. The concept and design of these dummies is introduced in this chapter.

5.1 Principle of Daisy-Chains

Several types of dummy modules have been designed during the development phase of ATLAS pixel modules. Alongside e.g. simple mechanical dummies which had none electrical functionality also more elaborate types were developed which can be used for tests of special aspects of module functionality. In the following so-called *daisy-chain modules* are introduced which are used to check the quality of the bump-bonding process.
These dummy modules for bump bond tests connect whole series of bump bonds to *daisy-chains*. Fig. 5.1 shows the concept of two types of daisy-chains as designed by [Da00][Kr00d]. The uppermost drawing in that figure shows the *conventional design*. The current flows alternately over conducting lines on the sensor dummy (light grey, top) and the FE replacement (dark grey, bottom). A missing bump breaks the chain what can easily be measured with a multimeter set to ohmic mode. The drawback of this design is that one cannot distinguish between the loss of one or of several bonds. Therefore, it is not sensible to make long chains but the implementation of a lot of short chains is more appropriate.
The second drawing from top in Fig. 5.1 shows the improved design, so-called *resistive daisy-chains*. In this design all bump-pads on the sensor dummy are connected by resistors R_D. After flip-chipping of the dummy module every second resistor is short-circuited by a metal-line on the FE dummy. A missing bump will increase the total resistance of the chain by R_D, two neighbouring merged bumps will reduce the total resistance by R_D (if it is at a sensitive position, see Fig. 5.1).

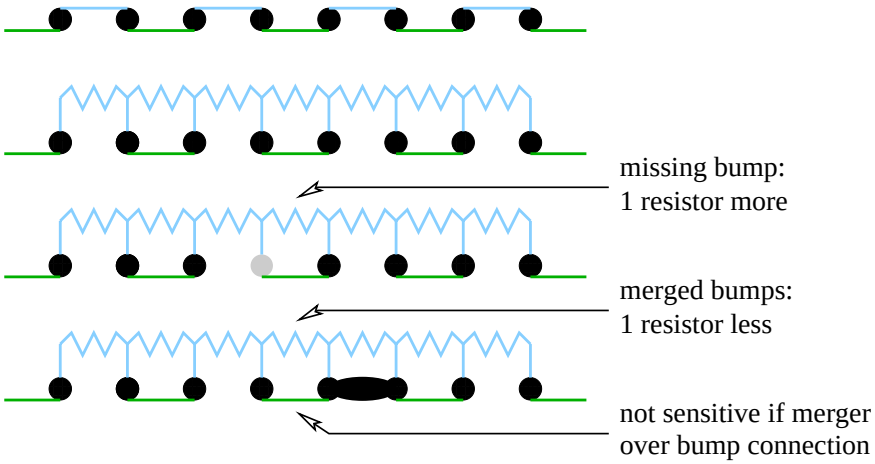

Fig. 5.1: The two top drawings show the designs of conventional and resistive daisy-chains with intact bump-bonds. The two lower drawings show the effects of missing and merged bumps in the resistive daisy-chain design.

The resistors are made by metal lines on the wafer surface. These metal lines have to be as long and as narrow as possible in order to achieve a resistance being as high as possible. Fig. 5.2 shows an array of several resistors in the form of meander-like lines. One resistor is build by a metal line with a width of 5 μm and a length of 2 800 μm. For typical values for the thickness of the metal layer (aluminium) on wafers one expects a resistance of 22 Ω ($\pm$50%).

5.2 Arrangement of Chains in Dummy Module

The dummy modules consist of a replacement for the sensor tile with the same dimensions as the real sensor tiles and 16 FE dummys. Therefore, a tile has 16 identical regions which correspond to one FE dummy. A FE dummy has 48 bond-pads where it can be connected by probes. So one restriction for the design of the daisy-chains is that all chains within a FE region must be connectable by a maximum of 48 pads. On the other hand it is desirable to have as many independent chains as possible in order to achieve a good granularity. Fig. 5.3 shows the arrangement of the chains in one FE region. Special care was taken in order to achieve that the rims and edges have only short chains since these regions are especially critical during the flip-chip process. With short chains at the rims it is easier to pin-down problems.

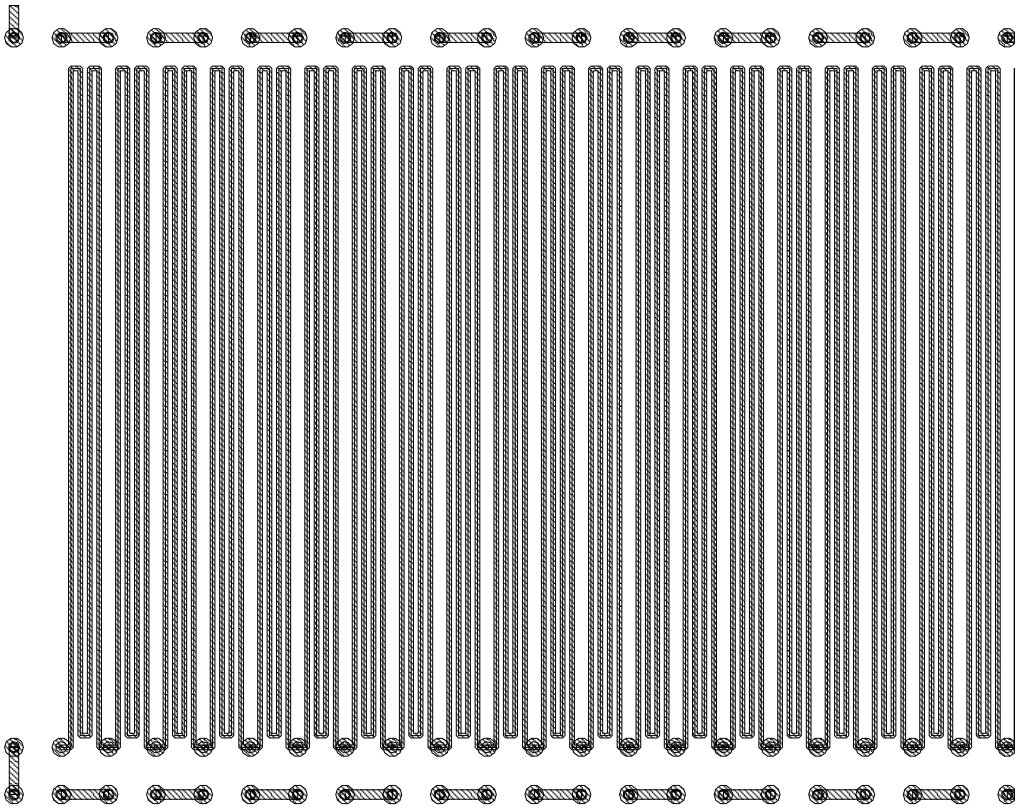

Fig. 5.2: Realisation of the resistors on the sensor dummy.

5.3 Daisy-Chain Dummy Sensor

5.3.1 Dummy Sensor

The layout of the dummy sensor having the conventional daisy-chain design is shown in Fig. 5.4. This figure shows pairs of connected neighbouring bumb-pads and some long connection lines which correspond to the light grey lines in Fig. 5.3. The shown area is one of the sixteen FE regions on a sensor tile.

Fig. 5.5 shows the same region of a dummy sensor but this time it has resistors between the bump-pads. Since the resistors' length has to be maximised almost all of the surface is covered by metal lines.

On one dummy tile 2 FE regions were made with resistive chains and 14 FE regions with the conventional daisy-chain design, see Fig. 5.6. This figure additionally shows the layout of so-called *small tiles* which could be used to make test with smaller dummy modules.

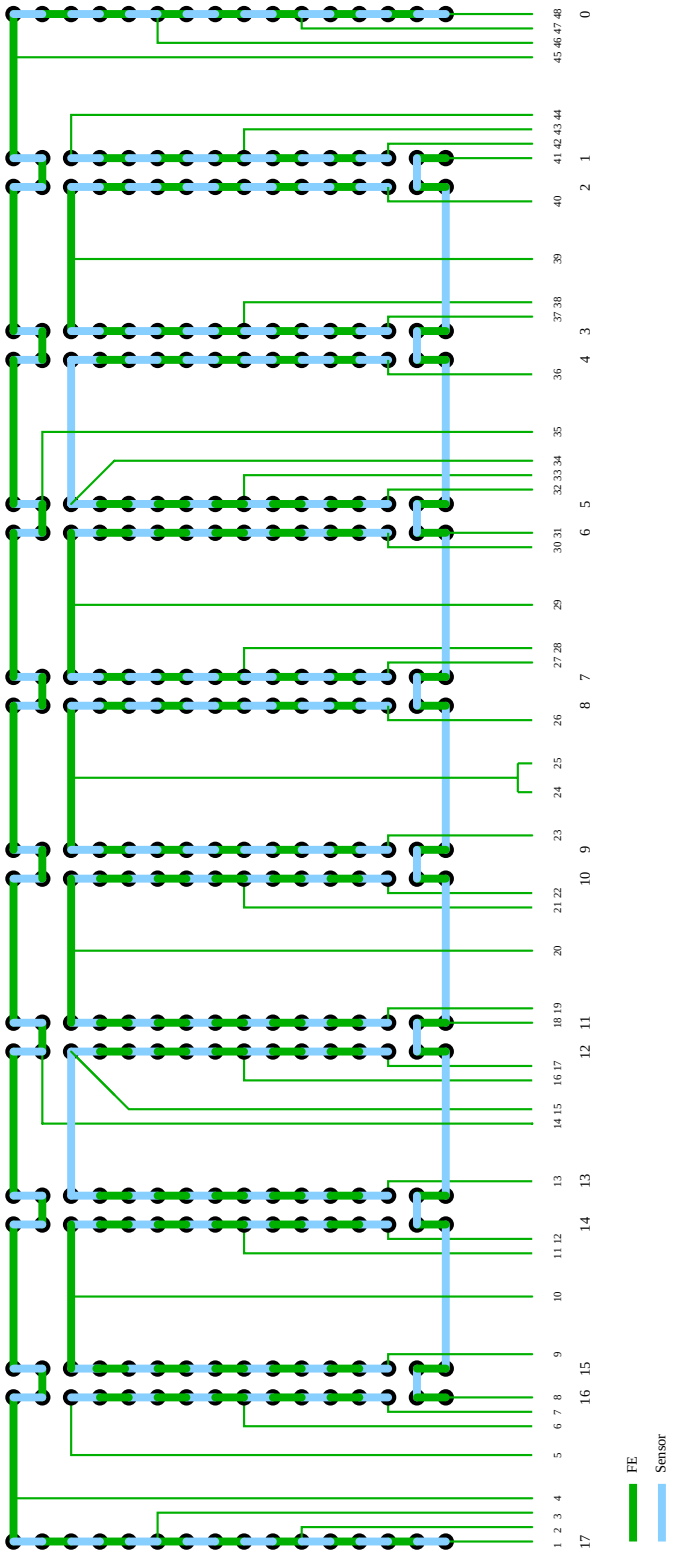

Fig. 5.3: Circuitry of the daisy-chains. Dark grey lines are located on the front-end electronics dummy, light grey connections are situated on the sensor dummy, black dots are bump connections. In the vertical direction only a part of the connections is displayed.

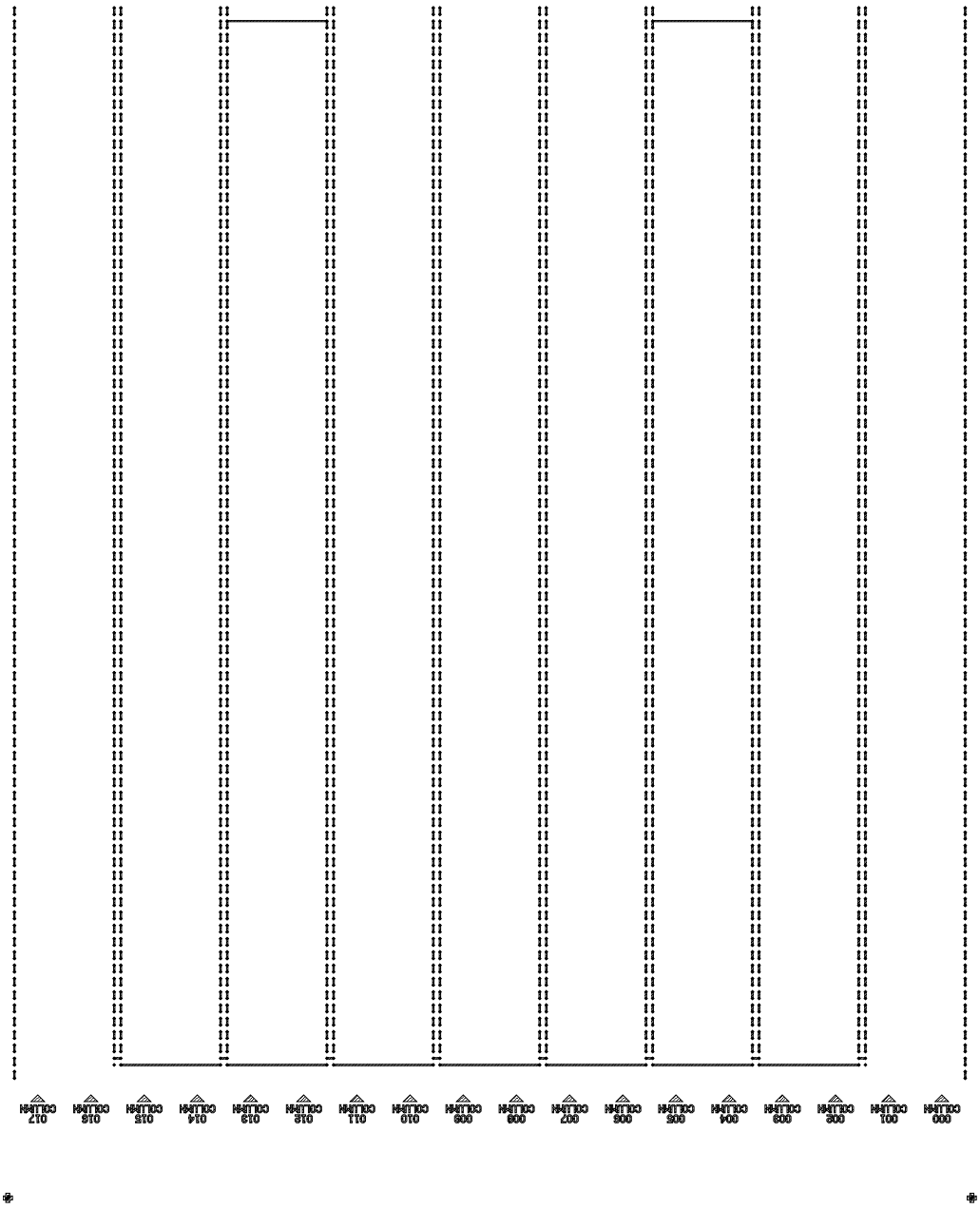

Fig. 5.4: Layout of dummy sensor with conventional daisy-chains.

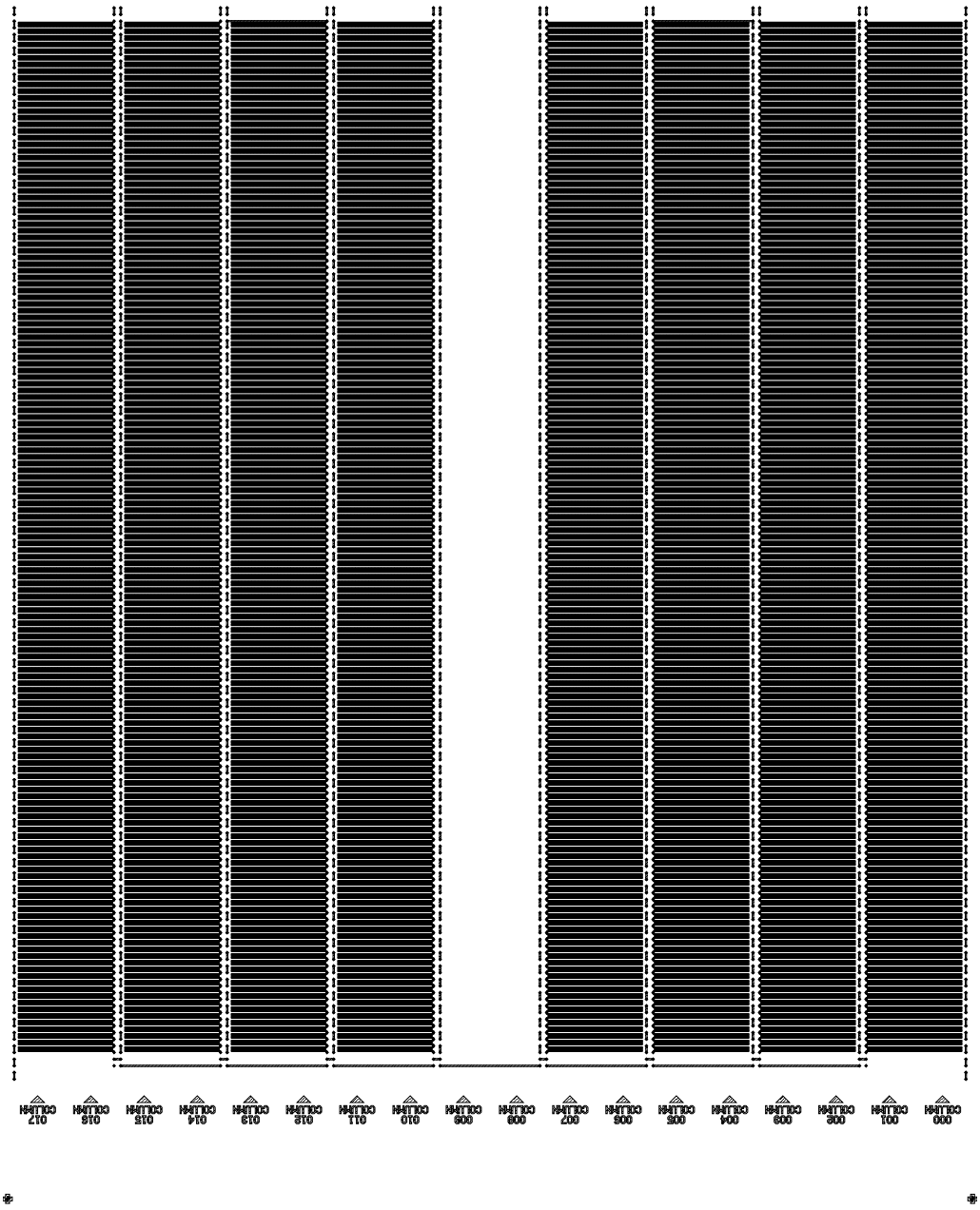

Fig. 5.5: Layout of dummy sensor with resistive daisy-chains.

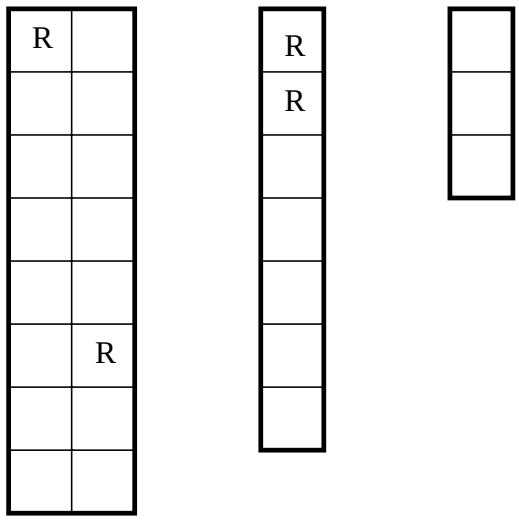

Fig. 5.6: Left: dummy sensor tile having 14 FE regions with conventional daisy-chains and 2 with resistive daisy-chains (marked with "R"). Centre and right: smaller sensor replacements (SmallMod7 and SmallMod3) for test with smaller dummy modules. (Drawings are not to scale.)

5.3.2 Dummy Sensor Test Structure

For the later test with dummy modules it is helpful to know the resistance of the resistors and the connection lines. Therefore, also a test structure was produced on the dummy sensor wafer as well. Fig. 5.7 shows its layout. The test structure has the same dimensions and bond-pad positions as a normal FE chip. This allows measurements on probe stations that are also used for FE probing. The test structure contains connection lines (the wide lines on the left-hand side in the drawing) and arrays of daisy-chain resistors. Connection lines were introduced in a way that rows of 1, 4, 9, 50 and 100 resistors can be measured.

5.3.3 Production Wafer

The dummy tiles were fabricated on wafers having the same size and thickness as production wafers of real sensors. These wafers have three dummy tiles in the centre (see wafer-map in Fig. 5.8) at the same positions as real tiles on the production wafers. Therefore, bump-deposition, dicing and flip-chipping can be done in the same fashion as with real modules. The space left-over was used to produce several small dummy tiles in the size of 3 or 7 FE regions (denoted by SmallMod3 and SmallMod7 in the wafer map) and further dummies in the size of single chips (SC_Sensor and SC_SensorR in wafer map for conventional and resistive daisy-chains). ResTest denotes the dummy sensor test structures. Additionally, the wafer layout contains some alignment marks.

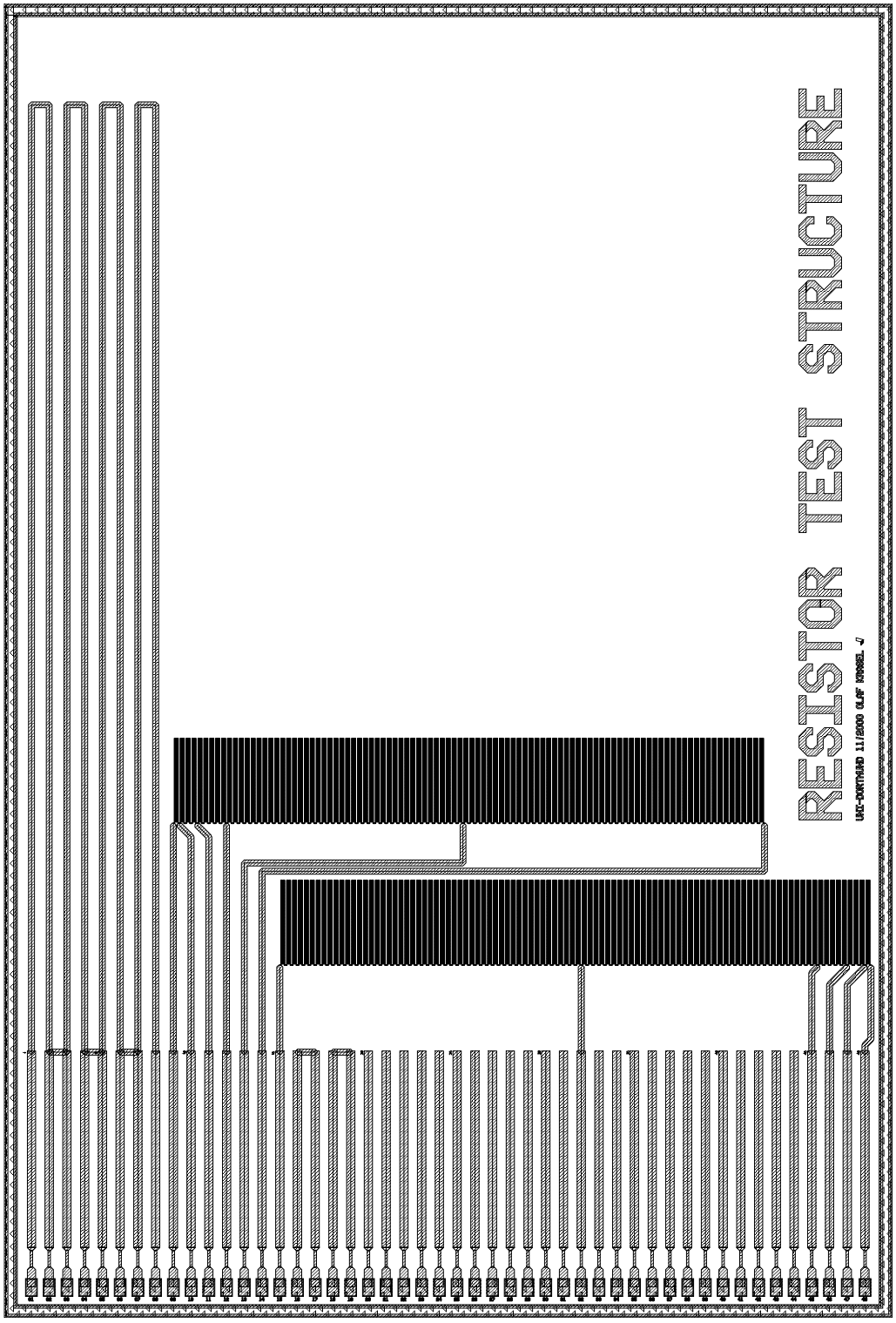

Fig. 5.7: Layout of test device for resistors on sensor replacement wafer.

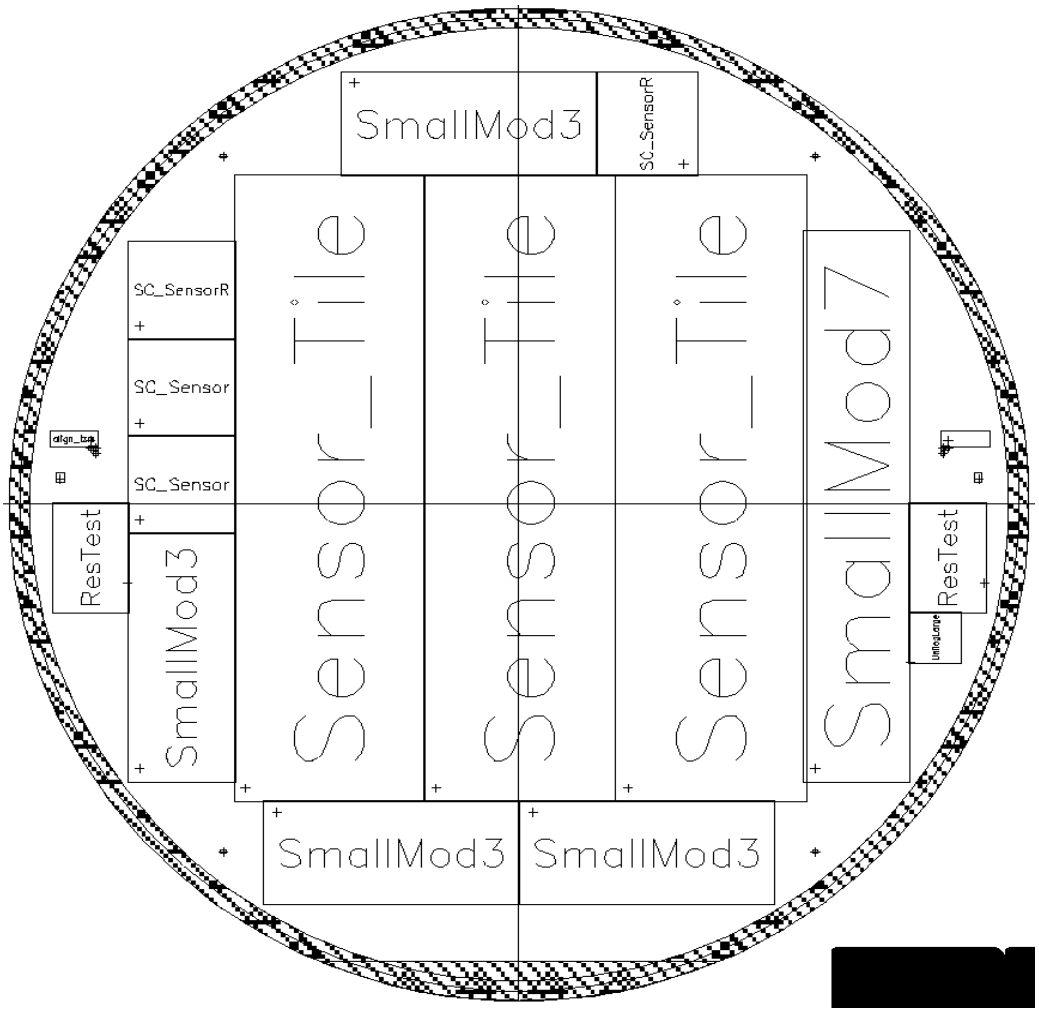

Fig. 5.8: Map of wafer with dummy sensors and test structures.

5.4 Daisy-Chain Dummy FE

5.4.1 Dummy FE Chip

The dummy FE chip is shown in Fig. 5.9. It contains bond-pads at the lower edge for wire-bonding and alongside the connections of neighbouring bump-bond-pads it carries also a lot of connection lines. These connection lines are considerably wider than the connection lines between bump-bond-pads or the resistor lines in order to reduce their resistance.

5.4.2 Dummy FE Test Structure

A further test structure layout has been provided for the dummy FE wafer. For this wafer no complete wafer mask has been prepared for the vendor but only a small reticle containing two dummy FEs and a small test structure has been designed. During production this reticle is stepped over all of the wafer. Therefore, the test structure could not be implemented only in a small number like on the dummy sensor wafer but was included in every instance of a reticle. Thus it had to be as small as possible in order not to wast place on the wafer. Fig. 5.10 shows the layout of the test structure where only a few long lines are implemented so that the measurement of the resistance of the metal layer is possible.

5.5 Measurements on Dummy Modules

Daisy-chain dummy modules with the design described in the previous sections have been produced during the development phase of pixel modules. These dummies can be used for several tests during the development and production, e.g.

Estimation of failure rate: Bare modules which consist of dummy sensor and dummy FE chip are produced in the same way as real modules. They are used to estimate the bumb-bond failure rate to be anticipated in the later series production of modules. The segmentation of the FE regions into several daisy-chains with its higher granularity towards the rims allows to check if problems occur in certain areas with a higher probability. This knowledge can be used to improve and qualifiy the production process beforehand.

Thermal cycling: In this reliability test daisy-chain modules are exposed to thermal cycling, i.e. they are repeatedly warmed up and cooled down over a temperature range that is larger than the expected one during ATLAS operation. This thermal cycling exhibits the bump bonds to stress due to shear forces between FE chips and sensor (see Fig. 5.11) and may lead to the breaking of bump-bonds.

Module reworking: In order to increase the yield in the series production it may become useful to replace single defective FE chips which have already

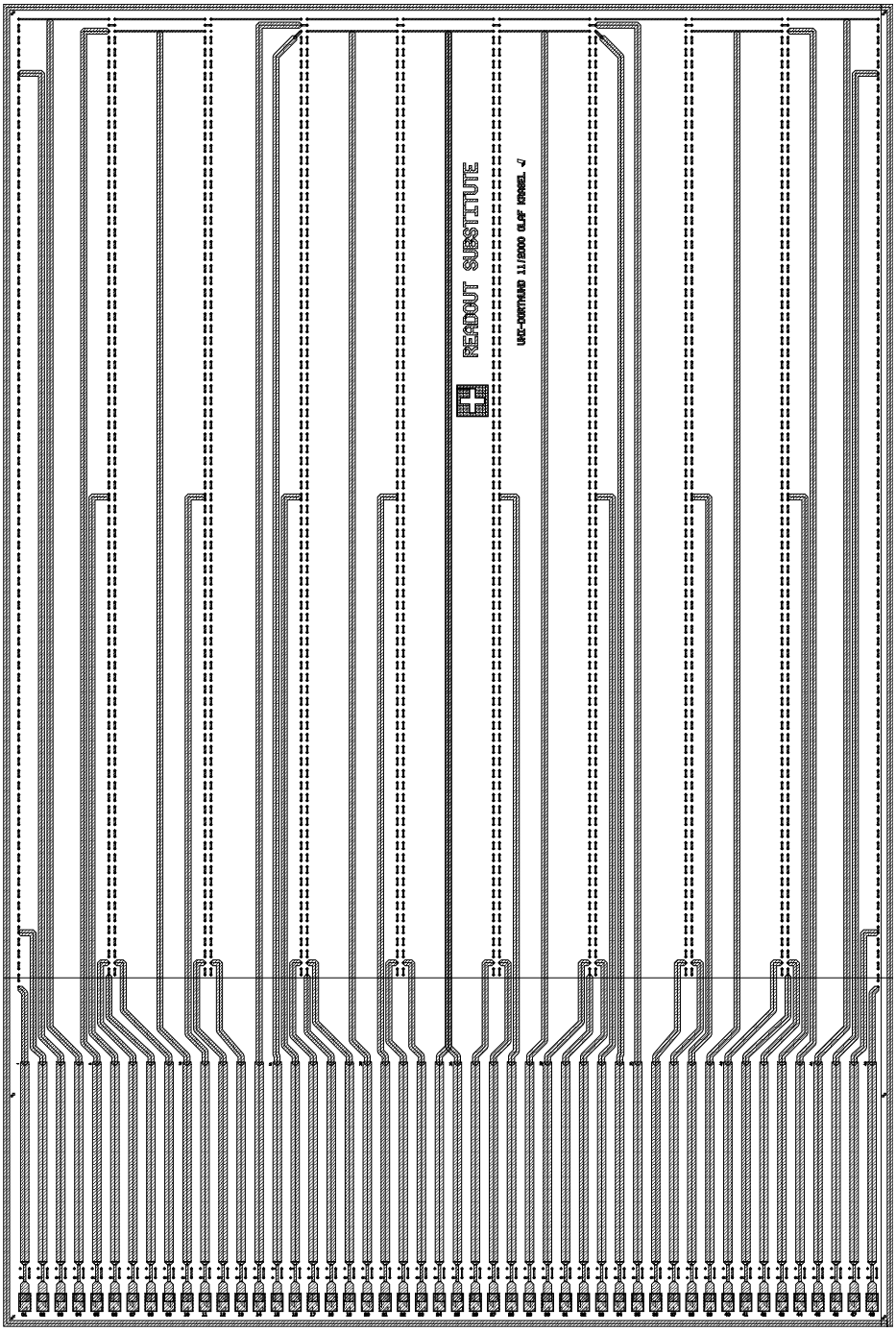

Fig. 5.9: Layout of dummy FE with daisy-chain connections. The "swiss flag" in the upper half is an alignment mark.

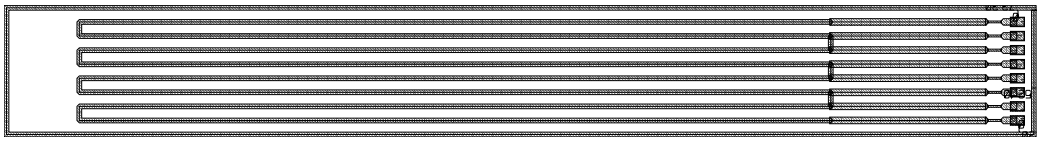

Fig. 5.10: Layout of test structures for resistors on dummy FE wafer.

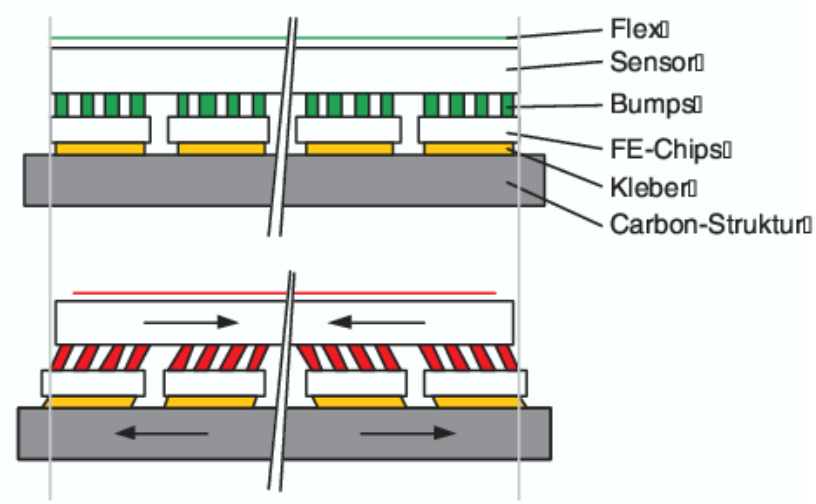

Fig. 5.11: Shear forces due to CTE mismatch of stave and sensor: Different coefficients of thermal expansions of the stave material and the sensor silicon lead to shear forces which act upon the bump-bonds. Figure is taken from [Ko02].

been flip-chipped to a sensor. Daisy-chain modules can be used to test the feasibility of module reworking.

Bump-bond resistance: For a proper functionality of read-out electronics the resistance of the bump-bonds must be within a certain range. The daisy-chains allow the measurement of this resistance. For these measurements it is important to know the contribution from the connection lines to the total resistance of a daisy-chain. The resistances of the connection line can be determined with the help of the teststructures which contain lines of all used widths.

Results from measurements on daisy-chain modules can be found in [Ko02].

Part III

Characterisation of Silicon Pad Detectors

Chapter 6

Experimental Techniques

CHAPTER 6 covers the experimental techniques which were used for the measurements within this work. The chapter starts with a section on the design of the pad-detectors. The second section introduces the facilities at CERN and Josef-Stefan-Institute which were used to irradiate the samples. Sec. 6.3 describes the mounting of the samples for measurements and the temperature control system of the measurement set-ups. The following section introduces the methods which were used to characterise the samples prior to the signal measurements. This chapter is completed by a section describing the transient current technique and the methods used for data analysis.

6.1 Design of Pad-Detectors

All samples used for this work are planar diodes with a size of 6 mm × 6 mm and have been produced by CiS [CiS]. The diodes were taken from seven different wafers which can be grouped in four sets (see Table 6.1): two wafers were taken from the preproduction for the ATLAS pixel detector. One wafer belonged to a common project (SRD) between CiS and a group from the University of Hamburg

Wafer Set	Wafer Number	Thickness [μm]
ATLAS	011_03	254
	4457_04	264
SRD, protons	4914_01	297
SCT	5194_07	293
	5195_01	297
	5195_15	300
	5195_16	291
SRD, neutrons	4914_01	297

Table 6.1: List of wafers from which the samples have been taken.

[HH]. The largest set are four wafers from the production of strip detectors for the ATLAS Inner Detector. Diodes from all of these wafers were proton-irradiated; neutron-irradiation was done only with samples from SRD wafers.
All wafers have an $\langle 111 \rangle$ crystal orientation and were oxygen enriched (24 h at 1200°C). The thicknesses vary between 254 μm and 300 μm.
Fig. 6.1 shows as an example the layout of the devices as they are produced on the ATLAS preproduction wafers. The p-side (Fig. 6.1(a)) has a circular opening (diameter 2 mm) in its metal layer. The square metal-layer above the active volume is 5 mm × 5 mm large and surrounded by a guard-ring. The n-side is completely covered by metal except for a square opening with dimensions of 1.7 mm × 1.7 mm. However, the samples from the SRD wafer have a grid metallisation of the n-side and the p-side has instead of one single guard-ring a multi-guard-ring structure (see Fig. 6.1(c), the displayed structure is in reality ≈ 1.0 mm × 1.0 mm).
SCT samples have completely metallised n-sides. Therefore, they did not allow n-side illumination with laser light.

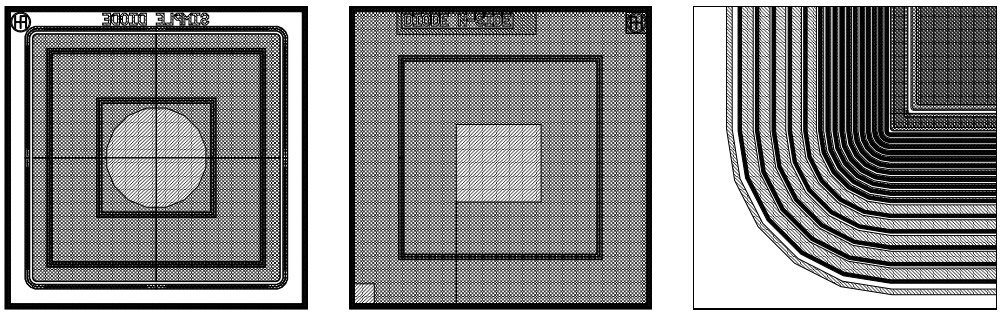

(a) p-side (b) n-side (c) multi guard-ring

Fig. 6.1: Design of pad-detectors. (a) and (b) show the two sides of a pad-detector, size 6 mm × 6 mm. (c) shows a magnified view of the multi-guard-ring structure, the shown region has in reality a size of 1 mm × 1 mm.

6.2 Irradiation Facilities and Sample Irradiation

6.2.1 Proton Synchrotron at CERN

Proton-irradiations have been done at the Proton Synchrotron (PS) at CERN [CPS] [Gl99]. This accelerator provides protons with an energy of 24 GeV coming in bunches with a beam spot diameter of about 2 cm in the irradiation zone, allowing homogeneous irradiation of samples with dimensions of 0.7 cm × 0.7 cm. Particle fluxes of $(2\text{–}9) \cdot 10^9\ p/(\mathrm{cm}^2\,\mathrm{s})$ can be achieved. During irradiation samples

were hold by card boards without biasing.
Dosimetry was done by measuring the activation of aluminium foils, which were irradiated together with the samples [Gl02]. Aluminium is transformed by the nuclear reactions

$$^{27}_{13}\mathrm{Al} + p \rightarrow {}^{24}_{11}\mathrm{Na} + 3p + n \quad \text{and} \tag{6.1}$$
$$^{27}_{13}\mathrm{Al} + p \rightarrow {}^{22}_{11}\mathrm{Na} + 3p + 3n \tag{6.2}$$

to sodium isotopes. $^{24}_{11}$Na emitts after a β^--decay photons with an energy of 1369 keV. $^{22}_{11}$Na sends out γs with an energy of 1275 keVafter a β^+-decay. The half-lifes of the β-decays are 15 h and 2.6 a, respectively.
The γ-activity of the Al sample was measured with an NaI or Ge spectrometer and corrected for irradiation time and the time after irradiation. This corrected activity is proportional to the particle fluence and can be converted with the help of the known nuclear cross-sections of the activation reactions. The accuracy of the dosimetry ranges from 7% to 10%.
The hardness factor used for calculating the equivalent fluences from the proton fluences is 0.62 [RD48c].

6.2.2 TRIGA Reactor at Ljubljana

The neutron irradiation facility of the Jožef Stefan Institute in Ljubljana (Slowenia) is a TRIGA Mark II type nuclear reactor for experimental purposes. It can be operated with powers ranging from few W to 250 kW. It provides a neutron spectrum with a significant portion of fast neutrons (about 1/3 of total flux above 0.1 MeV, [Ki98]). The fluxes of fast neutrons range from $(10^9 - 2) \cdot 10^{12}\, n/\,\mathrm{cm}^2 s$.
The samples are kept in irradiation capsules and inserted in the irradition channel F19. They were not biased during irradiation. Dosimetry is done by measuring the leakage current of dosimetry diodes being irradiated together with the samples. A series of simulations [Žo98] and measurements [Ki98] of the radiation field in the reactor core has been done to validate the dosimetry. The uncertainty of the measured fluence is estimated to be 10% [Kb01][Mi03].

6.2.3 Sample Irradiation

The irradiation of the samples was performed by collaborators at the two above described facilities. Altogether 24 samples have been irradiated. Table 6.2 gives an overview of the samples and the acquired fluences and particles. The fluence range starts with values already covered by other studies [Br00][Kb01], but also covers the fluence region expected for the ATLAS Pixel Detector.
For several fluences exist two samples to allow systematic studies of the experimental uncertainty at the same fluence. These sets (K_1/K_2, L_1/L_2, O_1/O_2, M/P, N/Q) were mounted in the same fixation during irradiation and afterwards always kept under the same temperature conditions in order to keep them always comparable.

Short Name	Origin (structure ID)	Thickness [μm]	Particles	Eq. Fluence Φ_{eq} [$10^{14}\, n_{eq}/\,cm^2$]	Error [%]
$\emptyset$	4914_01_d21	297	unirradiated	0	—
A	4457_04_d19	264	protons	3.22	10
B	4457_04_d18	264	”	8.9	10
C	011_03_d18	254	”	5.0	10
D	011_03_d19	254	”	1.06	10
E	4914_01_d07	297	”	4.46	7
F	4914_01_d10	297	”	6.51	7
G	4914_01_d15	297	”	8.06	7
P	4914_01_d26	297	”	0.924	8.0
Q	4914_01_d27	297	”	2.04	7.0
K_1	5194_07_d02	293	”	.223	8.4
K_2	5195_15_d01	300	”	.223	8.4
L_1	5194_07_d03	293	”	.524	9.0
L_2	5195_15_d03	300	”	.524	9.0
M	5195_01_d01	297	”	.924	8.0
N	5195_01_d02	297	”	2.04	7.0
O_1	5195_01_d03	297	”	4.24	7.9
O_2	5195_16_d01	291	”	4.24	7.9
R	4914_01_d35	297	neutrons	1.0	10
S	4914_01_d36	297	”	6.0	10
T	4914_01_d34	297	”	4.0	10
V	4914_01_d30	297	”	2.0	10

Table 6.2: Overview of all samples which were used within this work. The proton fluences are given with an accuracy of 7-10%, the neutron fluences with 10%. “Protons” means 24 GeV protons at CERN PS, “neutrons” are reactor neutrons at the Ljubljana reactor.

6.3 Diode Mount and Temperature Control

For the TCT- and charge collection measurement which are described in the following sections the samples were mounted on a custom designed board. The board fixes the diodes mechanically and provides electric connections to the electrodes. After several tests with different board designs a design was chosen where the board consists of an about 1.2 mm thick gold-plated copper plate (see Fig. 6.2). The diodes lie with their n-side down on the copper plate and are pressed onto the board with a small metal tongue on the p-side. This metal tongue provides the electrical connection to the p-side and fixes the diode by applying a small force. The metal tongue is insulated electrically from the copper plate. A BNC coaxial cable is attached to the board. The outer conductor is connected to the copper plate (electric ground) and the inner conductor to the metal tongue. Therefore, a negative bias voltage has to be applied.

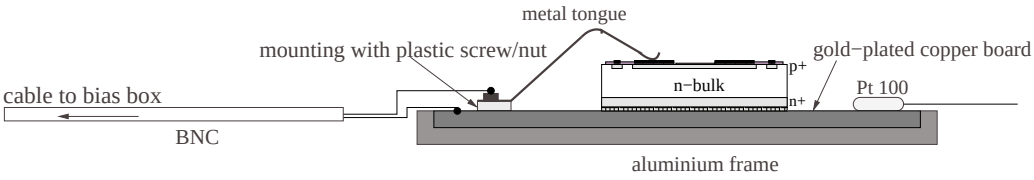

Fig. 6.2: Schematic drawing of the diode attachment board. Drawing taken from [Rj03].

This design enables an easy connection of diodes and showed the best behaviour in the point of signal integrity what is crucial for the TCT-measurements.

For CV- and IV-measurements a slightly different design has been chosen: diodes are again fixed with a metal tongue but this time on a PCB board which has two Lemo cables per electrode, i.e. two cables are connected to the board (ground) and two to the metal tongue. The double connections are needed for CV-measurements.

The board with the diode is mounted in a closed aluminium box (see Fig. 6.3) which provides electrical shielding and is flooded with gaseous nitrogen in order to keep the sample in a dry atmosphere when the set-up is cooled down. The cover of the box has an opening for light injection. The box is coated with foamed plastic for thermal insulation.

In order to control the temperature the aluminium box is attached to a peltier element. The temperature is measured with a Pt100 thermal resistor whose resistance is measured with a digital multi-meter and read out with a computer. The computer uses a custom written LABView software to read the temperature and control the power supply unit of the peltier element. The warm side of the peltier element is cooled with water taken from an ice-water-mixture. With this

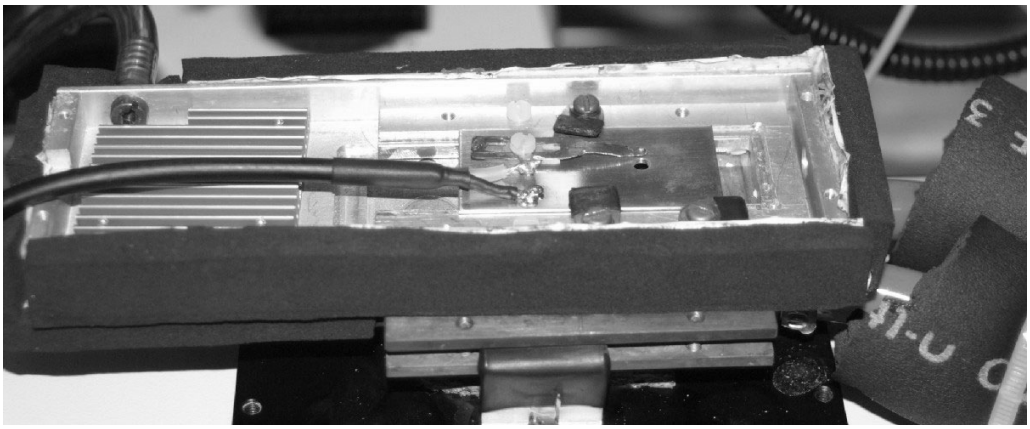

Fig. 6.3: Photograph of the aluminium box which was used to fix the board with diodes during measurements. In the upper left corner one sees the N_2-inlet. The gas flows over a cooling element. Pipes for cooling water are situated on the right side. The copper board with the metal tongue on top can be seen in the centre. The boxed is closed with a cover during measurements. See text for further informations.

set-up the temperature can be controlled in the range from -20°C to 20°C with an accuracy of ±0.3 K (rms).
A drawing of the whole mechanical and cooling set-up can be seen in Fig. 6.4.

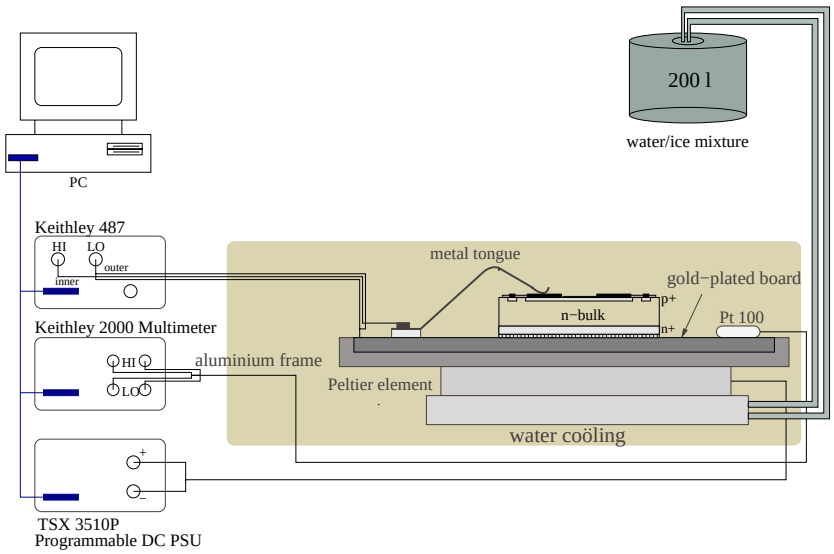

Fig. 6.4: Drawing of the mechanical and cooling set-up. The picture is taken from [Rj03].

6.4 Diode Characterisation

All diodes which were to be used in these studies were pre-characterised before any signal measurement. This was done by measurements of the capacitance-voltage (CV) and current-voltage (IV) characteristics. These measurements were also performed later during the charge-collection studies of irradiated diodes.

6.4.1 Current-Voltage Measurements

IV-measurements were done before irradiation in order to exclude defective devices from further use. Defective devices are those with a low break-down voltage (below 200 V) and therfore they cannot be biased with voltages as high as necessary.

The circuit used for these measurements is shown in Fig. 6.5. The diode is biased from the voltage source of a Keithley K487 pico-ammeter. The current is measured in the ground loop with the built-in pico-ammeter of the same device. A custom written LabVIEW software controls the set-up.

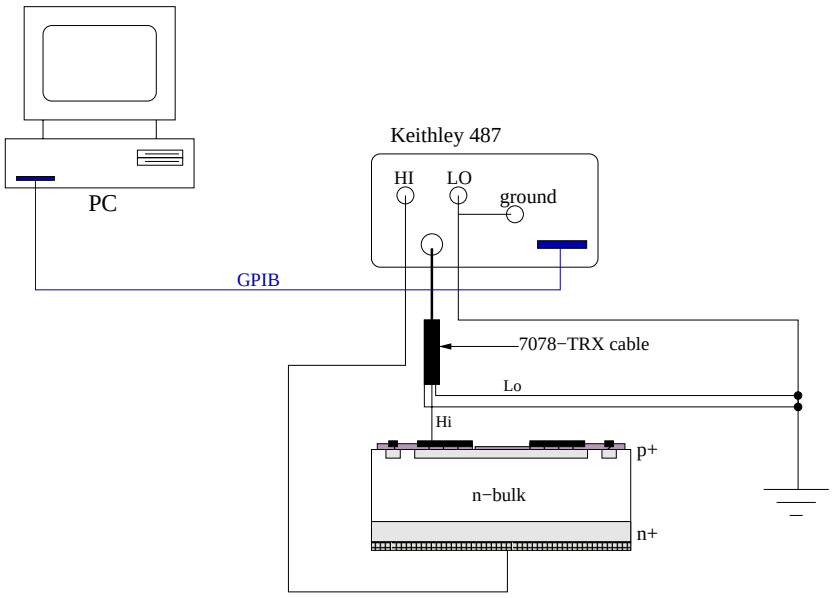

Fig. 6.5: Circuit for measurements of the IV-characteristics of diodes. The drawing is taken from [Rj03].

6.4.2 Capacitance-Voltage Measurements

The measurement of the CV-characteristics is an important tool to determine the depletion voltage of diodes. Fig. 6.6 shows the measurement set-up. According to eq. (3.63) the capacitance C of the diode is inverse proportional to the thickness d of the depletion zone. That means that the capacitance is increasing with falling bias voltage and stays constant after reaching depletion. Since the depth d of the depletion depth is proportional to $1/\sqrt{V_{\text{bias}}}$ the graph has straight lines below and above V_{dep} when plotting $1/C^2$ vs. V_{bias} or C vs. $1/\sqrt{V_{\text{bias}}}$ (see Fig. 6.7). A straight line is fitted to each of the two branches in the plots and the depletion voltage is obtained from the intersection point of the two fitted lines.
Technically the capacitance of the device is derived from the measurement of the complex impedance. A sinusoidal varying AC voltage (amplitude 50 mV) is applied to the device under test (DUT) and the amplitude and phase shift of the resulting current is measured.
To derive the capacitance from the complex impedance the LCR-meter provides two models for the DUT: In the C_sR_s model the DUT is modelled by a capacitance C_s and a serial resistor R_s. The alternative model C_pR_p uses a capacitance C_p with a parallel resistor R_p. Unfortunately, none of them gives an exact equivalent circuit diagram for a partially depleted diode. Such a diode can be viewed as a serial circuit of the undepleted and depleted part of the bulk (see Fig. 6.8). Each of these two parts is considered as capacitance with a parallel resistor. In order to take into account the surface currents which are caused by humidity and dirt a further parallel resistor R_{surf} is introduced.

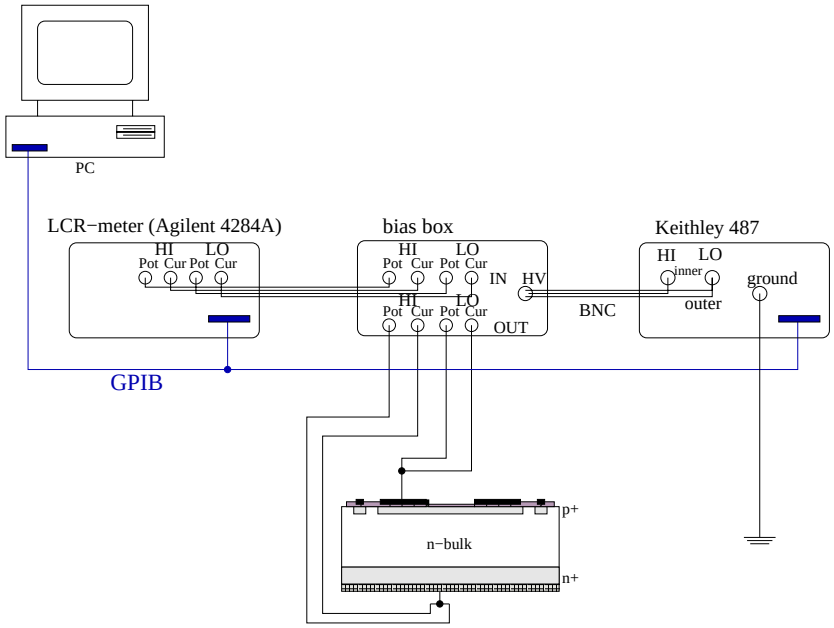

Fig. 6.6: Circuit for measurements of the CV-characteristics of diodes. The drawing is taken from [Rj03].

Due to the low conductivity of the depletion zone its complex resistivity is dominated by C_d. R_d takes into account the leakage current which becomes stronger with irradiation. The undepleted zone has a high conductivity. Therefore, (at low measurement frequencies[1]) the contribution from C_u can be neglected and the partially depleted pad-detector would be described best by a serial circuit of R_u and C_d. However, at voltages close to V_{dep} the undepleted zone has only little resistivity and the device can be described as a single capacitor. Therefore, both models should yield the same result for large depletion depths. In highly irradiated samples the parallel model gives the better results for large depletion depths since there R_d—which considers the DC leakage current—becomes significant. A further advantage of the parallel model is that it also takes into account surface currents by R_{surf}. A more detailed discussion of this problem can be found in [Žo98]. Therefore, the parallel model is chosen for the analysis of CV-measurements.

[1] For high measurement frequencies f_m the impedance of C_u is $Z_{cu} = 1/(2\pi f_m)$ which becomes dominant if it drops below R_u.

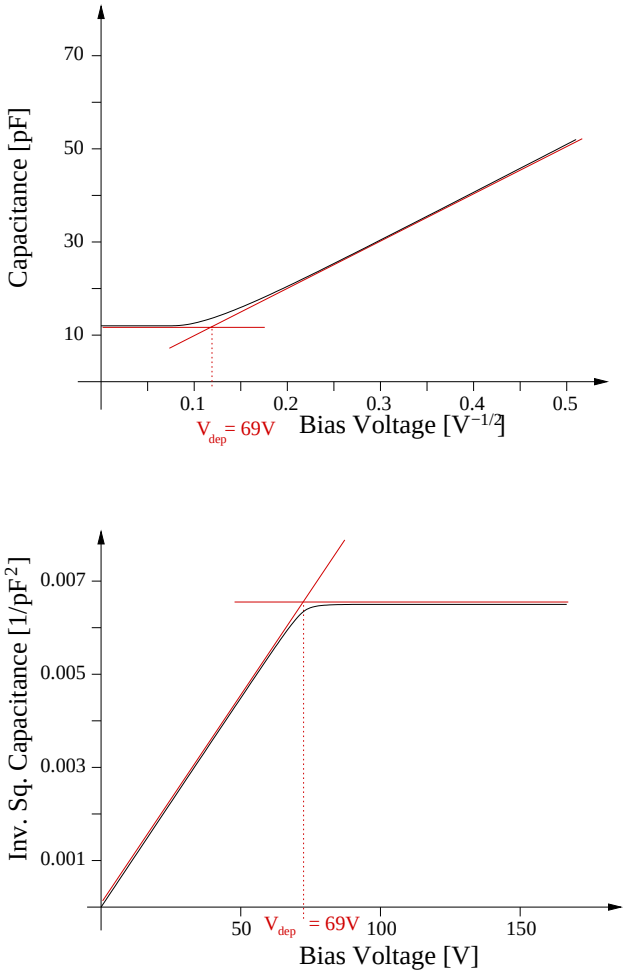

Fig. 6.7: Two plotting possibilities for CV-measurements. The depletion voltage is found by fitting straight lines to the data below and above the kink and taking the x-value of the intersection point.

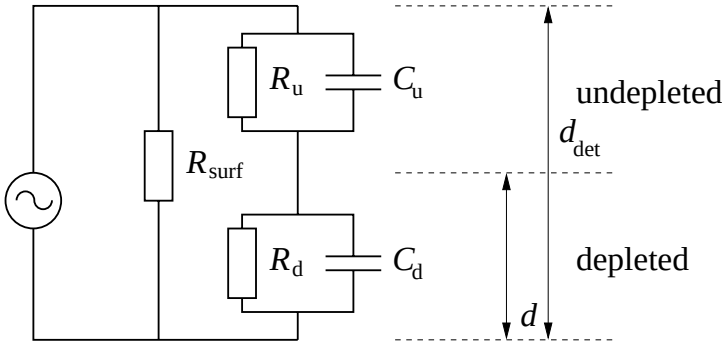

Fig. 6.8: Equivalent circuit diagram for a partially depleted diode [Žo98].

6.5 Transient Current Technique

6.5.1 Principle of TCT-Measurement

The *transient current technique* (TCT) measures the signal current from the detector vs. time (*not the charge* as it is usually done in spectroscopic measurements). As the measured current is caused by the drifting charge carriers—as described in section 3.3—the measurement of the signal shapes at different bias voltages reveals information about trapping times, drift velocities and field configuration. Since the charge collection times in pad-detectors with thicknesses of about 250-300 μm are in the regime of 3-40 ns the measurement set-up has to satisfy high requirements with respect to bandwidth and signal integrity. Especially the cabling and the board for the decoupling circuit were delicate aspects in designing the measurement set-up.

6.5.2 Charge Injection

In order to measure the signal current from a detector free signal charges have to be injected. This can be done by a variety of particles like laser-photons or radiation from α- and β-sources. The respective properties of these particle and their specific charge deposition profile have already been introduced in sec. 3.1. Now their usability for TCT-measurements shall be discussed on the basis of these properties.
In order to be suitable for TCT-measurement the charge deposition profile of the used particles should fulfill the following requirements:

Reproducibility: As it will be laid out later it is advantageous to average over several single measurements of the signal current of a detector in order to reduce the noise. This makes only sense if the signal current has always the same shape and is caused by a constant amount of charge.

Trigger Signal: The oscilloscope which is used to measure the signal current needs a trigger signal. This can be supplied by the signal itself (i.e. triggering on a certain threshold). However, if the signal is not constant (e.g. due to noise) this deteriorates the quality. Therefore, it is desirable to have an additional stand-alone trigger signal.

Short Penetration: For many interesting charge-collection parameters it is advantageous to measure them separately for holes and electrons. Sec. 3.3.6 explains how this can be achieved. In order to use the method introduced therein it is necessary to use particles with a charge deposition profile that is concentrated close to the surface.

α-particles from a ^{241}Am-source deposit always the same energy in the detector if the air gap between source and surface of the DUT is not too large. Their range also is quite constant as can be seen in Fig. 3.2. However, they deposit

most of their energy in a depth of about 25 μm (see Fig. 3.2). For the thin pad-detectors as used in this work this is up to 10% of the total thickness. Therefore, large part of the bulk is not used and the signals are shorter than necessary. A further argument against using an α-source is the lacking probability to obtain a stand-alone trigger signal.
The use of β-particles is disadvantageous due to their varying amount of deposited energy (see sec. 3.1.4). A stand-alone trigger signal could be supplied by an additional detector behind the DUT. However, such a set-up would be quite complicate. Furthermore, β-particles can only be used to imitate mips since they deposite energy throughout the whole detector but do not allow to separately measure hole and electron signals.
Most advantageous of all possibilities is the user of a laser: it supplies a reproducible signal. The oscilloscope can be triggered together with a laser so that it measures synchronously to the charge injection what delivers clean measurements. The depth of the charge deposition can be controlled by the choice of the laser wavelength as can be seen in Table 3.1: close-to-surface charge deposition which is concentrated within a few micrometer can be achieved by using a red laser. The close-to-surface characteristic of the charge deposition is enhanced by the exponential charge deposition profile of the laser.
These considerations have lead to the decision to use a laser with wavelength of 672 nm for the TCT-measurements.

6.5.3 Experimental Set-up

Optical Set-Up

The optical set-up includes a pico-second laser (Pulsed Diode Laser PDL 800, vendor Picoquant) for charge injection which is connected to a light-guide that directs the light to the DUT. The laser driver can be equipped with three different laser heads having the wavelengths 672 nm, 908 nm and 1057 nm. The penetration depths of these lasers into silicon are given in Table 3.1 on page 25.
The laser is triggered by the trailing edge of a rectangular signal from a pulse generator with a rate of 500 Hz. The laser light is sent through a 20 m long light-guide in order to delay the charge injection. Thus the detector signal is induced after the noise from the pulse generator and laser driver has ceased. Therefore, the signal is not disturbed by pick-up from one cable to another. The pulse generator supplies also the trigger signal for the oscilloscope which compensates the delay of the light pulse by an internal delay.
The end of the light-guide is directed on the diode's surface. Before reaching the DUT's surface the laser beam passages 1-3 cm of air and is widened to a light-spot of several mm.
Another possibility to send the laser light onto the diode is to couple it into a microscope via a beam-splitter. With the help of a camera the laser spot can be targeted on certain positions on the DUT. The position is controlled via an

xy-table where the whole diode mount is attached to. The minimum spot size is of about 100 μm, but the intensity drops very a lot due to the beam-splitter. Nevertheless, this technical possibility enables interesting position-resolved measurements on segmented devices or surface scans of pad-detectors.

Electrical Set-Up

The electrical set-up (see Fig. 6.9) consists of the cabling to connect the components and the electronic circuitry to amplify the signal and feed it into the oscilloscope. Fig. 6.9 shows the schematic circuit of the TCT set-up. The diode is mounted on a board (as described in 6.3) which has ground potential. Consequently, the metal tongue has negative bias voltage.

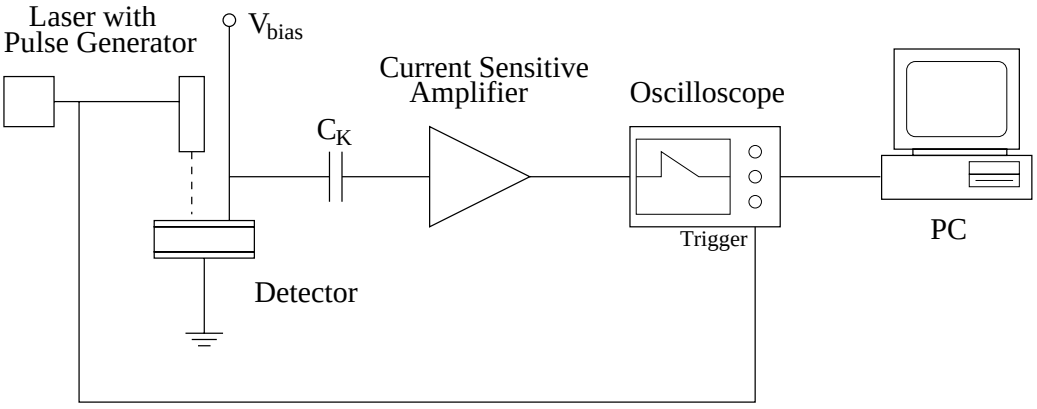

Fig. 6.9: Schematic circuit of the TCT set-up.

The detector signal is fed through a BNC cable with 50 Ω impedance to the so-called bias-box. Within this box an RC circuit couples out the AC signal $i_m(t)$ with the help of the coupling capacitor C_K (10 nF). This also eliminates the leakage current which is a DC component. The design of this circuit is very critical for the signal integrity. The capacitor has to be designed for high-frequency signals at high-voltages. The used capacitor limits the bias-voltage to 1 000 V.
A small part of the detector signal is reflected at the input of the RC circuit and a further part at the input of the amplifier after the bias box. These reflections run back to the diode, are again reflected and reach the amplifier input a second time. In order to avoid interference with the original signal before it has returned to zero the cable between diode and bias box has to have a minimum length. On the other hand this cable should not be too long, otherwise the signal integrity would be worsened due to attenuation and dispersion of the signal.
The AC signal which has been coupled out from the detector bias voltage is given on the input of a wide-band amplifier (Phillips Scientific 6954, 10$\times$ amplification).

The 3dB bandwidth of this device extends from 100 kHz to 1.8 GHz. The current signal i_m is converted to a voltage signal u_m at the 50 Ω input impedance.

A fast oscilloscope (Tektronix TDS784D, bandwidth 1 GHz) measures the amplified signal. It is triggered by the same pulse generator that triggers the laser driver and compensates the signal delay due to the 20 m long light-guide by an internal delay of about 150 ns. Signal noise is suppressed by averaging 250 single pulses. This is done by the oscilloscope and reduces statistical fluctuations to a negligible level. The oscilloscope is controlled by custom written software (LabVIEW environment) that also controls the bias voltage source. The software scales automatically the resolution of the y-axis of the oscilloscope according to the maximum voltage of u_m. Therefore, always a large range of the oscilloscope's ADC[2] is used.

Depending on the required regime of bias voltages two different sources were used: For bias voltages between 0 and 500 V a Keithley K487 is used. If bias voltages above 500 V are needed a Keithley K248 is used. This unit can supply voltages in the range 40–1000 V. Since the latter cannot supply voltages below 40 V and has a worse stability (±1 V) usage of the K487 is preferred whenever it is possible. The voltage sources are controlled by the same software as the oscilloscope. With this program complete measurement series with varied bias voltages can be done automatically. Alongside the control of the devices the software reads out the oscilloscope and writes the data to the hard disk of the PC. For each measurement the time, date, bias voltage and record length (of the oscilloscope sample) are written to harddisk. With the recorded time the temperature can be found from the log files of the temperature control program described in section 6.3.

Signal Integrity

Fig. 6.10(a) shows a measurement of the signal integrity. A test pulser signal is fed into the input of the RC circuit. This signal consists of a DC part with added rectangle pulse. The output signal is higher by roughly a factor 10 (take notice of different scales) and shows a good reproduction of the original signal. The rise time of the signal deteriorates from (1.255 ± 0.001) ns to (1.415 ± 0.001) ns, measured by the oscilloscope as an average of 250 single pulses. (The errors are only the statistical).

In Fig. 6.10(b) a magnified sample of the same pulses is shown: reflections occur ≈ 20 ns after the signal. In measurements with diodes these reflections occur after ≈ 50 ns because there a longer cable is used. This time restricts measurements to charge collection times below 35 ns but it is long enough to allow measurements at bias voltages which are low compared to the depletion voltages of irradiated diodes.

[2] **a**nalogue to **d**igital **c**onverter

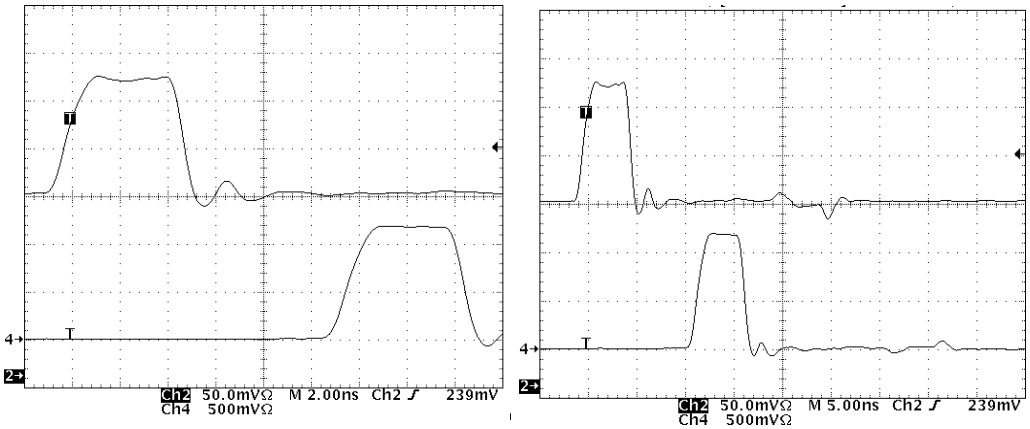

(a) (b)

Fig. 6.10: Measurement of the signal integrity. The figure shows the comparison between fed-in signal (top signal in each subfigure) and amplified signal (bottom signal in each subfigure). (b) shows a longer sample of the same measurement shown in (a). The scale of the bottom signals is 10 times larger than that of the top signal.

Signal from Unirradiated Diode

Fig. 6.11 shows measurements with an unirradiated diode with charge injection from p- and n-side and a bias voltage of 100 V. The electron-dominated signal after p-side illumination is significantly shorter than the n-side signal. This is caused by the different drift velocities of electrons and holes. The slopes of the two pulse-tops have different signs since the charge-carriers drift in opposite directions.

6.5.4 Signal Corrections

Bandwidth Limitation

The original detector signal i_s is distorted due to the limited bandwidth of the electronics. Especially rapidly changing parts of the signal—e.g. the edges—are affected. The consequences will be discussed with the help of the equivalent circuit diagram in Fig. 6.12. The detector is replaced by a current source with a parallel capacitance C_d which represents the detector's capacitance. The current flows over the decoupling capacitor C_K to the amplifier which has an input impedance of 50 Ω. Since $C_d \ll C_K$ the latter can be neglected for the further calculation. Thus the complex frequency dependent resistance Z which is seen by the signal current i_s is

$$\frac{1}{Z} = \frac{1}{R} + i\omega C_d \,. \tag{6.3}$$

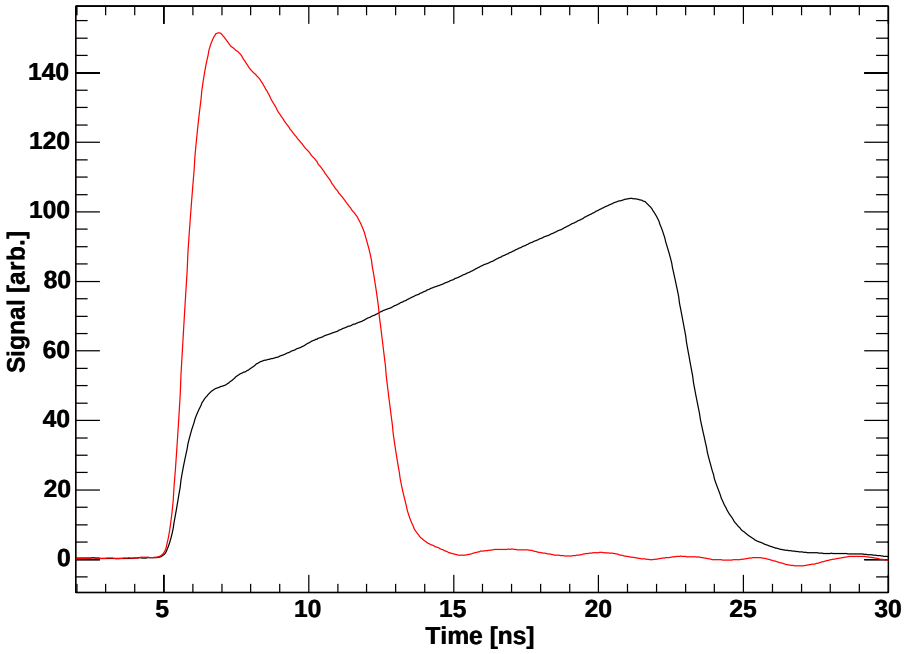

Fig. 6.11: Signals of an unirradiated diode after p- and n-side illumination with a 672 nm laser. The electron dominated p-side signal is significantly shorter than the n-side signal. The opposite drift direction of the charge-carrier types can also be seen on the inverted tilt of the signals.

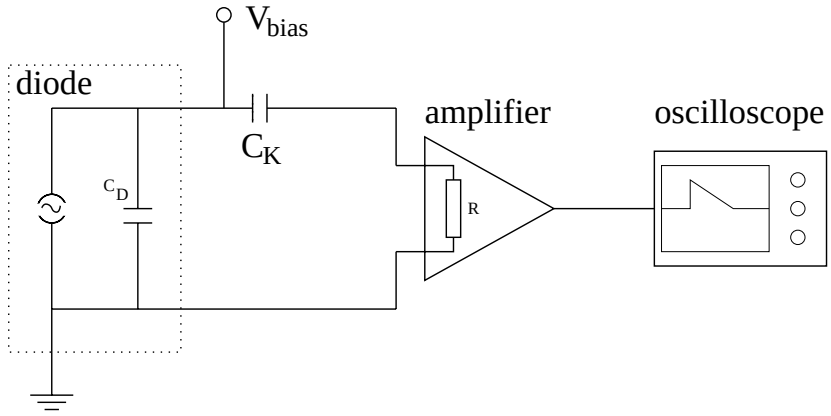

Fig. 6.12: Equivalent circuit diagram of the experimental set-up for an analysis of bandwidth limitations.

The current is amplified by a factor A. Therefore, the measured voltage u_m is given in the frequency domain by

$$u_m(\omega) = i_s(\omega) A Z =: i_s(\omega)\,\eta(\omega)\,. \tag{6.4}$$

The factor $\eta(\omega)$ is the frequency dependent transfer function of the system:

$$\eta(\omega) = \frac{AR}{1 + i\omega\tau_{\mathrm{RC}}}\,, \tag{6.5}$$

with $\tau_{\mathrm{RC}} = RC_d$ being the response time of the system. The corresponding cut-off frequency $f_g = 1/(2\pi\tau_{\mathrm{RC}})$ ranges for typical values of the resistance and the capacitance ($R = 50\,\Omega$, $10\,\mathrm{pF} < C_d < 30\,\mathrm{pF}$) between 100 MHz and 320 MHz, thus significantly below the bandwidths of the amplifier and the oscilloscope (1.8 GHz and 1 GHz, resp.). Therefore, the detector capacitance is the limiting factor for the bandwidth of the whole set-up.
As the oscilloscope measures the signal voltage $u_m = u_m(t)$ in the time domain, a relation between $u_m(t)$ and $i_s(t)$ must be found. In the frequency domain $u_m(\omega)$ is the product of $i_s(\omega)$ and $\eta(\omega)$. Therefore, $u_m(t)$ is the convolution (denoted by $\otimes$) of the Fourier transforms of these two functions [Bu00]:

$$u_m(t) = \eta(t) \otimes i_s(t) \tag{6.6}$$

$$= \int_{-\infty}^{+\infty} \eta(t - t')\, i_s(t')\, dt'\,. \tag{6.7}$$

The Fourier transform of the transfer function $\eta(\omega)$ is

$$\eta(\omega) \xrightarrow{\mathrm{FT}} \eta(t) = \begin{cases} 0 & \text{for } t < 0 \\ \frac{AR}{\tau_{\mathrm{RC}}} e^{t/\tau_{\mathrm{RC}}} & \text{for } t \geq 0 \end{cases}\,. \tag{6.8}$$

With this equation it follows

$$u_m(t) = \frac{AR}{\tau_{\mathrm{RC}}} e^{-t/\tau_{\mathrm{RC}}} \int_{-\infty}^{t} e^{t'/\tau_{\mathrm{RC}}}\, i_s(t')\, dt'\,. \tag{6.9}$$

The upper integration limit changes to t since $\eta(t - t') = 0$ for $t' > t$. Deriving this w.r.t. t and solving for $i_s(t)$ one obtains

$$i_s(t) = \frac{u_m(t)}{AR} + \frac{\tau_{\mathrm{RC}}}{AR}\dot{u}_m(t)\,. \tag{6.10}$$

This result can also be explained phenomenologically: the first term gives the result from Ohm's law with an infinite fast response of the electronics. The second term corrects the measured voltage by adding the derivative of the measured voltage, i.e. at rapidly changing parts of the signal a higher correction is added than at slowly changing parts. Rapidly changing parts are exactly the parts which

are mostly impaired by limited bandwidth. In Fig. 6.13 this correction is shown for an exemplary measured signal.
Since for the further analysis the absolute height of the signal is irrelevant as long as the calibration stays constant in the following

$$i(t) = u_m(t) + \tau_{\mathrm{RC}} \dot{u}_m(t), \quad [i] = \text{arb.}, \tag{6.11}$$

is representatively used for the signal shape and given in arbitrary units.

Post-Pulse Oscillations and Reflexions

As it will be described later in section 6.5.5 the measured signal has to be multiplied with a correction factor $\exp(t/\tau_{\mathrm{eff}})$ for analysis. In many cases τ_{eff} is equal or even smaller than the charge collection time, i.e. the correction factor grows significantly over the length of the signal. Therefore, even small post-pulse oscillations are extremely exaggerated (cf. Fig. 6.13). Furthermore, the measured signal does not necessarily return fast enough to base line so it is difficult to find a proper limit for integration of the curve in order to obtain the charge. Therefore, the integral over the signal which has been multiplied with $\exp(+t/\tau_{\mathrm{eff}})$ depends strongly on the upper limit.
In order to deal with this problem the trailing edge of the already bandwidth corrected signal $i(t)$ is replaced by a falling exponential function for times $t > t_2$. t_2 is the inflection point of the curve $i(t)$:

$$i(t) \rightarrow \begin{cases} i(t) & \text{for } t < t_2 \\ i_2 e^{-t/\tau_f} & \text{for } t \geq t_2 \end{cases} . \tag{6.12}$$

i_2 and τ_f are the free parameters of the function $i_2 e^{-t/\tau_f}$. They are extracted by a fit to the measured curve between the inflection point t_2 and a point t_3. The latter is the point where $i(t)$ has fallen to 50% of $i(t_2)$.

In the analysis which is described in the following all signal shapes $i(t)$ have been corrected for distortions by limited bandwidth and post-pulse oscillations and reflections. Therefore, no further symbol is introduced and in the following $i(t)$ is used in this sense.

6.5.5 Extraction of Effective Trapping Times

For the extraction of the effective trapping time two methods can be used: The *charge correction method* (CCM) according to [Kb01] and the *exponentiated charge crossing* (ECC) as described in [Br00]. Both methods require to integrate over the signals: the integration limit starts always well below the leading edge (≈2–3 ns before the inflection point). The upper end of the integration limit is several ns above the inflection point of the leading edge. Since the signal rises and falls very rapidly due to the corrections introduced in the previous section a more precise definition is not necessary.

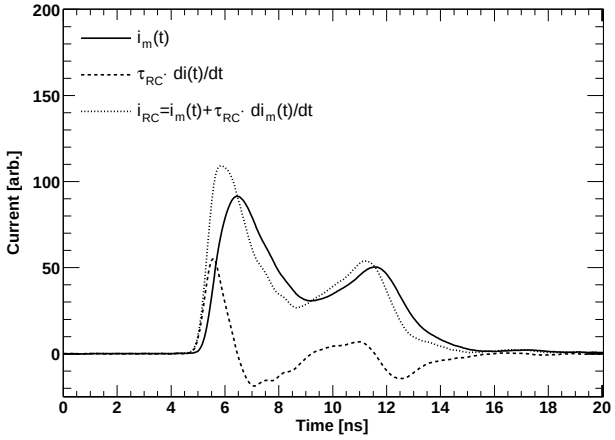

Correction of signal distortion due to limited bandwidth. From the measured curve (solid line) the derivative is calculated, multiplied with τ_{RC} (dashed line) and added to the measured signal. The result is the corrected curve (dotted line). See text for details.

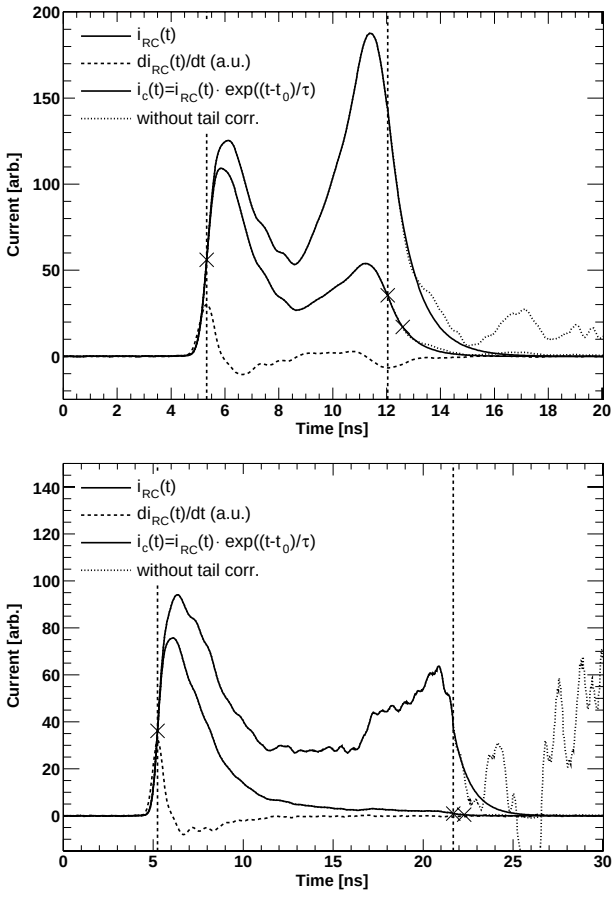

Suppression of post-pulse oscillations and reflections in signals after p-side (top) and n-side illumination (bottom). The measured signal shape (lower solid line) is replaced above the inflection point of the trailing edge by the function $i_0\, e^{-t/\tau_f}$. The dashed line is the 1st derivative which is used to find the inflection points (dashed vertical lines with first and second $\times$). The third $\times$ gives the point where the measured signal shape drops to 50% of its value at the inflection point. The upper solid line gives the exponentiated current. Dotted lines give the functions without tail-correction. See text for details.

Fig. 6.13: Signal corrections applied to measured signals. This example is taken from measurements on sample C ($\Phi_{\mathrm{eq}} = 5 \cdot 10^{14}\, n_{\mathrm{eq}}/\,\mathrm{cm}^2$) with 130 V bias after p-side illumination.

Charge Correction Method

By using the charge correction method all measured signal shapes $i(t)$ from one series—i.e. measured with different bias voltages on the same diode and same calibration of the set-up—are multiplied with a compensating factor $\exp(t/\tau'_{\text{eff}})$:

$$i_c(t) = i(t) \cdot \exp(t/\tau'_{\text{eff}}) \,. \tag{6.13}$$

Comparing with eq. (3.85) it can be seen that for the case of $\tau'_{\text{eff}} = \tau_{\text{eff}}$ this factor would exactly compensate the signal deficiency due to charge trapping. Subsequently the curves $i_c(t)$ are integrated giving the *compensated charge* Q_c. These compensated charges are plotted against V_{bias}. The resulting curves are called *compensated charge collection curves*. Since the correct value of τ_{eff} is still unknown, this procedure is repeated for several values of τ'_{eff} (see Fig. 6.14). By using the correct value for τ'_{eff} the corresponding compensated charge collection curve would be flat above full depletion voltage because the corrected charges become independent from the bias voltage.
In order to find the curve fulfilling this condition straight lines are fitted to the compensated charge collection curves above V_{dep}. The slopes of these fitted lines are plotted vs. the corresponding values of τ'_{eff} (see Fig. 6.15). The intersection point of this line with the x-axis—i.e. zero slope—yields τ_{eff}.

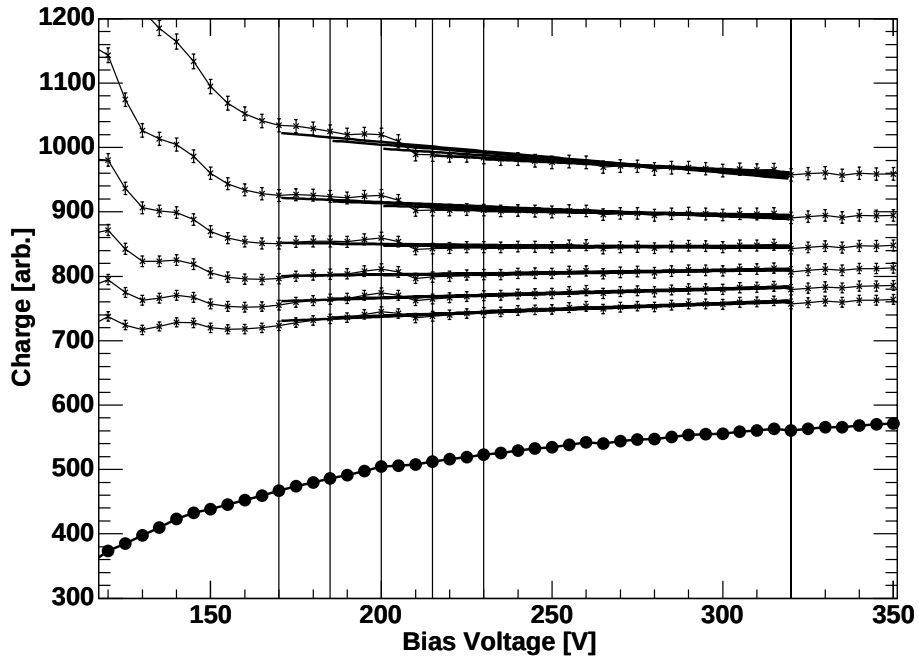

Fig. 6.14: Corrected charge collection curves for different values of τ'_{eff}. The values of τ'_{eff} grow from 3.5 ns (top curve) to 6.5 ns (bottom curve). The lowest line gives the uncorrected charge. The fitted lines are also displayed, vertical lines indicate the various fit ranges. Measurement on sample C ($\Phi_{\text{eq}} = 5 \cdot 10^{14}\, n_{\text{eq}}/\text{cm}^2$) with p-side illumination.

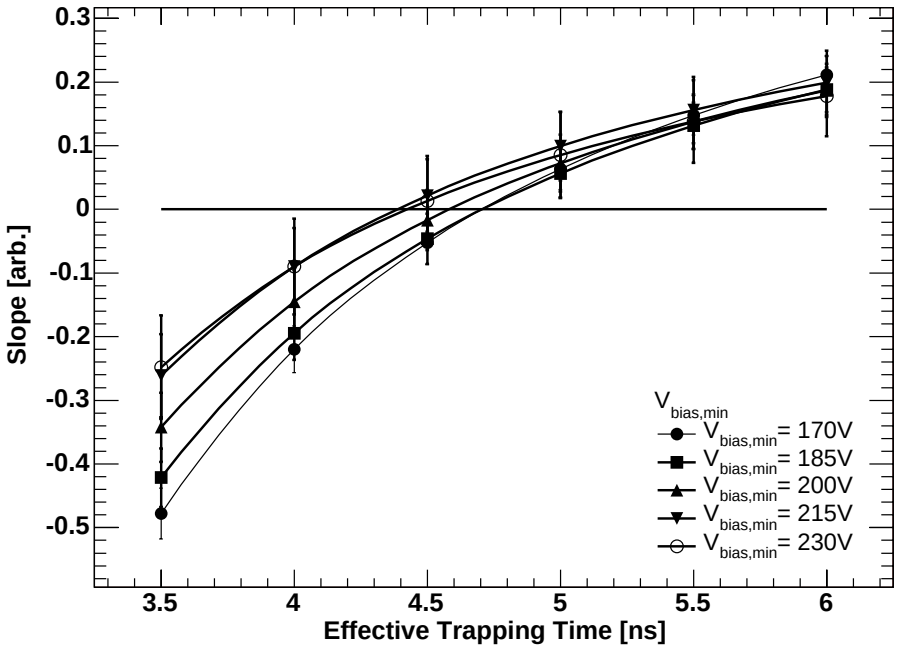

Fig. 6.15: Slopes of the lines fitted to the corrected charge curves in Fig. 6.14 above V_{dep} for different fit ranges. The intersection point of the curves with the x-axis gives the value for τ_{eff}. (The solid line shows a spline interpolation to ease the finding of the intersection point.) Measurement on sample C ($\Phi_{\mathrm{eq}} = 5 \cdot 10^{14}\, n_{\mathrm{eq}}/\mathrm{cm}^2$) with p-side illumination.

The error can be estimated by varying the lower limit of the fit region. These different fit region limits are indicated in Fig. 6.14 by vertical lines and correspond in Fig. 6.15 with the different slope vs. τ'_{eff} curves. The variation of the intersection point with the lower fit region limit is taken as error of τ_{eff}.

Exponentiated Charge Crossing

The second method ECC uses a different kind of plotting the compensated charges: measured signal shapes are again multiplied with an exponential factor as described in eq. 6.13 and integrated. The integrals over the compensated currents are called *exponentiated charges*[3]. The exponentiated charges Q_e are plotted vs. $1/\tau'_{\mathrm{eff}}$ for every measured bias voltage, see Fig. 6.16. The resulting plot contains curves with constant bias voltages while in the CCM the corrected charge collection curves represent lines with constant τ'_{eff}. In this plot the intersections of the curves with the y-axis are the measured charges since $1/\tau'_{\mathrm{eff}} = 0$ corresponds to no correction ($\tau'_{\mathrm{eff}} \to \infty$). Towards growing values on the abscissa the signals are compensated with an increasing factor. The curves intersect each other in

[3]The two different naming conventions stem from the two working groups which have first described the respective methods. In this work both conventions are used to distinguish between the two methods.

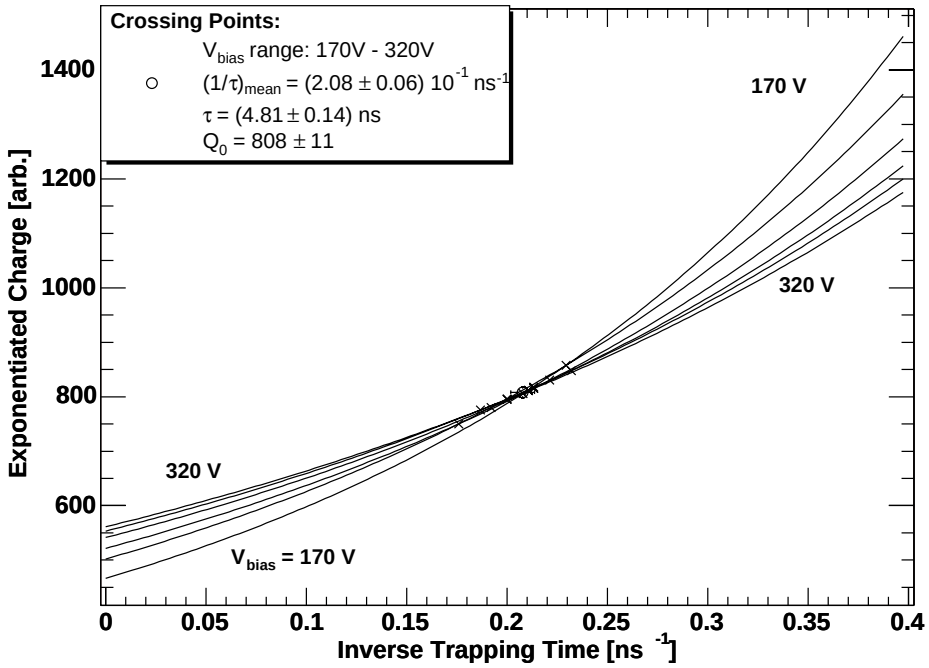

Fig. 6.16: Exponentiated charges Q_e vs. $1/\tau'_{\text{eff}}$ measured on sample C ($\Phi_{\text{eq}} = 5 \cdot 10^{14}\, n_{\text{eq}}/\,\text{cm}^2$) with p-side illumination. The abscissa value of the mean intersection point is $1/\tau_{\text{eff}}$, its ordinate value gives the initially injected charge in arbitrary units.

a certain point and swap their sequence from top to bottom. The intersection point gives the most probable value for $1/\tau_{\text{eff}}$. Since not all lines intersect in one point—as it would be in the ideal case—the intersection point for any pair of two curves is calculated and the mean of the intersection points is taken as the most probable value. The abscissa value of this point gives the value for τ_{eff} and the ordinate gives the initially injected charge Q_0 (in arbitrary units as long as no calibration has been made).
The errors σ_τ which are given for the trapping times are calculated as the quadratic sum of two contributions:

$$\sigma_\tau^2 = \sigma_{\text{cp}}^2 + \sigma_{\text{shift}}^2 \,. \tag{6.14}$$

σ_{cp} is derived from the variance of the crossing-points in the Q_e vs. $1/\tau$ plot (cf. Fig. 6.16). It is calculated by taking the rms and dividing it by the number of used measurements, i.e. the number of curves included in the plot[4].
σ_{shift} considers the systematic error due to the choice of the range of the analysed bias voltage and is obtained by calculating the change of $\tau_{e,h}$ when the analysed

[4]Normally the rms divided by the number of single values used for its calculation is used as the error of the mean value. However, since n curves have $\frac{1}{2}n(n-1)$ intersection points not all values are independent from each other. Therefore, the rms is divided only by the number of measured curves. This results in an $1/\sqrt{n}$ dependence of the error with n being the number of curves/measurements.

bias voltage range is shifted by 10 V up and down and considers thereby any uncertainty of V_{dep}.

Comparison between CCM and ECC

Both analysis techniques have been tested with measurements on several samples. This systematic study revealed no systematic difference between the two methods. Finally, ECC was chosen as analysis technique for some practical reasons: the determination of τ_{eff} as the average of the crossing-points in the Q_e vs. $1/\tau'_{\mathrm{eff}}$ plot also offers a straight-forward method to obtain the error. The error can be determined by calculating the variance. In the CCM method the estimation of the error is more difficult. A further advantage of ECC is the better possibility to recognize single bad measurements: the curve corresponding to a badly measured signal is in most cases significantly different from the other curves and contributes crossing-points which deviate clearly visible from the other crossing-points. In CCM a bad measurement leads to a single shifted point in the corrected charge collection curves. It is more difficult to decide to drop such a shifted point than to decide on a whole deviating curve.

For these reasons ECC has been chosen as standard method to determine the effective trapping times.

6.5.6 Lower Limit on Charge Collection Efficiency

The charge collection efficiency (CCE) can be determined from the TCT-measurements as well: both methods—ECC and CCM—give the initially injected charge Q_0 in arbitrary units. In ECC it is the ordinate of the crossing point in the Q_e vs. $1/\tau'_{\mathrm{eff}}$ plot, in the CCM it is the height of the zero-slope-line. With the knowledge of Q_0 the measured charge collection curve can be normalised to 1.

But one has to keep in mind one important fact: The CCE determined by this method—i.e. TCT-measurements with short range lasers—gives the CCE for electrons and holes separately. These CCEs are different from the one for mips because the charge clouds have to drift the whole way through the detector. With a MIP the charge would be injected homogeneously along the particle's track. In such a case only a small part of the charge has to drift a long way through the detector while a larger fraction has a shorter way and therefore suffers less trapping.

While the estimation of CCE from these measurements yields a lower limit for mips in pad-detectors, it might overestimate the CCE compared to the CCE of segmented detectors. Due to the small pixel effect the last part of the drift path has a much higher weight. In the case of n^+-on-n pixel detectors electrons are collected on the segmented side. When they reach the region close to the pixels they have already suffered trapping, so that only a fraction of the initially injected charge contributes to the signal.

6.5.7 Determination of Charge Collection Time

The charge collection time t_c is the interval between injection of the charge Q_0 and its collection at the electrodes. In the idealised case of a close-to-surface injection of a point charge, t_c is the time between injection and collection of this single charge. In the case of a distributed charge deposition—as it is the case in the exponentially with depth distributed charge after laser injection or the equally distributed charge of a mip—t_c is the time between injection and collection of the last charge-carrier. Since their drift lengths are different they also have different arrival times. Therefore, it is technically strongly correlated with the signal width. In this work the difference between the two inflection points of the edges is taken as charge collection time. This method has the advantage of being simple since the inflection points can easily be found by taking the extrema of the first derivative on a reasonable interval.

6.5.8 Extraction of Field Configuration

After exponentiation the signal current is corrected for charge loss and therefore proportional to the drift velocity of the charge-carriers. Thus, the exponentiated signal current can be used together with a parameterisation for the dependence of drift velocities on electric field strength to determine the distribution of electric field in the detector along the drift path of the charge-carriers. If the charge-carriers drift only in x-direction—i.e. if edge effects of the detector can be neglected—one measures $E(x)$.
The time-dependent drift velocity $v_d(t)$ is proportional to the corrected current $i_c(t)$:

$$v_d(t) = a \cdot i_c(t) \; . \tag{6.15}$$

The numerical value of the normalisation factor a can be obtained from the fact that in a close-to-surface injection of a point-like charge the charge-carriers drift a length d (detector thickness) in a time t_c (charge collection time). Thus,

$$\int_0^{t_c} v_d(t)\, dt \;=\; \int_0^{t_c} a \cdot i_c(t)\, dt \stackrel{!}{=} d \tag{6.16}$$

$$\Rightarrow a \;=\; \frac{d}{\int_0^{t_c} i_c(t)\, dt} \; . \tag{6.17}$$

The resulting $v_d(t)$ can be integrated to obtain the time-dependent driftlength $x_d(t)$:

$$x_d(t) = \int_0^t v_d(t')\; dt' \; . \tag{6.18}$$

The function $x_d(t)$ for the drift length can be inverted (it is a monotonous function) to obtain $t(x_d)$. This expression can be put into $v_d(t) = v_d[t(x_d)] = v_d(x_d)$. This is the dependence of the drift velocity on the drift length. In a measurement it is the drift velocity in a depth x_d from the illuminated surface.
By using a parameterisation $v_d(E)$ for the dependence of the drift velocity on the electric field strength $v_d(x_d)$ can be turned into a field map $E(x_d)$.

Chapter 7

CV-Measurements

THE main objective of measurements of the bias voltage dependent capacitance (CV-measurements) is to characterise the samples before the charge collection measurements are done. These measurements yield the depletion voltage which is an important parameter for choosing an appropriate range of bias voltage for the TCT-measurements.
Additionally to this purpose the data obtained from CV-measurements are also analysed with regard to fluence and annealing time dependence. The results of these studies are compared to published data in order to check the validity and reliability of the results obtained from the used samples.

7.1 Purpose of CV-Measurements

CV-measurements on the samples are done in order to serve three purposes:

- For the analysis of the charge-collection measurements it is important to know the depletion voltage.

- Since the samples had to be shipped from the irradiation facilities to Dortmund a complete control of the temperature was impossible. After shipment the samples were not annealed for the same time. Therefore, they had to be annealed at elevated temperature to a defined point in a controlled fashion. It is common practice to anneal samples to the minimum in V_{dep} in order to obtain comparable results. Within this work annealing was done at a temperature of 60° C.

- It has to be verified that the samples are usable for the charge collection studies. They are qualified by comparison of measured parameters with values from literature. In order to obtain comparable values the CV-measurements were performed with a frequency of 10 kHz and the LCR-meter was used in the C_pR_p mode as it is common practice in other laboratories as well. For measurements performed with different measurement frequencies the reader

is referred to sec. B.1. The CV-measurements were performed at a temperature of 0°C.

The following sections treat the CV-measurements and their analysis.

7.2 Initial Doping Concentration before Irradiation

Before irradiation the initial doping concentrations of the silicon material used is calculated from the depletion voltages obtained from the CV-characteristic. Table 7.1 contains the results. The given numbers are the mean value of measurements on three (in case of wafer 4457_04 only two) diodes from each wafer. This table gives also the specific resistances ρ_0 of the base material which are calculated by

$$\rho_0 = \frac{1}{e_0 N_{\text{eff}} \mu_e} = \frac{d^2}{2\, V_{\text{dep}} \cdot \mu_e \cdot \varepsilon_0 \varepsilon_{\text{Si}}} \,. \tag{7.1}$$

This equation is valid for n-type silicon. For the electron mobility μ_e the value given in Table A.2 is used.

Wafer Set	Wafer Number	Thickness [μm]	$N_{\text{eff},0}$ [$10^{12}\,\text{cm}^{-3}$]	ρ_0 [kΩcm]
ATLAS	011_03	254	0.85±0.15	5.05±0.86
	4457_04	264	0.865±0.031	4.98±0.18
SRD	4914_01	297	0.7275±0.0062	5.917±0.050
SCT	5194_07	293	0.9010±0.0056	4.778±0.030
	5195_01	297	0.8999±0.0019	4.784±0.010
	5195_15	300	0.6813±0.0067	6.319±0.063
	5195_16	291	0.888±0.023	4.85±0.12

Table 7.1: Initial doping concentrations $N_{\text{eff},0}$ and specific resistances ρ_0 for the used base materials.

7.3 Fluence Dependence of Effective Doping Concentration

Table 6.2 (p. 80) gives an overview of the samples used. All diodes—except few samples for annealing studies—were annealed to the minimum in V_{dep} prior to the measurements of trapping times. Annealing was accelerated by storage at 60°C and V_{dep} was measured in between.
Only on a few samples beneficial annealing could be observed—the results are given in sec. 7.4. For most of the samples annealing was already too advanced

after shipment from irradiation facility to the laboratory in Dortmund to observe the beneficial part of annealing sufficiently for a detailed study. Therefore, on these samples only a short series of 2-4 measurements in intervals of 15-20 min at 60°C was performed and stopped after a constant or the first increasing (due to beginning reverse annealing) V_{dep} was observed. After the accelerated annealing was stopped the samples were kept in a refrigator until further measurements.

In Table 7.2 the depletion voltages of all samples are compiled, showing the condition during signal measurements. The effective doping concentrations $|N_{\mathrm{eff}}|$ are computed from the measured depletion voltages by using eq. (4.4) on p. 47.

For comparison of sample pairs having the same fluence but coming from different wafers one has to look at ΔN_{eff} as defined in eq. (4.6) which gives the alteration of N_{eff} with respect to the initial doping concentration $N_{\mathrm{eff},0}$. In the sample pair

Sample	Fluence $[10^{14}\, n_{\mathrm{eq}}/\,\mathrm{cm}^2]$	Thickness [cm]	$V_{\mathrm{dep,min}}$ [V]	$\lvert N_{\mathrm{eff}}\rvert$ $[10^{12}\,\mathrm{cm}^{-3}]$	ΔN_{eff} $[10^{12}\,\mathrm{cm}^{-3}]$
$\emptyset$	0.00	0.0297	48.29±0.83	0.711±0.049	—
A	3.22	0.0264	108.0±3.9	2.01±0.17	2.88±0.17
B	8.90	0.0264	230.4±7.4	4.29±0.35	5.16±0.36
C	5.00	0.0254	121.8±3.7	2.45±0.21	3.30±0.26
D	1.06	0.0254	64.4±2.8	1.30±0.12	2.15±0.19
E	4.46	0.0297	135.8±5.6	2.00±0.16	2.73±0.16
F	6.51	0.0297	234.9±4.0	3.46±0.24	4.19±0.24
G	8.06	0.0297	296.3±8.8	4.36±0.32	5.09±0.32
K_1	0.22	0.0293	11.56±0.90	0.175±0.018	0.726±0.019
K_2	0.22	0.0300	7.53±0.25	0.109±0.008	0.790±0.010
L_1	0.52	0.0293	19.31±0.88	0.292±0.024	1.193±0.025
L_2	0.52	0.0300	16.38±0.45	0.236±0.017	0.918±0.018
M	0.92	0.0297	40.3±1.6	0.593±0.046	1.493±0.046
N	2.04	0.0297	76.8±2.3	1.130±0.083	2.030±0.083
O_1	4.24	0.0297	119.1±2.8	1.75±0.16	2.65±0.13
O_2	4.24	0.0291	115.5±4.6	1.77±0.14	2.65±0.14
P	0.92	0.0297	53.2±4.2	0.783±0.081	1.511±0.081
Q	2.04	0.0297	121.1±1.5	1.78±0.12	2.51±0.12
R	1.00	0.0297	139.8±5.9	2.06±0.16	2.79±0.16
S	6.00	0.0297	620±12	9.12±0.64	9.85±0.64
T	4.00	0.0297	479.7±2.2	7.06±0.48	7.79±0.48
V	2.00	0.0297	249.0±2.1	3.67±0.25	4.39±0.25

Table 7.2: Depletion voltages, effective doping concentrations N_{eff} and changes ΔN_{eff} in N_{eff} with respect to $N_{\mathrm{eff},0}$ for all samples after accelerated annealing to the minimum in $V_{\mathrm{dep}}(t)$. All samples except for K_1 are type-converted. The top part of the table contains the proton-irradiated samples, the bottom part the neutron-irradiated samples.

(K_1,K_2) the first sample has not been converted while K_2 is already converted[1]. This can be explained by the lower initial doping concentration of K_2. The disagreement between the two values for ΔN_{eff} can be explained by the difficulty of its determination in the region of the space charge sign inversion. Looking at pair (L_1,L_2) which comes from the same wafer combination a significantly higher ΔN_{eff} for the sample coming from the wafer having the smaller $N_{\text{eff},0}$ is observed. This disagreement can also be attributed to the proximity to SCSI. For the next pair (M,P) which also originates from wafers with significantly different initial doping concentrations the values for ΔN_{eff} are in good agreement. Pair (N,Q) which is a combination of the same wafers as (M,P) does not show a good agreement for ΔN_{eff}. The last remaining pair (O_1,O_2) which comes from wafers with the same $N_{\text{eff},0}$ shows a very good agreement for N_{eff} and ΔN_{eff}. The small difference in V_{dep}—which is smaller than the error—can be explained by the difference in the thickness of the samples. Most of the deviations observed in sample pairs irradiated to the same fluence are not large and can be attributed to the different base materials. Such deviations have also been observed by other groups. For a pair using the same base materials the results are in very good agreement.
Fig. 7.1 shows a plot of effective doping concentration vs. the equivalent fluence. Functions of the form $\Delta N_{\text{eff}} = A_{p,n} + \beta_{p,n}$ have been fitted separately to the neutron and proton data. The dashed lines represent the fit results with both parameters $A_{n,p}$ and $\beta_{n,p}$ varying. The result shows that ΔN_{eff} depends linearly on Φ_{eq} if the measurements at the lowest fluences ($< 0.9 \cdot 10^{14}\, n_{\text{eq}}/\text{cm}^2$) are excluded. This deviation can be explained by an incomplete donor removal at these low fluences. The solid lines show the results with $\beta_{p,n}$ fixed to the slope of corresponding data from [RD48b], see Fig. 7.2. For neutron-irradiated samples the increase with fluence is larger than in the reference cited above; for protons the data are in better agreement with the literature. Generally, the results for N_{eff} from this work are systematically higher than in [RD48b]. This can be attributed to different annealing conditions: the samples in [RD48b] were annealed for 4 min at 80°C.

7.4 Annealing of Effective Doping Concentration

7.4.1 Beneficial Annealing

As an example Fig. 7.3 shows a series of CV-curves measured during annealing of sample P. The obtained depletion voltages are plotted in Fig. 7.4 together with the results from other samples. This plot contains data from all samples which showed clearly a beneficial annealing behaviour after shipping from irradiation facility (CERN) to Dortmund. The point $t = 0$ in the plot refers to the start of accelerated annealing at 60°C, not to the end of irradiation. The time elapsed between irradiation and first measurement in Dortmund is not known exactly. A

[1] This is confirmed by the TCT-measurements of the pulse-shape.

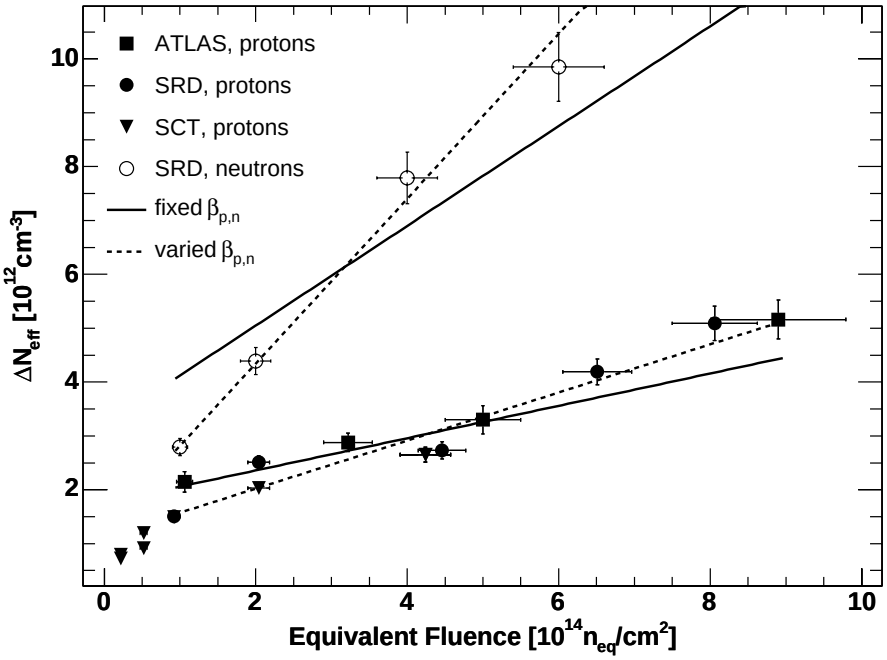

Fig. 7.1: Effective doping concentrations $N_{\rm eff}$ of the samples after annealing to the minimum in $|N_{\rm eff}|$. $|N_{\rm eff}|$ has been calculated from $V_{\rm dep}$. The solid lines are fits of straight lines with fixed slopes $\beta_{p,n}$, dashed lines are fits with varied slope. See text for details.

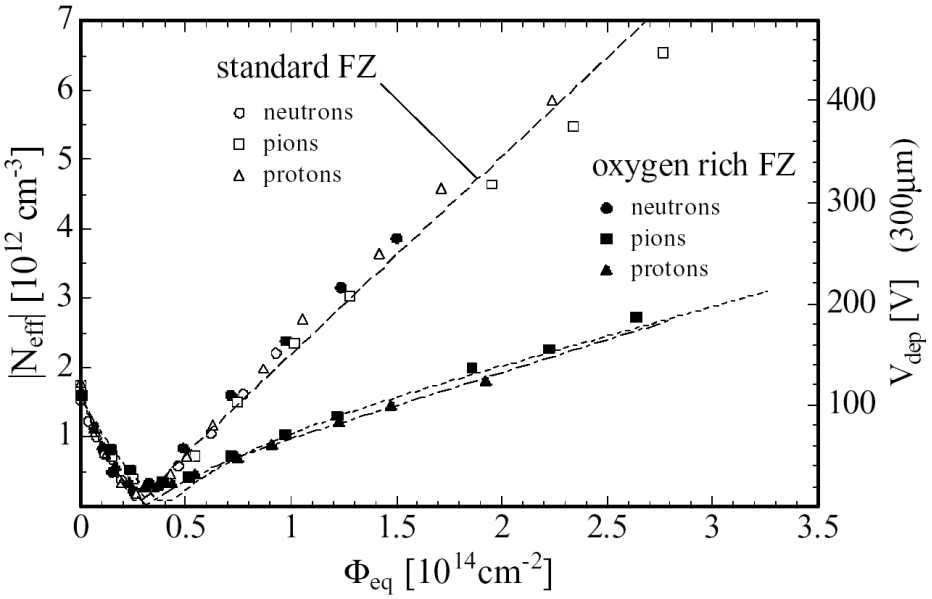

Fig. 7.2: Dependence of $N_{\rm eff}$ on the accumulated 1 MeV neutron equivalent fluence for standard and oxygen enriched FZ silicon irradiated with reactor neutrons (Ljubljana), 23 GeV protons (CERN PS) and 192 MeV pions (PSI) [RD48b]. Measurements were done after annealing for 4 min at 80°C.

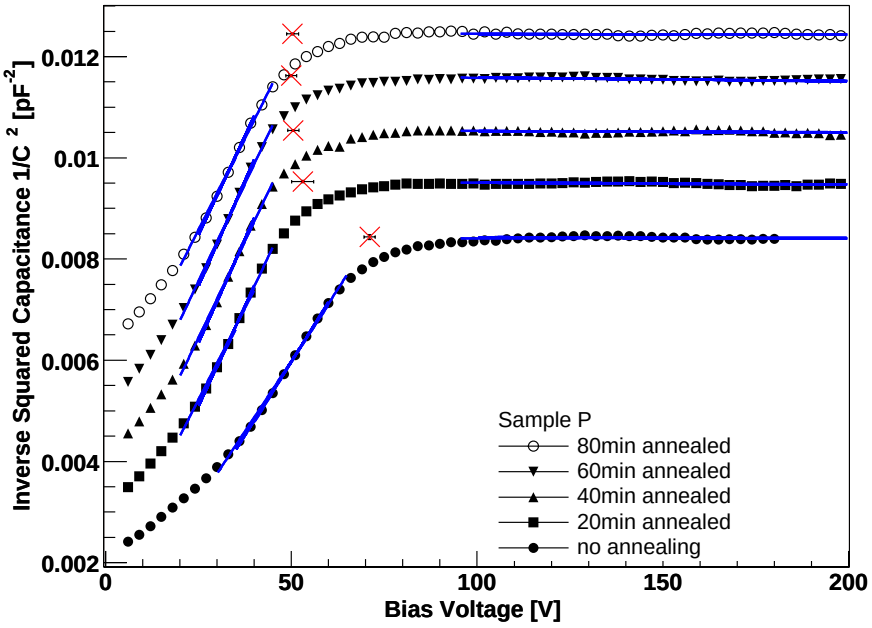

Fig. 7.3: CV-measurements on sample P during annealing at 60°C to the minimum in $|N_{\text{eff}}(t)|$. $\times$ indicate the intersection points of fitted lines. The curves are shifted vertically by $0.001\,\text{pF}^{-2}$ per curve in order to improve legibility of the plot, lowest curve is not shifted.

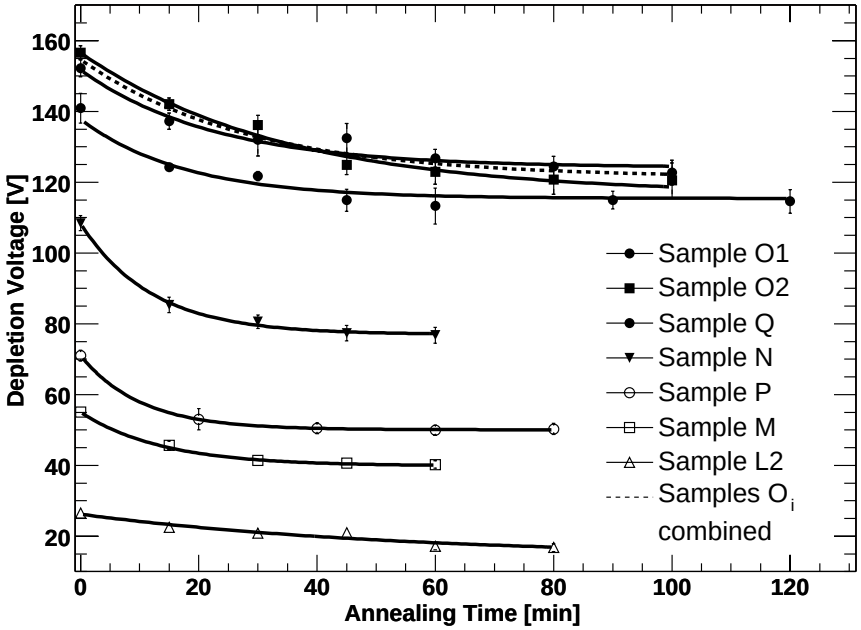

Fig. 7.4: Depletion voltages during the first 60-120 min of accelerated annealing at 60°C for selected samples. $t = 0$ refers to first measurement and start of accelerated annealing.

function of the form

$$V_{\mathrm{dep}}(t) = V_a \cdot \exp(-t/\tau_a) + V_C \tag{7.2}$$

has been fitted to the data points. τ_a is the time constant of beneficial annealing. The fit results for τ_a are in the range of 10–35 min for an annealing temperature of 60°C what is roughly the range of the values given in [Mo99] for the time constant of beneficial annealing.

7.4.2 Long Term Annealing

Three samples (E,F and Q) were annealed for long times, so that the reverse annealing became visible. Fig. 7.5 shows the resulting dependence of $|N_{\mathrm{eff}}|$ on the annealing time at 60°C. Two functions, describing first and second order processes (cf. eq. (4.18) and footnote 4 on p. 51), are fitted to the data. Both fitting functions describe the data quite well, the samples were not annealed long enough to distinguish between the first and second order description of reverse annealing. The values for the reverse annealing time constant obtained from the fit are in the range of 2500–3600 min for 60°C.

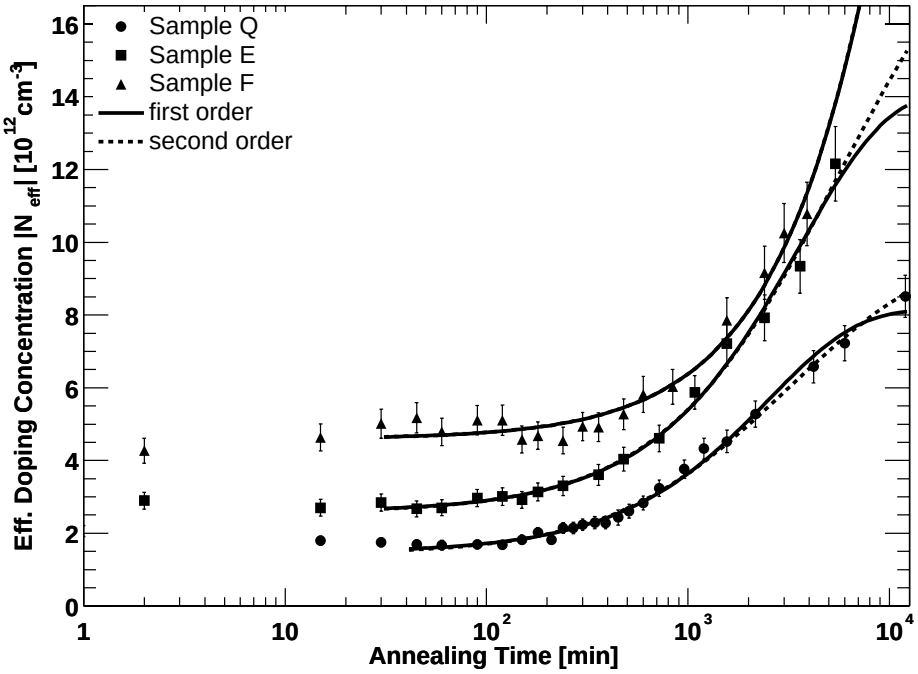

Fig. 7.5: Long term annealing of samples E, F and Q. The annealing was accelerated at 60°C. $t = 0$ refers to first measurement and start of accelerated annealing.

7.5 Discussion of CV-Measurements

CV-measurements on all of the samples delivered the depletion voltages which are necessary for the later analysis of charge measurements. V_{dep} was measured after irradiations with several fluences, the dependence of N_{eff} on Φ_{eq} showed the expected linear behaviour if the fluence was significantly higher than necessary for SCSI. The values for $\beta_{p,n}$ obtained within this study are different from the values published in [RD48b] (see also Fig. 7.2). This deviation is attributed to the different annealing procedure and material dependence. The observed beneficial and reverse annealing of the samples occurred as expected and the obtained data could be described by the formulae of the Hamburg model.
Since the measurements of the depletion voltages presented in this chapter produced the expected results the sample set used within this work is considered to be suitable for charge collection studies. The substrate materials are expected to be representative for the material used for the fabrication of the ATLAS pixel sensors.
All of the samples were annealed to a comparable point in the annealing curve, so the individual results obtained in the charge collection measurements can be combined with each other.

Chapter 8

TCT-Measurements

SEVERAL aspects of irradiated sensors are investigated with TCT-measurements: the first objective is the determination of effective trapping times and their dependence on fluence, particle type used for irradiation and annealing time. The section on this topic is followed by analysis of charge collection efficiency. The last and very important point is the analysis of the pulse shape in order to derive a model that describes the electric field configuration in irradiated silicon detectors in a practical way and can be used for simulations of charge drift.

8.1 Effective Trapping Times

8.1.1 Introductory Remarks on Signal Quality and Accuracy

At this point some consequences of the measurement technique and the signal quality for the accuracy of the determination of effective trapping times shall be treated. Generally, a poorer quality of the data on signals after n-side illumination is observed in irradiated pad-detectors. This can be explained by the following facts: firstly, hole-drift dominated signals suffer more trapping compared to p-side signals due to their longer duration but roughly the same trapping probability per time for holes. Additionally after n-side illumination the charge-carriers drift towards the low-field side of an converted pad detector. Thus the trailing edge is weaker due to lower drift velocities. These attenuated and noisy signal tails are multiplied by a large factor $\exp(t/\tau_{\text{eff}})$ blowing up the uncertainties of $i(t)$. Therefore, the problems of post-pulse oscillations and other signal distortions are worse in the hole signals.
The measurable range of the effective trapping time τ_{eff} is limited towards small values by the noise of the measured signal current: since τ_{eff} is comparable to or smaller than the charge collection time, the signal decreases significantly towards the trailing edge—in some cases so much that the signal cannot be distinguished from noise. This has two consequences: firstly, it is difficult to determine exactly the position of the trailing edge. Secondly, a current signal that suffers strongly

from noise is multiplied with a large factor $\exp(t/\tau_{\text{eff}})$ in order to compensate the charge loss. This factor is large due to the short effective trapping times.
The upper limit for measurable τ_{eff} can be derived from the following reasoning [Br00]: charge trapping leads to an exponential decrease of signal current as described by eq. (3.85). For bias voltages well above the depletion voltage the charge-carrier velocities can be considered as being constant throughout the pad-detector. In this case, the integration of eq. (3.85) yields the following relation:

$$Q = Q_0 \frac{\tau_{\text{eff}}}{t_c} \left(1 - e^{-t_c/\tau_{\text{eff}}}\right) . \tag{8.1}$$

For $\tau_{\text{eff}} \gg t_c$—as it is the case for lowly irradiated samples—this equation can be rewritten to

$$\frac{\Delta Q}{Q_0} = \frac{Q_0 - Q}{Q_0} = \frac{1}{2}\frac{t_c}{\tau_{\text{eff}}} . \tag{8.2}$$

Without considering drift velocity saturation, the charge collection time for a detector with thickness d and bias voltage V_{bias} can be written as

$$t_c = \frac{d^2}{\mu_{e,h} V_{\text{bias}}} . \tag{8.3}$$

With δ_Q being the smallest measurable value of $\Delta Q/Q_0$, the maximum measurable value of τ_{eff} is

$$\tau_{\text{eff,max}} = \frac{1}{2}\frac{d^2}{\mu_{e,h}\, V_{\text{bias}}\, \delta_Q} . \tag{8.4}$$

Filling in the parameters of the set-up and samples used here ($\delta_Q \approx 2\%$, $\mu_e = 1450\,\text{cm}^2/\,\text{V s}$, $\mu_h = 505\,\text{cm}^2/\,\text{V s}$, $d \approx 300\,\mu\text{m}$ and $V_{\text{bias}} = 70\,\text{V}$ for the lowest irradiated samples) the following an upper limits can be obtained:

$$\tau_{\text{eff,max}} \approx 220\,\text{ns} \quad \text{for electrons and} \tag{8.5}$$

$$\tau_{\text{eff,max}} \approx 640\,\text{ns} \quad \text{for holes.} \tag{8.6}$$

These numbers show that it would not be possible to measure the trapping times on unirradiated samples for checking the consistency of the method since the trapping times in unirradiated silicon are larger than $1\mu\,\text{s}$.
Additional problems origin from more noisy signals towards high bias voltages. This is probably caused by humidity and dirt on the diodes leading to currents over the surface and the edges of the diodes. The humidity is caused by precipitation of air humidity on cold samples taken out of the refrigerator. This problem can be handled by warming-up the samples to room temperature for some minutes and blowing dry nitrogen gas over them. Dirt can stick to the humid surface. It can be removed by a supersonic bath in aceton. This treatment makes it possible to bias diodes again with higher voltages after the breakdown voltage decreased significantly after several cycles in refrigerator and at room temperature [Rj03].

8.1.2 Fluence Dependence

Measurements

All measurements presented in this chapter were done at a temperature of 0°C if not stated otherwise. Charges were injected by a red laser with a wavelength of 672 nm.
The ECC analysis of measured signals is done in a certain range of bias voltage. In the following the lower and upper limit are called $V_{\mathrm{ecc,min}}$ and $V_{\mathrm{ecc,max}}$. It appeared to be important that a proper choice of the range for these voltages is made in order to obtain consistent results for trapping times. The lowest possible value for $V_{\mathrm{ecc,min}}$ is the depletion voltage but $V_{\mathrm{ecc,min}}$ is chosen to be

$$V_{\mathrm{ecc,min}} = V_{\mathrm{dep}} + 50\,\mathrm{V} \tag{8.7}$$

in order to have a better signal quality with more clearly defined tails. The maximum possible value for $V_{\mathrm{ecc,max}}$ is the break-down voltage of the device (reduced by a safety margin). Additionally, $V_{\mathrm{ecc,max}}$ must be low enough to be reachable for all samples. Thus, the upper limit is chosen as

$$V_{\mathrm{ecc,max}} = V_{\mathrm{dep}} + 200\,\mathrm{V}\,. \tag{8.8}$$

With these choices the range is large enough to include several measurements with different bias voltages into the ECC analysis. The voltage step between two included measurements is set to

$$V_{\mathrm{ecc,step}} = 30\,\mathrm{V}\,. \tag{8.9}$$

Thus, six measurements are used for analysis per fluence point. This increment is large enough to get clearly different curves in the exponentiated charge vs. trapping probability plot (cf. Fig. 6.16, p. 97). Additionally, using this range for analysis the trapping times are determined roughly for the bias voltage range which will be used for the operation of the ATLAS pixel detector since there an overdepletion of 50 V is foreseen.
For technical reasons the TCT-measurements have been done at bias voltages being multiples of 10 V. Thus the depletion voltages have been rounded to full 10 V. The rounded depletion voltage is denoted by V'_{dep}.
Table 8.1 gives the numerical values of the results for the effective trapping times in proton and neutron irradiated samples, respectively. They have been measured at a temperature of 0°C in the minimum of annealing curve for effective doping concentration. This table also includes the rounded depletion voltages which have been used to choose the bias voltage range in analysis.
Plots of the experimental results are shown in Fig. 8.1. Since a linear dependence between inverse trapping time and equivalent fluence corresponds to a linear introduction of trapping centres (cf. eq. (4.44)) a straight line going through zero

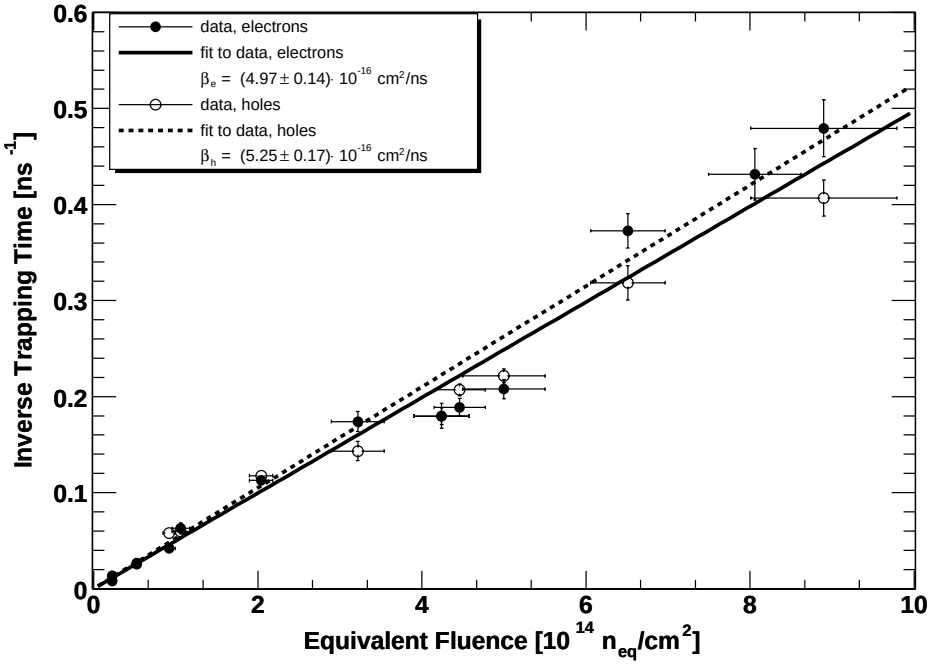

(a) Proton-irradiated samples.

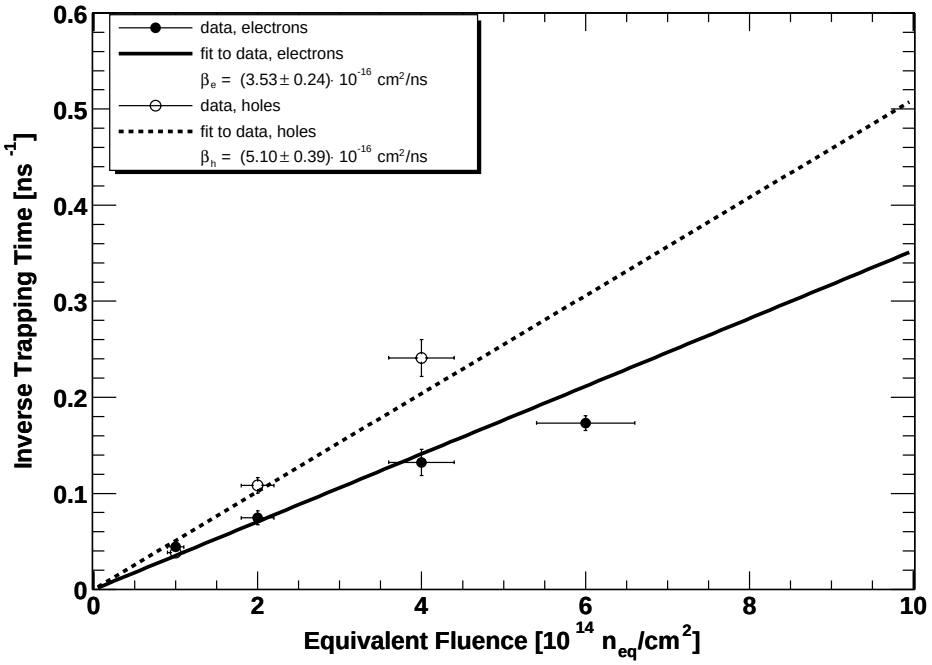

(b) Neutron-irradiated samples.

Fig. 8.1: Inverse effective trapping times for electrons and holes vs. equivalent fluence after proton (a) and neutron irradiation (b).

Sample	Eq. Fluence $[10^{14} n_{\mathrm{eq}}/\mathrm{cm}^2]$	V'_{dep} [V]	τ_e [ns]	τ_h [ns]
K_1	0.223 ± 0.019	10.00	74.224 ± 12.567	—
K_2	0.223 ± 0.019	10.00	125.000 ± 38.847	—
L_1	0.524 ± 0.047	20.00	37.701 ± 3.455	—
L_2	0.524 ± 0.047	20.00	39.385 ± 4.880	—
P	0.920 ± 0.074	50.00	23.885 ± 0.844	17.241 ± 0.408
D	1.060 ± 0.106	60.00	15.935 ± 1.493	16.786 ± 0.706
Q	2.040 ± 0.143	120.00	8.876 ± 0.183	8.494 ± 0.145
A	3.220 ± 0.322	110.00	5.747 ± 0.349	6.977 ± 0.491
O_1	4.240 ± 0.335	120.00	5.569 ± 0.267	—
O_2	4.240 ± 0.335	120.00	5.558 ± 0.404	—
E	4.460 ± 0.312	140.00	5.297 ± 0.260	4.832 ± 0.148
C	5.000 ± 0.500	120.00	4.812 ± 0.229	4.514 ± 0.149
F	6.510 ± 0.456	230.00	2.684 ± 0.129	3.140 ± 0.176
G	8.060 ± 0.564	290.00	2.318 ± 0.145	—
B	8.900 ± 0.890	230.00	2.086 ± 0.129	2.458 ± 0.114
R	1.000 ± 0.100	140.00	22.590 ± 1.883	25.994 ± 2.190
V	2.000 ± 0.200	250.00	13.405 ± 1.293	9.236 ± 0.689
T	4.000 ± 0.400	480.00	7.557 ± 0.780	4.149 ± 0.332
S	6.000 ± 0.600	620.00	5.773 ± 0.253	—

Table 8.1: Effective trapping times for holes and electrons for proton- (upper part) and neutron-irradiated samples (lower part).

is fitted to the data points. The results of fits to the proton data for the linear trapping centre introduction rates (eq. (4.44)) are

$$\gamma_{p,e} = (4.97 \pm 0.14) \cdot 10^{-16}\,\mathrm{cm}^2/\mathrm{ns} \quad \text{and} \tag{8.10}$$

$$\gamma_{p,h} = (5.25 \pm 0.17) \cdot 10^{-16}\,\mathrm{cm}^2/\mathrm{ns}\,. \tag{8.11}$$

The description of the data by a linear dependence is sufficient as can be seen in the graph ($\chi^2/\mathrm{ndf} = 22.2/14$ for electrons and $\chi^2/\mathrm{ndf} = 16.3/7$ for holes).
From the neutron data it is analogously:

$$\gamma_{n,e} = (3.53 \pm 0.24) \cdot 10^{-16}\,\mathrm{cm}^2/\mathrm{ns} \quad \text{and} \tag{8.12}$$

$$\gamma_{n,h} = (5.10 \pm 0.39) \cdot 10^{-16}\,\mathrm{cm}^2/\mathrm{ns}\,. \tag{8.13}$$

Neutron data can also be well described by a linear dependence ($\chi^2/\mathrm{ndf} = 6.4/3$ for electrons and $\chi^2/\mathrm{ndf} = 6.3/2$ for holes).

Discussion

An important fact in point of data quality is that the results of diodes irradiated to the same fluence are well consistent for the pairs L_1/L_2 and O_1/O_2. The large

difference in results for the pair K_1/K_2 may result from the large value for τ_{eff}, making a clean analysis more difficult. A systematic error coming from a sample-to-sample variation seems therefore to be negligible.
Table 8.2 gives a compilation of results for the introduction rates $\gamma_{e,h}$ obtained by other groups. The data from these references were measured on samples which had been irradiated in the same facilities as the samples used in this work. The results from [RD50]/[Li03] were measured in a fluence range of up to $5.5 \cdot 10^{14}\, n_{\text{eq}}/\text{cm}^2$ with epi-diodes. The study in [Kb02] was done on pad-detectors (DOFZ material) in a fluence range of up to $2.5 \cdot 10^{14}\, n_{\text{eq}}/\text{cm}^2$.
While the proton results from this work are compatible within errors with the results from [RD50][Li03], [Kb02] gives significantly higher results. For neutron-irradiated samples the results show a deviation as well. Up to now it is not obvious where the difference comes from.
The data set on trapping probabilities obtained in this work is considered to be the most appropriate one for the application to the ATLAS pixel detector since it covers the largest fluence range and is measured on the same material as used for the ATLAS pixel sensors.

Reference	24 GeV protons		reactor neutrons	
	$\gamma_{p,e}$ $[10^{-16}\,\text{cm}^2/\,\text{ns}]$	$\gamma_{p,h}$ $[10^{-16}\,\text{cm}^2/\,\text{ns}]$	$\gamma_{n,e}$ $[10^{-16}\,\text{cm}^2/\,\text{ns}]$	$\gamma_{n,h}$ $[10^{-16}\,\text{cm}^2/\,\text{ns}]$
this work	4.97±0.14	5.25±0.17	3.53±0.24	5.10±0.39
[Kb02]	5.6±0.2	7.7±0.2	4.1±0.1	6.0±0.2
[RD50],[Li03]	4.68±0.15	5.72±0.50	—	—

Table 8.2: Comparison of results from different authors for the trapping centre introduction rates $\gamma_{e,h}$.

8.1.3 Annealing of Trapping Times

Measurement

Alongside the fluence dependence of trapping also the long-term behaviour of the defects causing charge trapping is interesting for the later ATLAS operation. Knowlegde about the annealing of $\gamma_{e,h}$ is necessary in order to assess the consequences of warm-up periods. Therefore, annealing studies on two proton-irradiated samples (Q and E) were performed. The annealing was accelerated by placing the samples in an oven at 60°C. The trapping times were repeatedly measured during the successive annealing. Sample Q was annealed for 200 h, sample E for 40 h.
Fig. 8.2 displays the measurement results. The analysis range of the bias voltage has been chosen in the same way as in the investigation of the fluence dependence—i.e. always with a constant offset relative to V_{dep} which changed due to annealing.

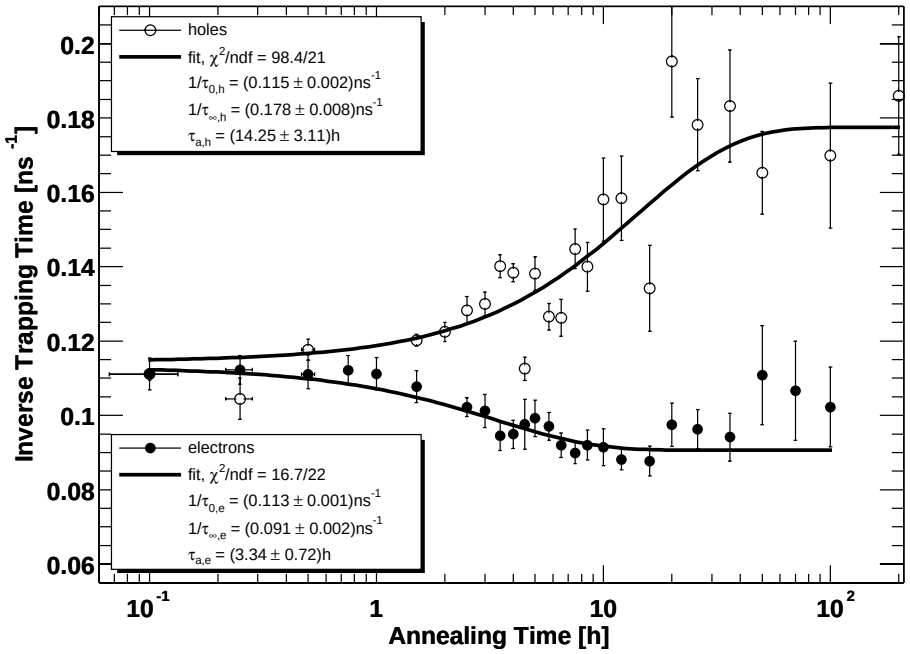

(a) Sample Q

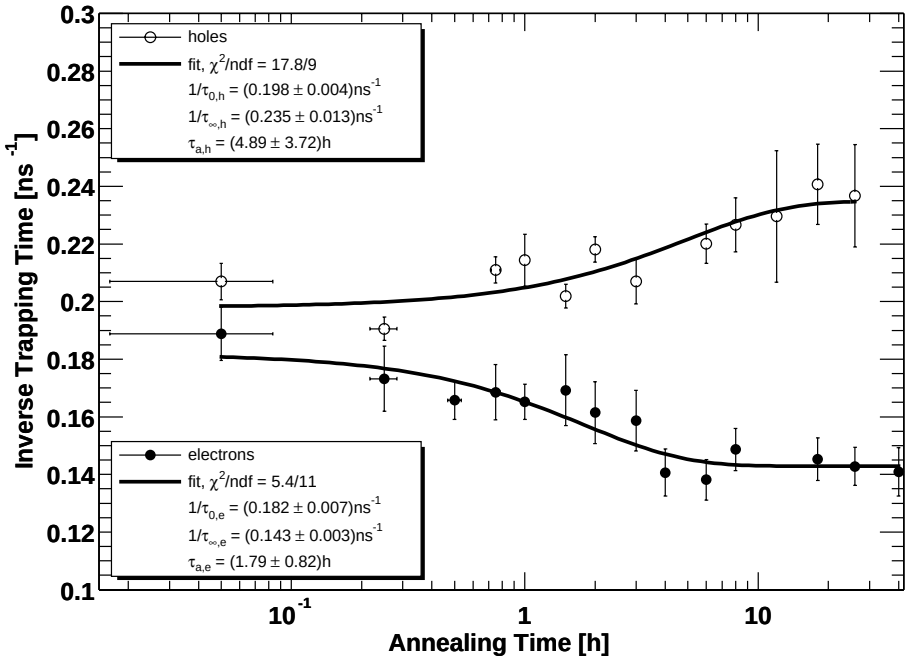

(b) Sample E

Fig. 8.2: Annealing of effective trapping times, measured on samples Q (a) and E (b).

Discussion

The plots in Fig. 8.2 show that the uncertainties of τ_{eff} are growing with annealing time. This is probably caused by the increasing applied bias voltage (due to reverse annealing) leading to short signals and more leakage current (see also discussion in sec. 8.1.1).
The measurements on both samples show a decreasing trapping probability for electrons and an increasing one for holes. The data can be explained by the decay of one kind of defects into another with a different trapping time as was done previously in [Kb02]. Hence the function

$$\frac{1}{\tau_{\text{eff}}(t)} = \frac{1}{\tau_0} \cdot \exp(-t/\tau_a) + \frac{1}{\tau_\infty}\left(1 - \exp(-t/\tau_a)\right) \tag{8.14}$$

is fitted to the data. A model explaining the variation of trapping probabilities with time by a sum of a non-annealing kind of defects (delivering a constant contribution) and the exponential decay of a second kind of trapping defects would have the same mathematical form. Table 8.3 shows the results of the fits: for electrons the results from both samples are consistent with each other: A $\approx 20\%$ decrease of trapping probability is observed. The annealing time constants for electron traps $\tau_{a,e}$ agree within (rather large) errors. Combining the two results by calculating the weighted mean yields for the annealing time constant for electron traps a value of

$$\tau_{a,e} = (2.67 \pm 0.77)\,\text{h} \quad \text{for annealing at } 60°\text{C}. \tag{8.15}$$

Also the values for χ^2/ndf are acceptible. Therefore, the model given in eq. (8.14) describes the data satisfactorily.
Contrary to the good quality of the data on annealing of electron trapping probabilities the data on holes are of poorer quality: errors of individual data points are larger and the two datasets are worse described by the assumed model as the significant worse values for χ^2/ndf show. The data from sample E are betterly described by the fitted function. The annealing time constants determined on the two samples do not agree. The magnitude of the variation is different in both

Sample	$1/\tau_0$ [ns^{-1}]	$1/\tau_\infty$ [ns^{-1}]	τ_a [h]	variation [%]	χ^2/ndf
electrons					
Q	0.113±0.001	0.091±0.002	3.34±0.72	-19	16.7/22
E	0.182±0.007	0.143±0.003	1.79±0.82	-21	5.4/11
holes					
Q	0.115±0.002	0.178±0.008	14.25±3.11	+54	98.4/21
E	0.198±0.004	0.235±0.013	4.89±3.72	+18	17.8/9

Table 8.3: Results of the fit of eq. (8.14) to the data shown in Fig. 8.2.

samples as well. Thus, combining the results seems not to be sensible for the hole data.
With respect to later long-term application it can be concluded that the variation of $\gamma_{e,h}$ with time is not large. The trapping of electrons even decreases which is positive because in the ATLAS pixel sensors electrons contribute mostly to the signal. Since in this work annealing studies have been done only at one temperature, it is not possible to give the equivalent time at room temperature what is more important. However, as the annealing leads to a saturation it can be stated that the trapping probabilities will not change more than $\approx 20\%$ for electrons and $\approx 20 - 55\%$ for holes during the ATLAS life-time.
This annealing behaviour has been observed in [Kb01] as well: this reference reports a decrease of electron trapping by $\approx 35\%$ and an increase of hole trapping by $\approx 30\%$. The observed time scale is in the order of 10 h.
The consequences of such a variation due to annealing are to be estimated later by corresponding simulation studies (see chapter 11).

8.2 Collected Charge

8.2.1 Depletion Voltage from Charge Collection

Charge Collection Curves

Integrating the currents measured by TCT and plotting them vs. the bias voltage charge collection curves $Q(V_{\text{bias}})$ are obtained. These curves obtained by integration of the measured currents will be called *measured charge collection curves* (denoted by $Q_m = Q_m(V_{\text{bias}})$) in the following. If the currents are corrected for charge loss prior to integration the resulting curves will be called *corrected charge collection curves* ($Q_c = Q_c(V_{\text{bias}})$).
Figs. 8.3 and 8.4 show measured and corrected charge collection curves after p-side and n-side illumination for unirradiated and irradiated samples, respectively.
The charges have been normalised to the initially injected charge Q_0 which is determined from ECC and are plotted vs. $\sqrt{V_{\text{bias}}/V_{\text{dep}}}$, V_{dep} is taken from CV-measurements.

Unirradiated Sample

In the p-side illuminated unirradiated sample (Fig. 8.3) $Q_m(V_{\text{bias}})$ rises from 0 V on because the depletion zone grows from the p-side into the n-bulk and therefore charge is injected into the sensitive volume. $Q_m(V_{\text{bias}})$ rises roughly linearly with $\sqrt{V_{\text{bias}}}$ and thereby proportional to depleted thickness. For n-side illumination $Q(V_{\text{bias}})$ does not start to rise before a certain threshold is reached by V_{bias}, going afterwards almost instantly to the saturation of charge collection efficiency. This effect is caused by the circumstance that for $V_{\text{bias}} < V_{\text{dep}}$ charges are injected into the undepleted part of the bulk. Therefore, they recombine before reaching the field zone and cannot contribute to the signal. After full depletion of the bulk

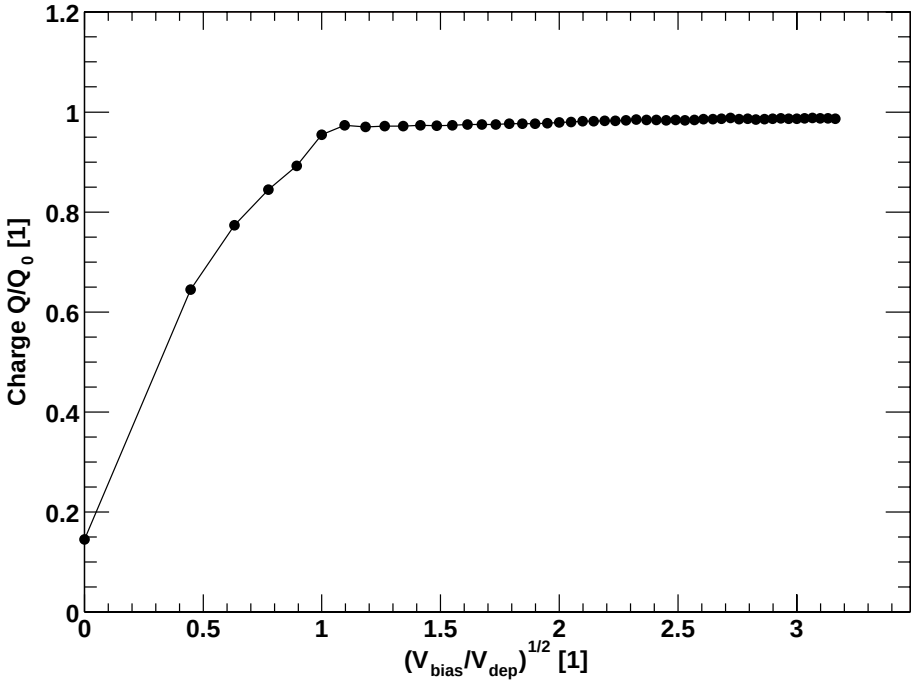

(a) p-side illumination

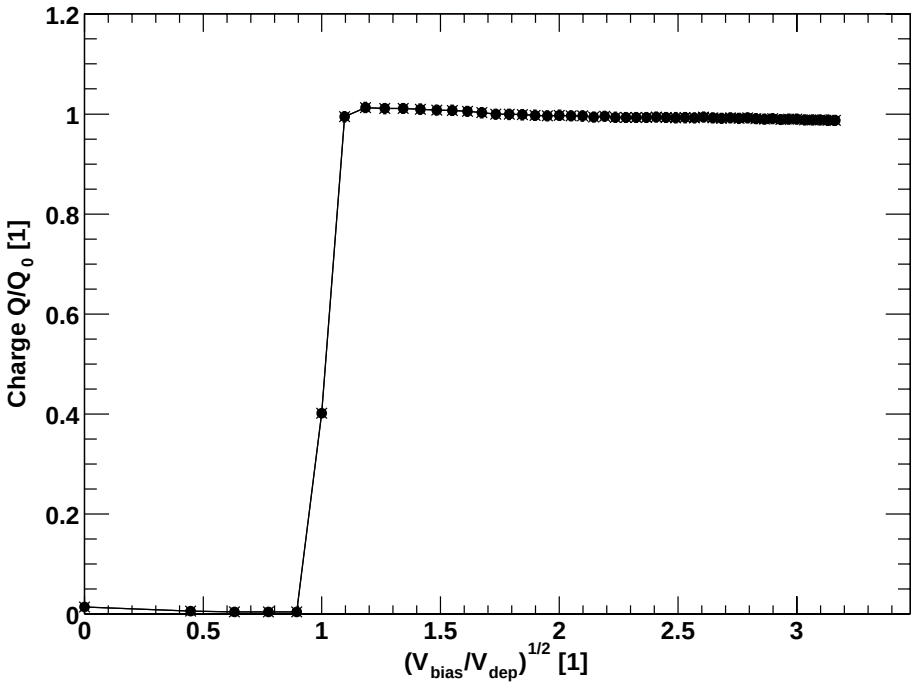

(b) n-side illumination

Fig. 8.3: Charge collection efficiencies vs. $\sqrt{V_{\mathrm{bias}}/V_{\mathrm{dep}}}$ as measured with an unirradiated sample with p-side illumination (a) and n-side illumination (b).

they are injected into the sensitive zone and give full signal. The position of the strong increase is almost exactly at the depletion voltage.

Irradiated Sample, p-Side Illumination

Contrary to the behaviour of an unirradiated sample the depletion zone grows in an irradiated diode simultaneously from the n- to the p-side as soon as the sample is irradiated with fluences beyond type conversion, as it is the case for the sample in Fig. 8.4. However, different from the unirradiated sample where the collected charge stays almost at zero before the steep increase starts the irradiated samples show an increase in collected charge as soon as V_{bias} is non-zero. The increase is linear in the Q_c vs. $\sqrt{V_{\mathrm{bias}}/V_{\mathrm{dep}}}$ plot. This can be attributed to a depletion zone growing from the p-side (called p-depletion-zone in the following) whose thickness is proportional to $\sqrt{V_{\mathrm{bias}}}$. This is caused by the so-called *double-junction effect*: in highly irradiated samples the depletion zone grows from both sides towards the centre. Q_c increases proportional to $\sqrt{V_{\mathrm{bias}}}$ until the bias voltage reaches a certain point which is denoted by V_{th}. This point is presumably the voltage where the two depletion zones merge. For $V_{\mathrm{bias}} > V_{\mathrm{th}}$ the charge collection shows a steep increase and returns after an overshoot to a plateau. The voltage where the plateau is reached the first time (i.e. before the overshoot) is denoted by V_{fcc}.
V_{th} and V_{fcc} are determined by taking the intersection points of three straight lines fitted to Q_c below, between and above the kinks (see Fig. 8.4). This is done with the measurements taken from several samples. Fig. C.1 and C.2 (p. 242-243) show the charge collection curves from further samples. The obtained values for V_{th} and V_{fcc} are given in Table 8.4. $\sqrt{V_{\mathrm{th}}/V_{\mathrm{dep}}}$ decreases with increasing fluence. This is an indication that the depth of the p-side depletion zone increases with fluence and it takes less bias voltage to merge the two depletion zones. The merging of the two depletion zones means that the sensor reaches its maximum sensitive volume, i.e. it is already fully depleted for $V_{\mathrm{bias}} < V_{\mathrm{dep}}$. The further increase in Q_c above V_{th} can be explained by improved charge collection due to higher electric field strength. This assumption is supported by the fact that also V_{fcc} is in almost all cases smaller than V_{dep}.
$Q_c(V_{\mathrm{bias}})$ shows a significant overshoot above V_{fcc}. The reason for this behaviour is up to now unknown, but may be explained by the following considerations: For $V_{\mathrm{bias}} \approx V_{\mathrm{dep}}$ the electric field is very low in the region where the two depletion zones merge. As described by eqs. (4.53) and (4.54) the concentration of free carriers (from leakage current) is very high in low field regions since there the drift velocity is low. This leads to high occupation probabilities for traps. Henceforth these defects trap signal-charges less effectively (see eq. 4.42) than traps in regions with higher electric fields. This idea is supported by the fact that the overshoot becomes more pronounced with increasing fluence where also the leakage current is higher.
If the signal charges leave this low-field area they are over-compensated by multiplication with $\exp(t/\tau_{\mathrm{eff}})$ since the τ_{eff} used for exponentiation is measured for

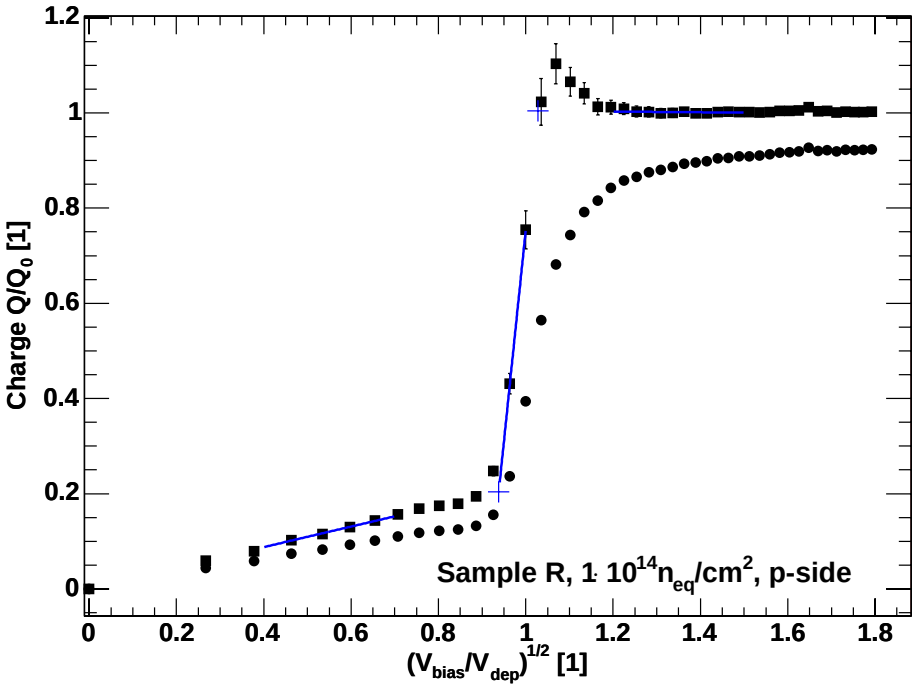

(a) p-side illumination

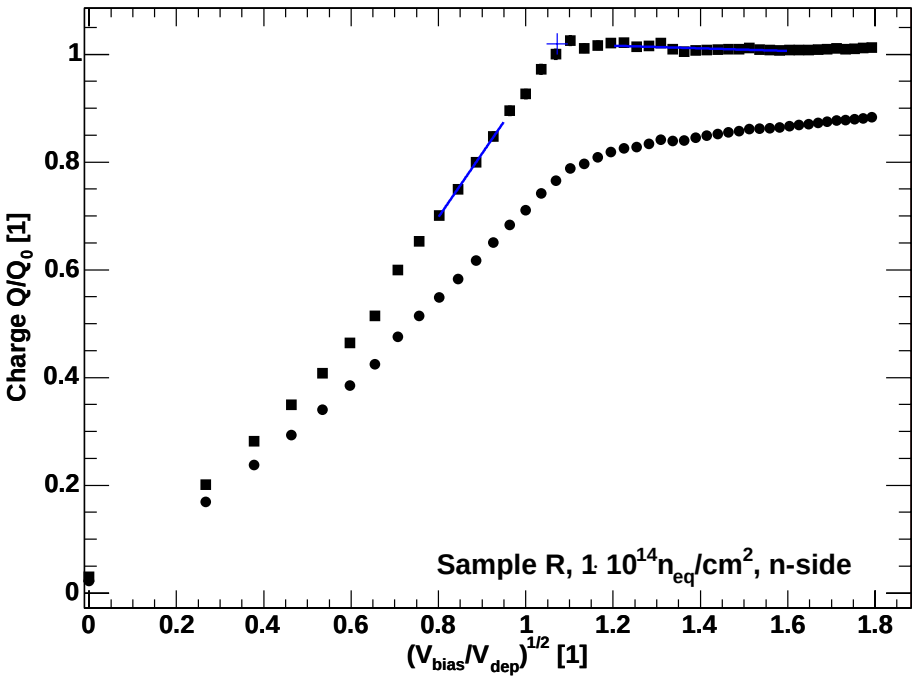

(b) n-side illumination

Fig. 8.4: Measured (lower curves) and corrected (upper curves) charge collection efficiencies vs. $\sqrt{V_{\mathrm{bias}}/V_{\mathrm{dep}}}$ as measured with neutron-irradiated sample R ($\Phi_{\mathrm{eq}} = 1 \cdot 10^{14}\, n_{\mathrm{eq}}/\mathrm{cm}^2$).

V_{bias} being well above V_{dep} and therefore, the trapping in low-field regions is overestimated. Beyond the overshoot Q_c drops to its final value.

Irradiated Sample, n-Side Illumination

The charge collection curves which are measured with n-side illumination have a simpler structure: They grow linearly in the $Q_c(V_{\mathrm{bias}})$ vs. $\sqrt{V_{\mathrm{bias}}/V_{\mathrm{dep}}}$ plot until they reach a plateau. The voltage at which this saturation is reached could be equivalent to V_{dep} and is also called V_{fcc} in the following. However, V_{fcc} is on all samples significantly higher than the depletion voltage V_{dep} obtained from CV-measurements: $\sqrt{V_{\mathrm{fcc}}/V_{\mathrm{dep}}}$ has in most cases a value between 1.1 and 1.3. Fig. 8.5 shows results for V_{dep} and V_{fcc} from the neutron irradiated samples and during annealing of sample Q. The plots show that the bias voltages V_{fcc} where full charge collection is reached are not identical to the depletion voltages V_{dep} obtained from CV-measurements. Charge collection with p-side illumination will result in lower "depletion voltages" while n-side illumination will yield higher ones.
The charge collection curves after n-side illumination show no overshoot for $V_{\mathrm{bias}} \approx V_{\mathrm{dep}}$. This may be explained by the fact that only electron traps are filled by leakage current in low-field regions while holes are trapped with the same probability than in high-field regions.

Sample	Fluence	V_{dep} [V]	$\sqrt{V_{\mathrm{th}}/V_{\mathrm{dep}}}$	$\sqrt{V_{\mathrm{fcc}}/V_{\mathrm{dep}}}$ p-side	$\sqrt{V_{\mathrm{fcc}}/V_{\mathrm{dep}}}$ n-side
P	0.92	53.2±4.2	1.01±0.05	1.20±0.06	1.34±0.07
Q	2.04	121.1±1.5	0.81±0.10	0.88±0.09	1.11±0.04
E	4.46	135.8±5.6	0.76±0.25	0.80±0.31	1.02±0.16
R	1.00	139.8±5.9	0.92±0.07	1.05±0.07	1.08±0.13
V	2.00	249.0±2.1	0.84±0.11	0.94±0.11	1.13±0.20
T	4.00	479.7±2.2	0.70±0.06	0.78±0.05	1.11±0.32

Table 8.4: Results for V_{th} and V_{fcc} for several samples.

8.2.2 Charge Collection Efficiencies from TCT

Measurement

From the ECC method also the charge Q_0 which is initially injected into the pad-detector can be derived. Without having a calibration of the experimental set-up Q_0 is determined only in arbitrary units. Numbers for the CCE are derived by integrating the measured signal currents and dividing them by Q_0. The CCE derived by this method after p- or n-side illumination is lower than the CCE for mip detection: while after close-to-surface charge deposition the signal charges

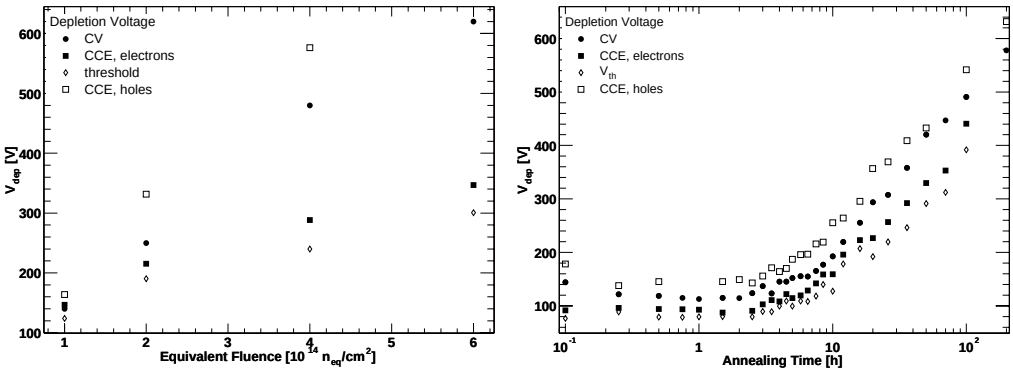

(a) Fluence dependence.

(b) Annealing behaviour.

Fig. 8.5: Depletion voltages extracted from CV-measurement and full charge collection voltages V_{fcc} from TCT-measurements. Additionally the threshold voltages V_{th} for p-side signals are displayed. Left plot is fluence dependent for the neutron irradiated samples. The right plot shows the development during annealing of sample Q.

have to drift through the whole thickness d of the detector mips deposit charge homogeneously along their tracks and thus only a small part of the signal charge has to drift through the full detector thickness; on average the drift length is only $d/2$.
Fig. 8.6 shows the charge collection efficiencies for electrons and holes measured on proton and neutron irradiated samples. In these plots CCE is plotted vs. the overdepletion voltage $V_{\mathrm{bias}} - V_{\mathrm{dep}}$. These plots contain results from samples with different thicknesses. Therefore, in some cases a thin sample has the same or a higher CCE than a thicker sample with a lower fluence.

Discussion

Especially the lowly irradiated samples show an CCE that rises significantly with V_{bias} above depletion voltage. With increasing fluence this rise becomes less significant: the gain in CCE is caused by decreasing charge collection times and thereby less trapping. However, due to high depletion voltage in highly irradiated samples the drift velocities are much closer to their saturation value in these samples. Therefore, the charge collection times cannot be shortened significantly by increasing bias voltage.

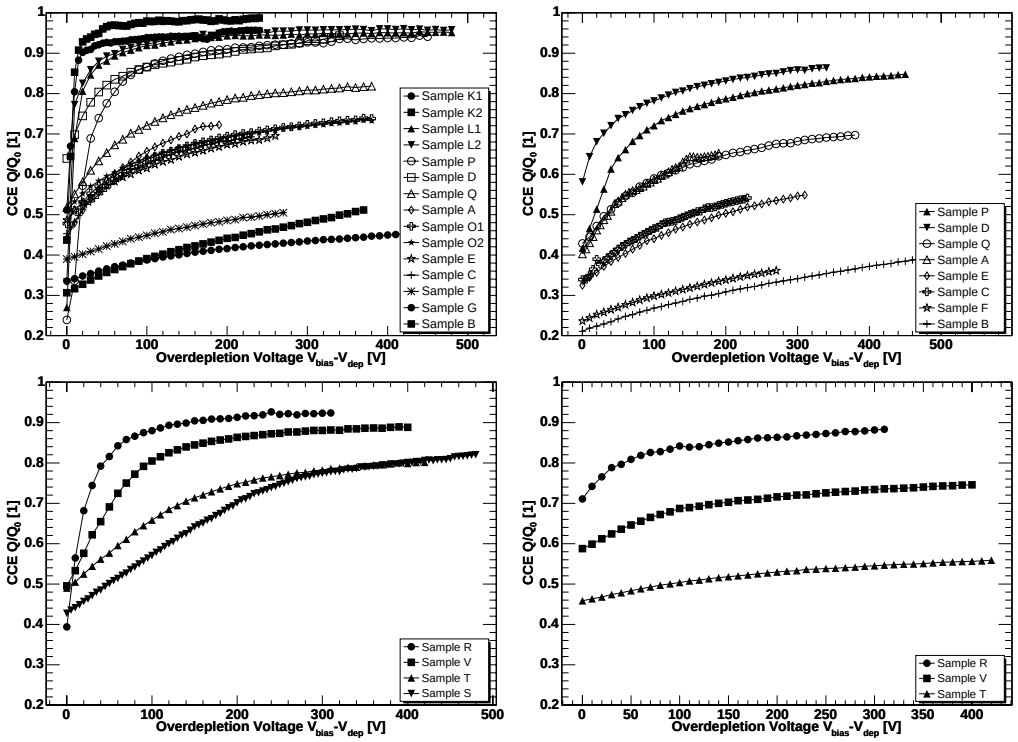

Fig. 8.6: Charge collection efficiency for electrons (left) and holes (right) from TCT-measurements for close-to-surface charge injection. The two upper plots show results from proton-irradiated samples, the lower ones from neutron-irradiated samples.

8.3 Pulse Shape and Electric Field

8.3.1 Unirradiated Sample

From a set of measured signal currents the electric field distribution is deconvoluted by the method described in sec. 6.5.8. As a consistency check this method is firstly employed on measurements with the unirradiated sample $\emptyset$. This has the advantage that the field configuration can be compared to the theoretically expected one which can be easily calculated (eq. (3.53), p. 35).

The first steps in the deconvolution of the signals are the correction for limited bandwidth (eq. (6.11)) and the elimination of post-pulse oscillations (eq. 6.12). These two steps are followed by the exponentiation of the signal to obtain the signal shape that would have been measured without charge-trapping. (This step is dropped when processing data from unirradiated samples.)

After these measures the next step is the determination of the parameter a as defined in eq. (6.17). Generally, for the deconvolution the inflection point t_1 of the leading signal edge is taken as starting point and the trailing edge's inflection point t_2 corresponds to the end of charge drift. Thus the charge collection time is $t_c = t_2 - t_1$. Fig. 8.7 shows the results for a for different bias voltages as calculated

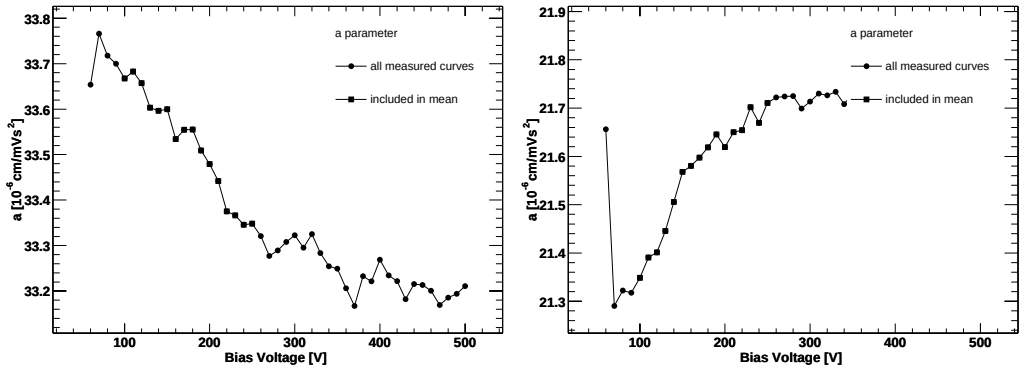

(a) p-side illumination (b) n-side illumination

Fig. 8.7: Parameter a for deconvolution vs. V_{bias} for electron (a) and hole signal (b). Measurement on unirradiated sample $\emptyset$.

from p-side and n-side signals.
Only bias voltages above V_{dep} (as derived from CV-measurements) are used for the determination of a. The parameter depends only slightly on the bias voltage as can be seen on the graphs; the variation of a over the full range shown in Fig. 8.7 is less than 2%. In order to get a more precise value and also to deconvolute the signals below V_{dep}, where a cannot be derived from the signal, the average value of a in the bias voltage range between $V_{\text{dep}} + 50V$ and $V_{\text{dep}} + 200$ is taken (this subset is indicated by square symbols in the plots). This is allowed since the factor between current and drift velocity is the same for all measurements with varied bias voltage as long as the measurement and its calibration has not been changed.
After that drift velocity $v_d(t)$ and drift length $x_d(t)$ are calculated (eqs. (6.15) and (6.18), resp.). As an example Fig. 8.8 shows the results for sample $\emptyset$ with $V_{\text{bias}} = 80\,\text{V}$. Practically, the software calculates v_d and x_d for the discrete times t_i at which the signal currents have been digitised by the oscilloscope. Therefore, these two functions exist as sets of pairs $(t_i, v_{d,i})$ and $(t_i, x_{d,i})$.
From the functions $x_d(t)$ and $v_d(t)$ the function $v_d(x_d)$ is derived. This problem is solved by combining the discrete values of $x_d(t_i)$ and $v_d(t_i)$ to pairs $(v_{d,i}, x_{d,i})$. The function $v_d(x_d)$ is also shown in Fig. 8.8.
With the help of the parameterisation of $v_d(E)$ given in [Se90] (MINIMOS 4, see also sec. 9.3.4) the desired electric field strengths $E(x_d)$ are determined. As a check, the reconstructed bias voltage $V_{\text{bias,rec}}$ is calculated by integrating the electric field $E(x_d)$:

$$V_{\text{bias,rec}} = \int_0^d E(x_d)\, dx_d \,. \tag{8.16}$$

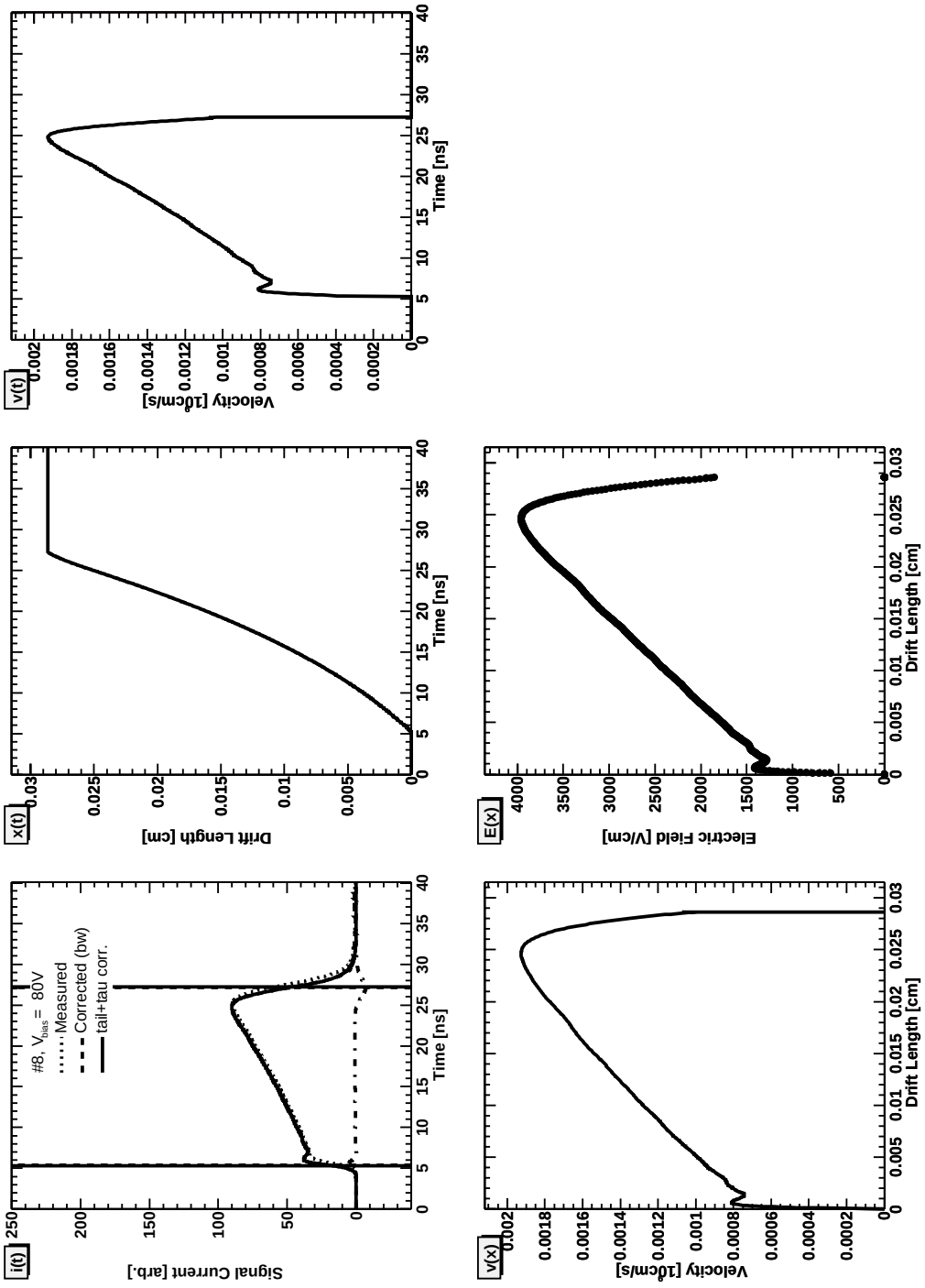

Fig. 8.8: Steps of deconvolution of electric field for sample ∅ with $V_{\text{bias}} = 80\,\text{V}$, n-side illumination. Top left: measured, bandwidth and trapping corrected currents (no difference between bandwidth and trapping corrected currents seeable since $\tau_{\text{eff}} \to \infty$ for unirradiated sample). Top centre: Drift length vs. time. Top right: Drift velocity vs. time. Bottom left: Drift velocity vs. drift length. Bottom centre: Electric field vs. drift length.

In the ideal case the result should be equal to the applied bias voltage $V_{\mathrm{bias,app}}$. However, this is not the case. Fig. 8.9 shows the deviation of $V_{\mathrm{bias,rec}}$ from $V_{\mathrm{bias,app}}$. The increase of deviation with $V_{\mathrm{bias,app}}$ can be explained by the decreasing signal duration and therefore larger relative influence of the signal distortion at the edges. The average deviation in the voltage range 50-200 V above V_{dep} is about 15%.

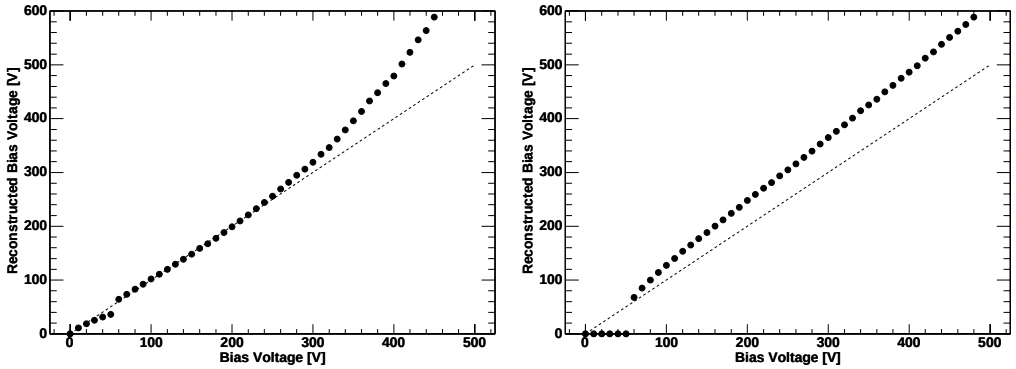

(a) p-side illumination (b) n-side illumination

Fig. 8.9: Reconstructed $V_{\mathrm{bias,rec}}$ vs. applied $V_{\mathrm{bias,app}}$ for electron (a) and hole signal (b). The dashed line gives the ideal relation $V_{\mathrm{bias,rec}} = V_{\mathrm{bias,app}}$. Measurement on unirradiated sample ∅.

Fig. 8.10 shows the resulting $E(x_d)$ for different V_{bias} after p- and n-side illumination. The deconvoluted field distributions after n-side illumination are closer to the theoretically expected ones since the edges are steeper compared to the field distributions from p-side illuminations. This can be explained by the longer signal durations and thereby less influence of the limited rise time of the edges as already stated above. The p-side signals develop a "bump" towards higher bias voltages. The exact reason for this deconvolution artefact cannot be given but probably it results also from limitations by short signals since at the lowest bias voltages this artefact is not visible.
In the further analysis the effective doping concentration N_{eff} is determined by using the differential form of Gauss' law:

$$\frac{dE}{dx} = -\frac{e_0}{\varepsilon\varepsilon_{\mathrm{Si}}} N_{\mathrm{eff}} \,. \tag{8.17}$$

N_{eff} is extracted from $E(x_d)$ by fitting a straight line between $x_d = 0.2 \cdot d$ and $x_d = 0.8 \cdot d$, the product of the slope with $\varepsilon\varepsilon_{\mathrm{Si}}/e_0$ is taken as N_{eff}. The results from measurements at $V_{\mathrm{bias}}+10$ V are $(0.6342 \pm 0.0014) \cdot 10^{12}\,/\mathrm{cm}^3$ and $(0.8689 \pm 0.0012) \cdot 10^{12}\,/\mathrm{cm}^3$ for p-side and n-side illumination, respectively. The given errors are the errors of the fits and do not include further systematic errors from deconvolution

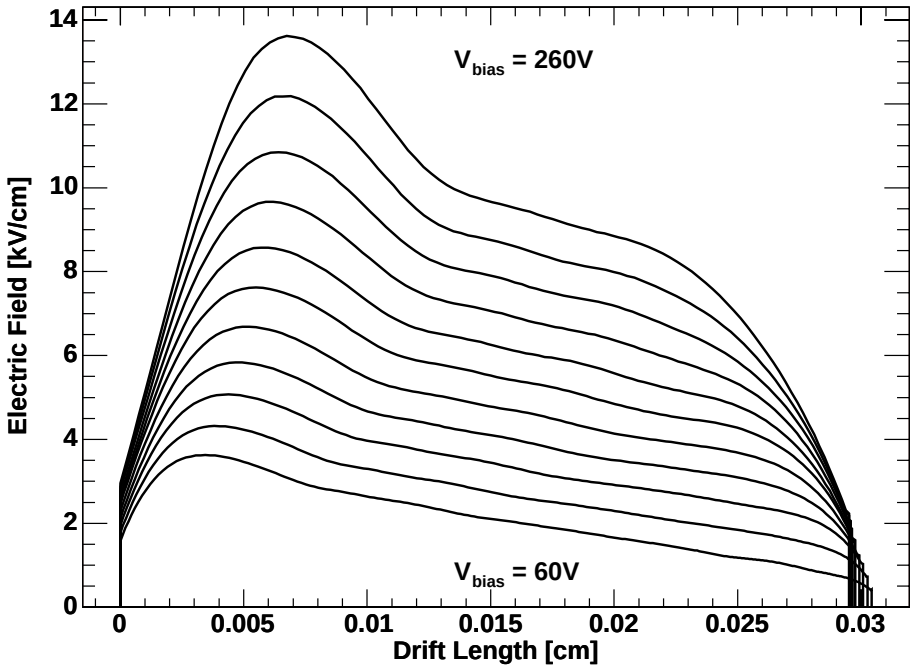

(a) p-side illumination

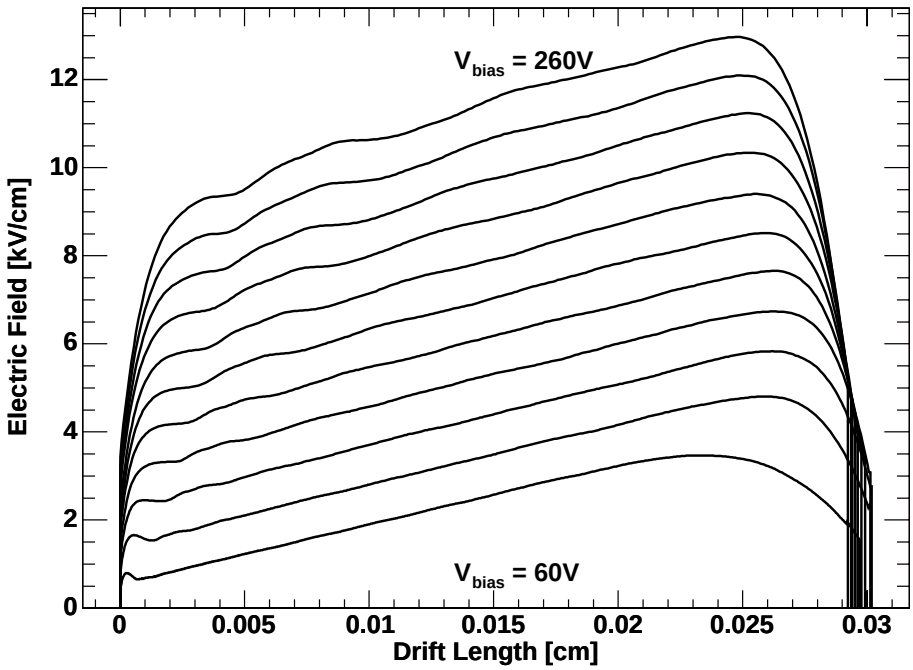

(b) n-side illumination

Fig. 8.10: Reconstructed electric field distributions measured on the unirradiated sample ∅ for electron (a) and hole signal (b).

which should be significantly larger as can already be seen on the deviation of the reconstructed bias voltage from applied bias voltage. Both values do not agree with $N_{\mathrm{eff,CV}} = (0.71 \pm 0.05) \cdot 10^{12}/\mathrm{cm}^3$ as calculated from V_{dep} from CV-characteristic but the result from the p-side signal is closer. The mean value of these two measurements is $0.75 \cdot 10^{12}/\mathrm{cm}^3$ which is inside the error margin of $N_{\mathrm{eff,CV}}$. Fig. 8.11 shows the reconstructed N_{eff} vs. bias voltage. The deviation of the reconstructed N_{eff} from $N_{\mathrm{eff,CV}}$ grows with V_{bias}. This can be explained by an increasing systematic error of the deconvolution since the signal durations decrease. If averaged over the range $V_{\mathrm{dep}} + 20\,\mathrm{V} \leq V_{\mathrm{bias}} \leq V_{\mathrm{dep}} + 70\,\mathrm{V}$ the results are $N_{\mathrm{eff}} = (0.6993 \pm 0.0169) \cdot 10^{12}/\mathrm{cm}^3$ and $(0.8967 \pm 0.0040) \cdot 10^{12}/\mathrm{cm}^3$ for p-side and n-side illumination, respectively.

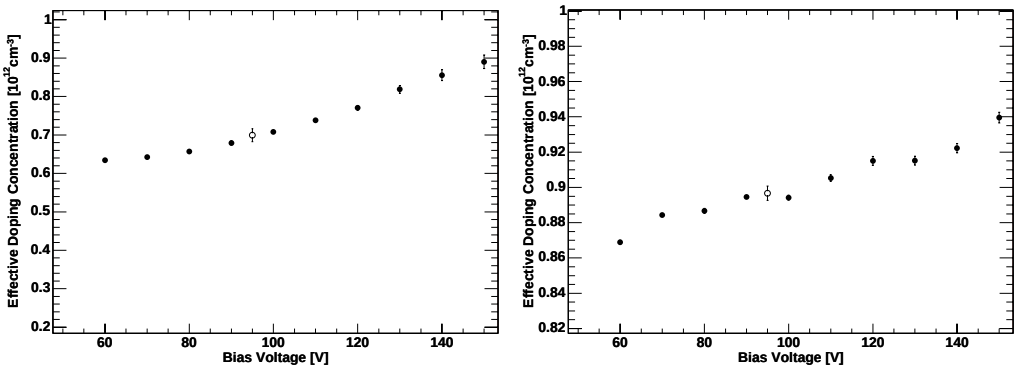

(a) p-side illumination (b) n-side illumination

Fig. 8.11: Reconstructed effective doping concentration vs. the bias voltage for electron signals (left) and hole signals (right). Open symbols show the mean value (averaged over $V_{\mathrm{dep}} + 20\,\mathrm{V} \leq V_{\mathrm{bias}} \leq V_{\mathrm{dep}} + 70\,\mathrm{V}$, errors of single points smaller than symbols). Measurement on sample ∅.

Generally, one can state that the deconvolution works best at low bias voltages since in slow signals the signal integrity is better. The systematic error on reconstructed bias voltages is estimated to be $\approx 15\%$, N_{eff} has an estimated error of 25%.

8.3.2 Lowly Irradiated Samples

The deconvolution method which has been introduced in the previous section is now applied to irradiated samples with different obtained fluences. Samples K_1 and L_1 are irradiated with only low fluences where the field has still a mainly linear behaviour. The latter sample shows already space charge sign inversion.

Sample K_1, $\Phi_{eq} = 0.22 \cdot 10^{14}\, n_{eq}/cm^2$ (no SCSI)

On sample K_1 only p-side signals can be measured since it has no opening for light injection on the n-side. Similar to the analysis of the unirradiated sample, a depends only weakly on $V_{bias,app}$ and the bias voltage is well reconstructed at voltages being not too high above V_{dep}.
Fig. 8.12 shows the reconstructed electric field distributions. N_{eff} obtained from deconvolution is $(0.1404 \pm 0.0009) \cdot 10^{12}/cm^3$ (measured at $V_{bias} = V_{dep} + 10\,V$, error takes into account only uncertainty of fit). Considering the systematic error of 25% of N_{eff} (as estimated at the end of sec. 8.3.1) this value agrees within errors with $N_{eff,CV} = (0.17 \pm 0.02) \cdot 10^{12}/cm^3$.

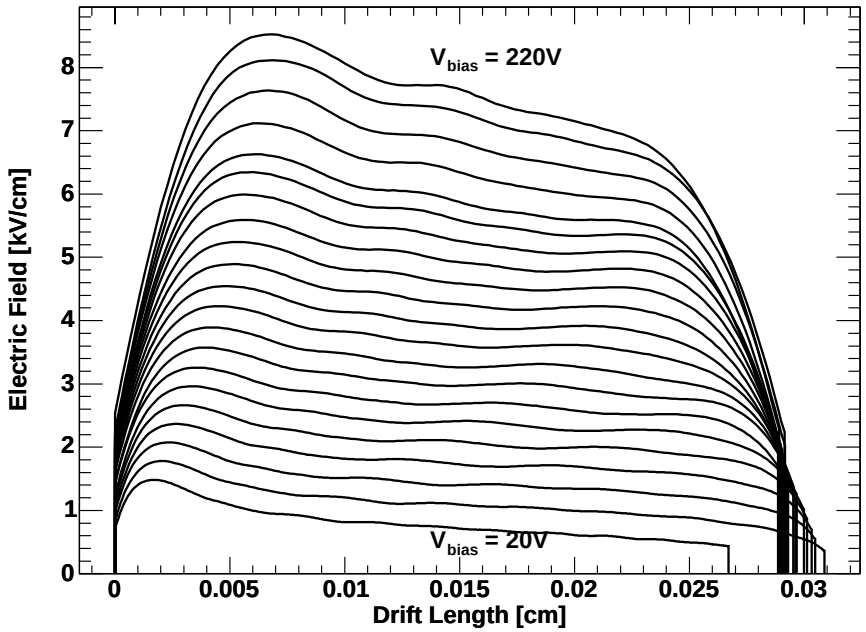

Fig. 8.12: Reconstructed electric field distributions measured on sample K_1 ($\Phi_{eq} = 0.22 \cdot 10^{14}\, n_{eq}/cm^2$) for electron signal.

Sample L_1, $\Phi_{eq} = 0.52 \cdot 10^{14}\, n_{eq}/cm^2$ (SCSI)

Sample L_1 is the most lowly irradiated sample showing SCSI. The results for $E(x_d)$ are shown in Fig. 8.13. Different from sample K_1 the slope of the electron signal is now positive. This indicates the occurence of space charge sign inversion. The resulting effective doping concentration $N_{eff,e}$ is $(-0.5488 \pm 0.0043) \cdot 10^{12}/cm^3$ (measured at $V_{bias} = V_{dep} + 10\,V$). Compared with $|N_{eff,CV}| = (0.29 \pm 0.02) \cdot 10^{12}/cm^3$ this value deviates from the value expected from CV-measurement. The

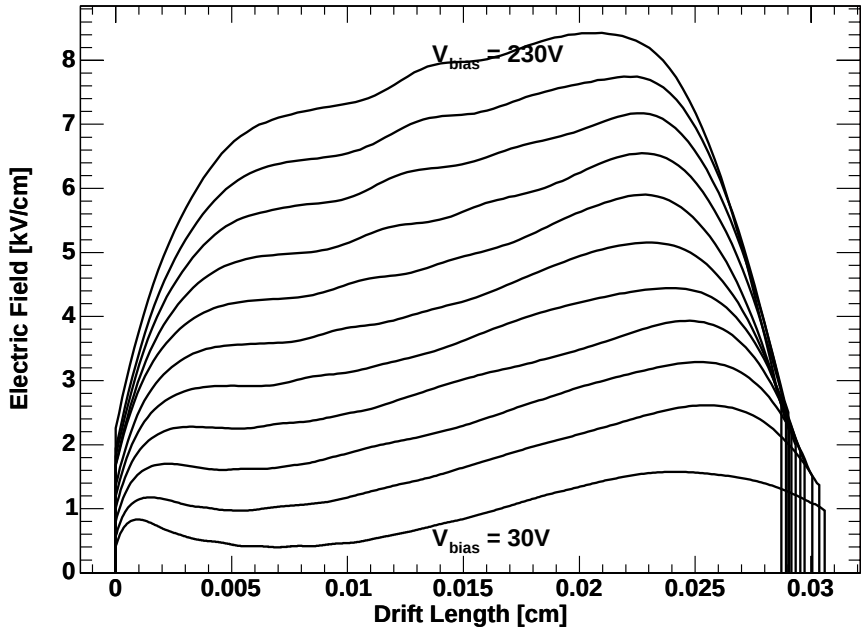

Fig. 8.13: Reconstructed electric field distributions measured on sample L_1 ($\Phi_{eq} = 0.52 \cdot 10^{14}\, n_{eq}/cm^2$) for electron signal.

reason may be that the field distribution shows already a slight occurence of a double peak at the lowest bias voltages.

8.3.3 Highly Irradiated Samples

Application of Deep Level Model

The samples analysed in this section have obtained such a high fluence that the electric field can no longer be considered as being linear. Consequently, N_{eff} is no longer homogeneous in the detector and thus cannot be determined by fits of straight lines to $E(x)$. Therefore, a more refined parameterisation based on the deep level model introduced in sec. 4.2.4 is used to describe the field configuration. The aim of the analysis presented here is to determine parameters for the deep level model. This model will later be used for the description of the electric fields in simulations of the charge collection in irradiated silicon-detectors.
Therefore, priority is not given to obtaining exact results for microscopic properties of the substrate but to find a few useful parameters to describe the electric field in highly irradiated detectors.

Method

The analysis method is demonstrated on sample C: the steps to obtain $v_{dr}(x)$ and $E(x)$ by deconvolution are the same as in the low fluence samples. After obtain-

ing $v_{\mathrm{dr}}(x)$ (Fig. 8.14(a)) the corresponding carrier densities $n_e(x)$ and $n_h(x)$ are calculated by eqs. (4.53/4.54), see Fig. 8.14(b). This method develops further the method used in [Er02] since in that paper the drift velocities are considered as being constant. Contrary to this, in this analysis the dependence on the field strength is considered. Furthermore, the drift velocities are obtained from measurement while [Er02] calculates them by the approximation $v_{\mathrm{dr}} \approx \mu_{e,h} \cdot V_{\mathrm{bias}}/d$.
In the following step the filling factors $F(x)$ (eq. (4.66)) and charged fractions F^-, F^+ are calculated from $n_{e,h}(x)$ (eq. (4.67)/(4.68)), see Fig. 8.15(a). For this calculation only the deep donor and deep acceptor contributing most to the space charge are considered [Er02]. The parameters used for the calculation are[1]:

label	type	E_t [eV]	σ_e [cm^2]	σ_h [cm^2]
DA4	e-trap	$E_C - 0.52$	$1 \cdot 10^{-15}$	$1 \cdot 10^{-15}$
DD3	h-trap	$E_V + 0.53$	$1 \cdot 10^{-15}$	$3 \cdot 10^{-14}$

(8.18)

In the next step the concentrations N_{DA} and N_{DD} of deep acceptors and deep donors have to be determined. In order to do this a fit range $[x_1, x_2]$ in $E(x)$ is chosen. This range consists of the middle part of the deconvoluted electric field and should not be extended too close to the less accurately reconstructed edges. From eq. (4.70) the electric field on the interval $[x_1, x_2]$ is obtained by integration (Gauss's law):

$$E(x) = E(x_1) - \frac{q_0}{\varepsilon_{\mathrm{Si}}\varepsilon_0} \int_{x_1}^{x} N_{\mathrm{eff}}(x')\,dx' \tag{8.19}$$

$$= E(x_1) - \left(N_{\mathrm{sh}}\,(x - x_1) + N_{\mathrm{DD}} \int_{x_1}^{x} F^+(x)\,dx \right.$$
$$\left. - N_{\mathrm{DA}} \int_{x_1}^{x} F^-(x)\,dx \right) \tag{8.20}$$

$$= E(x_1) - N_{\mathrm{sh}}\,(x - x_1) - N_{\mathrm{DD}}\,\Xi_{\mathrm{DD}}(x) + N_{\mathrm{DA}}\,\Xi_{\mathrm{DA}}(x)\,. \tag{8.21}$$

The electric field is directed towards negative x and points therefore into the integration volume at x_2. Henceforth the minus sign is introduced in the first line. In the last line the abbreviations

$$\Xi_{\mathrm{DD}}(x) = \int_{x_1}^{x} F^+(x)\,dx \quad \text{and} \tag{8.22}$$

$$\Xi_{\mathrm{DA}}(x) = \int_{x_1}^{x} F^-(x)\,dx \tag{8.23}$$

have been introduced. They are plotted in Fig. 8.15(b) for sample C.

[1] The labelling of the defects is the same as in [Er02].

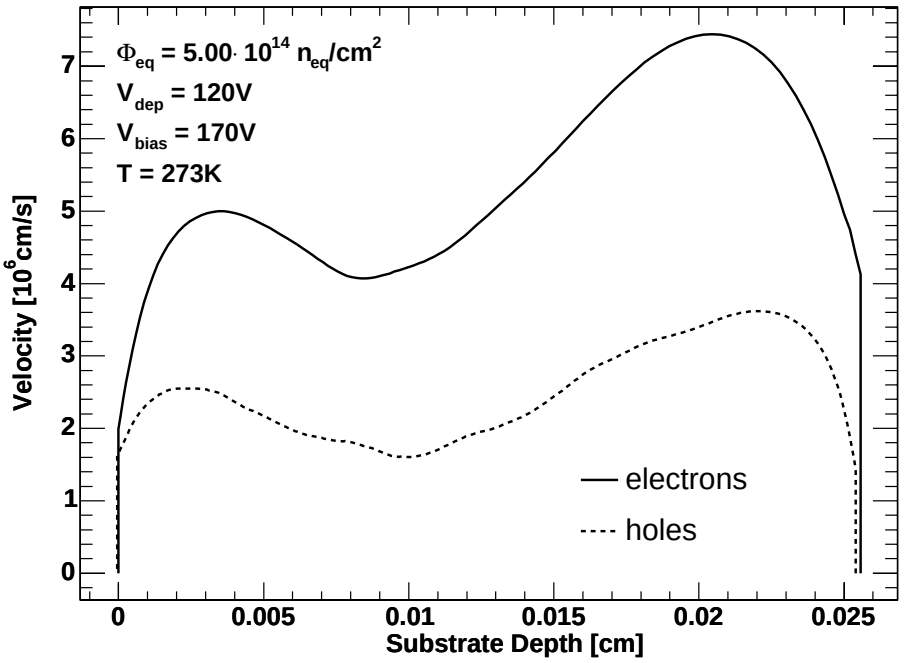

(a) Drift velocities

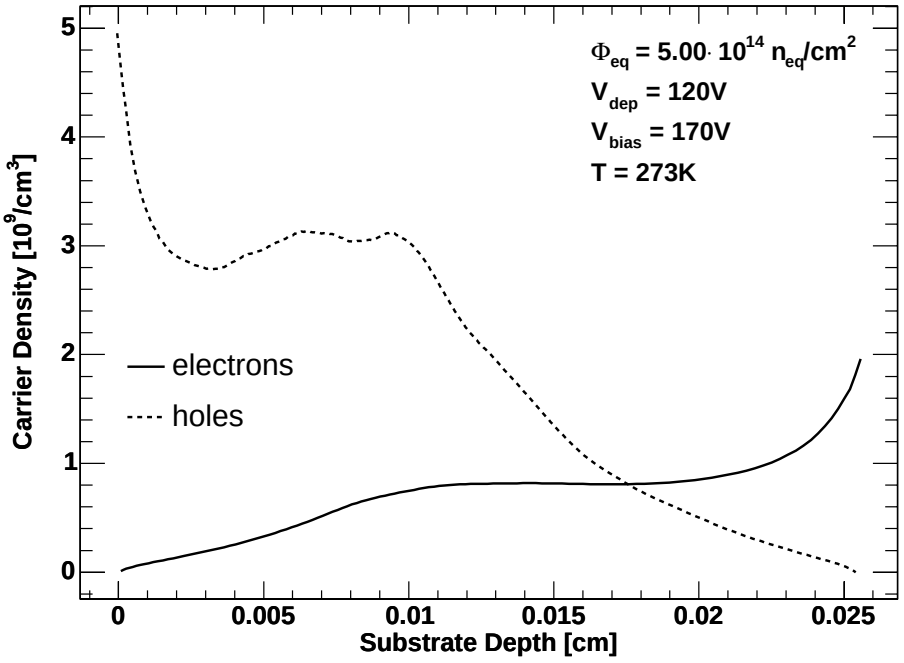

(b) Carrier densities

Fig. 8.14: Plots of drift velocities v_{dr} and corresponding carrier densities vs. substrate depth x for electrons and holes in sample C ($\Phi_{\mathrm{eq}} = 5 \cdot 10^{14}\, n_{\mathrm{eq}}/\mathrm{cm}^2$, $V_{\mathrm{bias}} = 170\,\mathrm{V}$).

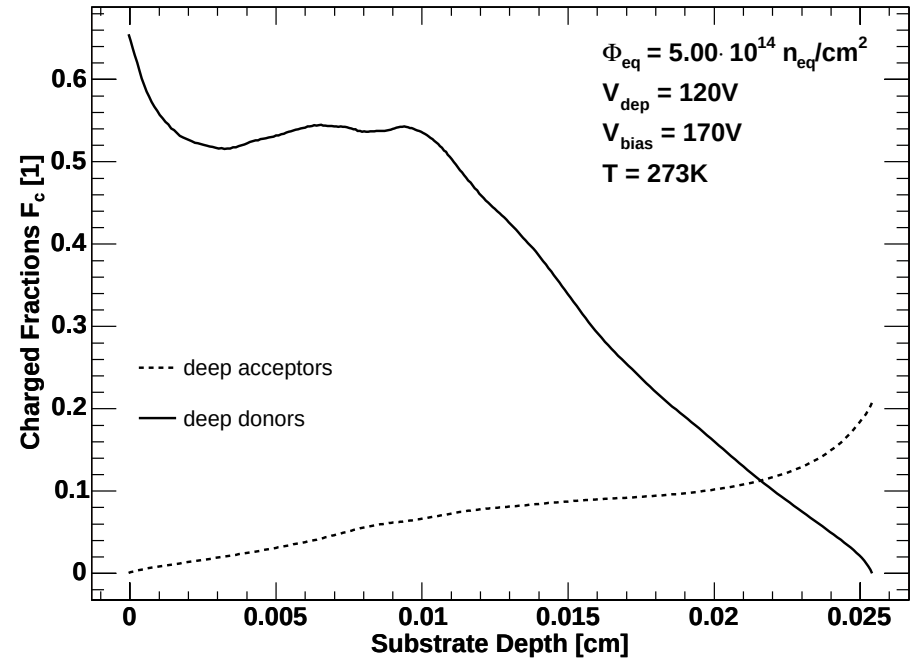

(a) Charged fractions of deep levels

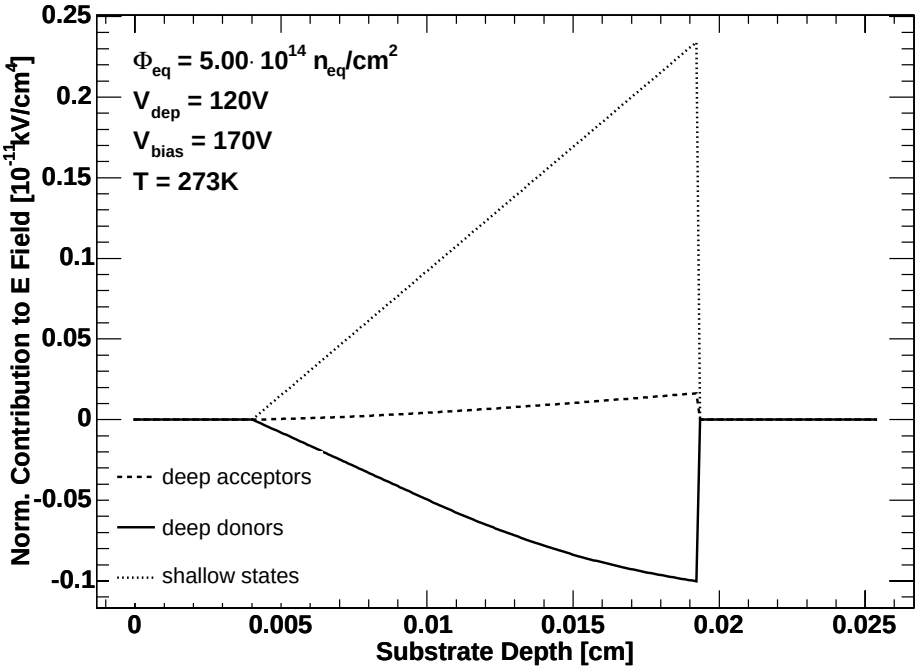

(b) Normalised contribution to electric field

Fig. 8.15: Charged fractions of deep levels (a) and their contributions divided by concentration to the electric field ($\Xi_{\mathrm{DD}}(x)$ and $\Xi_{\mathrm{DA}}(x)$, cf. eq. (8.21)) (b). The contribution from N_{sh} is also shown.

N_{DA} and N_{DD} are obtained by a fit of eq. (8.21) to the deconvoluted electric field on the interval $[x_1, x_2]$. $E(x_1)$ is taken from $E(x)$, N_{sh} is calculated with the equations for the stable damage (cf. eq. (4.13), parameters given on same page):

$$N_{\mathrm{sh}} = N_{\mathrm{D}} - N_{\mathrm{A}} \tag{8.24}$$

$$= -N_{c,0} \cdot (1 - \exp(-c\Phi_{\mathrm{eq}})) + g_c \Phi_{\mathrm{eq}} \, . \tag{8.25}$$

Fig. 8.16 shows the deconvoluted electric fields from p-side and n-side illumination signals together with the fitted functions according to eq. (8.21).

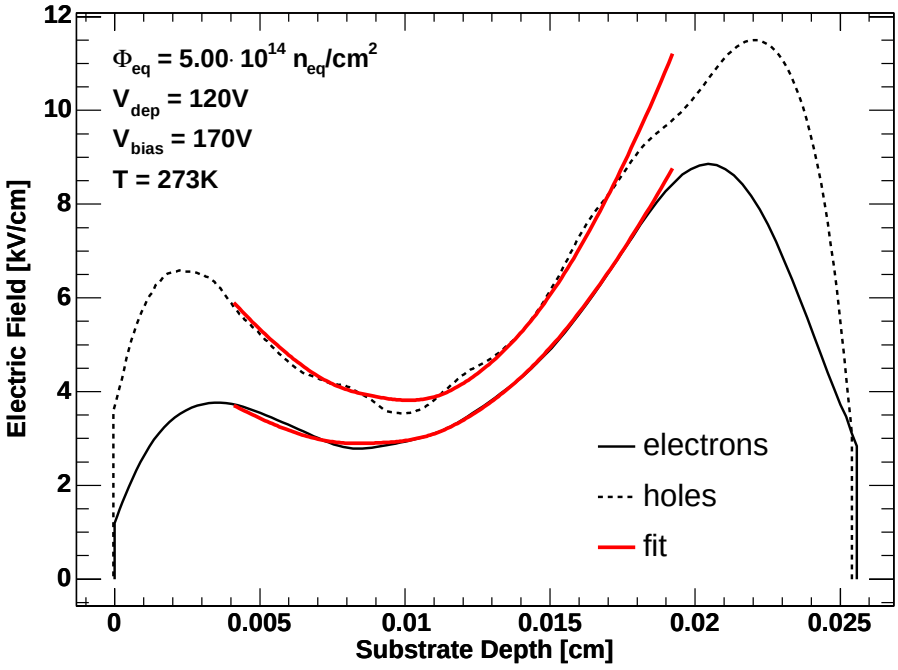

Fig. 8.16: Electric fields from deconvolution of electron and holes signals as measured on sample C together with fitted deep level model.

This analysis is applied to measurements at several bias voltages above V_{dep}. The results for the concentrations of deep acceptors and deep donors from measurements after p- and n-side illumination are shown in Fig. 8.17. The errors shown in that figure are the errors of the fits to the individual measurements and do not include systematic errors. These systematic errors are larger as can be seen on the variation of the concentration with bias voltage.
The concentration of deep acceptors N_{DA} shows a strong variation with V_{bias} and the results from n- and p-side illumination are inconsistent with each other. The variation of N_{DD} with V_{bias} is smaller than that of N_{DA}. The results from p-side and n-side illumination are still inconsistent but the difference is much smaller.

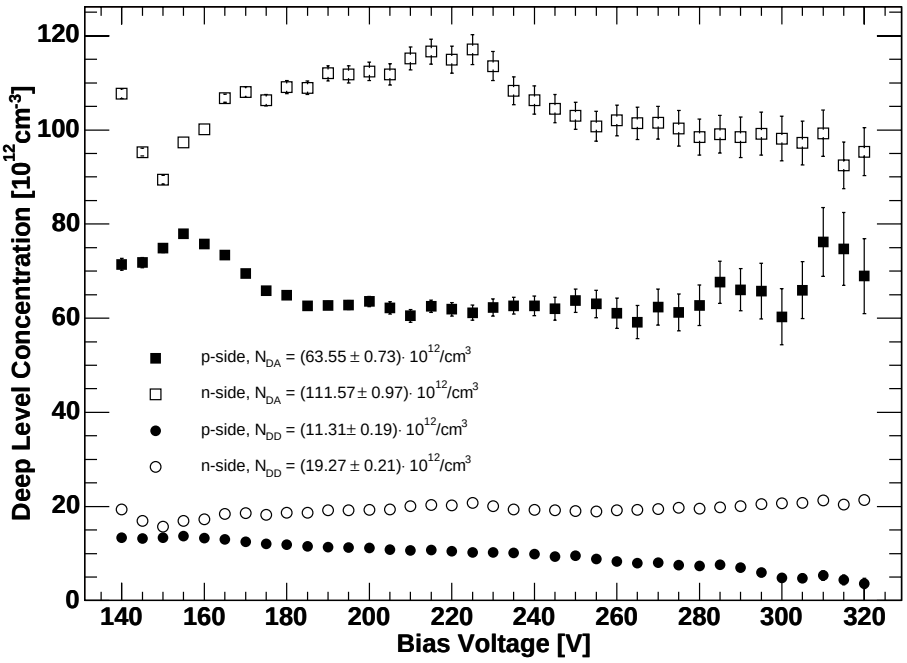

Fig. 8.17: Concentration of deep acceptors and donors vs. V_{bias}. The data are extracted from measurements on sample C with p- and n-side illumination. Not visible errors are smaller than the symbols.

As final results for N_{DA} and N_{DD} the single results have been averaged in the bias voltage range $V_{\mathrm{dep}} + 50\,\mathrm{V} \leq V_{\mathrm{bias}} \leq V_{\mathrm{dep}} + 100\,\mathrm{V}$.

Fluence Dependence of N_{DA}

Fig. 8.18 shows the dependence of N_{DA} on the equivalent fluence in proton- and neutron-irradiated samples. In both cases N_{DA} shows no distinct dependence on the fluence, the variations are quite large and do neither suggest a linear introduction with fluence ($N_{\mathrm{DA}} \propto \Phi_{\mathrm{eq}}$) nor a saturating behaviour ($N_{\mathrm{DA}} \propto (1 - \exp(-\Phi_{\mathrm{eq}}/c_\phi))$). Therefore, for a description of the fluence dependence a concentration that is constant at the fluences considered here is assumed. The average values for N_{DA} are given in Table 8.5. The numbers from n- and p-side illumination agree within errors with each other. Table 8.5 gives also the combined values from n- and p-side signals. For the averaging the p-side result from sample T ($\Phi_{\mathrm{eq}} = 4 \cdot 10^{14}\ n_{\mathrm{eq}}/\mathrm{cm}^2$) is discarded since it deviates strongly from the other values. Due to the high V_{dep} in this sample (480 V) the measurements on the sample had to be done with high bias voltages and thus the signals were short. Therefore the electron signal delivers hardly usable results.

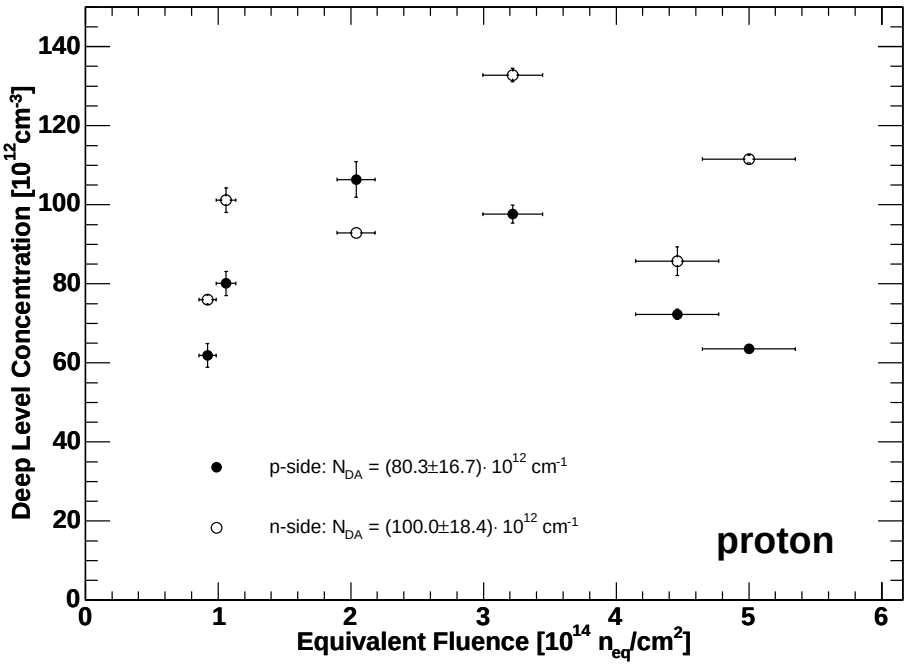

(a) proton irradiation

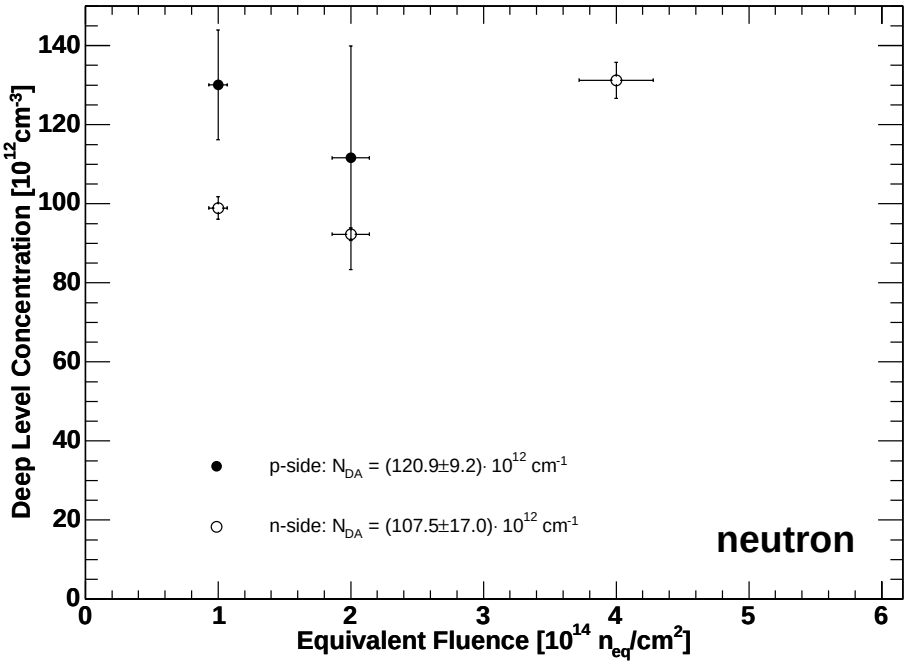

(b) neutron irradiation

Fig. 8.18: Concentration of deep acceptors vs. equivalent fluence in proton- and neutron-irradiated samples. Values given are averaged for $V_{\mathrm{dep}} + 50\,\mathrm{V} \leq V_{\mathrm{bias}} \leq V_{\mathrm{dep}} + 100\,\mathrm{V}$.

	$N_{DA}\,[10^{12}/\mathrm{cm}^3]$		
irradiated with	p-side	n-side	combined
protons	80±17	100±18	90±20
neutrons	120.9±9.2	107±17	112±16

Table 8.5: Concentrations of deep acceptors measured on proton and neutron-irradiated samples.

Fluence Dependence of N_{DD}

The concentration of deep donors N_{DD} shows a linear increase with equivalent fluence as can be seen in Fig. 8.19. Thus it can be described with a linear introduction rate g_{DD} according to

$$N_{DD} = g_{DD} \cdot \Phi_{eq} \,. \tag{8.26}$$

The results for the introduction rates are given in Table 8.6. Again the value measured on sample T with p-side illumination has been discarded from the fits for the reasons given above.

	$g_{DD}\,[10^{-2}/\mathrm{cm}]$		
irradiated with	p-side	n-side	combined
protons	3.08±0.10	3.92±0.12	3.54±0.08
neutrons	2.87±0.35	1.87±0.16	2.07±0.15

Table 8.6: Introduction rates for deep donors measured on proton and neutron-irradiated samples.

Discussion

The double peak structure of the electric field has been parameterised based on a model that contains one deep acceptor and one deep donor level. This model is a strong simplification since in reality irradiated silicon contains a variety of deep levels with different energy levels and capture cross-sections. It does not make sense to include further levels into the analysis since the contributions to the electric field would be too similar to be distinguished by fits to the deconvoluted electric fields. But in spite of this strong simplification the deconvoluted electric fields can be fitted by this model quite well. However, the fit parameters N_{DA} and N_{DD} depend strongly on the bias voltage what should be different in an ideal case.

The fluence dependence of N_{DA} can be best described by a constant for all fluences considered here. Two possible explanations can be given for this behaviour:

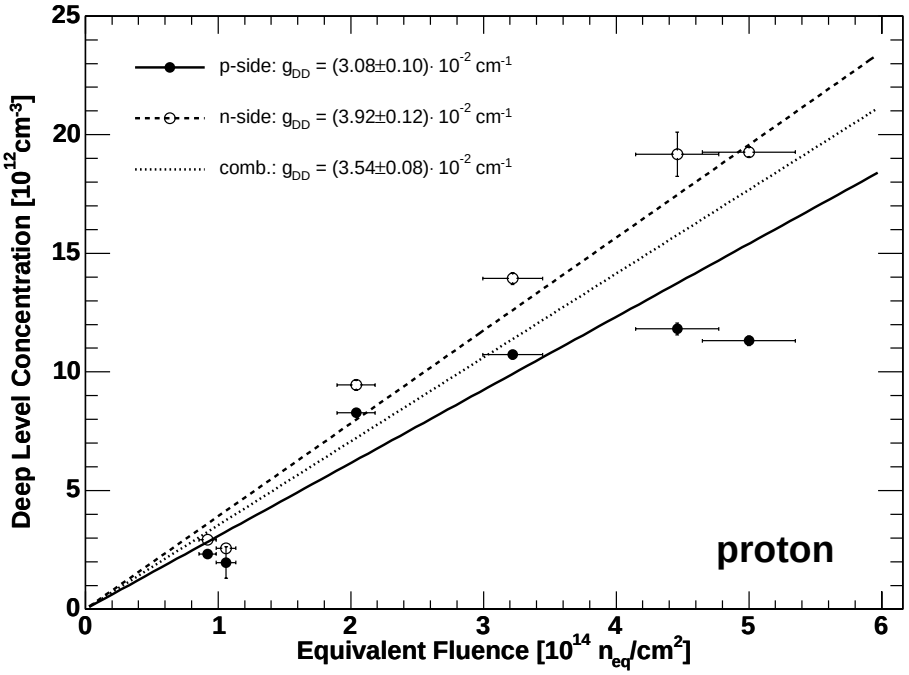

(a) proton irradiation

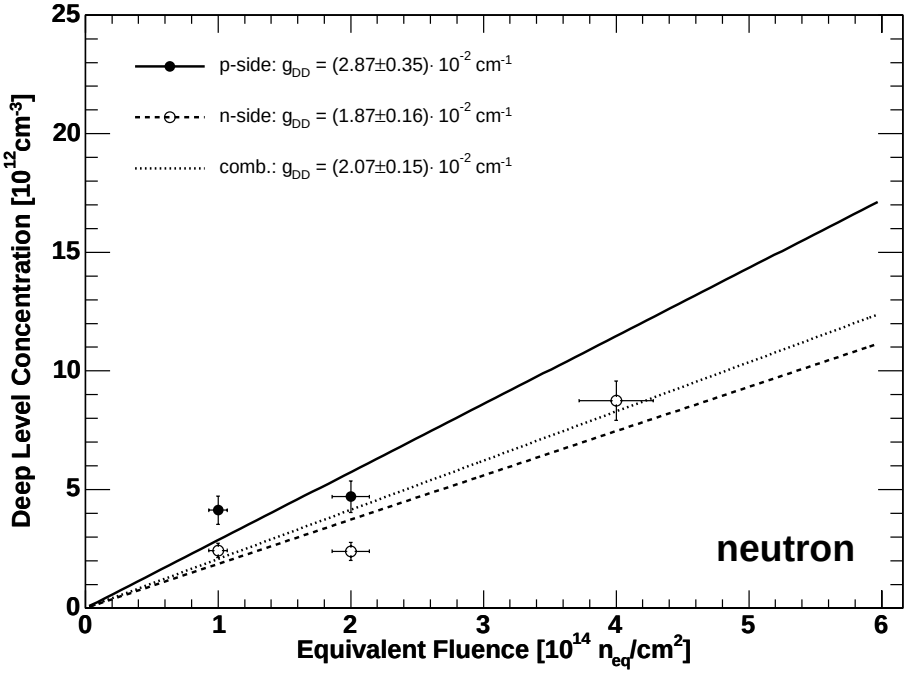

(b) neutron irradiation

Fig. 8.19: Concentration of deep donors vs. equivalent fluence in proton- and neutron-irradiated samples. Values given are averaged for $V_{\mathrm{dep}} + 50\,\mathrm{V} \leq V_{\mathrm{bias}} \leq V_{\mathrm{dep}} + 100\,\mathrm{V}$.

1. N_{DA} saturates at low fluences and thus only a constant concentration is observed at the high fluences considered in this work.

2. Due to systematic errors a systematic variation of N_{DA} with Φ_{eq} cannot be observed. Additionally, N_{DA} is strongly correlated with N_{sh} which gives also a fluence dependent acceptor-like contribution and can therefore "shadow" a variation of N_{DA} with fluence.

The concentration of deep donors N_{DD} shows a linear dependence on equivalent fluences. This behaviour can easily be explained by typical radiation damage mechanisms.
For these reasons the N_{DA} and N_{DD} should not be compared to the concentrations of deep levels as found by other studies. They should be considered as parameters to describe the electric field in irradiated pad detectors with a practical model as it is the scope of this study. The test of the usefulness of this model and its parameters as determined with the methods introduced in this section will be performed later in part IV when it is used to simulate detector signals.

8.3.4 Electric Field in Partially Depleted Sensors

Within this work *underdepletion operation* is defined as operation with a bias voltage which is lower than V_{dep} as determined by CV-measurements.
The analysis of the exponentiated charge collection curves presented in sec. 8.2 have shown that the sensitive volume of the sensor reaches its maximum already for bias voltages below full depletion voltage. This corresponds to a nonzero electric field strength and should therefore also be observable when looking at the deconvoluted electric field strengths. Fig. 8.20 shows plots with the electric fields in sample Q for several bias voltages below and around the depletion voltage (further plots are given in sec. C.2 for sample C).
These plots show for several voltages the electric field vs. the substrate depth as obtained by deconvolution from signals after p- and n-side illumination. The two complementary results (i.e. measured with the same V_{bias}) are always plotted in the same diagram.
The depletion voltage of the sample is 120 V. The plots in Fig. 8.20 show how the regions with non-zero field grow from both sides into the substrate. It is not clear why the depletion zone growing from the n-side (n-depletion-zone) ends abruptly with a quite high field strength. From basic semiconductor physics it is expected that the field drops smoothly to zero with increasing substrate depth. However, the border of the n-depletion-zone is probed with a quite weak signal due to strong trapping of the hole dominated signal. The combination of low drifting charge and low field may lead to an abrupt end of the measured depletion. Thus, it can be considered as a deconvolution artefact. The p-depletion-zone shows in principal the same behaviour but the border of this depletion zone shows a smoother transition to zero field. This observation supports the assumption that

the abrupt end of the measured n-depletion-zone is an deconvolution artefact caused by trapping.

However, the most remarkable observation is that a non-zero electric field reaches throughout the whole detector already at bias voltages being significantly lower than V_{dep} as determined by CV-measurements. For sample Q it can be concluded that it reaches its maximum sensitive volume at $\approx 80\,\mathrm{V}$. This corresponds to $\sqrt{V_{\mathrm{bias}}/V_{\mathrm{dep}}} \approx 0.82$ which can be compared to $\sqrt{V_{\mathrm{fcc}}/V_{\mathrm{dep}}} \approx 0.87$ (see Table 8.4 on p. 121). The same conclusions can be drawn for sample C even if the

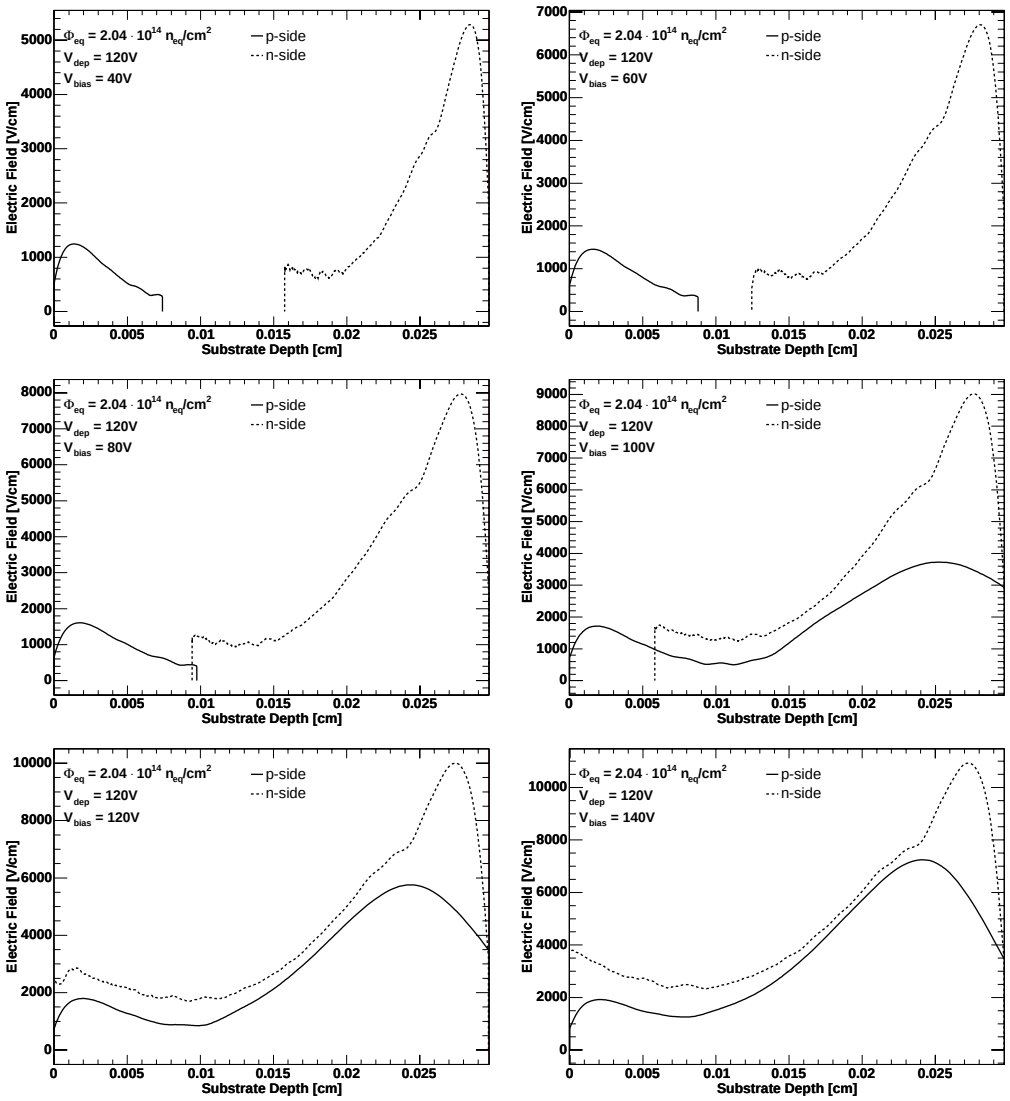

Fig. 8.20: Deconvoluted electric fields for bias voltages below the depletion voltage. Measured on sample Q, $\Phi_{\mathrm{eq}} = 2.04 \cdot 10^{14}\, n_{\mathrm{eq}}/\mathrm{cm}^2$. Solid lines show the result from p-side illumination, dashed lines from n-side illumination.

measurement of the depletion zone in this sample is of worse quality due to large trapping effects.
The observation of nonzero electric field in all of the detector volume in the deconvolution agrees in principle with the determination of V_{fcc} in sec. 8.2. Thus, it can be concluded that the double peak effect which is called *double junction effect* below full-depletion leads to a depletion voltage which is significantly lower than that determined by CV-measurements.

Part IV

Simulation Studies

Chapter 9

Simulation Tools

EFFECTIVE doping concentration, leakage current, trapping times and electric field distributions are key parameters to describe detector performance. Their behaviour is known from measurements in the laboratory. Simulations are done in order to derive predictions for the operation conditions of the ATLAS pixel detector from these laboratory measurements.

In this first chapter of the part on simulation studies the simulation tools are described. Effective doping concentrations and leakage currents are calculated by the same software which is described in sec. 9.2. The second section treats the simulation of charge drift: the important effects of drift, diffusion, trapping, and electric field distribution are included in a second software package. The third section covers the numerical methods which are used to calculate Ramo potentials.

9.1 Software Packages

The calculations necessary for detector simulation studies are performed by three software packages which have been developed within this work: EDCALC[1] for the calculation of effective doping concentration and leakage current after irradiation and annealing. CDCALC[2] calculates the resulting signal currents from the drift of signal charges in the detectors. The third package RACALC[3] is used for numerical calculations of the Ramo potential for different detector geometries.

All packages have been written in C++ on Linux machines. The ROOT package [Bn96] has been used to visualise the results. The software packages are described more detailed in the following sections.

[1] **E**ffective **D**oping **C**oncentration **A**nd **L**eakage **C**urrent
[2] **C**harge **D**rift **CALC**ulation
[3] **RA**mo potential **CALC**ulation

9.2 Effective Doping Concentration & Leakage Current (EDCALC)

9.2.1 Coverage

EDCALC allows prediction calculations of effective doping concentrations and leakage currents and takes into regard annealing of these properties. It consists of three major parts (*history*, *doping concentration calculation*, *leakage current calculation*) which are described in the following sections.

9.2.2 Temperature and Irradiation History

The software allows to define a *history* of the simulated device which has a user-defined number of bins N_{bins}. For every bin b_i the length Δt_i in time (which may vary from bin to bin), the temperature T_i and the fluence $\Phi_{\text{eq},i}$ obtained during the time interval corresponding to b_i is stored. The times at the end of b_i are denoted by t_i. The calculations of N_{eff} and I_{leak} are based on this history.

9.2.3 Doping Concentration

Implementation of Hamburg Model

The part of EDCALC calculating the depletion voltage uses the Hamburg model. It considers DOFZ silicon and uses the formulae and parameters given in sec. 4.2.1. Some additional assumptions are used in order to make the Hamburg model usable for prediction calculations: to establish the Hamburg model samples that received their full fluence within a relatively short time compared to the ATLAS life time were used for investigation. After this "point-irradiation" the annealing behaviour was studied for various temperatures. The situation during ATLAS operation will be different: the radiation load will be accumulated over a long time (10 years) and therefore always a mixture of radiation damages with different ages will exist in the silicon bulk. For the simulation it is assumed that no interaction between these damages exist; ΔN_{eff} is calculated as superposition of a series of single irradiations. Especially, second order reactions are excluded.

Further differences between laboratory studies and operation are the irradiation with a mixture of neutral and charged particles during LHC operation and the variation of temperature.

Analogously to eq. (4.7) for every bin b_i the change of the effective doping concentration

$$\Delta N_{\text{eff},i} = N_{a,i} + N_{c,i} + N_{y,i} \tag{9.1}$$

is calculated.

Beneficial Annealing

The contribution to $N_{a,i}$ from the beneficially annealing part is calculated by

$$N_{a,i} = \sum_{j=1}^{i} \left(\eta_c \, g_{a,p} \Phi_{\mathrm{eq},j} + (1-\eta_c) \, g_{a,n} \Phi_{\mathrm{eq},j}\right) \cdot \exp(-t_{i,j}^{\mathrm{ben}} / \tau_a(20^\circ\mathrm{C})) \, . \tag{9.2}$$

η_c is the charged fraction of the fluence, $t_{i,j}^{\mathrm{ben}}$ is the annealing time between t_i and t_j which is normalised to the equivalent annealing time at 20°C:

$$t_{i,j}^{\mathrm{ben}} = \sum_{j=1}^{i} \Delta t_j \cdot \frac{\tau_a(20^\circ\mathrm{C})}{\tau_a(T_j)} \, . \tag{9.3}$$

$\tau_a(T)$ is the temperature dependent beneficial annealing time constant according to eq. (4.10). Eq. (9.2) also considers different introduction rates $g_{a,p}$ and $g_{a,n}$ for protons and neutrons, respectively.

Stable Acceptor Introduction

The contribution $N_{c,i}$ from stable damage is split into two parts,

$$N_{c,i} = N_{c,i}^{\mathrm{acc}} + N_{c,i}^{\mathrm{don}} \, . \tag{9.4}$$

$N_{c,i}^{\mathrm{acc}}$ is the contribution from stable acceptor introduction, $N_{c,i}^{\mathrm{don}}$ considers donor removal. The introduction of stable acceptors is given by

$$N_{c,i}^{\mathrm{acc}} = \sum_{j=1}^{i} \left(\eta_c \, g_{c,p} \, \Phi_{\mathrm{eq},j} + (1-\eta_c) \, g_{c,n} \, \Phi_{\mathrm{eq},j}\right) \, . \tag{9.5}$$

Again different introduction rates for proton ($g_{c,p}$) and neutron irradiation ($g_{c,n}$) are considered.

Stable Donor Removal

The calculation of the stable donor removal contribution $N_{c,i}^{\mathrm{don}}$ is more complicated since the behaviour for protons and neutrons is different with respect to the removable fraction of donors. Therefore, the initially existing donor concentration, i.e. the initial doping concentration $N_{\mathrm{eff},0}$, is split into two types: type I can be completely removed by protons *and* neutrons. Their concentration is given by

$$N_{c0,\mathrm{I}} = N_{\mathrm{eff},0} \cdot 0.8 \exp(-[O_i]/(4.3 \cdot 10^{17}\,\mathrm{cm}^{-3})) \tag{9.6}$$

(cf. eq. (4.14), p. 50). Type II consists of the remaining donors which can be removed only by protons:

$$N_{c0,\mathrm{II}} = N_{\mathrm{eff},0} - N_{c0,I} \, . \tag{9.7}$$

Consequently, $N_{c,i}^{\mathrm{don}}$ is given by

$$\begin{aligned} N_{c,i}^{\mathrm{don}} &= N_{c0,\mathrm{I}} \cdot \left(1 - \exp\left(-c \cdot \sum_{j=1}^{i} \Phi_{\mathrm{eq},j}\right)\right) \\ &\quad + N_{c0,\mathrm{II}} \cdot \left(1 - \exp\left(-c \cdot \eta_c \sum_{j=1}^{i} \Phi_{\mathrm{eq},j}\right)\right) . \end{aligned} \tag{9.8}$$

It has to be stated that this splitting of the removable donors into two types has no direct experimental proof beyond the fact that neutrons and protons remove different fractions of the initial donor concentration. Therefore, this model does not reflect necessarily the physical reality on a microscopic level. However, it seems to be the most simple model that takes this effect into regard. The modelling of the donor removal has its largest influence on the prediction of N_{eff} after low fluences of mixed (neutral and charged) radiation fields. For high fluence—where the most important predictions for the ATLAS pixel sensor have to be made—the chosen model of donor removal becomes less significant since there all donors will be removed by the protons in any case.

Reverse Annealing

For the calculation of reverse annealing the different behaviour of silicon under proton and neutron irradiation has to be considered, too. The contribution from neutral particles $N_{y,i}^{n}$ to $N_{y,i}$ is calculated by

$$N_{y,i}^{n} = \sum_{j=1}^{i} N_{y0,j}^{n} \cdot \left(1 - \exp(-t_{i,j}^{\mathrm{rev}} / \tau_y(20^\circ\mathrm{C}))\right) \tag{9.9}$$

with amplitude

$$N_{y0,j}^{n} = (1 - \eta_c)\, g_{y,n}\, \Phi_{\mathrm{eq},j} \tag{9.10}$$

using the introduction rate $g_{y,n}$ and the scaled annealing time $t_{i,j}^{\mathrm{rev}}$ which is defined by (cf. eq. (4.23))

$$t_{i,j}^{\mathrm{rev}} = \sum_{j=1}^{i} \Delta t_j \cdot \frac{\tau_y(20^\circ\mathrm{C})}{\tau_y(T_j)} . \tag{9.11}$$

The proton contribution $N_{y,i}^{p}$ has to be calculated in a more difficult way due to its saturation behaviour for the reverse annealing amplitude. The reverse annealing amplitude for the proton fluence obtained during b_j is given by

$$N_{y0,i}^{p} = g_{y,p} \cdot \phi_0 \left[\left(1 - \exp\left(-\sum_{k=1}^{j} \eta_c \Phi_{\mathrm{eq},k}\right)\right) - \left(1 - \exp\left(-\sum_{k=1}^{j-1} \eta_c \Phi_{\mathrm{eq},k}\right)\right)\right] . \tag{9.12}$$

Then the contribution to b_i is given by the sum over all bins up to i:

$$N^p_{y,i} = \sum_{j=1}^{i} N^p_{y0,j} \cdot \left(1 - \exp(-t^{\text{rev}}_{i,j}/\tau_y(20^\circ\text{C}))\right) . \tag{9.13}$$

The annealing time scaling is done in the same fashion as for the neutron contribution.

9.2.4 Leakage Current

For the calculation of the leakage current EDCALC uses eq. (4.35) as starting point since contrary to eq. (4.27) this equation allows time scaling. The current generation density rate G_i (in A/cm^3) is calculated for each bin b_i. Its contribution from the exponential part G_i^{exp} is given by

$$G_i^{\text{exp}} = \sum_{j=1}^{i} \Phi_{\text{eq},j} \cdot \alpha_I \cdot \exp\left(-t^I_{i,j}/\tau_I(20^\circ\text{C})\right) \tag{9.14}$$

and the scaled annealing time $t^I_{i,j}$ is given by

$$t^I_{i,j} = \sum_{j=1}^{i} \Delta t_j \cdot \frac{\tau_I(20^\circ\text{C})}{\tau_I(T_j)} . \tag{9.15}$$

The logarithmic part is considered by

$$G_i^{\log} = \sum_{j=1}^{i} \alpha_0^* - \beta \cdot \ln t^{\log}_{i,j} \tag{9.16}$$

with the scaled annealing time $t^{\log}_{i,j}$ defined by

$$t^{\log}_{i,j} = \sum_{j=1}^{i} \Delta t_j \cdot \Theta(T_j) \tag{9.17}$$

with $\Theta(T_j)$ as defined in eq. (4.34), $T_{\text{ref}} = 21^\circ$C. Fig. 9.1 shows $\alpha(t)$ for several temperatures between -20°C and $+60^\circ$C.
The full leakage current density for a given bin b_i is given by

$$G_i = G_i^{\text{exp}} + G_i^{\log} , \tag{9.18}$$

the leakage current of a simulated device is obtained by multiplying G_i with the *depleted* volume.

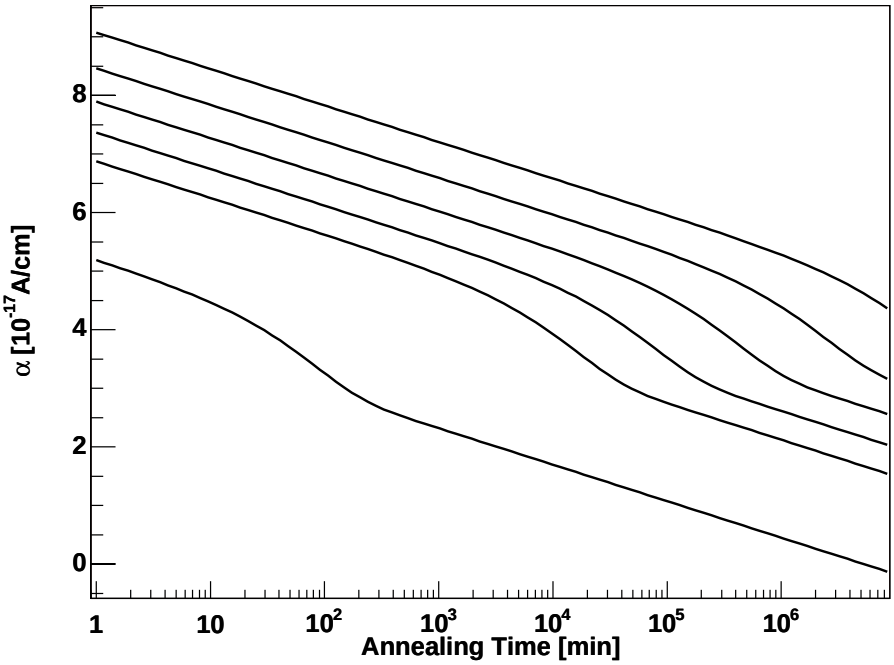

Fig. 9.1: Calculated $\alpha(t)$ for several annealing temperatures (-20°C, -10°C, 0°C, 10°C, 20°C and 60°C from top to bottom).

9.3 Charge Collection (CDCALC)

9.3.1 Coverage

The software package CDCALC calculates the drift of free charge-carriers. It includes routines for the following physical items: charge deposition, charge drift, diffusion, trapping and electric field distribution. Routines to calculate the Ramo potential for a given detector configuration are not included in CDCALC: this calculation is done in a separate software package due to its complexity and time consumption even on fast computers (see sec. 9.4). The numerical results for the Ramo potential from this programme are put into the drift simulations in the form of a look-up table.

9.3.2 Basic Structure

CDCALC simulates the one-dimensional drift of charge-carriers along the x-axis. The thickness d of the simulated device is divided in N_x bins, their number is chosen by the user. Every bin represents a layer of thickness $\Delta x = d/N_x$ of the simulated device. The time steps are given by $\Delta t = 0.025$ ns. At the beginning of the simulation charge is "injected" by assigning the charge q_i to bin i. The p-side has index $i = 0$, the n-side is set at $i = N_x - 1$ (analogously to the convention $x = 0$ for p-side as it has been used throughout this thesis).

In the next step the movement of the charge from every bin is calculated until it reaches its target electrode. The influenced signal current is calculated and stored for every time step.

9.3.3 Charge Deposition

For the charge deposition several profiles can be used. The most important profiles for application in the simulation studies presented in this thesis are the *laser-like* and the *mip-like* charge deposition profile. In every bin always equal amounts of negative and positive charges are deposited.
Using the laser-like charge deposition profile the charge deposited in the interval $[x_1, x_2]$ is

$$q = Q_0 \int_{x_1}^{x_2} e^{-\mu x}\, dx\,. \tag{9.19}$$

Thus the bins are filled with charge according to

$$q_i = \left(e^{-\mu\, i\Delta x} - e^{-\mu\,(i+1)\Delta x}\right) \tag{9.20}$$

for p-side illumination and

$$q_i = \left(e^{-\mu(d-(i+1)\Delta x)} - e^{-\mu(d-i\Delta x)}\right) \tag{9.21}$$

for n-side illumination. $1/\mu$ is the absorption length of the chosen laser wave length (cf. eq. (3.1) and Table 3.1). If not chosen different the normalisation of the charge is 1 as long as the absorption length is much shorter than the device thickness.
For simulation of mips every bin is filled with the same amount of charge

$$q_i = \frac{Q_0}{N_x}\,. \tag{9.22}$$

9.3.4 Charge Drift/Mobility Parameterisation

Charge drift is simulated by calculating the position x_{j+1} of the charge-carrier from its previous position x_j for every time step j:

$$x_{j+1} = x_j + v_{\mathrm{dr},j} \cdot \Delta t\,. \tag{9.23}$$

$v_{\mathrm{dr},j}$ is the field strength dependent drift velocity,

$$v_{\mathrm{dr},j} = v_{\mathrm{dr}}(E_j) \tag{9.24}$$

with E_j being the field strength at position x_j. The drift of every charge q_i is calculated until it reaches its target electrode.
For parameterisation of drift velocities the formulae given in [Se90] are used. This paper summarises the development of the mobility model used for MINIMOS,

which is a software for the two-dimensional simulation of miniaturised MOS devices. Further references regarding the parameterisations can be found in that paper. For this work the functions and parameter sets developed for version MINIMOS 4 are used.
Drift velocity v_{dr} is the product of mobility μ and electric field E:

$$v_{\mathrm{dr}} = \mu \cdot E \,. \tag{9.25}$$

The description of mobility considers several effects. The first one, *lattice scattering*, is modeled by a simple power law:

$$\mu_e^L = 1430\,\mathrm{cm}^2/\,\mathrm{V\,s} \cdot \left(\frac{T}{300\,\mathrm{K}}\right)^{-2} , \tag{9.26}$$

$$\mu_h^L = 460\,\mathrm{cm}^2/\,\mathrm{V\,s} \cdot \left(\frac{T}{300\,\mathrm{K}}\right)^{-2.18} . \tag{9.27}$$

Ionised impurity scattering is modeled by the expression

$$\mu_{e,h}^{LI} = \mu_{e,h}^{\min} + \frac{\mu_{e,h}^L - \mu_{e,h}^{\min}}{1 + (N_{\mathrm{eff}}/N_{e,h}^{\mathrm{ref}})^{\alpha_{e,h}}} \quad \text{with} \tag{9.28}$$

$$\mu_e^{\min} = 80\,\mathrm{cm}^2/\,\mathrm{V\,s} \cdot \left(\frac{T}{300\,\mathrm{K}}\right)^{-0.45} \quad \text{for} \quad T \geq 200\,\mathrm{K}\,, \tag{9.29}$$

$$\mu_h^{\min} = 45\,\mathrm{cm}^2/\,\mathrm{V\,s} \cdot \left(\frac{T}{300\,\mathrm{K}}\right)^{-0.45} \quad \text{for} \quad T \geq 200\,\mathrm{K}\,, \tag{9.30}$$

$$N_e^{\mathrm{ref}} = 1.21 \cdot 10^{17}\,\mathrm{cm}^{-3} \cdot \left(\frac{T}{300\,\mathrm{K}}\right)^{3.2} , \tag{9.31}$$

$$N_h^{\mathrm{ref}} = 2.23 \cdot 10^{17}\,\mathrm{cm}^{-3} \cdot \left(\frac{T}{300\,\mathrm{K}}\right)^{3.2} \text{ and} \tag{9.32}$$

$$\alpha_{e,h} = 0.72 \cdot \left(\frac{T}{300\,\mathrm{K}}\right)^{0.065} . \tag{9.33}$$

The third effect is the *velocity saturation* being described by

$$\mu_e^{LIF} = (2 \cdot \mu_e^{LI}) \Bigg/ 1 + \sqrt{1 + \left(\frac{2 \cdot \mu_e^{LI} \cdot E}{v_e^{\mathrm{sat}}}\right)^2} \quad \text{and} \tag{9.34}$$

$$\mu_h^{LIF} = \mu_e^{LI} \Bigg/ \left(1 + \frac{\mu_h^{LI} \cdot E}{v_h^{\mathrm{sat}}}\right) . \tag{9.35}$$

The saturation velocities $v_{e,h}^{\mathrm{sat}}$ are

$$v_e^{\mathrm{sat}} = 1.45 \cdot 10^7\,\mathrm{cm/s} \cdot \sqrt{\tanh \frac{155\,\mathrm{K}}{T}} \quad \text{and} \tag{9.36}$$

$$v_h^{\mathrm{sat}} = 9.05 \cdot 10^6\,\mathrm{cm/s} \cdot \sqrt{\tanh \frac{312\,\mathrm{K}}{T}} \,. \tag{9.37}$$

Fig. 9.2 shows a plot of drift velocities calculated with these formulae for different temperatures. The influence of different effective doping concentrations (ionised impurity scattering) is negligible. Therefore, an averaged value of $N_{\text{eff}} = 2 \cdot 10^{12}\,\text{cm}^{-3}$ (corresponding to $\Phi_{\text{eq}} \approx 5 \cdot 10^{14}\, n_{\text{eq}}/\,\text{cm}^2$) is used for simulations of all devices.

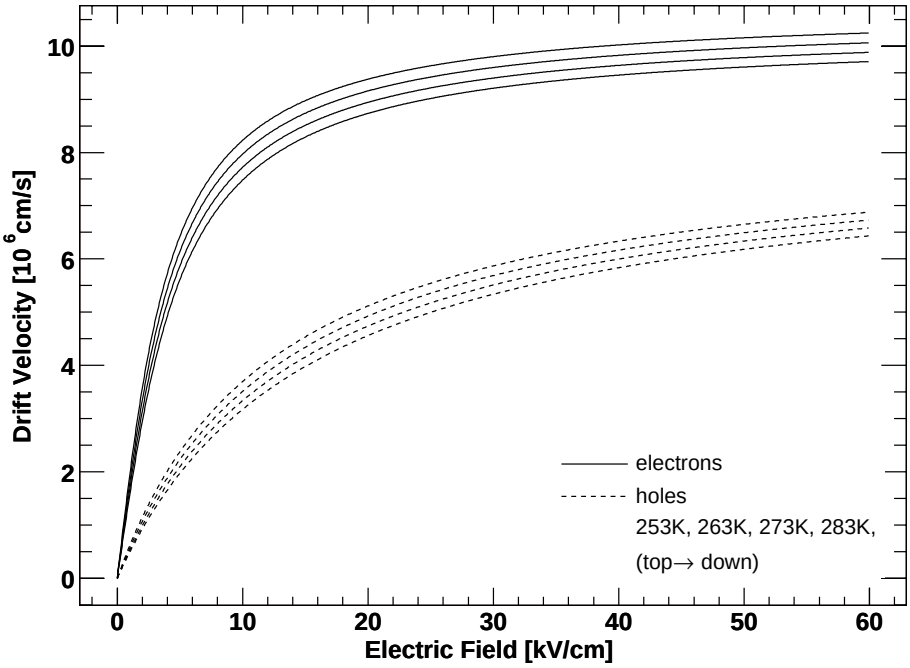

Fig. 9.2: Drift velocities of holes and electrons at different temperatures (from top to down with increasing temperature). The data are computed with the parameterisation from [Se90].

9.3.5 Diffusion

Diffusion is considered by inserting a further component $x_{\text{diff},j}$ into eq. (9.23):

$$x_{j+1} = x_j + v_{\text{dr},i} \cdot \Delta t + x_{\text{diff},j}\,. \tag{9.38}$$

$x_{\text{diff},j}$ is randomly distributed following a gaussian distribution with

$$\sigma = \sqrt{2D_{e,h} \cdot \Delta t}\,. \tag{9.39}$$

The random numbers for every step are calculated by the pseudo-random number generator which is included in ROOT.
$D_{e,h}$ are the diffusion constants for electrons and holes according to eq. (3.26) [Lu99]. In order to obtain more realistic results the charges q_i are divided in

N_q smaller charges q_i/N_q which drift separately towards the target electrode and thereby have different drift paths $\{x_j\}$. For useful results N_q should be $\approx$ 15–20.

9.3.6 Electric Field

The electric field in unirradiated detectors is given by eq. (3.53). Eq. (4.5) is used as linear approximation of the field in low irradiated detectors.
CDCALC also contains a routine to calculate the influence of charged deep levels with the model already described in sec. 4.2.4, p. 55. This model has also been used for the determination of deep level concentrations in sec. 8.3.3. As values for N_{DA} and g_{DD} the p-side results from Tables 8.5 and 8.6 are used. The p-side results have been chosen since the simulation reproduces the measured signal shapes better when using this parameter set. This better quality of the p-side data is probably caused by the better quality of measured signal shapes due to less trapping.
The calculation of the electric field considering deep levels starts with the linear description from eq. (4.5). With this approximation the drift velocities, carrier densities, filling factors and charged fractions of deep levels are calculated for every bin.
From the concentrations of charged deep levels and shallow states a new approximation of the electric field is calculated by using Gauss' law. In an iterative procedure the routine can be started several times, in each step using the output for the electric field from the previous iteration. This procedure converges within 10–15 iterations to a stable result. At low bias voltages ($\approx 50\,\mathrm{V}$ above V_{dep} and lower) problems with convergence occur since the field strength in the minimum is quite low leading to overestimated carrier concentrations. This problem can be fixed by starting the first iteration with V_{bias} set to 105 V above the desired value and then reducing it by 7 V in every iteration step until the desired V_{bias} is reached after 15 iteration steps. The final result reproduces much better the measured result. Its stability is proven by five further iterations with unaltered bias voltage.
Additionally the convergence is improved by setting the minimum field strength to 100 V/cm which is quite low compared to typical field strengths in biased sensors but limits the concentrations of free charge-carriers.

9.3.7 Charge Trapping

Charge trapping is considered by reducing the charge q_i exponentially with every timestep:

$$q_{i,j} = q_{i,0} \exp(-j\,\Delta t/\tau_{e,h}) \tag{9.40}$$

with $q_{i,0}$ being the initially deposited charge q_i.
Alternatively, the charge trapping could be simulated by calculating the trapping probability with the deep level concentrations N_{DA} and N_{DD} and the properties

of the assumed deep levels. However, as stated above the parameters obtained for the deep level model cannot be considered to describe the crystal correctly on a microscopic level. Therefore, the use of effective trapping times is preferred. This has the additional advantage that these effective trapping times have been directly measured and that the simulation works faster with this simpler model what is important for larger simulation studies.
The disadvantage is a non-realistic description especially in low-field regions where in real sensors trapping is reduced due to filled traps as discussed in sec. 8.2.1.

9.3.8 Influenced Signal

Every movement of a charge q_i contributes to the signal current at time $t_j = j \cdot \Delta t$ by adding a component

$$q_{i,j} \cdot (v_{\mathrm{dr},j}\, \Delta t + x_{\mathrm{diff}}) \cdot E_R \tag{9.41}$$

to the current. E_R is the respective Ramo field of the simulated device. For the simulation of pad-detectors it is simply

$$E_R = \frac{1}{d}\,. \tag{9.42}$$

For more complicated detector geometries E_R is calculated numerically (see sec. 9.4). The result is integrated into the charge drift routine as a look-up table giving E_R for discrete values of x. The Ramo potential at the position x_j is found by interpolation of this look-up table.

9.4 Ramo-Potential (RACALC)

9.4.1 Numerical Solution for Potentials

Except for some simple cases like a pad-detector with infinite plates the Ramo potential cannot be given analytically in a simple way. Thus a numerical method has been chosen for its calculation.
The Ramo potential $\Phi_R = \Phi_R(x, y)$ is calculated on a lattice $\{x_i, y_j\}$ with $x_i = i \cdot a$, $1 \le i \le n_x$ and $y_j = j \cdot a$, $1 \le j \le n_y$. The device layout is assumed to be independent from z, i.e. for example a strip detector with infinite long strips. For the Laplacian the second derivatives are needed. The first and second partial derivatives with respect to x can be expressed as

$$\partial_x \Phi_R(x,y) = \frac{\Phi_R(x-\frac{a}{2},y) - \Phi_R(x+\frac{a}{2},y)}{a} \qquad \text{and} \tag{9.43}$$

$$\begin{aligned} \partial_x^2 \Phi_R(x,y) &= \frac{\partial_x \Phi_R(x-\frac{a}{2},y) - \partial_x \Phi_R(x+\frac{a}{2},y)}{a} \\ &= \frac{\Phi_R(x-a,y) + \Phi_R(x+a,y) - 2\Phi_R(x,y)}{a^2}\,. \end{aligned} \tag{9.44}$$

Analogously, the second partial derivative with respect to y is

$$\partial_y^2 \Phi_R(x,y) = \frac{\Phi_R(x,y-a) + \Phi_R(x,y+a) - 2\Phi_R(x,y)}{a^2} \tag{9.45}$$

Within the considered volume Φ_R has to fulfill $\Delta\Phi_R = 0$. According to

$$\Phi_R(x,y) \to \Phi_R(x_i,y_j) =: \Phi_{ij} \tag{9.46}$$

and the eqs. (9.44) and (9.45) it follows

$$\begin{aligned} \Delta\Phi_{ij} &= \partial_x^2\Phi_{ij} + \partial_y^2\Phi_{ij} \\ &= \tfrac{1}{a^2}\left(\Phi_{i-1,j} - 2\Phi_{ij} + \Phi_{i+1,j} + \Phi_{i,j-1} - 2\Phi_{ij} + \Phi_{i,j+1}\right) . \end{aligned} \tag{9.47}$$

This equations are completed by the boundary conditions. In y-direction a periodic boundary condition is chosen:

$$\Phi_R(x_i,y_1) = \Phi_R(x_i,y_{n_y}) \Leftrightarrow \Phi_{i,1} = \Phi_{i,n_y} . \tag{9.48}$$

The boundary condition in x-direction is chosen according to the considered problem, $\Phi_R(1,y_j)$ and $\Phi_R(x_{n_x},y_j)$ are either 0 or 1 (0 for a noncollecting electrode, 1 for a collecting electrode). For instance, a pad-detector with read-out on p-side has $\Phi_{1,y_j} = 1$ and $\Phi_{n_x,y_j} = 0$.
This system of linear equations is brought into matrix form and the result for Φ_{ij} is found with the Gauss algorithm. The software implementation of this algorithm is taken from [Lo03]. The solution is even on fast computers quite time consuming due to the large numbers of equations, e.g. a lattice with 51 by 71 points has 3 621 lattice points and consequently the same number of equations. This requires solving an $3\,621 \times 3\,621$ matrix.

9.4.2 Pad-Detector

For a pad-detector the boundary condition is given by

$$\begin{aligned} \Phi_{1,y_j} &= 1 \quad \text{(p-side, read-out)} \\ \Phi_{n_x,y_j} &= 0 \quad \text{(n-side)} \end{aligned} \tag{9.49}$$

This is a quite simple case which can also be solved easily analytically and henceforth, it can be used to check the numerical algorithm. The solution for a pad-detector with thickness d and infinite extension in y- and z-direction is

$$\Phi_R(x,y) = -\frac{x}{d} \quad \Rightarrow \quad E_R = -\partial_x\Phi_R = \frac{1}{d} . \tag{9.50}$$

Fig. 9.3 shows the numerical solution for a pad-detector with a thickness of 250 μm calculated on a 21×105 lattice. Derivation of the potential w.r.t. x yields the expected result.

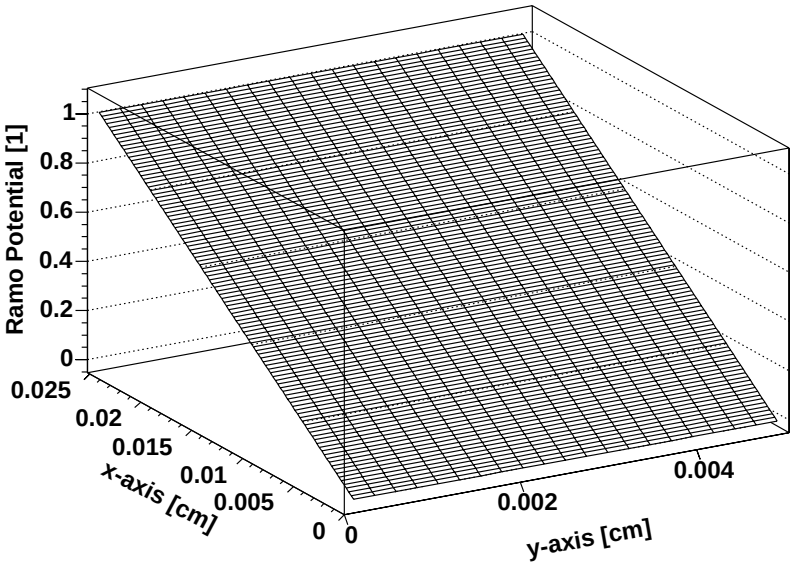

Fig. 9.3: Numerical solution for the Ramo potential of a pad-detector with thickness $d = 250\,\mu$m calculated on a 21×105 lattice.

9.4.3 Infinite Strip Detector

Fig. 9.4 shows the result for a strip detector which is assumed to have infinite long strips. This model will also be used as approximation for the pixel detector. The implantation of the read-out pixel has potential 1, the potential of three neighbouring pixels to each side is set to zero. Fig. 9.4 shows the numerical result for the Ramo potential, Fig. 9.5 shows the x- and y-components of the Ramo field ($E_{R,x} = -\frac{\partial}{\partial x}\Phi_R$ and $E_{R,y} = -\frac{\partial}{\partial y}\Phi_R$, respectively). Contrary to the pad-detector, where the Ramo field is constant for any x, the Ramo field of the strip-detector shows a significant inhomogeneity. Fig. 9.6 shows for better visibility projections of Fig. 9.5(a) for the region $y_c \leq y \leq y_c + 50\,\mu$m where y_c is the centre of read out strip.
The legend of this figure also shows the deviation of the integral

$$S = \int_0^d E_R(x)\,dx \tag{9.51}$$

from one or zero. This integral is calculated on an integration path being parallel to the x-axis from n-side towards p-side and yields the potential difference with respect to the n-side. In the ideal case this potential difference is either one if the integration path ends on the n^+ implantation or zero otherwise. The deviation is a measure for the accuracy of the simulation, e.g. $S < 1$ for an integration path ending on the implantation would look like a charge loss, $S > 1$ would give a

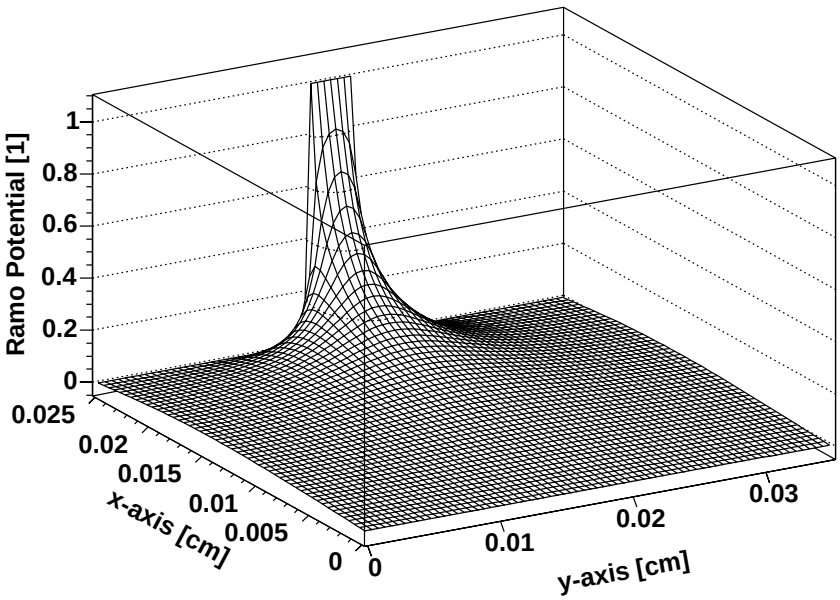

Fig. 9.4: Numerical solution for the Ramo potential of an infinite strip-detector with thickness $d = 250\,\mu$m, pitch $50\,\mu$m and an implantation width of $30\,\mu$m. The sensor has been simulated with an extension in y covering seven strips on a 51×71 lattice.

charge gain what is physically impossible. The deviation is in all cases $< 5 \cdot 10^{-9}$ which is considered as being sufficient since the charge losses due to trapping in the simulated fluence range will be much larger.
As can be seen on the plot, the charge drift is almost equally weighted throughout most of the bulk like in a pad-detector, but with a much smaller weight than in the latter one. However, close to the pixel implantations the strength of the Ramo field increases strongly. Therefore, the last part of the drift path of electrons (in the case of an n-on-n detector) contributes most to the signal while holes contribute only little since most of them do not even enter the highly weighted area.
The numerical results for $E_{R,x}$ is inserted into CDCALC as a look-up table for drift simulations.

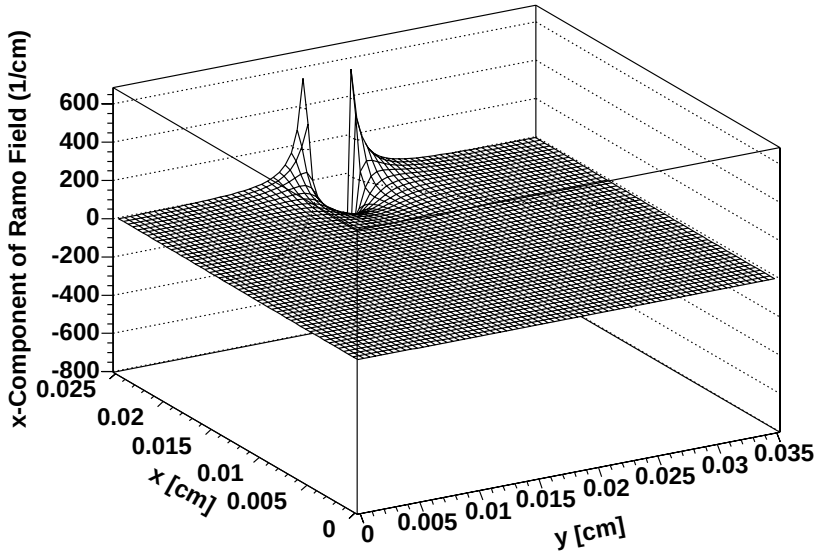

(a) x-component of Ramo field

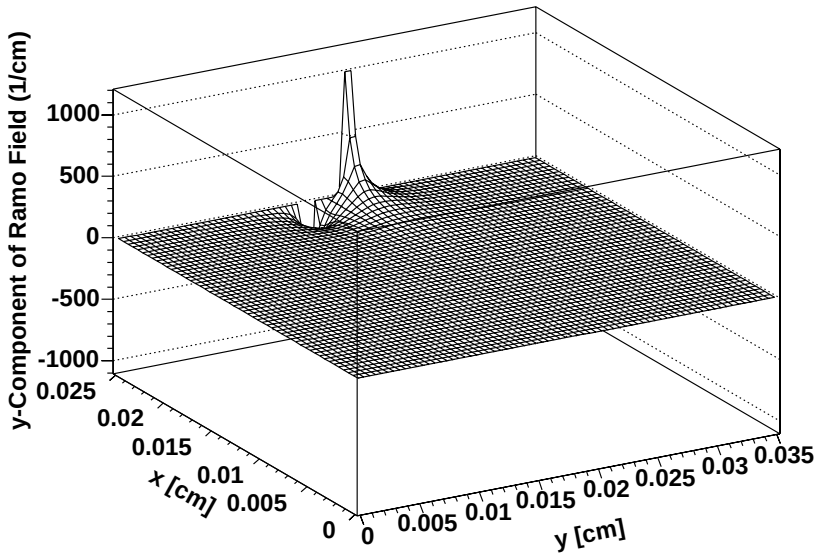

(b) y-component of Ramo field

Fig. 9.5: x- and y-components of Ramo field. The Ramo field is obtained from the potential shown in Fig. 9.4 by derivation.

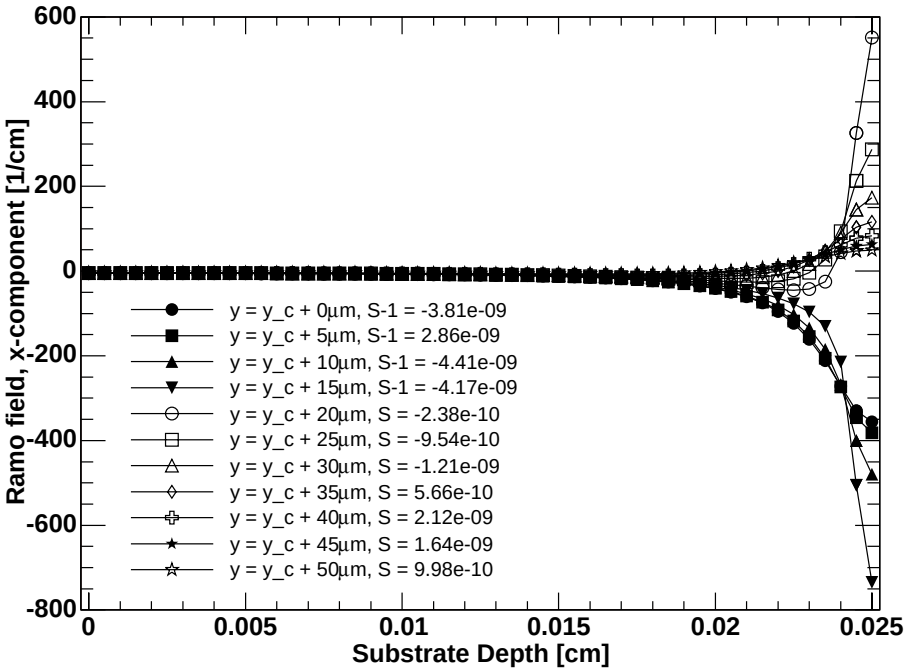

Fig. 9.6: x-component of Ramo field under the implantation. Projections of 3D plot shown in Fig. 9.5(a).

Chapter 10

Simulations of Pad-Detectors

THE simulation tools presented in the previous chapter are now applied. In this chapter simulation results are compared to the measurements done with pad-detectors that have been presented in part III of this thesis. The intention of this comparison is the verification of the developed simulation tools before these are used to make predictions for the operation of pixel sensors in the ATLAS experiment.

10.1 Depletion Voltages

In order to calculate the depletion voltages after the irradiation of test samples the following typical scenario is used:

Step	Measure	Temperature	Duration
1.	irradiation	28°C	up to 7d
2.	storage	-18°C	up to 7d
3.	shipping	20°C	3d
4.	annealing	60°C	1d

In the calculation proton irradiation is done with a flux of $2.41 \cdot 10^{13}\, n_{\mathrm{eq}}/(\mathrm{cm}^2 \cdot \mathrm{h})$. This value is found as the average over all irradiated samples. This number is used to calculate the necessary duration of irradiation in order take into account the annealing during irradiation. The difference of irradiation duration to 7 d is assumed as storage time in a refrigerator.
After irradiation and storage the samples had to be shipped. It is assumed that the shipment took three days at 20°C. After shipment the samples were annealed at 60°C. As an example Fig. 10.1 shows the simulated evolution of depletion voltage for sample C with $\Phi_{\mathrm{eq}} = 5.0 \cdot 10^{14}\, n_{\mathrm{eq}}/\mathrm{cm}^2$. The rapid increase of V_{dep} during irradiation is visible and is followed by an (almost) constant part corresponding to the cold storage. This is followed by a decrease of V_{dep} during shipment. This decrease is accelerated during the first part of accelerated annealing, reaches a minimum and increases finally due to reverse annealing.

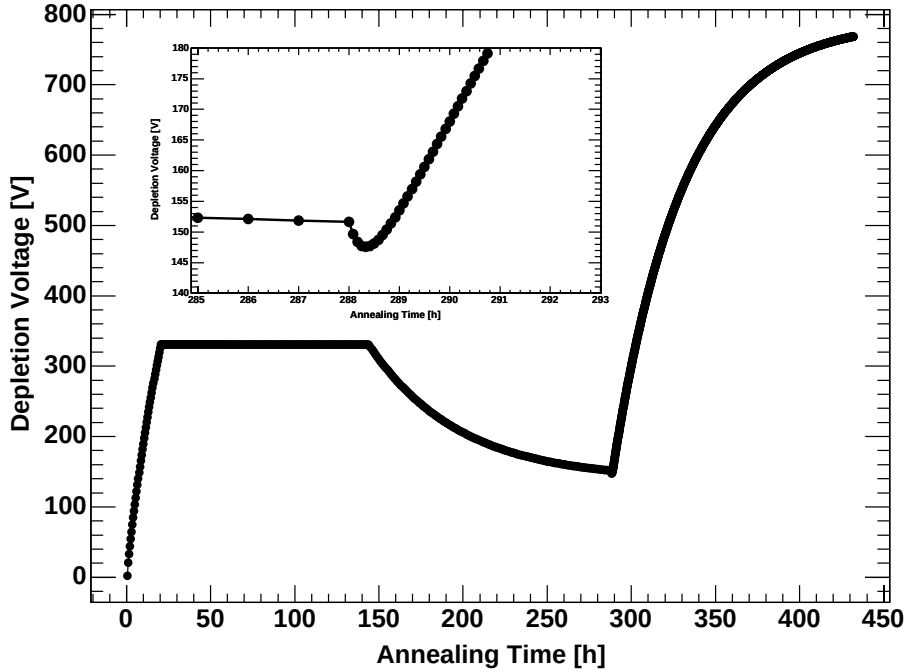

Fig. 10.1: Simulated evolution of depletion voltage during irradiation and accelerated annealing, $\Phi_{\mathrm{eq}} = 5 \cdot 10^{14}\, n_{\mathrm{eq}}/\mathrm{cm}^2$ (sample C). The inset shows a magnification of the accelerated annealing around the minimum in V_{dep} ($285\,\mathrm{min} \leq t_a \leq 293\,\mathrm{min}$).

For every simulated sample the minimum in V_{dep} during accelerated annealing is taken (see inset in Fig. 10.1) and plotted vs. the equivalent fluence, see Fig. 10.2(a). This plot also contains the depletion voltages taken from CV-measurements from the real samples (see sec. 7.3, Table 7.2). In Fig. 10.2(b) a comparison between simulated and measured effective doping concentration (also Table 7.2) is shown. The deviation of the simulated V_{dep} from the measured ones is in all but one cases less than 50 V even at high fluences. Taking into regard the strong material dependence of the damage parameters in the Hamburg model the simulation reproduces the irradiation results sufficiently well.

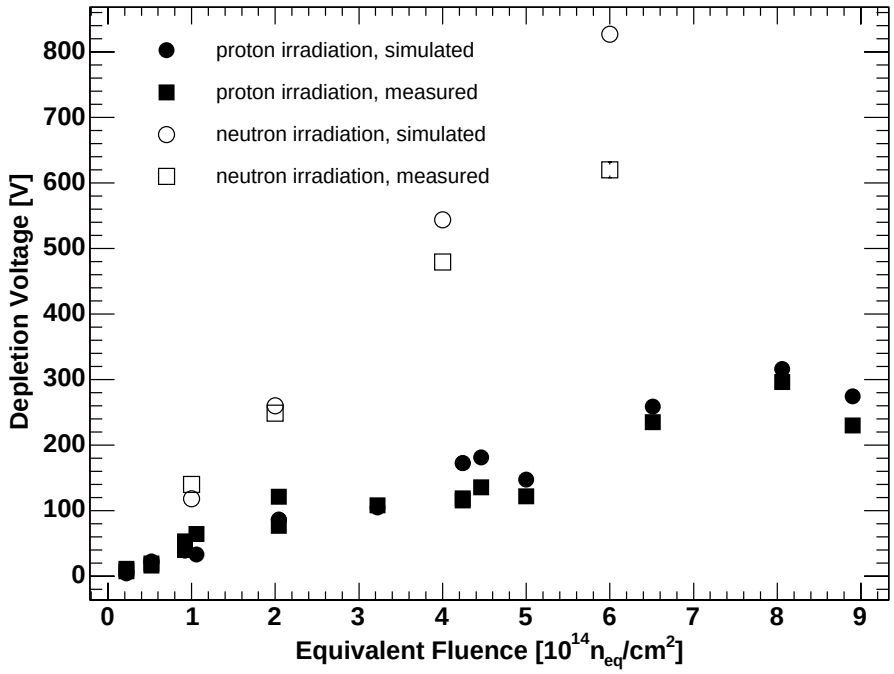

(a) Depletion voltage

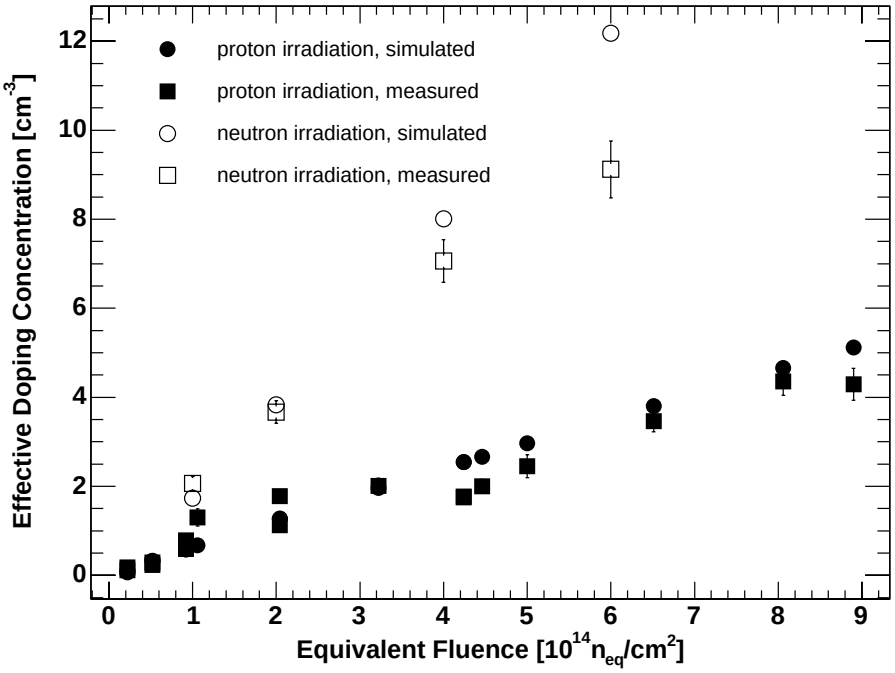

(b) Effective doping concentration

Fig. 10.2: Calculated and measured (a) depletion voltages and (b) effective doping concentrations for proton- and neutron-irradiated samples of various thicknesses.

10.2 Pulse Shapes

10.2.1 Principle

In this section simulated and measured pulse shapes are compared. For these comparisons measurements taken on samples P, D, Q, A, E and C for proton-irradiation and samples R,V and T for neutron-irradiation are used. All included measurements have been made with a red laser ($\mu = 3.6\,\mu$m) and corrected for limited bandwidth before plotting. Finally, they are shifted along the time-axis so that the inflection point of the leading edges is at $t = 4$ ns.
The simulated devices have the same fluence, thickness and temperature as the corresponding measured devices. The starting time of drift is set to $t = 4$ ns. Diffusion is considered by splitting the charge in every bin into 20 portions. Charge trapping is simulated by using the parameters for trapping times given in eqs. (8.10)-(8.13). After charge drift calculation the signal is smeared by folding it with a gaussian, $\sigma = 0.4$ ns. This is done in order to consider the pulse width of the laser (≈ 50 ps) and additional signal distortion caused by the read-out electronics that is not compensated by the bandwidth correction of the measured signals. The value for σ has been determined by requiring the same slope of trailing edges for measurement and simulation. Finally, the areas under the measured and simulated signals are normalised to one.

10.2.2 Linear Field

Fig. 10.3 shows simulated pulse shapes for various fluences with $V_{\mathrm{bias}} = V_{\mathrm{dep}} + 100$ V. For these simulations the electric fields have been calculated using eq. (4.5) with a linear dependence of the electric field on x. For comparison the corresponding measured pulse shapes are plotted in Fig. 10.3 as well. Contrary to the measured pulses the simulated ones show no double peak structure. In the electron signals the slopes of the pulse tops change from positive to negative sign with increasing fluence what is caused by increasing trapping. A striking difference between measurement and simulation is the shorter charge collection time of the simulated pulses.
From comparison of simulation and measurement it can be concluded that a linear description of the electric field does not describe the measured pulse shapes well. Therefore, in the following simulations the more elaborated model which takes into account also occupied deep levels is used.

10.2.3 Deep Level Model

Electric Field

The parameterisation for the electric field which is based on the deep level model is now checked considering several aspects. The first aspect is the fluence (and particle) dependence of the field configuration. Fig. 10.4 shows calculated electric

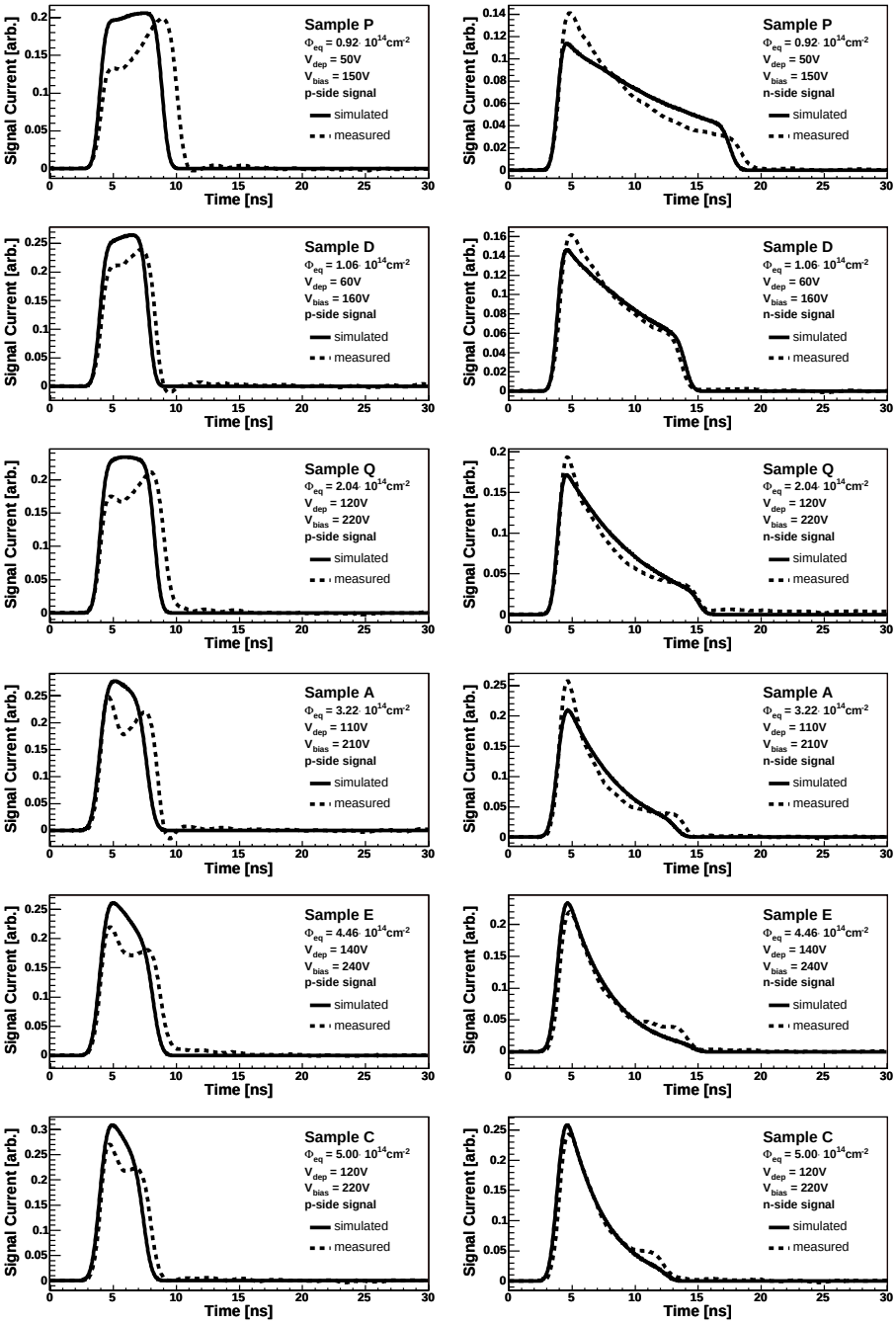

Fig. 10.3: Comparisons of simulated and measured pulse shapes with $V_{\rm bias} = V_{\rm dep} + 100\,{\rm V}$. Proton fluence increases from top to bottom, left-handside p-side illumination, right-handside n-side illumination with red laser. Eq. (4.5) (linear x-dependence) has been used for the electric field. Temperature is 0°C.

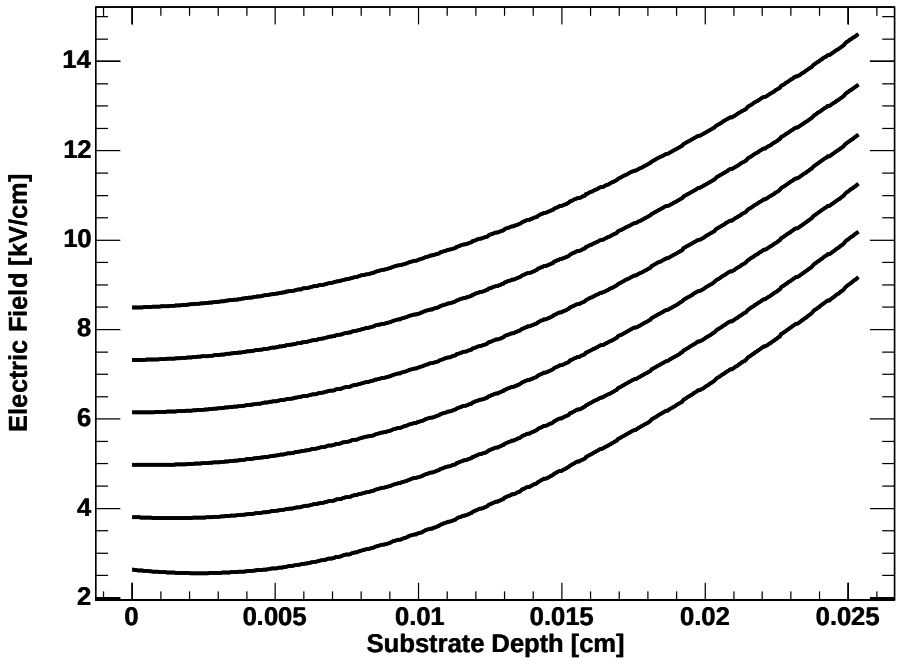

(a) Sample D

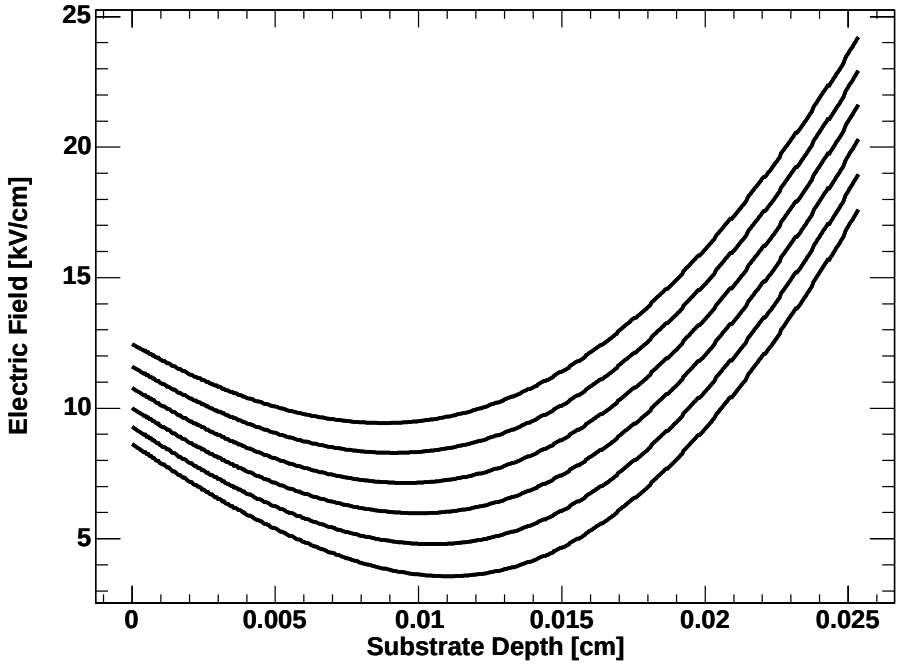

(b) Sample C

Fig. 10.4: Electric fields calculated with deep level model for samples D and C. The lowest lines refer to $V_{\text{bias}} = V_{\text{dep}} + 50\,\text{V}$, the uppermost to $V_{\text{bias}} = V_{\text{dep}} + 200\,\text{V}$, the steps are equidistant (30 V). Temperature is 0°C.

fields for two devices with different fluences (corresponding to sample D, $\Phi_{\mathrm{eq}} = 1.06 \cdot 10^{14}\ n_{\mathrm{eq}}/\mathrm{cm}^2$ and sample C, $\Phi_{\mathrm{eq}} = 5.00 \cdot 10^{14}\ n_{\mathrm{eq}}/\mathrm{cm}^2$) at bias voltages varied in the range $V_{\mathrm{dep}} + 50\,\mathrm{V} \leq V_{\mathrm{bias}} \leq V_{\mathrm{dep}} + 200\,\mathrm{V}$ with equidistant steps of 30 V. As can be seen in the plots the double peak structure with its two maxima at the p- and n-side becomes more pronounced with increasing fluence. With increasing bias voltage the minimum of electric field strength becomes less pronounced; in the simulated sample with the lower fluence the double peak structure even vanishes. The maximum field strength is still at the n-side like in the linear model. Therefore, the largest differences between the two models are situated towards the p-side. This will be of importance later.

Dependence on Bias Voltage

Firstly, the agreement between simulated and measured pulse-shapes is tested for bias voltages being at least 50 V above V_{dep}. The more complicated case of lower bias voltages is discussed after that.
Fig. 10.5, 10.6 and 10.7 show pulse shapes for several proton fluences. They have been measured or simulated with V_{bias} set to 50 V, 100 V and 150 V above depletion voltage, respectively. Fig. 10.8 and 10.9 show the corresponding plots for neutron-irradiated samples. All measurements and simulations have been done for a sensor temperature of 0°C.
By comparing the results for 100 V overdepletion in Fig. 10.3 (linear field) with Fig. 10.6 (deep level model) it is clearly visible that the deep level model is in better agreement with the measurements; especially in p-side signals the double peak structure is better reproduced. For n-side signals the difference is less significant. Generally, the agreement between measurement and simulation is better for n-side signals and the difference between using the linear or deep level model for the electric field is also smaller in these hole-dominated signals. This can be explained by the following reasoning: in the minimum of electric field strength the simulation overestimates charge-trapping since the simulation works with effective trapping times which are the same for the whole bulk. Thus, it is not taken into account that the traps are occupied with a higher probability in the low field region. A further important point is that the minimum of $E(x)$ is closer to the p-side and the maximum of field strength is at the n-side. After p-side illumination the electrons drift slowly through the low-field strength region and suffer there an overestimated trapping. After passage through the minimum they enter the high-field region and induce the major part of their signal *after* they have been impaired by trapping. For hole-drift after n-side illumination the situation is vice-versa: they start in the high-field region and induce the major part of their signal *before* reaching the low-field region. Since they move more slowly than the electrons they suffer more trapping before they reach the critical zone. Therefore, their signal is less sensitive to the field and occupation probabilities of traps in the fraction of their drift-path that is closer to the p-side.
For the simulation of ATLAS sensors it will be important to be able to simulate

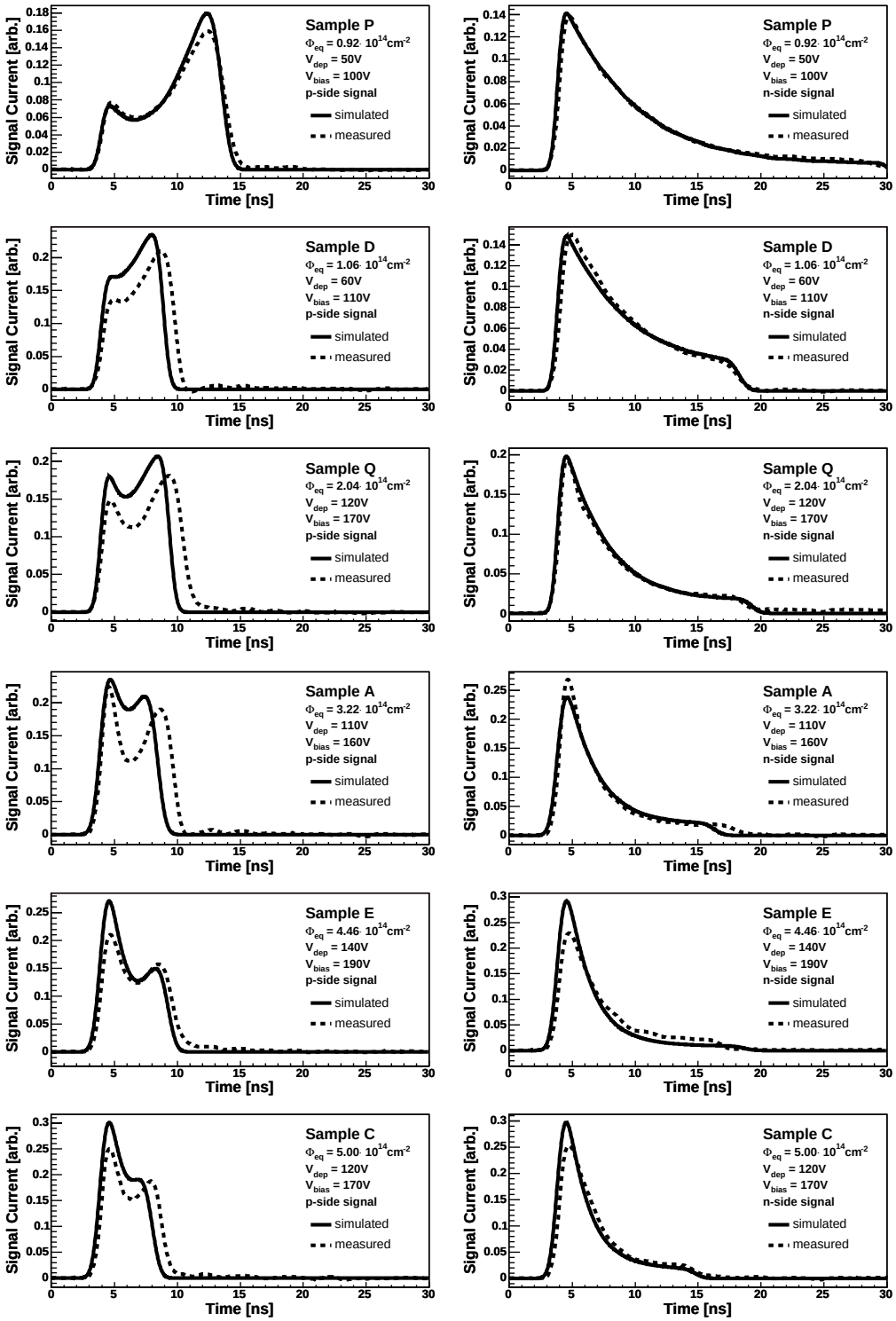

Fig. 10.5: Comparisons of simulated and measured pulse shapes with $V_{\mathrm{bias}} = V_{\mathrm{dep}} + 50\,\mathrm{V}$. Proton fluence increases from top to bottom, left-handside p-side illumination, right-handside n-side illumination. Electric field is parameterised based on deep level model, temperature is 0° C.

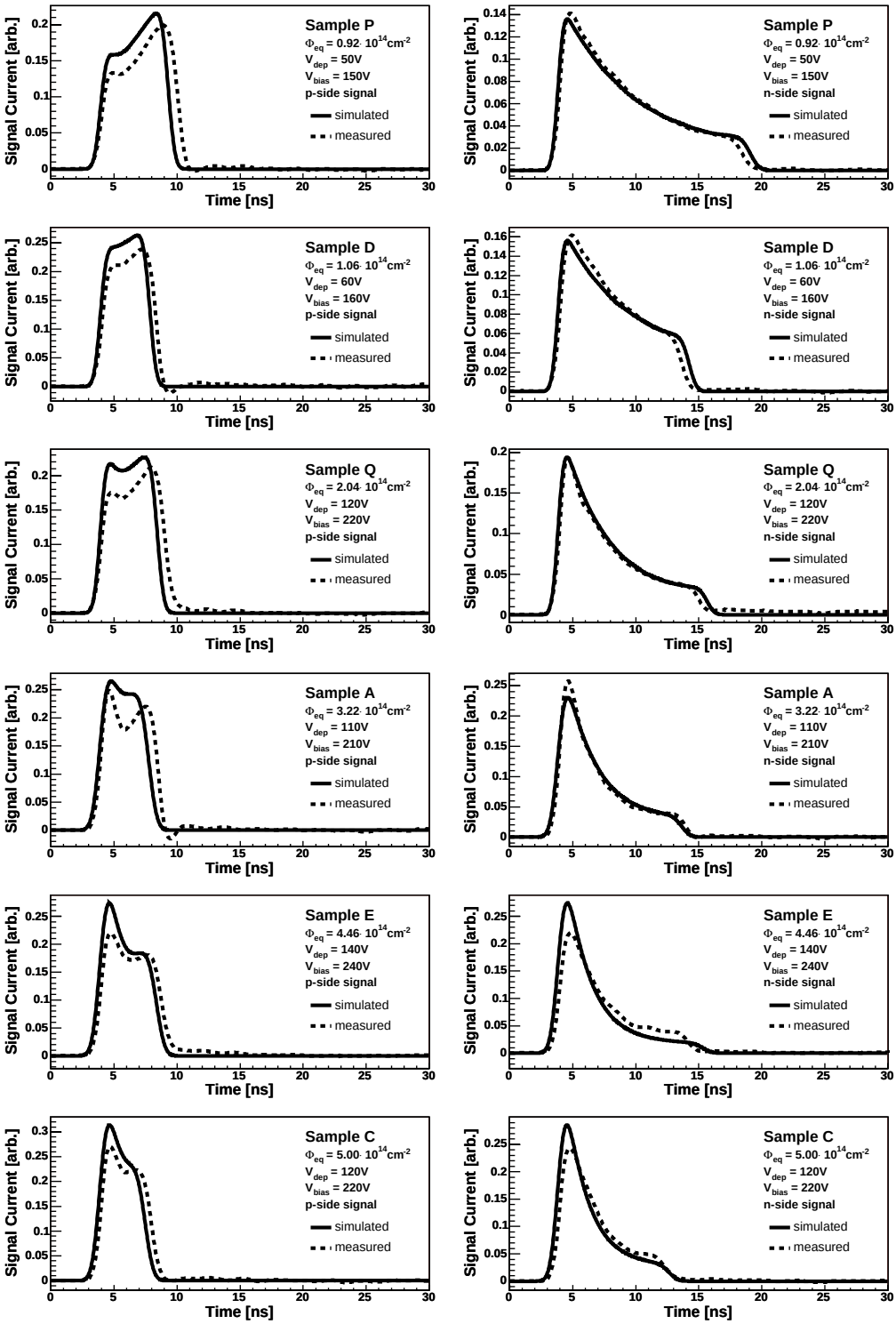

Fig. 10.6: Comparisons of simulated and measured pulse shapes with $V_{\mathrm{bias}} = V_{\mathrm{dep}}+100\,\mathrm{V}$. Proton fluence increases from top to bottom, left-handside p-side illumination, right-handside n-side illumination. Electric field is parameterised based on deep level model, temperature is 0°C.

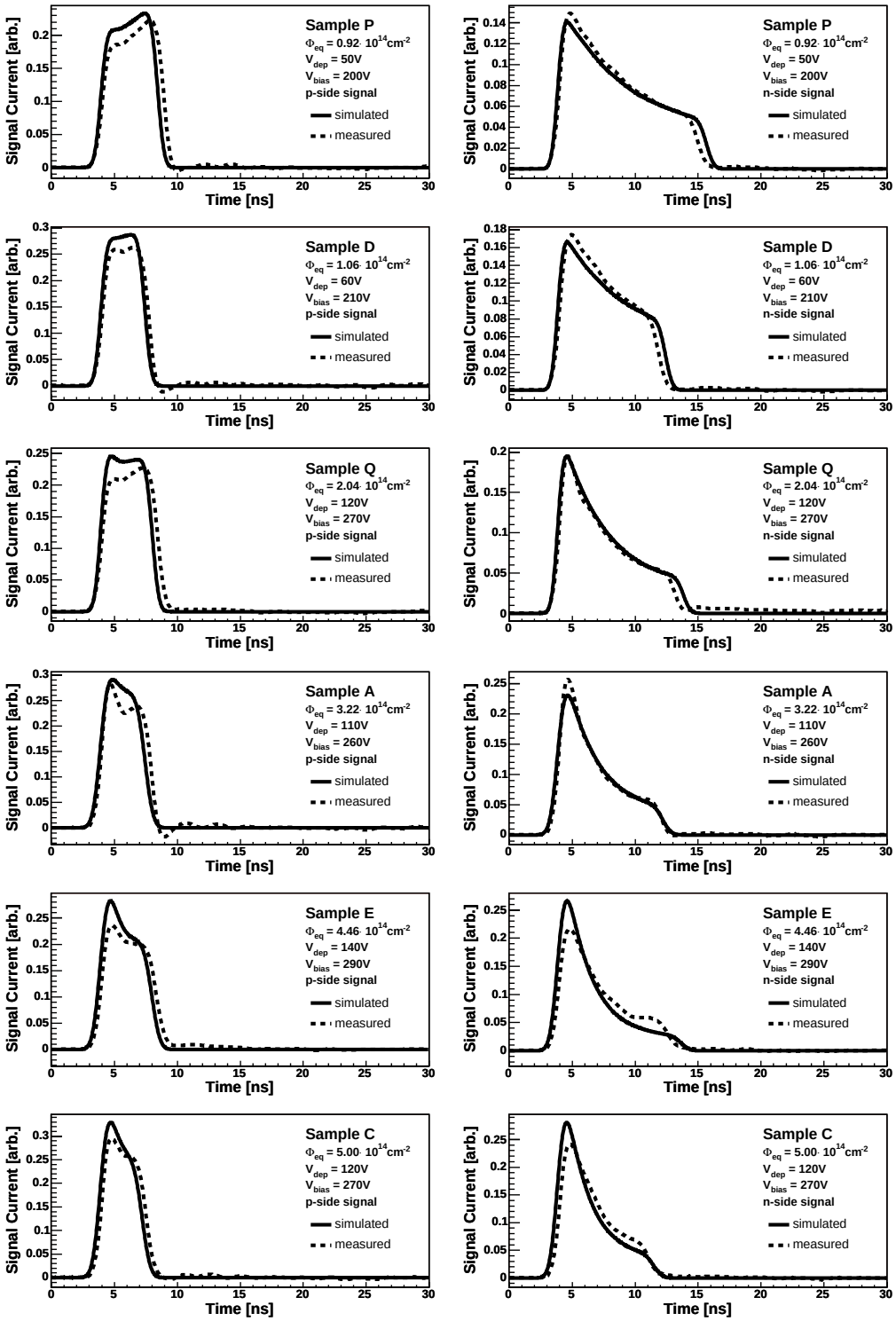

Fig. 10.7: Comparisons of simulated and measured pulse shapes with $V_{\mathrm{bias}} = V_{\mathrm{dep}}+150\,\mathrm{V}$. Proton fluence increases from top to bottom, left-handside p-side illumination, right-handside n-side illumination. Electric field is parameterised based on deep level model, temperature is $0^{\circ}\mathrm{C}$.

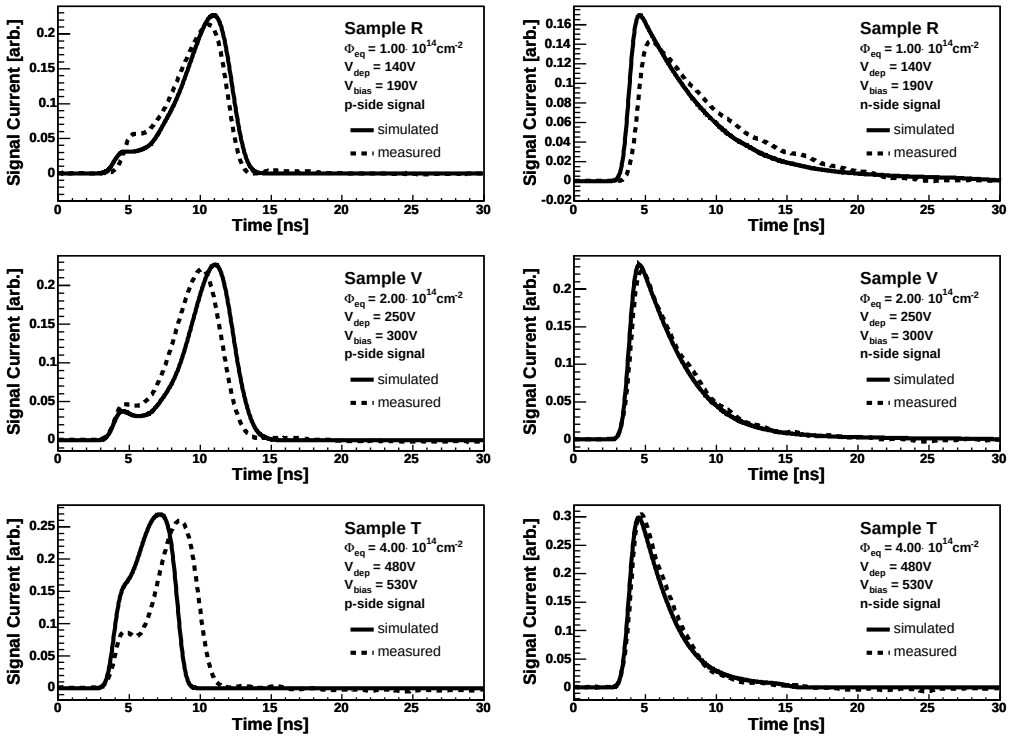

Fig. 10.8: Comparisons of simulated and measured pulse shapes with $V_{\mathrm{bias}} = V_{\mathrm{dep}} + 50\,\mathrm{V}$. Neutron fluence increases from top to bottom, left-handside p-side illumination, right-handside n-side illumination. Deep levels are considered for calculation of electric fields, temperature is 0°C.

also sensors biased with voltages being equal to or lower than the depletion voltage. Looking at results obtained for $V_{\mathrm{bias}} = V_{\mathrm{dep}}$ (see Fig. 10.10) it can be seen that hole dominated signals can still be sufficiently simulated while the quality of the p-side signal decreases significantly. At even lower bias voltages the deep level model fails in most cases. The problems at low bias voltages will be discussed again in sec. 10.3.

With increasing bias voltages these problems become less significant since the electric field is strong enough also in its minimum. Therefore, trapping is described correctly by the effective trapping times at high bias voltages.

For the simulation of mip detection a better agreement between simulation and reality is expected since there the electrons are injected homogeneously along the particle track. Therefore, the problematic bulk region close to the p-side has less weight in the total signal.

The width of the signals are sufficiently reproduced. The start time of charge drift in simulation and the inflection point of the leading edge of the measured pulse are set to the same time. This results in a very good consistency of the leading edges. This justifies the choice of the inflection point as the starting point of charge collection as it was done for analysis of TCT-measurements.

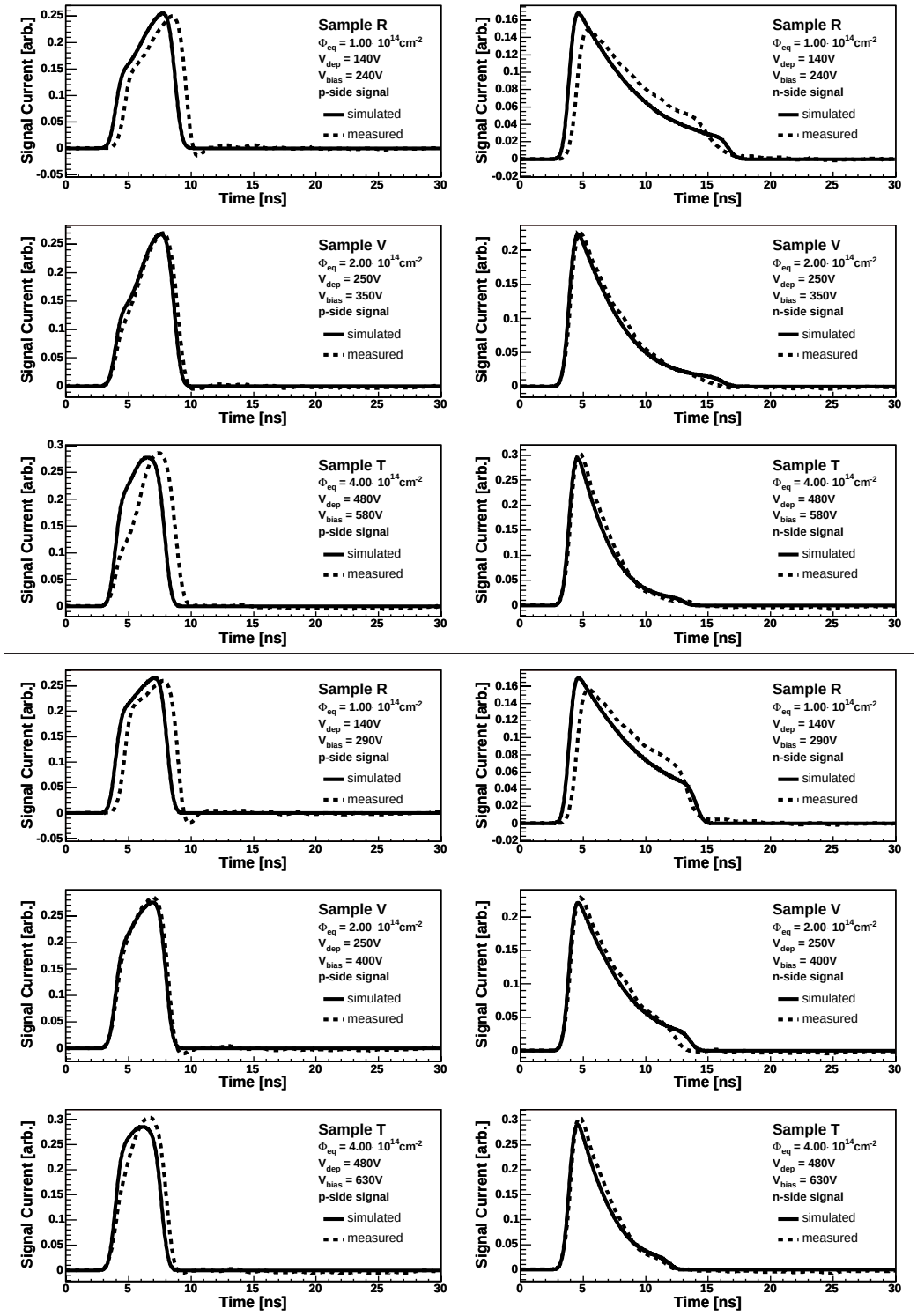

Fig. 10.9: Comparisons of simulated and measured pulse shapes with $V_{\mathrm{bias}} = V_{\mathrm{dep}} + 100\,\mathrm{V}$ (top) and $V_{\mathrm{bias}} = V_{\mathrm{dep}} + 150\,\mathrm{V}$ (bottom). Neutron fluence increases from top to bottom, left-handside p-side illumination, right-handside n-side illumination. Electric field is parameterised based on deep level model, temperature is 0°C.

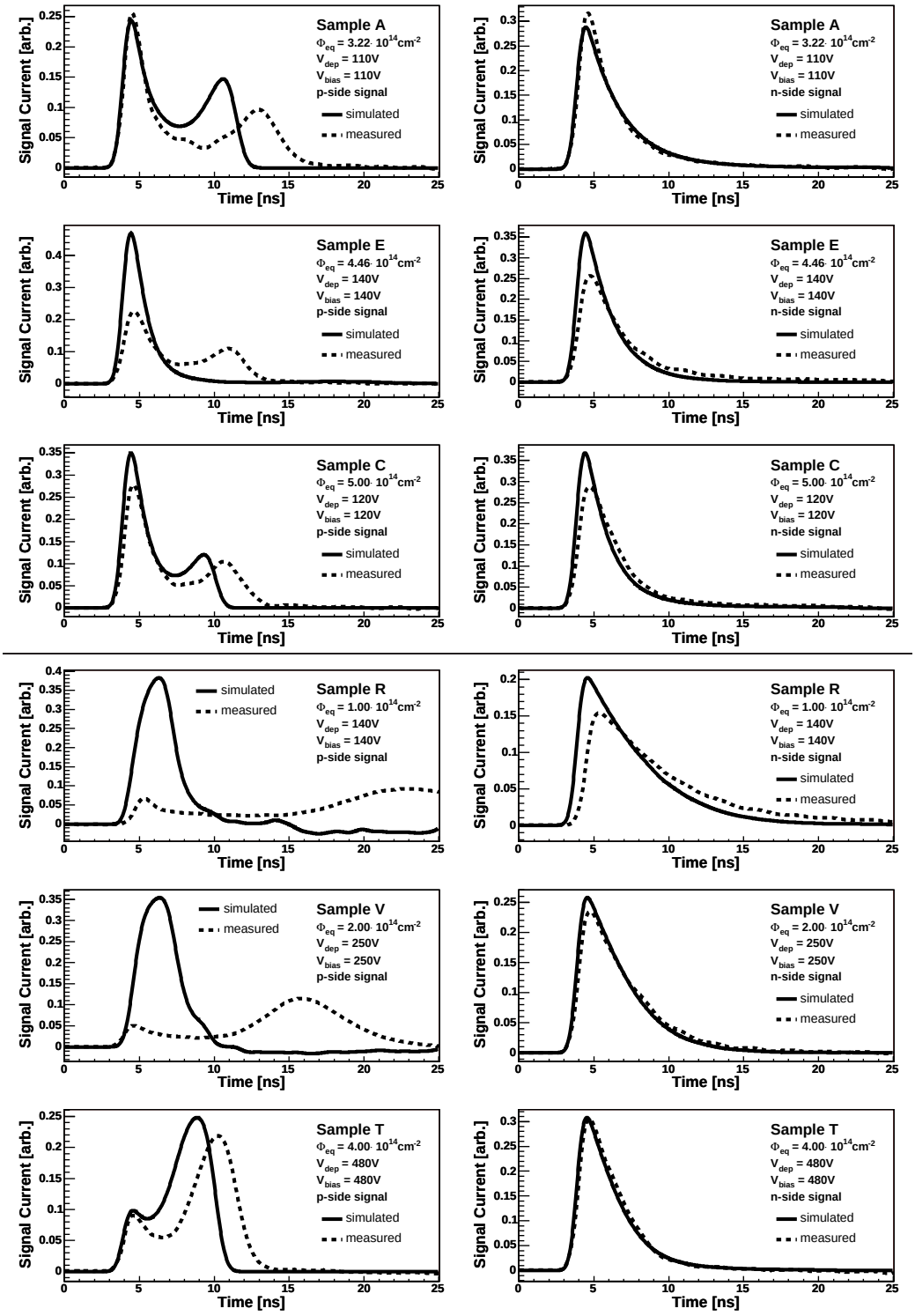

Fig. 10.10: Comparisons of simulated and measured pulse shapes with $V_{\mathrm{bias}} = V_{\mathrm{dep}}$. Fluences increase from top to bottom (top: proton-irradiated, bottom: neutron-irradiated), left-handside p-side illumination, right-handside n-side illumination with red laser. Electric field is parameterised based on deep level model, temperature is 0°C.

Temperature Dependence

The temperature dependence is an important aspect that has to be checked: since the occupation probabilities of deep levels vary with temperature their contribution to space-charge and therefore the field configuration are temperature dependent as well.
The influence of the temperature on the field configuration can be seen in Fig. 10.11: electric fields for simulated detectors corresponding to samples R and V with varied temperatures are plotted. The temperature range in the simulation

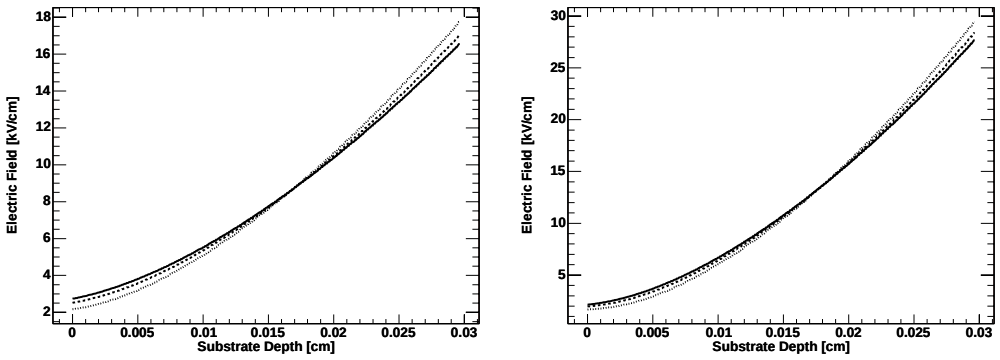

(a) Sample R, V_{dep}=140 V (b) Sample V, V_{dep}=250 V

Fig. 10.11: Electric fields calculated with deep level model for samples R and V ($1 \cdot 10^{14}\, n_{\mathrm{eq}}/\mathrm{cm}^2$ and $2 \cdot 10^{14}\, n_{\mathrm{eq}}/\mathrm{cm}^2$, resp.). The lines refer to temperatures of $-20°$C (solid line), $-12°$C (dashed) and $0°$C (dotted). Bias voltages are set to $V_{\mathrm{dep}} + 100$ V.

covers the possible range of operation temperature for the ATLAS pixel detector. The variation of the field configuration within this temperature range is only small. Fig. 10.12(a) and 10.12(b) show the resulting pulse shapes for samples R and V at temperatures of $-20°$C, $-12°$C and $0°$C. This temperature range covers the operation conditions of the ATLAS pixel detector which will be operated between $-10°$C and $0°$C.
For $-12°$C and $0°$C simulation reproduces the pulse-shapes well for both fluences. At $-20°$C—what is outside the operational temperature range of the ATLAS pixel detector—the agreement is slightly worse but still satisfying.

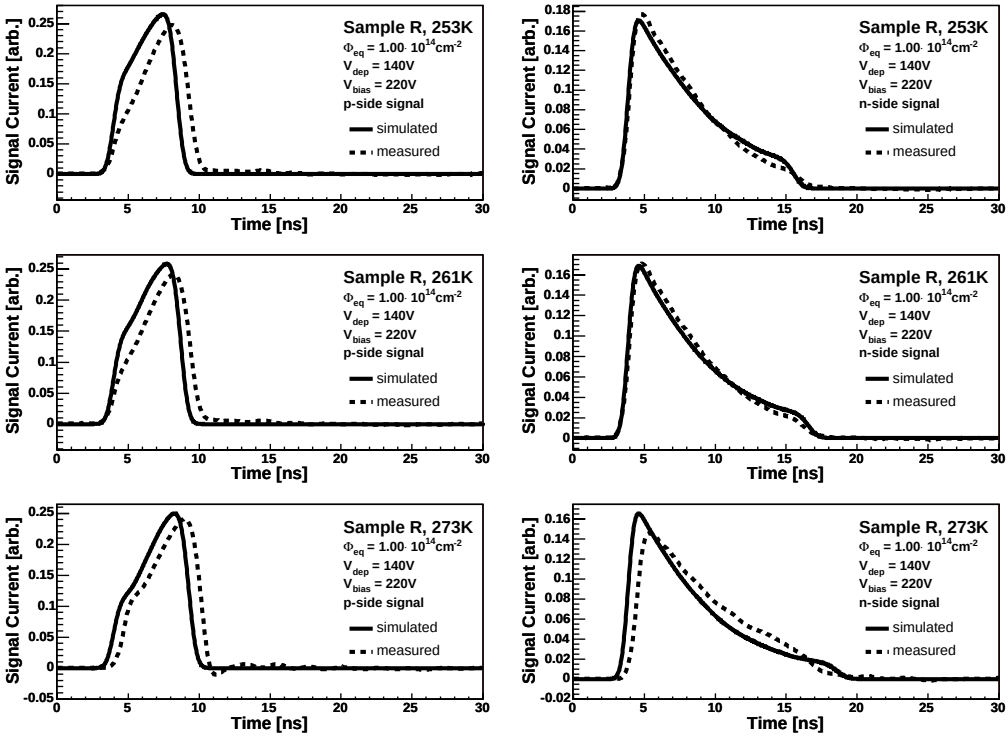

(a) Sample R, V_{bias}=V_{dep}+80 V

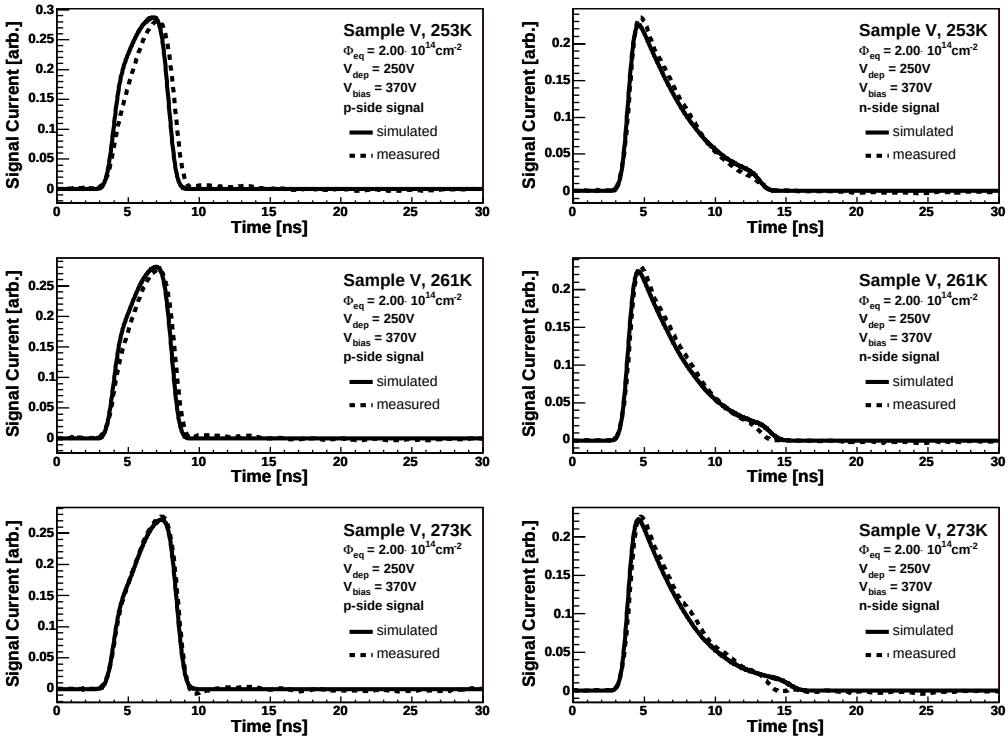

(b) Sample R, V_{bias}=V_{dep}+120 V

Fig. 10.12: Comparisons of simulated and measured pulse shapes for (a) sample R ($\Phi_{\mathrm{eq}} = 1 \cdot 10^{14}\, n_{\mathrm{eq}}/\mathrm{cm}^2$) and (b) for sample V ($\Phi_{\mathrm{eq}} = 2 \cdot 10^{14}\, n_{\mathrm{eq}}/\mathrm{cm}^2$). Temperature rises from top to bottom, left-handside p-side illumination, right-handside n-side illumination with red laser.

10.3 Charge Collection Efficiency

10.3.1 Fully Depleted Operation

The last check for the simulation software is the calculation of charge collection efficiencies. Fig. 10.13 shows the simulated and measured charge collection efficiencies for the proton-irradiated samples, Fig. 10.14 the same quantities for the neutron-irradiated samples.
The simulations are done with the same parameters which have been used for the pulse shape calculations. The bias voltages are varied from 50 V to 200 V above V_{dep}. Measured CCEs are derived from TCT-measurements by the method described in sec. 8.2.2 (see also Fig. 8.6).
For low proton fluences (samples P and D) the simulation fits nicely the measured CCE. With increasing proton fluence the deviation grows and the simulation overestimates CCE by a value of up to ≈ 0.1. In the neutron irradiated samples the measured CCE for holes is well reproduced for all fluences, for electrons only for the samples R and V. The simulation of sample T deviates significantly from the measurements but this sample already showed problems in the reproduction of the pulse shape. It is assumed that the measurement (which is done on the sample with the highest fluence) is bad since the simulation results (pulse shape and CCE) fit nicely in the fluence series and show no unexpected behaviour.

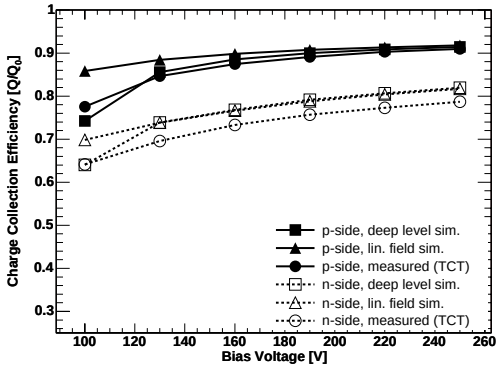

(a) Sample P, V_{dep}=50 V

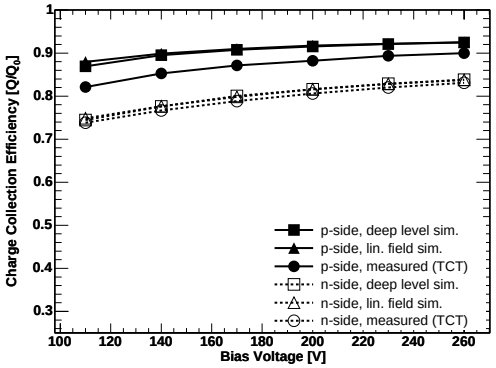

(b) Sample D, V_{dep}=60 V

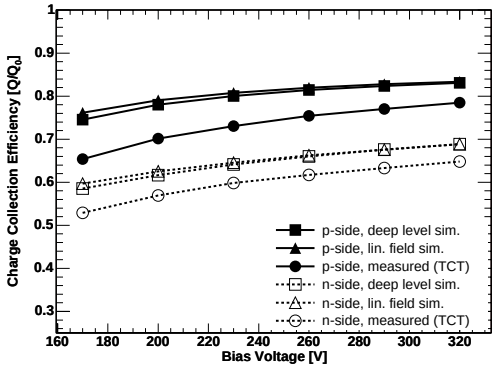

(c) Sample Q, V_{dep}=120 V

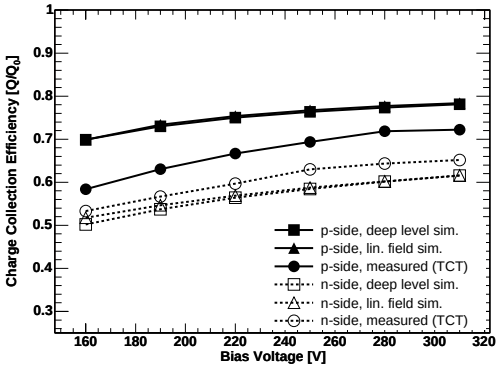

(d) Sample A, V_{dep}=110 V

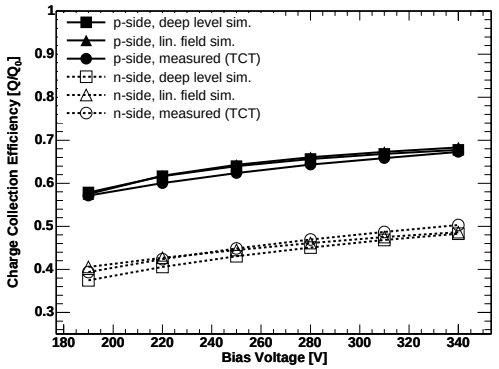

(e) Sample E, V_{dep}=140 V

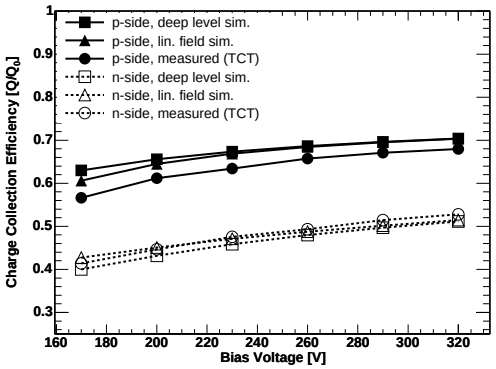

(f) Sample C, V_{dep}=120 V

Fig. 10.13: Measured and calculated charge collection efficiencies vs. bias voltage for proton irradiated samples. Values for V_{dep} are rounded to full 10 V.

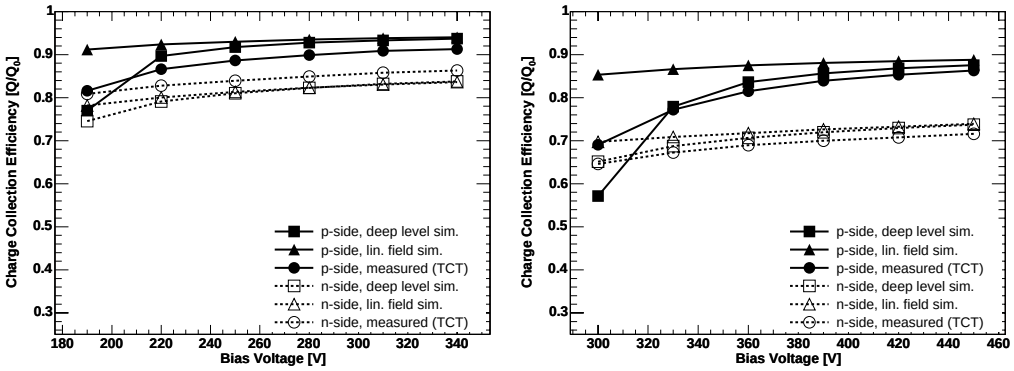

(a) Sample R, V_{dep}=140 V

(b) Sample V, V_{dep}=250 V

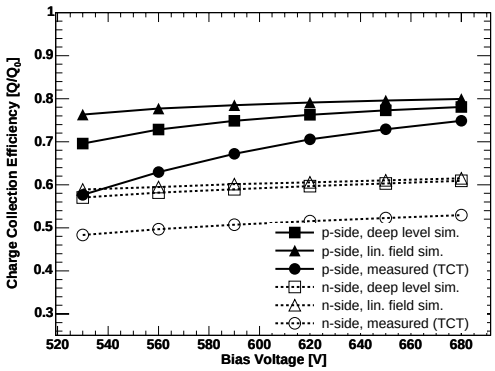

(c) Sample T, V_{dep}=480 V

Fig. 10.14: Measured and calculated charge collection efficiencies vs. bias voltage for neutron irradiated samples. Values for V_{dep} are rounded to full 10 V.

10.3.2 Underdepleted Operation

As already discussed in sec. 10.2.3 the deep level model fails for bias voltages equal to or lower than the depletion voltage. The simulation results for pixel sensors cannot be compared to measurements in order to validate them. Therefore, it has to be found a criterion if the simulation works correctly or not. This decision must be solely based on the simulation results.
Fig. 10.15, 10.16 and 10.17 show CCEs from measurements and simulations. n-side signals always show a better agreement between measurement and simulation than p-side signals. Comparing measured and simulated results it can be seen that the minimum voltage V_{sw} where the simulation starts to give correct results is decreasing with fluence relatively to V_{dep}. In the proton-irradiated samples $V_{\mathrm{sw}} - V_{\mathrm{dep}}$ falls from $\approx 60\,\mathrm{V}$ (sample P) to $\approx -20\,\mathrm{V}$ (sample C). Therefore, it can be expected that the simulation improves with increasing bias voltages.
Next to each CCE plot the corresponding electric fields are shown. The electric fields are calculated for the bias voltages denoted by the markers in the corresponding CCE plots. If the calculation of the electric field with the deep level model failed the result is given by a dashed line. Looking at minimum field strengths and agreement in CCE between measurement and simulation it can be concluded that the simulation works well as soon as the minimum field strength becomes larger than $\approx 1\,\mathrm{kV/cm}$.

10.4 Discussion of Usability

It has been demonstrated that the developed software can be used to simulate the properties of irradiated pad-detectors. EDCALC is capable to predict the depletion voltage as has been shown in sec. 10.1 by comparing calculations with measurements on the irradiated pad-detectors used for this work. The deviation between measurement and calculation is in all but one cases for all fluences less than 50 V (see Fig. 10.2(a)). This deviation can be considered as acceptable since the parameters of the Hamburg model have a dependence on the individual material and additionally the exact history of the irradiated samples is unknown. Comparisons of calculated leakage currents with measurements are not possible within this work since no exact measurements of the leakage currents have been done. For these measurements it would have been necessary to contact the guardrings of the diode but that was not possible because such a further contact would have disturbed the TCT-measurements.
Pulse shape and pulse width can be properly simulated for bias voltages being higher than the depletion voltage. In this voltage range the deep level model describes the pulse shapes better than the model using a linear dependence of the electric field.
From comparisons between measured and simulated CCEs a lower limit for the electric field strength of $1\,\mathrm{kV/cm}$ has been found; below this limit the deep level model fails to describe the charge collection correctly.

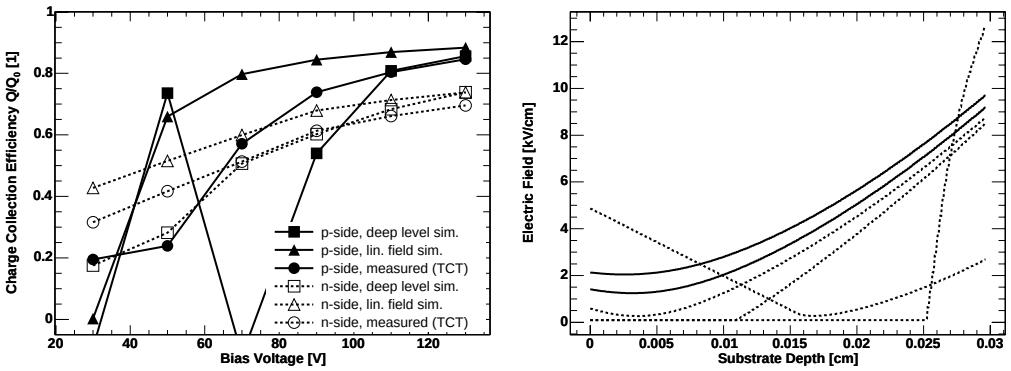

(a) Sample P, V_{dep}=50 V

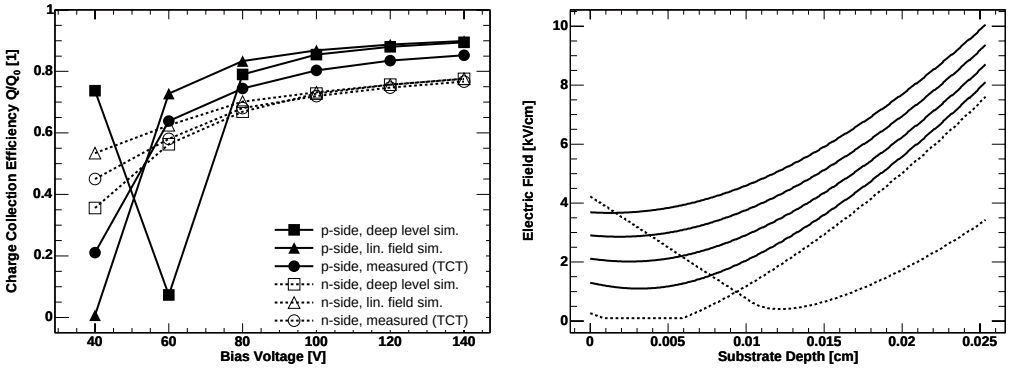

(b) Sample D, V_{dep}=60 V

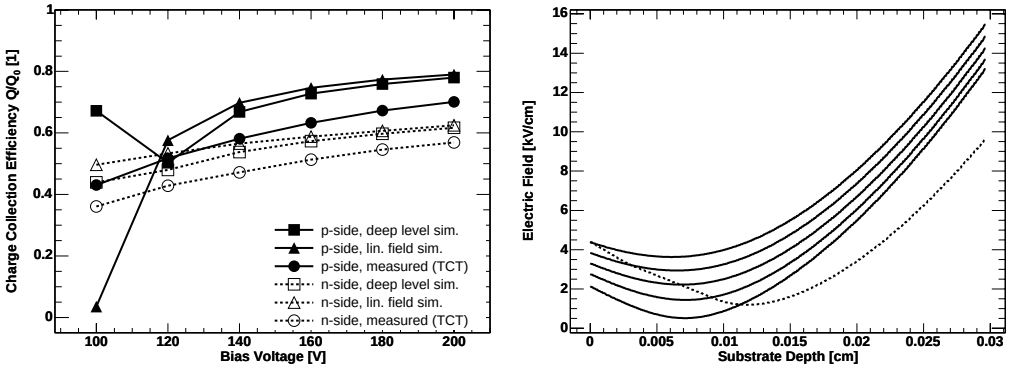

(c) Sample Q, V_{dep}=120 V

Fig. 10.15: Measured and calculated charge collection efficiencies vs. bias voltage for proton irradiated samples. Values for V_{dep} are (rounded) to full 10 V. See text for more details.

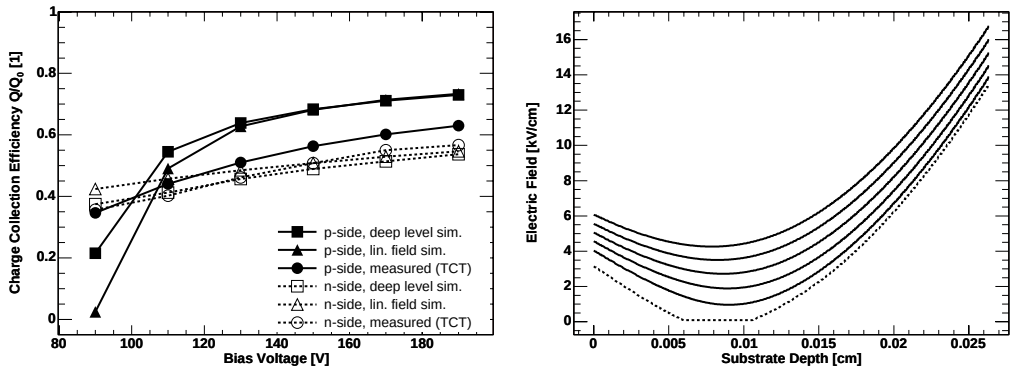

(a) Sample A, V_{dep}=110 V

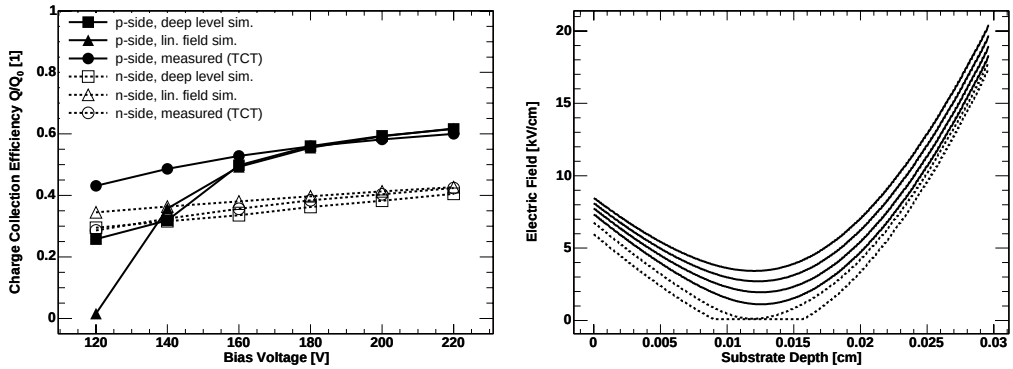

(b) Sample E, V_{dep}=140 V

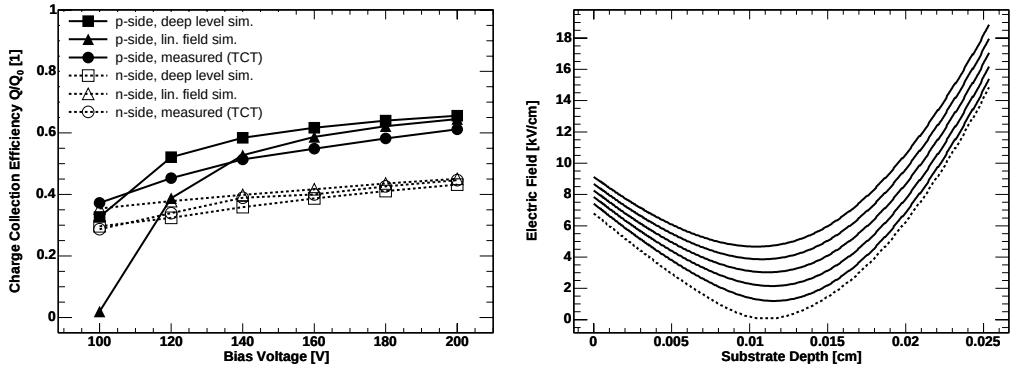

(c) Sample C, V_{dep}=120 V

Fig. 10.16: Measured and calculated charge collection efficiencies vs. bias voltage for proton irradiated samples. Values for V_{dep} are rounded to full 10 V. See text for more details.

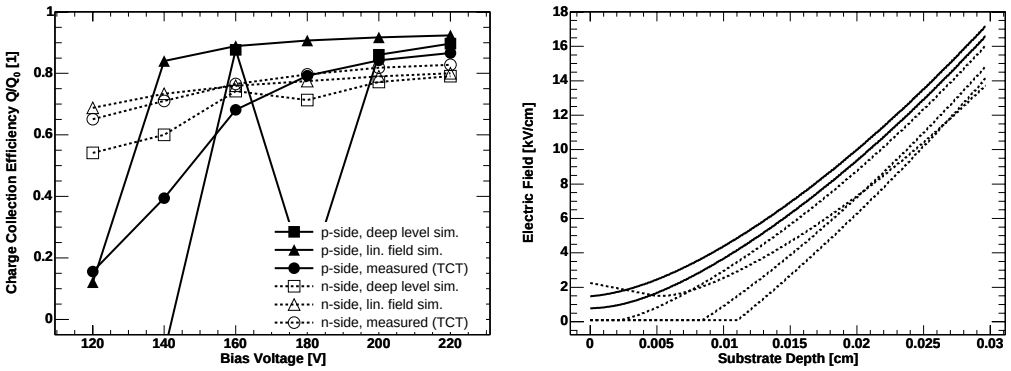

(a) Sample R, V_{dep}=140 V

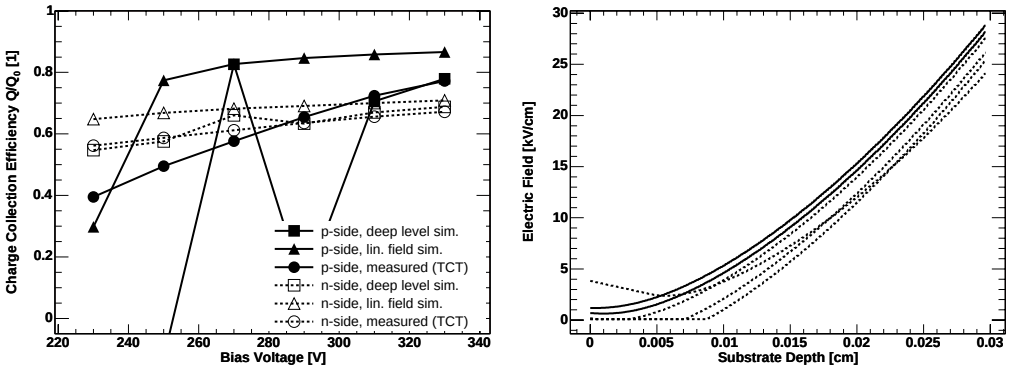

(b) Sample V, V_{dep}=250 V

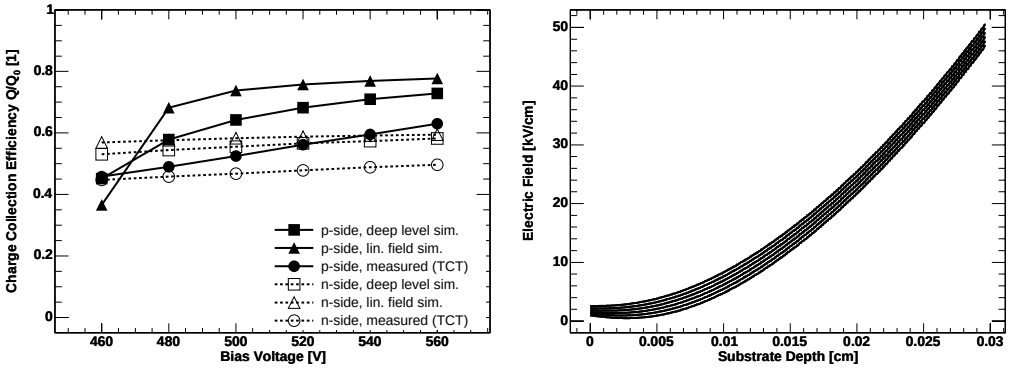

(c) Sample T, V_{dep}=480 V

Fig. 10.17: Measured and calculated charge collection efficiencies vs. bias voltage for neutron irradiated samples. Values for V_{dep} are rounded to full 10 V. See text for more details.

The simulation also used the results for the effective trapping times determined in this work. Thus the good reproduction of the pulse shapes and charge collection efficiencies underlines the validity of the determination of trapping times in this work as well.
From the comparisons between measurements and simulations performed in this chapter it can be concluded that the developed software is suitable to simulate pad-detectors irradiated with fluences which are relevant for the operation of tracking detectors at LHC experiments.
Simulation of electron pulse-shapes after mip-passage are expected to reproduce the reality better than the simulation of p-side illumination: the main problems result from the electrons drifting through the not well described low field region before inducing the larger part of their signal. Due to the homogeneous charge deposition after a mip-passage this part of the drift path has less weight in the total signal. Therefore, the systematic errors of CCE calculation after mip-passage are estimated to be significantly lower than that for close-to-surface charge injection.

Chapter 11

Simulations of ATLAS Pixel Sensors

THIS chapter is dedicated to simulations of pixel detector modules for the ATLAS experiment. The focus is set to the operation conditions with respect to depletion voltage, leakage current and charge collection efficiency of the sensor. The first section of this chapter includes simulations of modules that have been used in test beam. These test beam measurements were accompanied by simulation studies in order to define useful settings for bias voltage and to improve the understanding of the results.
The remaining sections of this chapter treat predictions for the later ATLAS operation. They explain several simulation studies that were done during the design phase of the pixel detector in order to evaluate the consequences of different scenarios. One of the most important calculation is presented in the last section where the charge collection efficiencies are estimated.

11.1 Test Beam Modules

Scope

During the development phase of the ATLAS pixel detector several modules with so-called single-chips have been built. Single-chips are smaller variants of sensor tiles covering the sensor area of one front-end chip but having the same pixel geometry. These single-chip modules have been used for testing several different designs of pixel cells [Hü01] and for making tests with irradiated modules in the test beam area H8 of the Super Proton Synchrotron (SPS) at CERN.
These measurements are time-consuming and as a reason of limited available beam-time it is not possible to make scans of the bias voltage in small steps. Most modules were tested at a maximum of three different bias voltages. In order to obtain significant results from these few measurements it is important to know the depletion voltages before starting the measurements. This was achieved by

simulations with the software presented in this work and by additional source-scans done in the laboratory of a collaborating group [Ge00]: in source scans the modules are illuminated with 60 keV photons from a ^{241}Am source and the count rate of the sensor is measured as function of the bias voltage. Since the γs make point-like energy depositions the count rate is proportional to the depleted volume of the sensor and the depletion voltage can be derived from these measurements. Comparisons between the source-scans, test beam results and simulation were used for consistency checks. It is important to remark that the simulations were done solely based on the irradiation and temperature history and not adapted to the measured results.
During the test beams in the year 2000 radiation hard front-end electronics was not available. Therefore, the single-chip sensors were irradiated before module assembly. After irradiation they were connected to unirradiated electronics. Since flip-chipping needs elevated temperatures for several minutes one question was how large the effect on depletion voltage of this heat-up is and if it was critical for sensor-operation. Since the simulation disagreed with the source-scans in a first iteration a more refined second iteration became necessary. In this thesis the results from both iterations are presented since also the first results are still interesting.

1st Iteration

The first step of the flip-chipping is the deposition of solder bumps on the FE chips and the sensor before irradiation. After irradiation the FE chips are positioned on the sensor and the devices are heated to 100°C for up to three minutes. During this step the module is fixed with the FE chips onto the heater. The temperature during the process is measured on the heater. Fig. 11.1(a) shows the assumed temperature profile for a typical module whose 250 μm thick sensor has been irradiated with a proton fluence of $5.6 \cdot 10^{14}\, n_{\mathrm{eq}}/\mathrm{cm}^2$. This irradiation took 4 days at 20°C, then the sensor was stored 11 days in a refrigerator at -15°C. After this period it was kept at 20°C. During this period also the flip-chipping has been done. The inset in Fig. 11.1(a) gives the magnified temperature profile during the flip-chip process: in the mathematical description used in the simulation the temperature rises exponentially during the heating time from the start temperature (20°C) to the maximum temperature (100°C) with a time constant of 12 s. After the flip-chipping the device cools down exponentially with a time constant of 72 s. In order to obtain an estimation for the systematic error the simulation was done with a heat-up time of 90 s, 180 s and 270 s and without flip-chipping.
Fig.11.1(b) shows the resulting profiles of the depletion voltage for the three different heat-up times plus the case without flipping but storing the module at 20°C instead. The results show a strong dependence on the heat-up time, depletion voltage rises by ≈ 50 V per 30 s heat-up time.
Additionally, the same scenarios are calculated with 180 s heat-up time but varied maximum temperature (90°C, 100°C, 110°C and 120°C). Fig. 11.1(c) gives

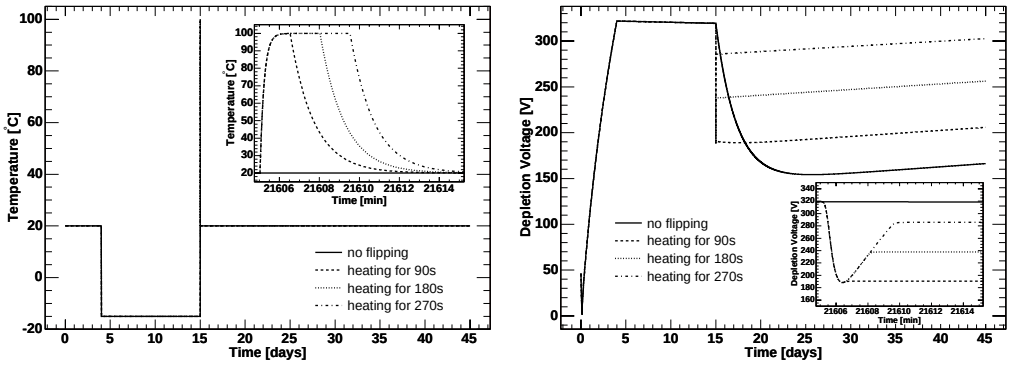

(a) Temperature Profile

(b) Depletion Voltage Profile

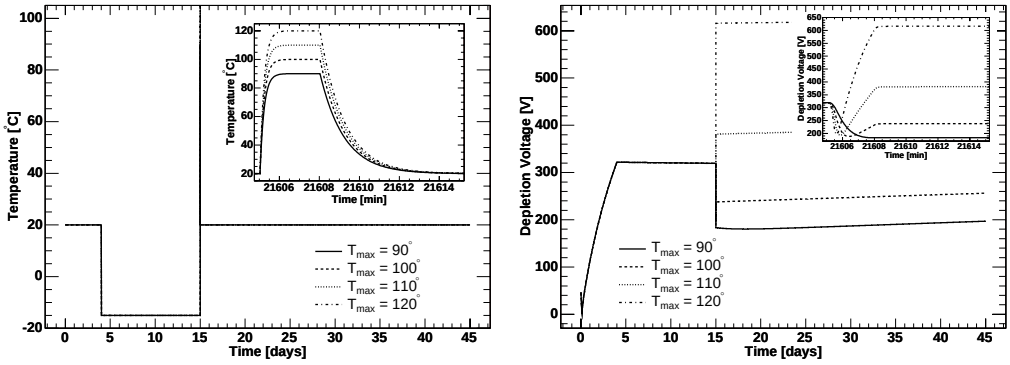

(c) Temperature Profile

(d) Depletion Voltage Profile

Fig. 11.1: Flip-chip scenario with a maximum temperature of 100°C.

the temperature profiles and Fig. 11.1(d) shows the resulting evolution of depletion voltage. The resulting depletion voltage depends strongly on the maximum temperature.

Table 11.1 gives the results for several modules having been irradiated to different fluences. The depletion voltages are taken after several days at 20°C in order to consider warm periods for shipment and handling. This table shows the values for depletion voltage obtained from source scans [Ce01] as well. A comparison reveals that the simulated results deviate significantly from the measured ones. The following conclusions are drawn from the simulation results and their comparison with measurements:

1. The depletion voltage depends strongly on the maximum temperature and duration of flip-chipping. Before doing this simulation study the effect of

Module	Fluence $[10^{14}\, n_{eq}/cm^2]$	V_{dep} [V] source scan	V_{dep} [V] simulation I	V_{dep} [V] simulation II
ge_b_15	10.0	290	390	280
oxy1	5.6	150	255	160
oxy2	3.2	100	175	80
oxy3	3.2	100	175	80

Table 11.1: Results for the depletion voltage from source scans [Ce01], from the first iteration of simulation (max. temperature 100°C) [Kr00b] and the second iteration (max. temperature 46°C) [Kr00e].

the heat-up during flip-chip was considered to be negligible.

2. Even with rather large variations from the used values for maximum temperature and heat-up time the difference to the measured values cannot be explained.

As a consequence the temperature measurement during the flip-chip process was improved [Ge00]: instead of measuring the temperature on the heating element the temperature is determined on the sensor. The new measurements show a significantly lower temperature at the sensor which can be explained by the thermal isolation from the heated FE chips by the bump bonds.

Although this first iteration simulation was not successful in describing the test modules it can still be used to assess the consequences of a short heat-up of the pixel detector due to a failure of its cooling system. Since the detector is built with little and light materials it has only a small thermal capacity which will cause a fast heating up if the power supplies are not shut off fast enough after a cooling system failure.

2nd Iteration

The new results for the temperature profile (see Fig. 11.2(a)) are used as input for a second iteration of the simulation. The maximum temperature has been determined to be 46°C. The simulation is done again with varied heat-up time (Fig. 11.2(a)/11.2(b)) and varied maximum temperature (Fig. 11.2(c)/11.2(d)). Variations with heat-up time and maximum temperature are considerably smaller than in the first iteration. A comparison with the results from source scans (Table 11.1) shows a much better agreement, the simulation results deviate less than 20 V from the measurements.

A further conclusion from simulation is that the flip-chip process with irradiated sensors is not critical. The typical heat-up is even too short (or too low in temperature) to bring the sensor beyond the minimum of the annealing curve.

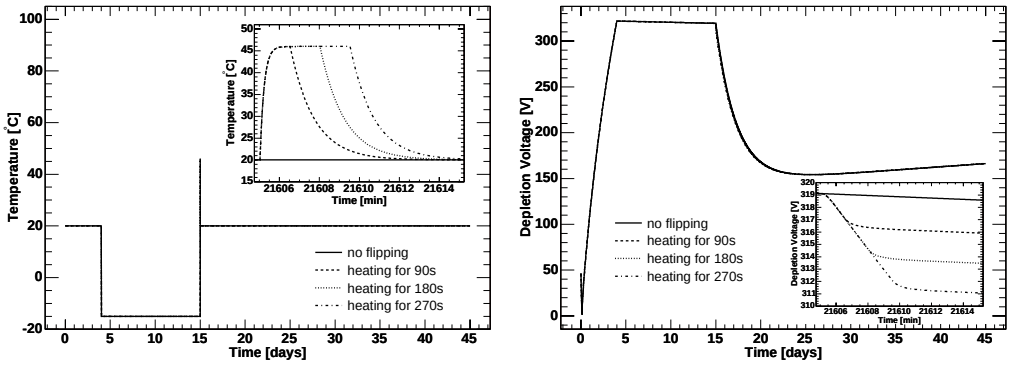

(a) Temperature Profile

(b) Depletion Voltage Profile

(c) Temperature Profile

(d) Depletion Voltage Profile

Fig. 11.2: Flip-chip scenario with a maximum temperature of 46°C.

11.2 ATLAS Standard Scenario

11.2.1 Irradiation Profile

The foreseen operation conditions for the ATLAS pixel detector are summarised in the so-called *standard scenario*. Table 11.2(a) contains the equivalent fluences for the individual layers of the pixel detectors at their old positions (see sec. 2.4.3). Fig. 11.3 shows a plot of fluence vs. radius (at $z = 0$). Since the numbers for the radii of the layers are outdated the expected fluences for the layers also have changed. In order to derive expected fluences for the new positions the following distribution of charged and neutral particle fluxes is assumed:

- Charged particles come from the interaction point (IP) which is considered as a point-like source. Therefore, the fluence of charged particles is described

layer	radius	total eq. fluence	charged fraction
B-layer	4.3 cm	$28 \cdot 10^{14}$ $n_{\mathrm{eq}}/\mathrm{cm}^2$	85%
layer 1	10.1 cm	$6.6 \cdot 10^{14}$ $n_{\mathrm{eq}}/\mathrm{cm}^2$	70%
layer 2	13.2 cm	$4.0 \cdot 10^{14}$ $n_{\mathrm{eq}}/\mathrm{cm}^2$	—

(a) old positions

layer	radius	total eq. fluence	charged fraction
B-layer	5.05 cm	$20.75 \cdot 10^{14}$ $n_{\mathrm{eq}}/\mathrm{cm}^2$	83.4%
layer 1	8.85 cm	$7.76 \cdot 10^{14}$ $n_{\mathrm{eq}}/\mathrm{cm}^2$	72.6%
layer 2	12.25 cm	$4.76 \cdot 10^{14}$ $n_{\mathrm{eq}}/\mathrm{cm}^2$	61.7%

(b) new positions

Table 11.2: Equivalent fluences after ten years of operation at the old (a) and new (b) radial positions ($z = 0$) of the pixel detector layers.

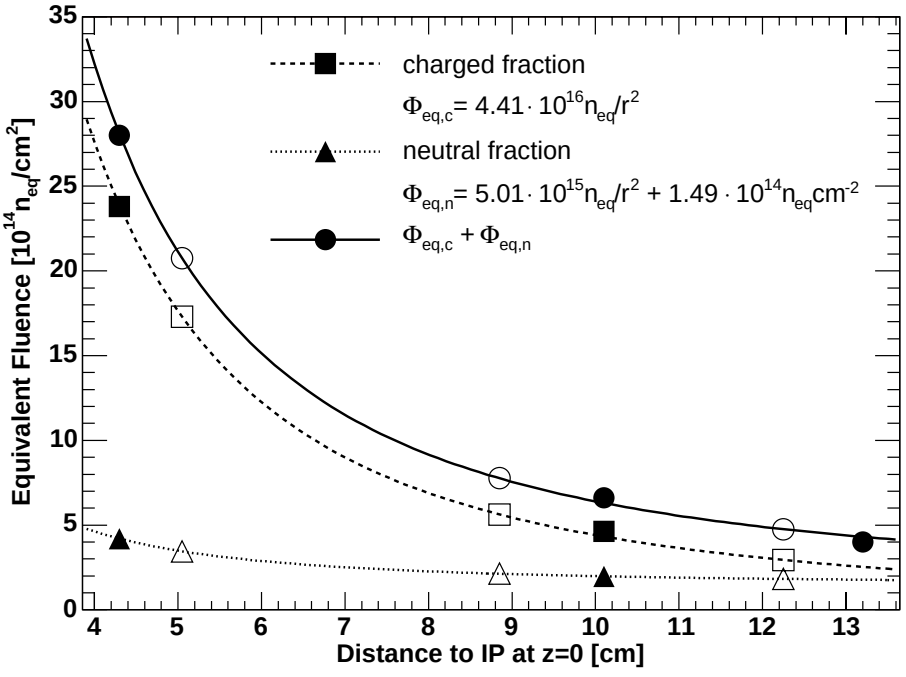

Fig. 11.3: Equivalent fluences vs. radius (distance to IP at $z = 0$). Closed symbols show fluences from simulation for old layer positions, lines show the results of fitting a model (see text for details) and open symbols represent the interpolated values for the new radii.

by a $1/r^2$ dependence:

$$\Phi_{\mathrm{eq},c} = \frac{a}{r^2}\,. \tag{11.1}$$

- The neutral fluence is distributed like

$$\Phi_{\mathrm{eq},n} = \frac{b}{r^2} + c \tag{11.2}$$

since it has contributions from the particle interaction and from a constant background of neutrons that have been back-scattered by detector material.

A fit of this model to the data given in Table 11.2(a) for B-layer and layer 1 yields for the parameters a, b and c:

$$\begin{aligned} a &= 4.41 \cdot 10^{16}\, n_{\mathrm{eq}} \\ b &= 5.0 \cdot 10^{15}\, n_{\mathrm{eq}} \\ c &= 1.5 \cdot 10^{14}\, n_{\mathrm{eq}}/\mathrm{cm}^2 \end{aligned} \tag{11.3}$$

Fig. 11.3 shows the resulting curves as well. As can be seen on this plot the model describes the expected fluences quite well. Since later all calculations will be done for fluences increased by 50% with respect to nominal fluences as well (see below) the accuracy of this model is good enough.
The actual radii of the three barrel layers are 5.05 cm, 8.85 cm and 12.25 cm. The fluences at the new positions are calculated by using these fit parameters (see also Fig. 11.3). The results for the fluences are compiled in Table 11.2(b).
In the first three years 2.89%, 6.36% and 9.83% of the lifetime fluence are applied, respectively. In each of the following seven years 11.56% of total fluence are obtained. Since the expected total pp-cross section at LHC energies has an uncertainty of 50% the fluences have this uncertainty, too. Therefore, the scenarios for the individual layers are additionally calculated with fluences increased by this percentage in order to cover also the worst case. The fraction of charged particles in the radiation changes from layer to layer due to decays of the particles and the different geometric dependence of charged and neutral particle fluxes.
It is assumed that ATLAS will be taking data with beam during the first 100 days per year. Fig. 11.4 shows the integrated fluence vs. time.

11.2.2 Temperature Profile

During operation the detector will be kept at 0°C. The 100 days of operation will be followed by 30 days at 20°C (room temperature) for access (maintenance). After the access period the detector will be kept cold (-10°C) for the rest of the year in order to minimise annealing effects. Fig. 11.5 shows a plot of the detector temperature vs. time.

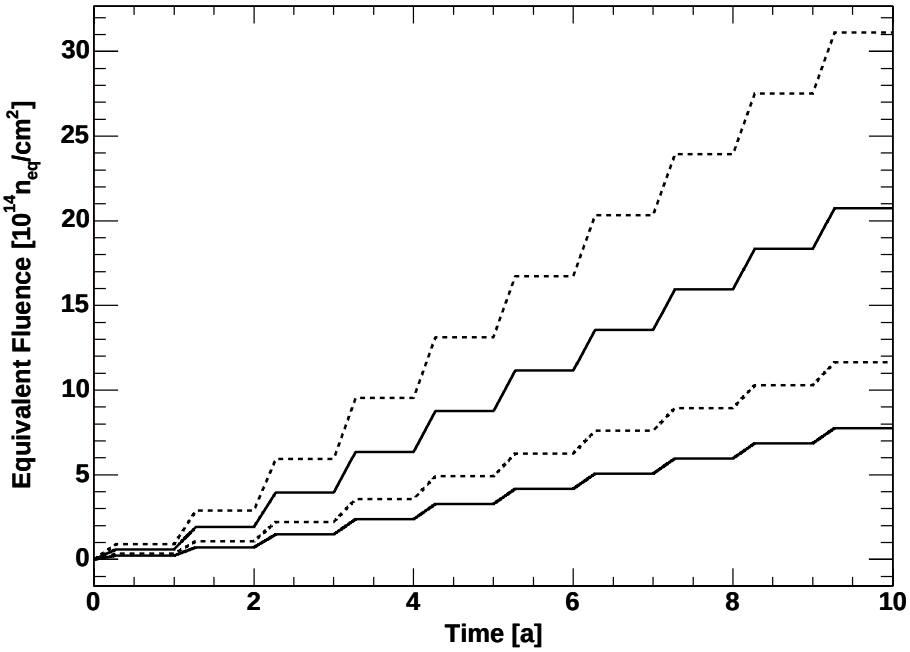

Fig. 11.4: Equivalent fluence vs. time for the ATLAS standard scenario (operation on 100 days per year). The lower two lines show the fluence for layer 1, the upper two for the B-layer. Dashed lines show fluences increased by 50%.

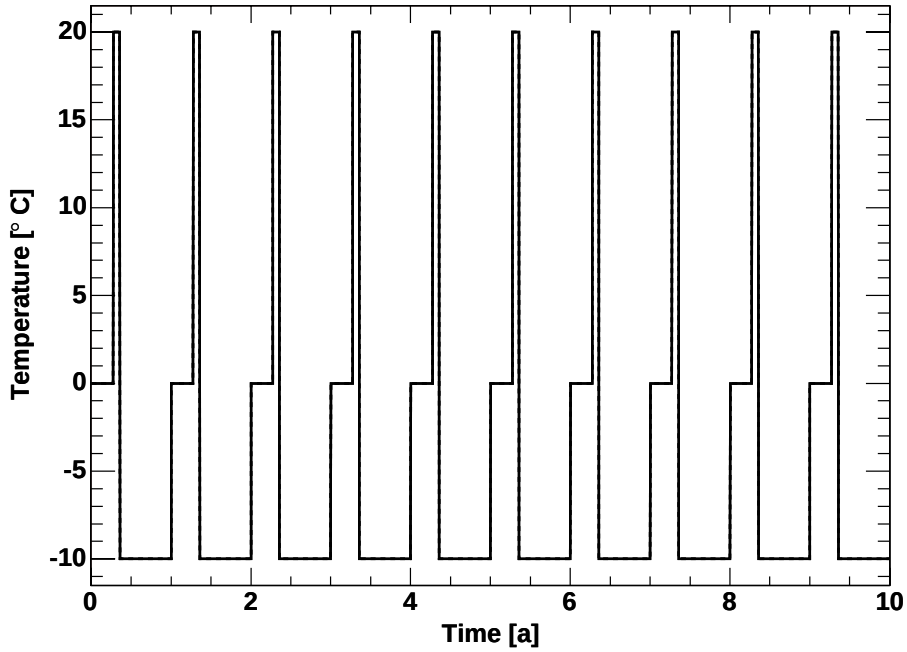

Fig. 11.5: Temperature vs. time for the ATLAS standard scenario (operation at 0°C, access at 20°C, storage at -10°C).

11.2.3 Depletion Voltage

Annual Development

The scenario described above is now used to calculate the development of the depletion voltage during ATLAS operation. In the following the calculations are restricted to B-layer and layer 1 since they represent the worst case: due to the high radiation load for B-layer it is planned to operate it for five years only. For layer 1 a life-time of ten years is foreseen. It represents the worst case for modules with this life-time since all other detector parts (layer 2, disks) are farther away from the interaction point. Fig. 11.6 shows the result for ten years of operation.

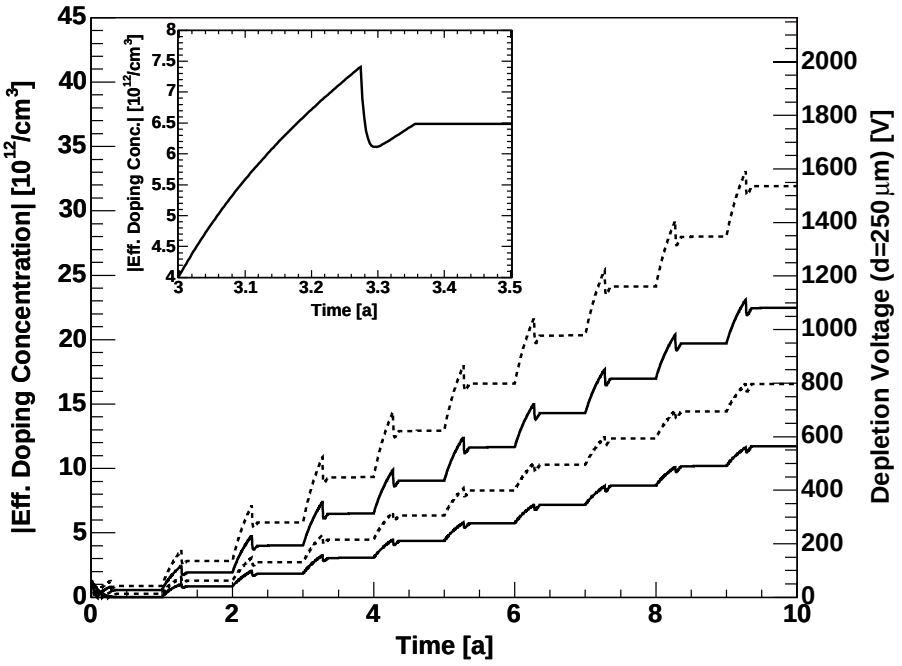

Fig. 11.6: Development of effective doping concentration and depletion voltage for B-layer and layer 1 for the ATLAS standard scenario. The inset shows a magnification of the large plot.

After an initial decrease (until SCSI is reached) the depletion voltage rises in every beam period. The inset in the figure gives a magnification of a half-year period: during the the first 100 days the depletion voltage rises to a maximum. After the end of the beam period it drops due to beneficial annealing and starts to rise again (reverse annealing). The annealing is almost stopped when the cold storage begins after 30 days at 20°C.

Layer 1

In order to achieve a good charge collection it is planned to operate the pixel detector with a bias voltage being 50 V above the full depletion voltage and the minimum bias voltage is 150 V. However, due to technical limitations implied by the power supplies and cabling the maximum bias voltage is 600 V. Table 11.3 contains the results for the depletion voltages of the layer 1 sensors. Considering nominal fluence the sensors of layer 1 reach a depletion voltage of ≈ 570 V after ten years. Thus it can be expected that they will still be fully sensitive after their lifetime fluence. With a fluence increased by 50% they reach the limit of 600 V after about seven years, after ten years their depletion voltage reaches $\approx$ 800 V. Considering a growth of the depletion zone being proportional to $\sqrt{V_{\text{bias}}}$ this corresponds to a depleted thickness of $\approx 216\,\mu$m.

year	Φ_{eq}		$V_{\text{dep},0}$		$V_{\text{dep},1}$		$V_{\text{dep,min}}$		$V_{\text{dep},2}$	
[a]	[$10^{14}\,n_{\text{eq}}/\text{cm}^2$]		[V]		[V]		[V]		[V]	
1	0.22	(0.34)	61	(61)	2	(16)	0	(10)	0	(13)
2	0.72	(1.08)	1	(14)	44	(67)	37	(55)	41	(62)
3	1.48	(2.22)	42	(63)	91	(137)	80	(119)	89	(131)
4	2.38	(3.57)	90	(132)	148	(219)	135	(200)	147	(216)
5	3.27	(4.91)	148	(217)	207	(305)	195	(286)	210	(305)
6	4.17	(6.26)	211	(307)	270	(395)	259	(377)	277	(399)
7	5.07	(7.60)	278	(400)	337	(489)	326	(471)	346	(495)
8	5.97	(8.95)	347	(497)	407	(585)	396	(568)	417	(594)
9	6.86	(10.29)	418	(595)	478	(684)	468	(667)	490	(695)
10	7.76	(11.64)	491	(696)	551	(785)	541	(768)	565	(797)

Table 11.3: Depletion voltages for layer 1. $V_{\text{dep},0}$ denotes the depletion voltage at the beginning of a year, $V_{\text{dep},1}$ is the depletion voltage after the irradiation and $V_{\text{dep},2}$ is its value at the end of the respective year. Fluences are given after the respective's year beam period. Values in parentheses give the values for fluence increased by 50%.

B-Layer

Considering nominal fluence the B-layer's sensors will have a depletion voltage of $\approx$ 450 V after five years (see Table 11.4) which was the originally planned operation time without replacement of this layer. The critical voltage of 600 V will be exceeded after about six years. With a fluence increased by 50% the depletion voltage will be at ≈ 620 V, therefore the B-layer will certainly be operable for 5 years.

After ten years of operation at nominal fluence the depletion voltage will reach almost 1 100 V which corresponds to a depleted thickness of $\approx 185\,\mu$m if the sensor is biased with 600 V. Depending on the FE electronics this may still be enough to operate the B-layer.

year [a]	Φ_{eq} [$10^{14}\,n_{eq}/cm^2$]		$V_{dep,0}$ [V]		$V_{dep,1}$ [V]		$V_{dep,min}$ [V]		$V_{dep,2}$ [V]	
1	0.60	(0.90)	59	(57)	34	(51)	24	(37)	28	(42)
2	1.92	(2.88)	29	(44)	104	(156)	83	(124)	93	(136)
3	3.96	(5.94)	95	(139)	211	(312)	178	(262)	193	(280)
4	6.36	(9.54)	196	(283)	332	(487)	294	(428)	313	(449)
5	8.76	(13.13)	315	(452)	452	(656)	415	(598)	435	(622)
6	11.15	(16.73)	438	(626)	575	(830)	538	(772)	561	(799)
7	13.55	(20.33)	563	(802)	700	(1007)	664	(950)	688	(978)
8	15.95	(23.93)	691	(982)	828	(1187)	792	(1131)	817	(1162)
9	18.35	(27.53)	820	(1165)	957	(1370)	922	(1315)	948	(1348)
10	20.75	(31.12)	951	(1351)	1088	(1557)	1053	(1502)	1081	(1537)

Table 11.4: Depletion voltages for B-layer. $V_{dep,0}$ denotes the depletion voltage at the beginning of a year, $V_{dep,1}$ is the depletion voltage after the irradiation and $V_{dep,2}$ is its value at the end of the respective year. Fluences are given after the respective's year beam period. Values in parentheses give the values for fluence increased by 50%.

11.2.4 Leakage Current

Annual Development

Fig. 11.7 shows the expected development of the leakage current for ATLAS operation. The right axis gives the leakage current of a module (sensor tile with dimensions 6.08 cm × 1.64 cm × 0.025 cm). All leakage current densities and leakage currents are given for 0°C. The inset in Fig. 11.7 shows the development of leakage current for one beam period: during beam time it rises. After the beam time it shows only a decrease which stops when the detector is cooled down again for storage. Contrarily to the depletion voltage reverse annealing does not occur. Tables 11.5 and 11.6 contain the results for leakage current generation rates G_{leak} for layer 1 and B-layer, respectively.
The given numbers in Fig. 11.7 refer to fully depleted sensors even when $V_{dep} > 600\,V$. In case of incomplete depletion the leakage currents are lower since they are generated only in the depleted volume. Fig. 11.8 shows the leakage currents with considered partial depletion.

Current Limits

The sensors of layer 1 will reach a leakage current of $\approx 850\,\mu A$ for nominal fluence. For 150% of nominal fluence the leakage current is already limited by partial depletion.
In B-layer the leakage currents are already strongly suppressed by partial depletion. Even with 150% of nominal fluence the leakage current per pixel stays below the limit of 50 nA. This limit is critical since the leakage current per pixel must not exceed the specification of the front-end electronics, too high leakage current increases the noise.

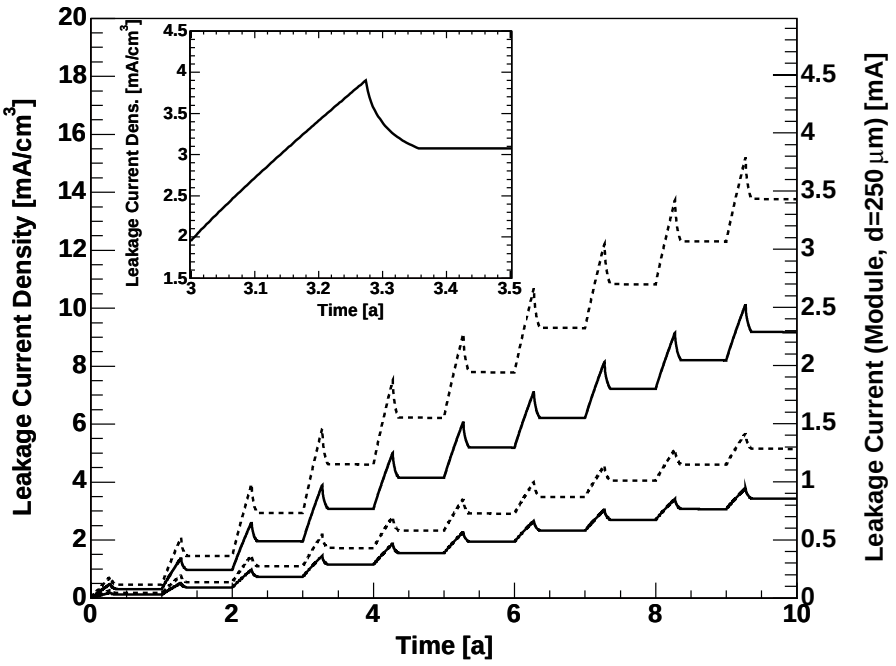

Fig. 11.7: Development of leakage current density and leakage current for module for B-layer and layer 1 for the ATLAS standard scenarion at 20°C. The inset shows a magnification of the large plot.

year	Φ_{eq}		$G_{leak,0}$		$G_{leak,1}$		$G_{leak,2}$	
	$[10^{14}\ n_{eq}/cm^2]$		$[mA/cm^3]$		$[mA/cm^3]$		$[mA/cm^3]$	
1	0.22	(0.34)	0.013	(0.020)	1.006	(1.509)	0.676	(1.015)
2	0.72	(1.08)	0.705	(1.058)	2.879	(4.318)	2.109	(3.163)
3	1.48	(2.22)	2.154	(3.231)	5.503	(8.254)	4.261	(6.392)
4	2.38	(3.57)	4.314	(6.471)	8.240	(12.359)	6.704	(10.057)
5	3.27	(4.91)	6.757	(10.136)	10.669	(16.003)	9.049	(13.573)
6	4.17	(6.26)	9.101	(13.652)	13.005	(19.508)	11.329	(16.993)
7	5.07	(7.60)	11.381	(17.072)	15.280	(22.920)	13.559	(20.339)
8	5.97	(8.95)	13.612	(20.418)	17.506	(26.259)	15.749	(23.623)
9	6.86	(10.29)	15.801	(23.702)	19.692	(29.538)	17.904	(26.855)
10	7.76	(11.64)	17.956	(26.934)	21.843	(32.765)	20.028	(30.042)

Table 11.5: Leakage current generation rates for layer 1. $G_{leak,0}$ denotes the generation rate at the beginning of a year, $G_{leak,1}$ is the generation rate after the irradiation and $G_{leak,2}$ is its value at the end of the respective year. Fluences are given after the respective's year beam period. Values in parentheses give the values for fluence increased by 50%.

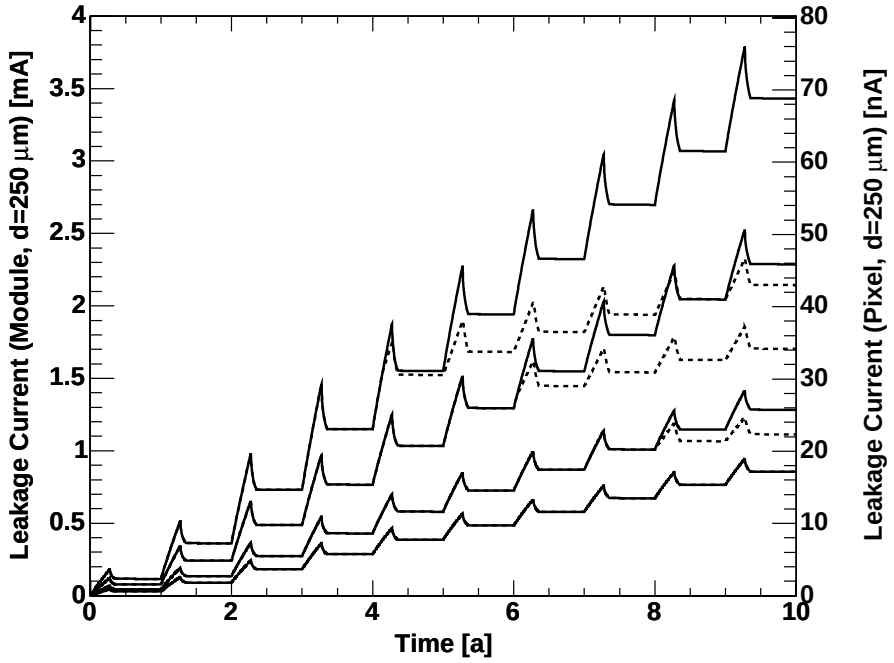

Fig. 11.8: Development of module leakage current at 0°C for B-Layer (two upper solid lines) and layer 1 (two lower solid lines) with fully depleted sensors. The two lines belonging to the same layer correspond to 100% and 150% of nominal fluence. The dotted lines give the leakage currents if partial depletion is considered. The depletion depths were calculated with the depletion voltages from Fig. 11.6. The right axis gives the leakage current for single pixel cells ($400\,\mu\text{m} \times 50\,\mu\text{m}$).

year	Φ_{eq} [$10^{14}\,n_{\text{eq}}/\text{cm}^2$]		$G_{\text{leak},0}$ [mA/cm^3]		$G_{\text{leak},1}$ [mA/cm^3]		$G_{\text{leak},2}$ [mA/cm^3]	
1	0.60	(0.90)	0.04	(0.05)	2.69	(4.03)	1.81	(2.71)
2	1.92	(2.88)	1.89	(2.83)	7.70	(11.55)	5.64	(8.46)
3	3.96	(5.94)	5.76	(8.64)	14.71	(22.07)	11.39	(17.09)
4	6.36	(9.54)	11.54	(17.30)	22.03	(33.05)	17.93	(26.89)
5	8.76	(13.13)	18.07	(27.10)	28.53	(42.79)	24.20	(36.29)
6	11.15	(16.73)	24.34	(36.50)	34.78	(52.16)	30.29	(45.44)
7	13.55	(20.33)	30.43	(45.65)	40.86	(61.29)	36.26	(54.39)
8	15.95	(23.93)	36.40	(54.60)	46.81	(70.22)	42.11	(63.17)
9	18.35	(27.53)	42.25	(63.38)	52.66	(78.98)	47.87	(71.81)
10	20.75	(31.12)	48.01	(72.02)	58.41	(87.61)	53.55	(80.33)

Table 11.6: Leakage current generation rates for B-layer. $G_{\text{leak},0}$ denotes the generation rate at the beginning of a year, $G_{\text{leak},1}$ is the generation rate after the irradiation and $G_{\text{leak},2}$ is its value at the end of the respective year. Fluences are given after the respective's year beam period. Values in parentheses give the values for fluence increased by 50%.

11.2.5 Power Consumption

The leakage current causes not only noise in the read-out electronics but also contributes to the power consumption of the module. The resulting heating-up has to be considered for the design of the cooling system. Fig. 11.9 shows the development of the power consumption due to leakage current in one sensor tile vs. operation time. The power consumption is calculated by $P_{\text{leak}} = V_{\text{bias}} \cdot I_{\text{leak}}$. Towards high fluences its increase becomes slower due to more slowly increasing leakage currents (due to partial depletion) and the limitation of the maximum bias voltage to 600 V.

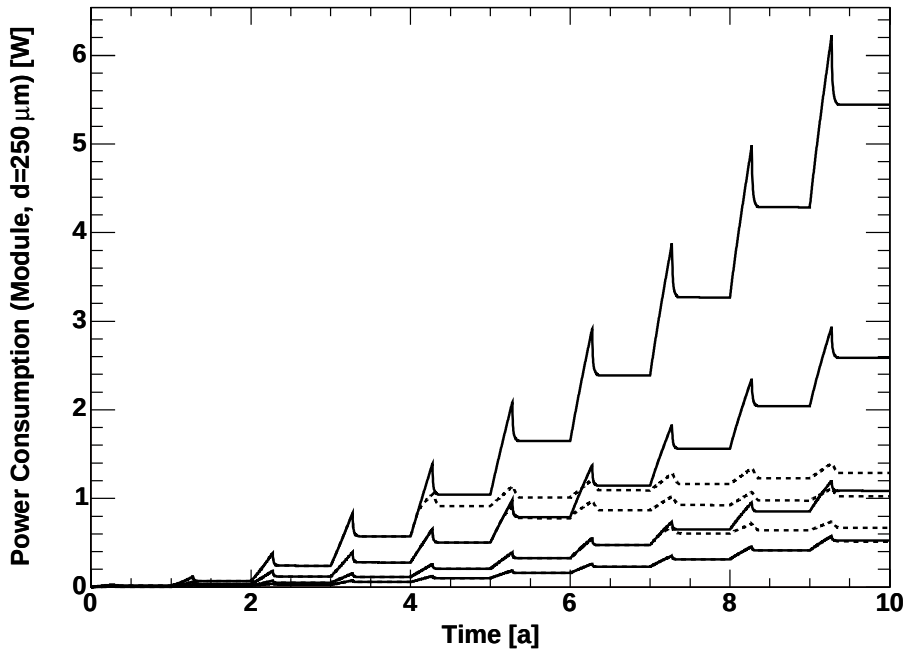

Fig. 11.9: Development of sensor tile power consumption at 0°C for B-Layer (two upper solid lines) and layer 1 (two lower solid lines) with fully depleted sensors. Two lines belonging to the same layer correspond to 100% and 150% of nominal fluence. Dotted lines give the leakage currents if partial depletion is considered. The depletion depths were calculated with the depletion voltages from Fig. 11.6.

11.3 Dependence on Radius

Before deciding to change the radii[1] of the pixel detector's layers from the values given in [AT98] simulations were done in order get estimations for the performance at the new positions. Fig. 11.10 shows the results for the depletion voltage at various radii after 5 and 10 years of operation. For the calculation of the fluence and temperature profiles the ATLAS standard scenario has been used. The fluences at the different radii have been calculated with eqs. (11.1)–(11.3).

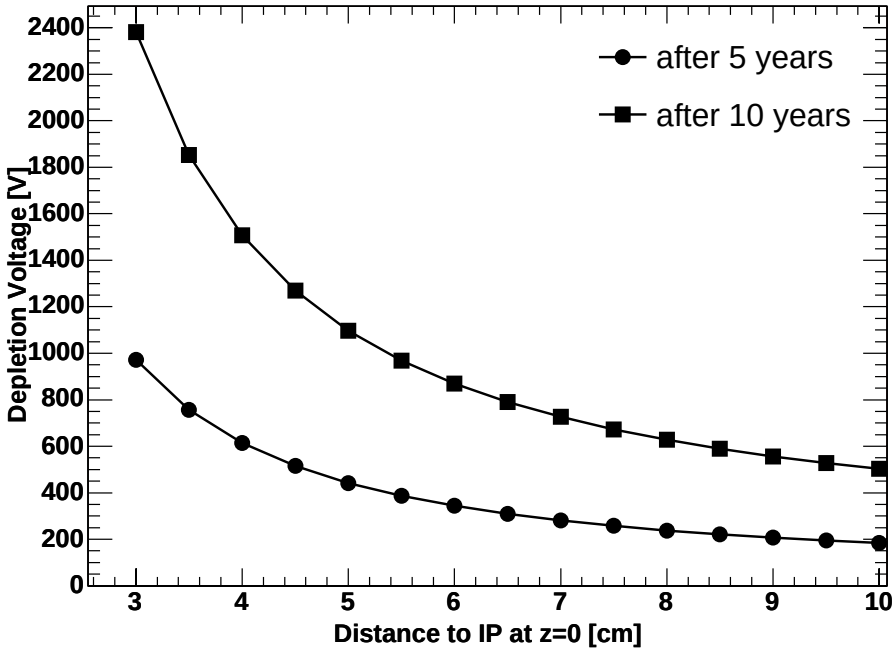

Fig. 11.10: Depletion Voltage vs. radius at $z = 0$ for 250 μm thick sensors after 5 and 10 years of operation with the ATLAS standard scenario. The lines are guides to the eye.

As a result of this study placing the sensors at the new position was considered feasable. Additionally, the data shown in Fig. 11.10 can be used to estimate the consequences of an off-center placement in the r-ϕ-plane of the whole pixel-detector with respect to the IP position. For instance, a displacement by 5 mm will lead to radial positions of 4.5 cm and 5.5 cm for the B-layer which is normally situated at 5.05 cm. After five years this would result in a depletion voltage of 515 V for the closest part of B-layer and 385 V for the farther part instead of 440 V at the nominal position.

[1] The pixel detector was redesigned in order to allow inserting it after the other components of the Inner Detector are installed. Therefore, the outer dimensions had to be decreased by reducing the radii of layers 1 and 2. Since these two layers were now closer to the IP, the B-layer could be moved outwards in order reduce its radiation load.

11.4 Extended Access Scenarios

An annually warm-up period of 30 days at 20°C for maintenance is included in the ATLAS standard scenario. However, maintenance or possible detector upgrades may require additional and longer warm-up periods since the detector can be handled only at room temperature. For the leakage current such additional warm-ups have only beneficial effects but the depletion voltage may increase significantly. Therefore, a scenario with extended access after the second beam period is given as an example. Fig. 11.11 shows the variation of the depletion voltage after 5 years

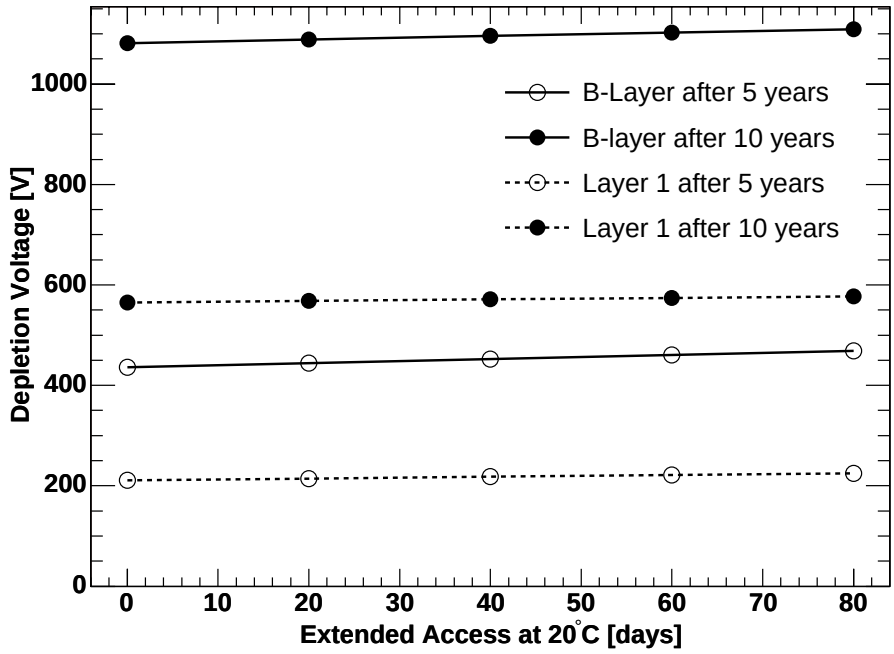

Fig. 11.11: Depletion voltage after 5 and 10 years for B-layer and layer 1 for several lengths of additional maintenance times at 20°C.

and 10 years if such an extended maintenance access is done once after the second beam period. From the results can be concluded that even a quite long extended access period of up to 80 days has only a small effect on the depletion voltage. This can be explained by the fact that the beneficial annealing has already finished during the regular access and the reverse annealing has a large time constant. This is an important result for the ATLAS pixel detector since it allows to exchange parts of it without having to work in a cold atmosphere.

11.5 Pulse Shape and Electric Field

11.5.1 Model of Pixel Detector

The model which is chosen to describe the pixel sensors within the simulation uses some simplifications for the detector geometry:

- The electric field is considered to be that of a pad-detector. It will be calculated with the same algorithms which have been used in chapter 10. Especially modifications of the electric fields by surface effects are neglected, the whole detector surface at the n-side is considered to be on the same potential.

  This restricts the charge drift to the x-direction and eases therefore the drift calculation since a one-dimensional implementation of the electric field and usage of the profile of the Ramo-field along the drift path are sufficient.

- The pixel cells of an ATLAS sensor have dimensions of $400\,\mu$m $\times$ $50\,\mu$m. However, in order to be able to use a two-dimensional simulation the sensor is approximated in simulation by a strip detector having $50\,\mu$m pitch, $30\,\mu$m wide implantations and infinite long strips. This approximation has its largest accuracy at the centre of the long side of the pixel cell and deteriorates towards the ends of the pixel cells.

11.5.2 Ramo-Potential

The Ramo potential is calculated by the method decribed in sec. 9.4. For the simulation of pixel sensors the Ramo-potential is calculated on a lattice with n_x = 51 and n_y=71 points in the x- and y-direction, respectively. The results for the potential and the Ramo fields are shown in Figs. 9.4 and 9.6. This lattice size results for a $250\,\mu$m thick sensor in a spatial resolution of $5\,\mu$m. In order to obtain also the values between the lattice points a parabolic interpolation between three points is used. Fig. 11.12 shows the numeric result for the Ramo field (markers) together with its interpolation (solid line). Additionally, this figure shows the Ramo field of a pad-detector of same thickness for comparison.
From the integral of the Ramo-field—which is also shown in Fig. 11.12—it can be derived that a charge-carrier drifting from the p-side to the n-side deposites 90% of its signal on the last $100\,\mu$m and 50% on the last $20\,\mu$m of its drift-path.

11.5.3 Unirradiated Sensor

As a first step in simulating pixel sensors the signal shapes for an unirradiated sensor has been calculated using a linear electric field as described by eq. (3.53). The charge deposition profile in the simulation is mip-like, i.e. the charge is equally distributed along the x-direction. Fig. 11.13 shows the resulting signal shape for a pad-detector. This figure shows separately the contributions from drifting electrons and holes and the resulting sum. The next figure, Fig. 11.14, shows the same

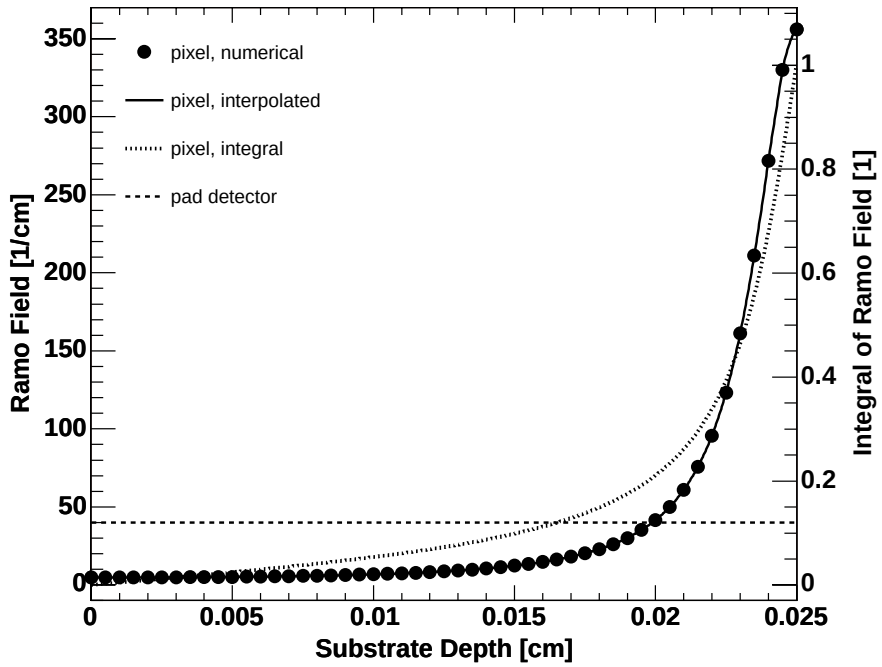

Fig. 11.12: Ramo-Field in x-direction for pad-detector (dashed line) and pixel-detector (solid line). For the pixel detector the Ramo field is taken at the centre of the pixel ($y = y_c$). Markers indicate the numeric results obtained from RACALC with a 5 μm lattice, the solid line shows the parabolic interpolation. The dotted line gives the integral of the Ramo-field. Both detectors are 250 μm thick.

calculation using the Ramo field of an infinite strip detector. A comparison of the two last simulations shows a significant difference between the two detector types with respect to pulse shape. As expected, in the pixel detector the contribution from the electron signal is much larger than the hole signal.

In this pixel simulation the mip track is situated at y_c underneath the centre of the pixel in y-direction. Fig. 11.15 and 11.16 show the pulse shapes for varied offsets of up to 25 μm. For every offset the pulse shape $i(t)$ and its integral $Q(t)$ is plotted. If the mip-track is situated underneath the pixel-implantation (up to y_c+15 μm) the pulse shape stays almost the same for holes and electrons. Electrons contribute $\approx$ 85% of the total signal as can be seen on the Q vs. t plots. For tracks displaced more than 15 μm from the centre—i.e. those which are no longer under the implantation—the induced charges are zero at the end of the charge collection time. This effect is expected in the simulation because these charge-carriers do not reach the read-out area. However, this behaviour is unrealistic since test beam results show a rather homogeneous charge collection efficiency over the whole sensor area. The deviation of the simulation from measurement can be explained by the wrong electric field: in reality the field lines would be bent towards the implantations in the region bounding the surface. The simulation of

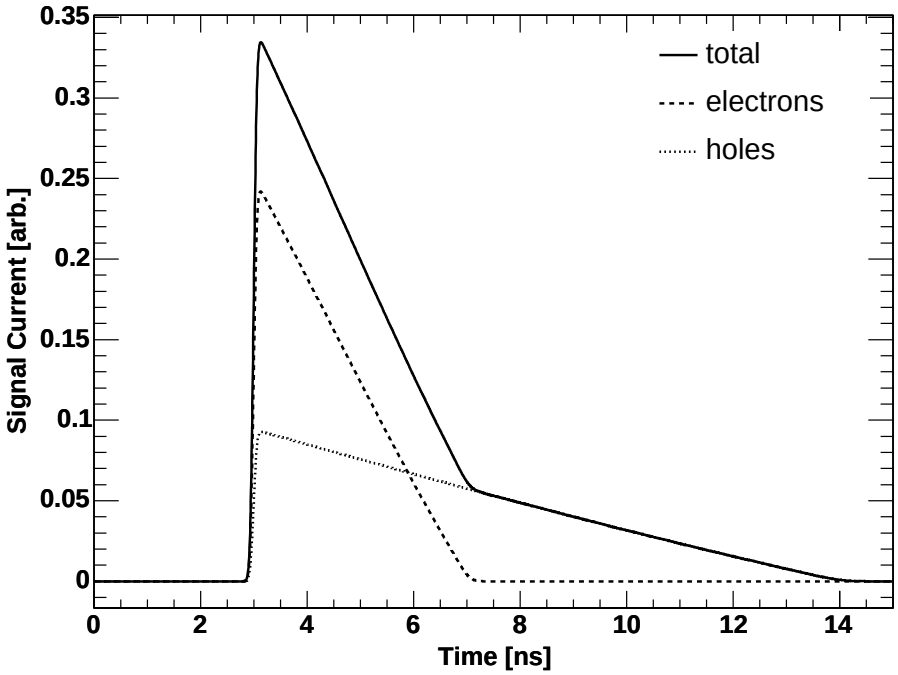

Fig. 11.13: Pulse shape of an unirradiated-pad detector for mip-like charge deposition ($d = 250\,\mu$m, $V_{\mathrm{dep}} = 70\,$V, $V_{\mathrm{bias}} = 150\,$V).

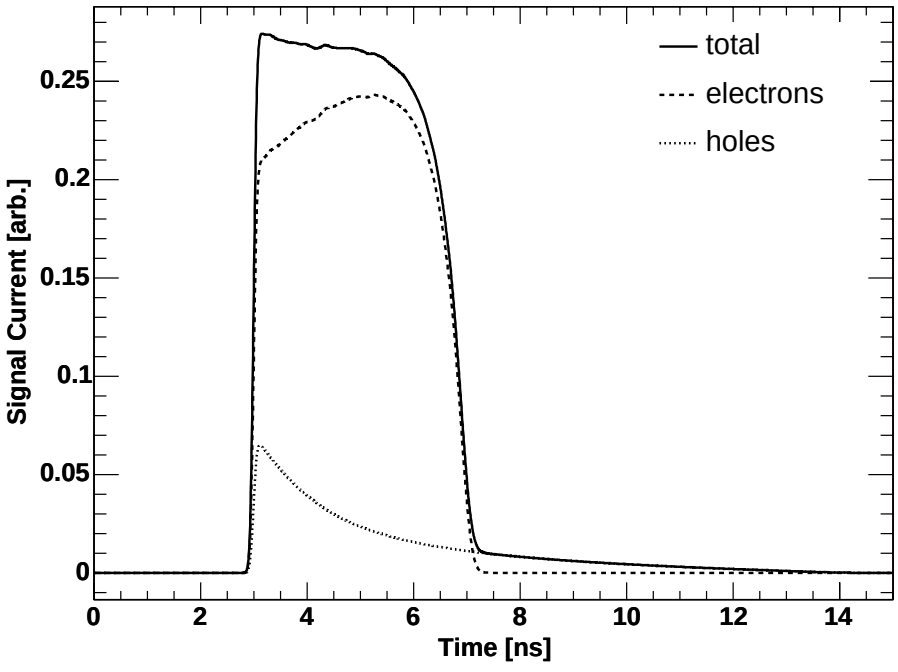

Fig. 11.14: Pulse shape of an unirradiated pixel-detector for mip-like charge deposition under the centre of a pixel ($y = y_c$, $d = 250\,\mu$m, $V_{\mathrm{dep}} = 70\,$V, $V_{\mathrm{bias}} = 150\,$V).

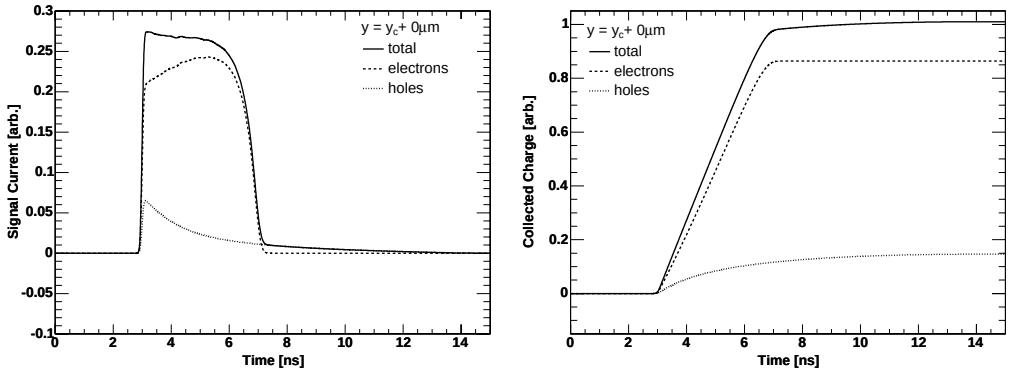

(a) $y = y_c$

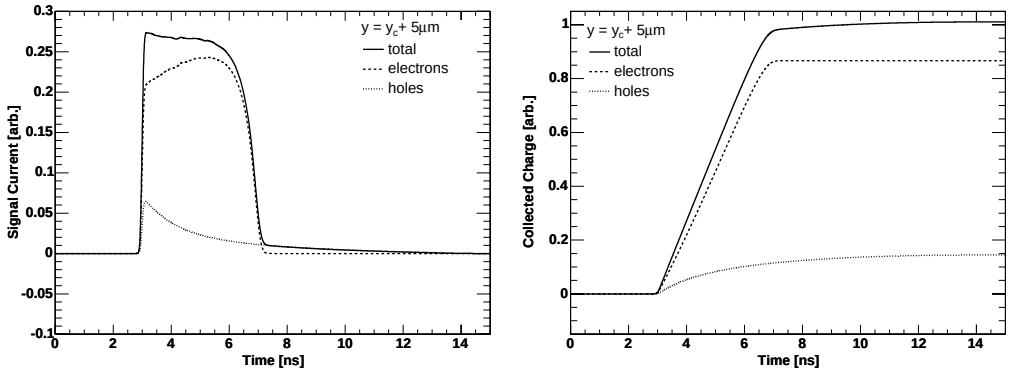

(b) $y = y_c + 5\,\mu\mathrm{m}$

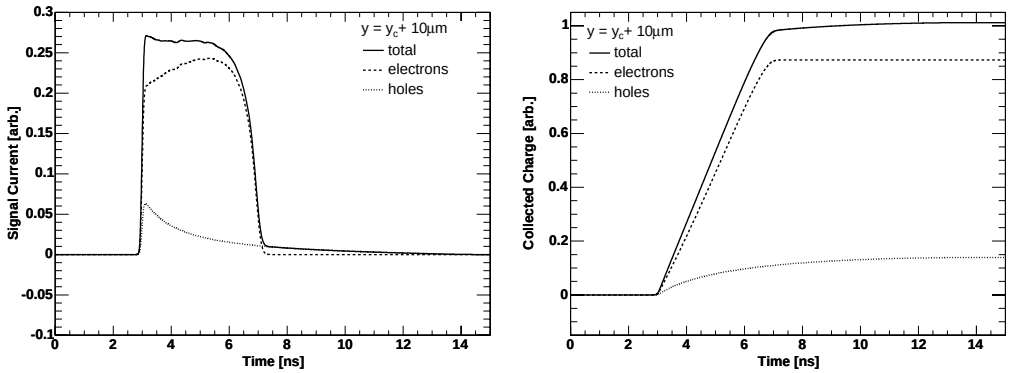

(c) $y = y_c + 10\,\mu\mathrm{m}$

Fig. 11.15: Pulse shapes and charges after mip-like charge deposition in a pixelised sensor for different distances to the pixel centre.

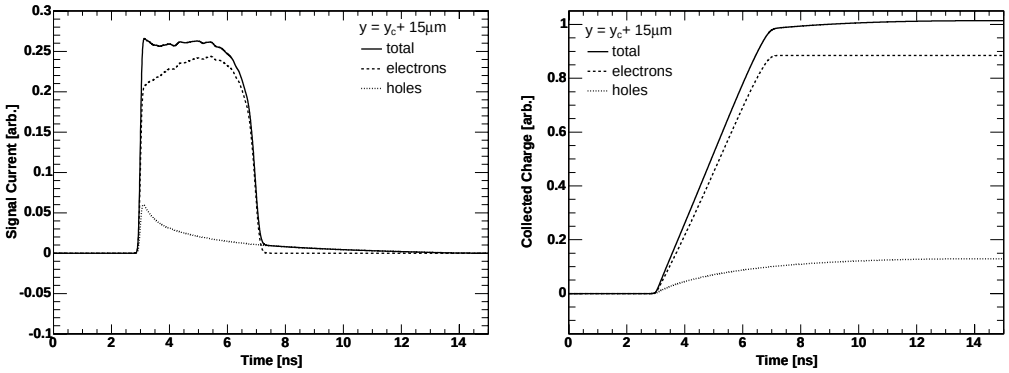

(a) $y = y_c + 15\,\mu\mathrm{m}$

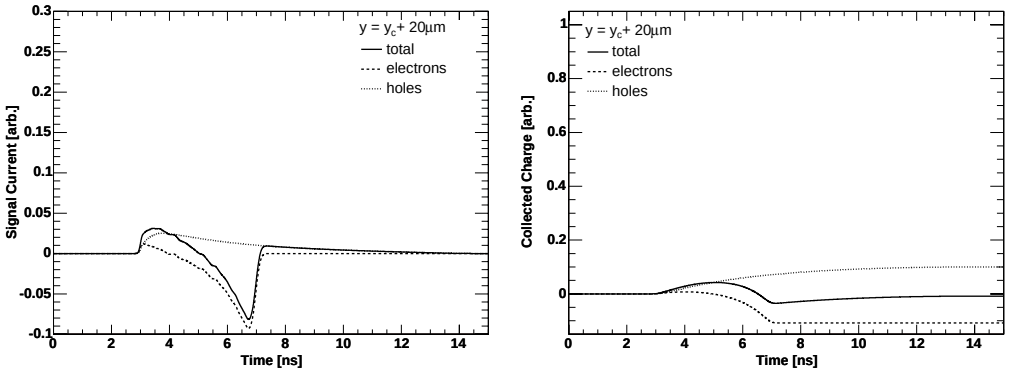

(b) $y = y_c + 20\,\mu\mathrm{m}$

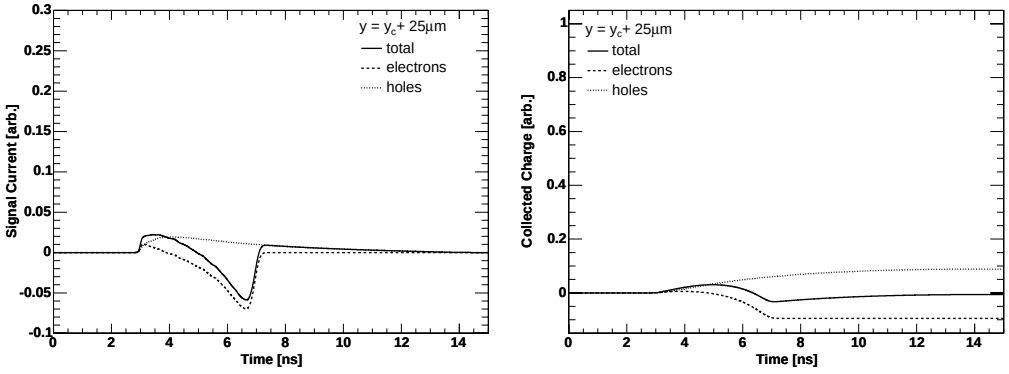

(c) $y = y_c + 25\,\mu\mathrm{m}$

Fig. 11.16: Pulse shapes and charges after mip-like charge deposition in a pixelised sensor for different distances to the pixel centre.

the real electric field is quite complicated since all charged surface states have to be considered.
Nevertheless, the simulation is considered as being realistic at least for tracks underneath the implantations. In the next section this detector geometry will be used for the simulation of irradiated detectors.

11.5.4 Irradiated Sensor

Model

The simulation of irradiated sensors uses the following model to describe the irradiation and the electric field:

- Equivalent fluences of protons and neutrons are given by the ATLAS standard scenario. This scenario is also used to obtain numbers for the depletion voltages and the leakage current generation rates which are needed for the deep level model. The bias voltage is set to be 50 V above full depletion but minimum 150 V and maximum 600 V.

- Above full depletion the electric field in the sensor is described by the deep level model which has already been used for the simulation of pad-detectors in chapter 10. Different from these simulations now irradiation in a mixed field has to be considered. Thus the concentrations of deep levels have to be calculated in a modified way:

  - For the deep acceptor concentration N_{DA} an averaged value from proton- and neutron-irradiation is taken. The contributions from proton- and neutron-irradiation are weighted with η_c and $1-\eta_c$; η_c is the charged fraction of radiation:

    $$N_{\mathrm{DA}} = \eta_c \cdot N_{\mathrm{DA},p} + (1-\eta_c) \cdot N_{\mathrm{DA},n} \,. \tag{11.4}$$

  - The introduction rate for deep donors g_{DD} is averaged accordingly:

    $$g_{\mathrm{DD}} = \eta_c \cdot g_{\mathrm{DD},p} + (1-\eta_c) \cdot g_{\mathrm{DD},n} \,. \tag{11.5}$$

  In order to take into account the problems of the deep level model at bias voltages below V_{dep} a model with an electric field that depends linearly on substrate depth is used for this bias voltage range (see eq. (4.5)). The maximum of the field is situated at the n-side, its slope corresponds to the doping concentration as given by the Hamburg model. The part of the bulk which is adjacent to the p-side remains undepleted and has zero electric field. This approximation is valid since charges deposited in the region near the p-side will anyway contribute only little to the total signal since they start their drift in a low electric field region. Before they start to move quickly they have already suffered from trapping and only a small fraction will drift through the highly weighted region close to the sensor's n-side.

- The values for the inverse trapping times are also calculated by averaging the introduction rates obtained from measurement on proton- and neutron-irradiated samples:

$$\gamma_e = \eta_c \cdot \gamma_{p,e} + (1 - \eta_c) \cdot \gamma_{n,e} \quad \text{and} \tag{11.6}$$

$$\gamma_h = \eta_c \cdot \gamma_{p,h} + (1 - \eta_c) \cdot \gamma_{n,h} \; . \tag{11.7}$$

  The annealing of the effective trapping times is not considered in the simulation but the values measured in the minimum of V_{dep} during annealing are used. This is considered being justified since the trapping probabilities reach a saturation after a while and do not change any more. The consequences of annealing are investigated later in a worst case consideration.

Electric Field

Fig. 11.17 and 11.18 show the electric fields in the sensors during ten years of layer 1 operation. For every year the calculation has been done with the numbers for depletion voltage and leakage current generation rate G taken at the end of the access period of the respective year. The plots of the electric field show no double peak configuration as would be expected from the measurements and simulations of the pad-detectors done before. This result can be explained by the long accumulated annealing time at room temperature. Therefore, the leakage current is significantly lower than for the pad-detectors considered in this work. The lower leakage current results in lower occupation probabilities for deep levels and thereby less positive charge at the p-side of the sensor.
The electric fields in the sensors of the B-layer are shown in Fig. 11.19 and 11.20. In this layer the leakage current becomes high enough to cause a double peak field configuration after five years of operation. A further difference compared to layer 1 is that after five years with a maximum bias voltage of 600 V only partial depletion is possible in the linear field model while the deep level model still predicts full depletion. For years 7–10 the deep level model fails in converging to a realistic field.
For both layers the electric fields derived from the deep level model are quite similar to the linear approximation in the sensor part adjacent to the n-side. Towards the p-side the difference between the two models increases as expected. In the next section it will be investigated how large the differences in the calculated CCE are.

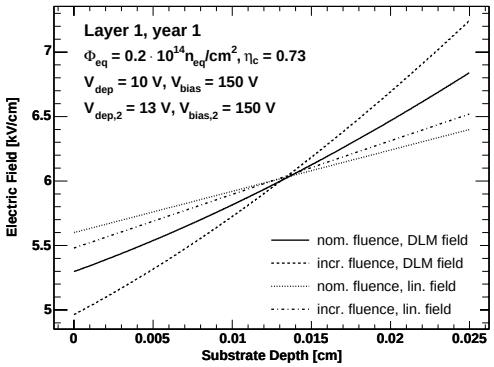

(a) year 1

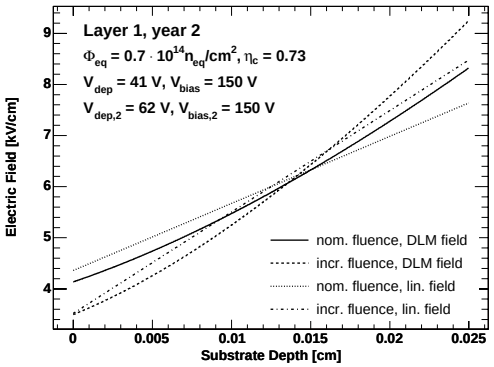

(b) year 2

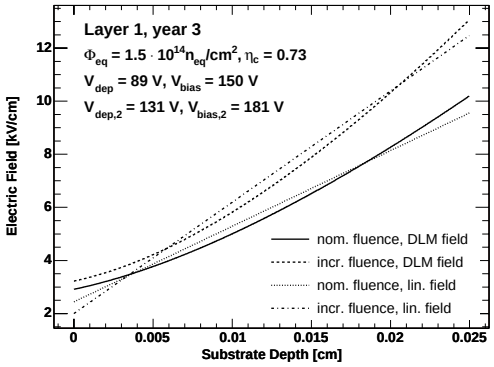

(c) year 3

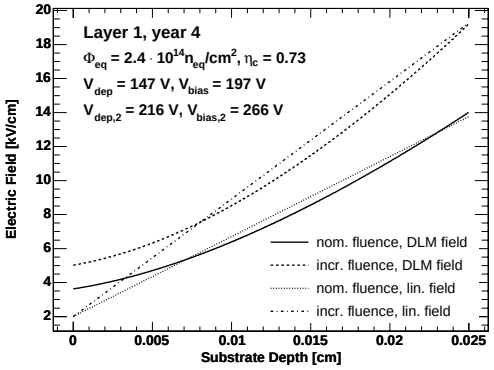

(d) year 4

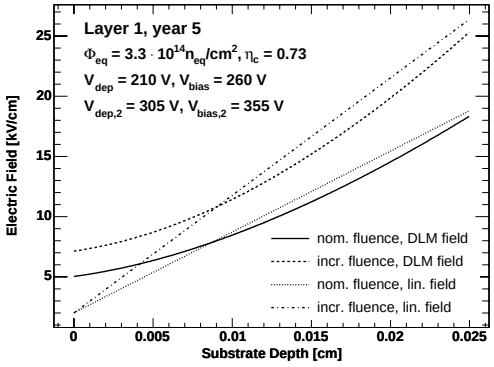

(e) year 5

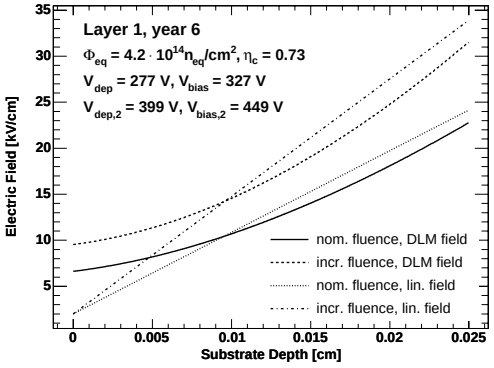

(f) year 6

Fig. 11.17: Electric field distribution in ATLAS sensors in layer 1. The calculation is done with the ATLAS standard scenario. Solid lines give electric field for nominal fluence, dashed lines for 150% of nominal fluence (both calculated with deep level model for electric fields), dotted and dashed-dotted lines give results with linear field approximation for nominal and increased fluences, respectively.

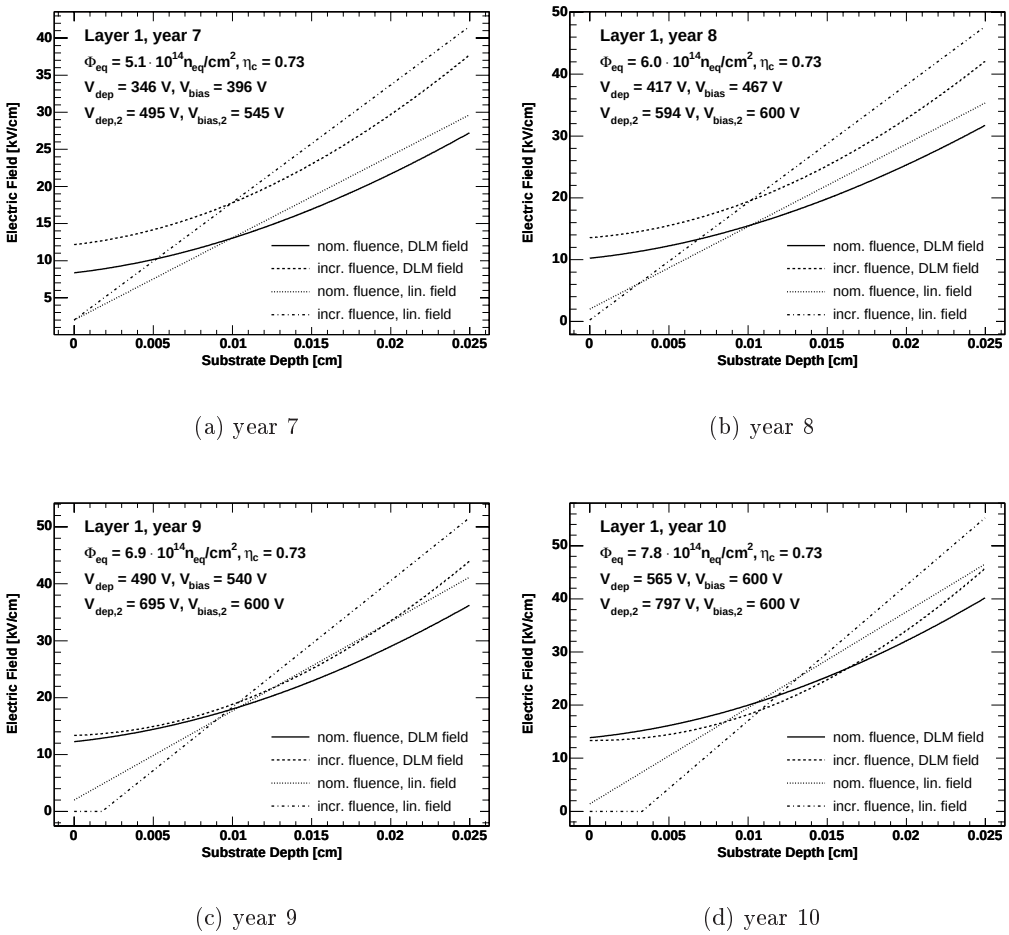

(a) year 7

(b) year 8

(c) year 9

(d) year 10

Fig. 11.18: Electric field distribution in ATLAS sensors in layer 1. The calculation is done with the ATLAS standard scenario. Solid lines give electric field for nominal fluence, dashed lines for 150% of nominal fluence (both calculated with deep level model for electric fields), dotted and dashed-dotted lines give results with linear field approximation for nominal and increased fluences, respectively.

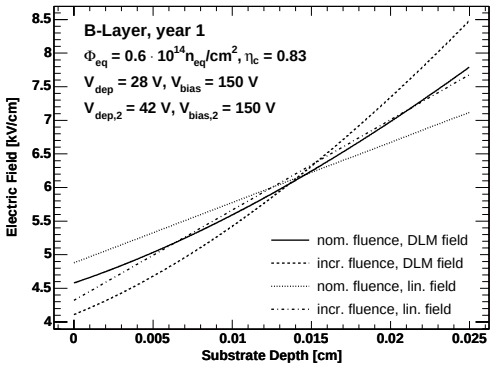

(a) year 1

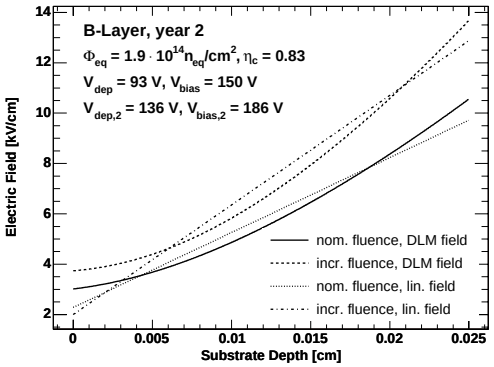

(b) year 2

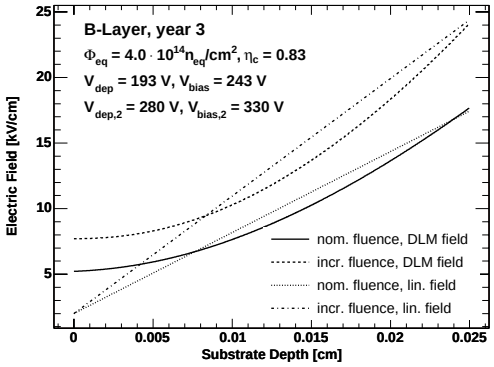

(c) year 3

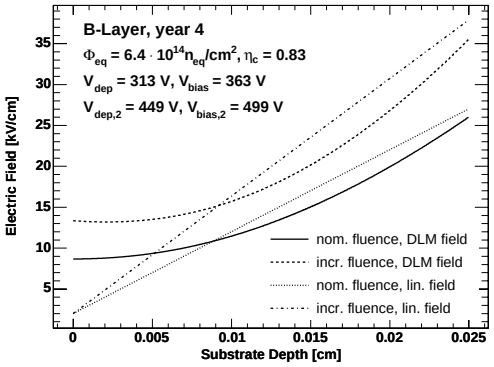

(d) year 4

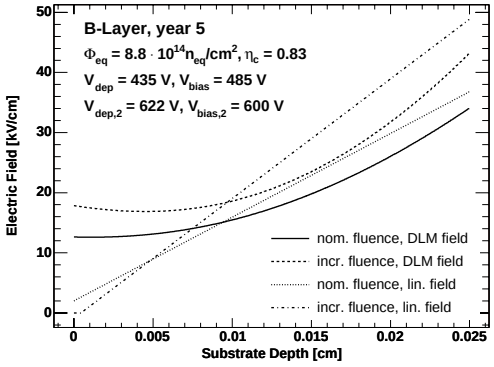

(e) year 5

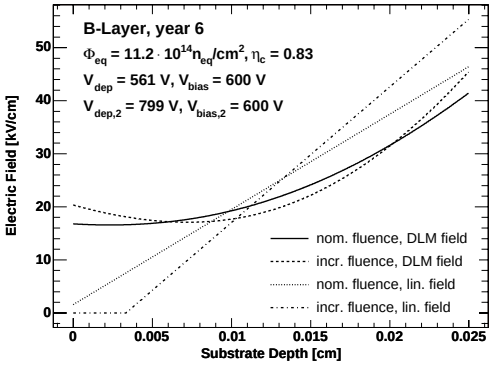

(f) year 6

Fig. 11.19: Electric field distribution in ATLAS sensors in B-layer. The calculation is done with the ATLAS standard scenario. Solid lines give electric field for nominal fluence, dashed lines for 150% of nominal fluence (both calculated with deep level model for electric fields), dotted and dashed-dotted lines give results with linear field approximation for nominal and increased fluences, respectively.

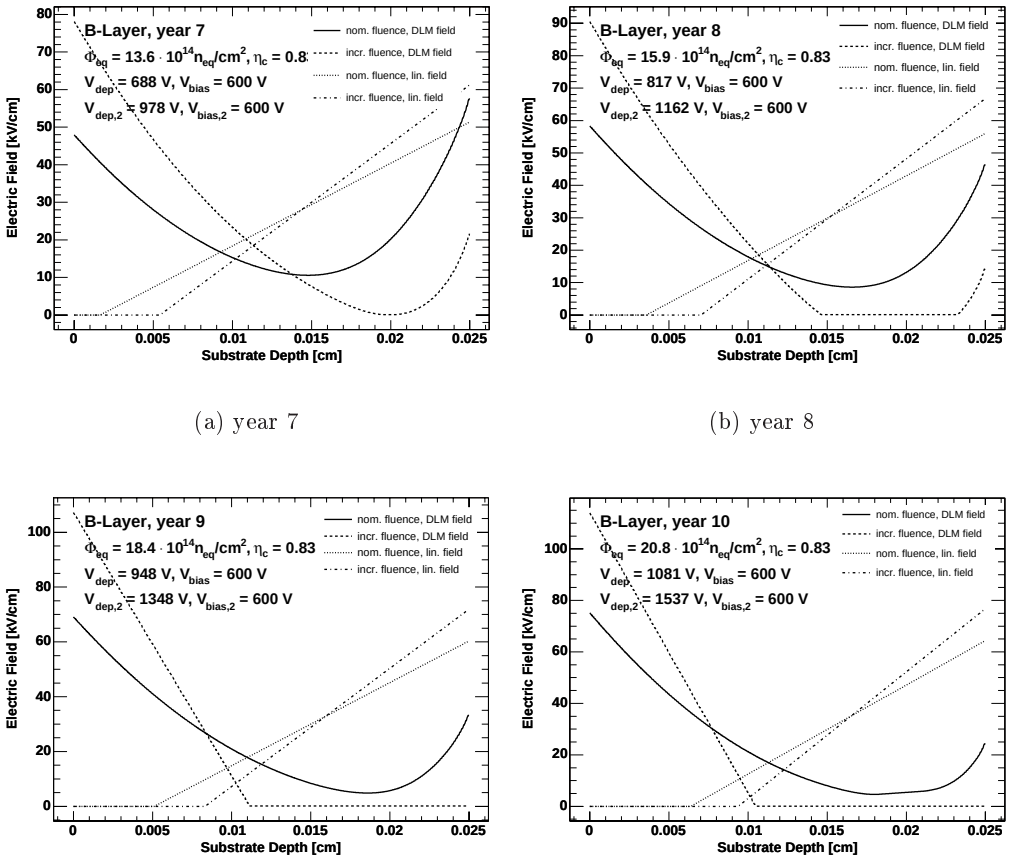

(a) year 7

(b) year 8

(c) year 9

(d) year 10

Fig. 11.20: Electric field distribution in ATLAS sensors in B-layer. The calculation is done with the ATLAS standard scenario. Solid lines give electric field for nominal fluence, dashed lines for 150% of nominal fluence (both calculated with deep level model for electric fields), dotted and dashed-dotted lines give results with linear field approximation for nominal and increased fluences, respectively. For these calculations the results obtained from the deep level model are considered to be wrong. See text for details.

11.6 Charge Collection Efficiency

11.6.1 ATLAS Standard Scenario

Fig. 11.21 shows the prediction for the charge collection efficiency of the sensors of layer 1 assuming the ATLAS standard scenario. The collected charge given in that plot corresponds to 95 keV deposited energy what is the mean energy loss of mips in 250 μm silicon. For nominal fluence the deep level model and the linear model for the electric field agree with each other well. For fluences increased by 50% the difference between the two models increases the linear model predicts a CCE which is lower by ≈ 0.05 compared to the deep level model field. This difference can be explained by the higher electric field towards the p-side in the latter model. In the linear model the sensor is no longer completely depleted (see Fig. 11.18).

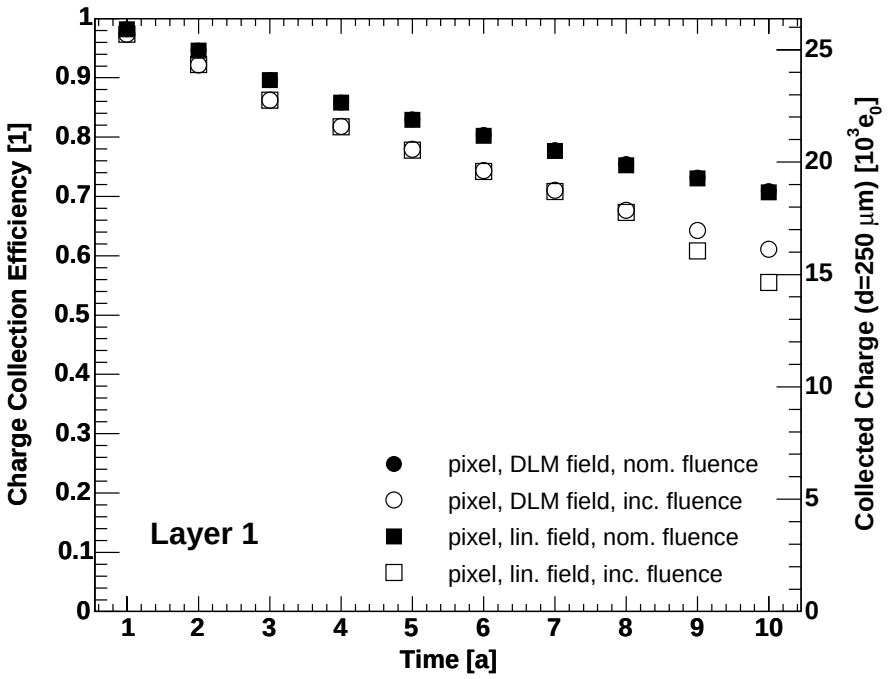

Fig. 11.21: Charge collection efficiency for the layer 1 vs. operation time with nominal and increased (+50%) fluence. For comparison the results from simulation with both models for electric field are given. The charge axis corresponds to 95 keV deposited energy (mean value of Landau).

The CCE for the B-layer's sensors is displayed in Fig. 11.22. The CCE drops to $\approx 60\%$ after five years which is the planned life-time of the B-layer. After ten years the prediction gives a CCE of $\approx 30\%$. For nominal fluence the two models

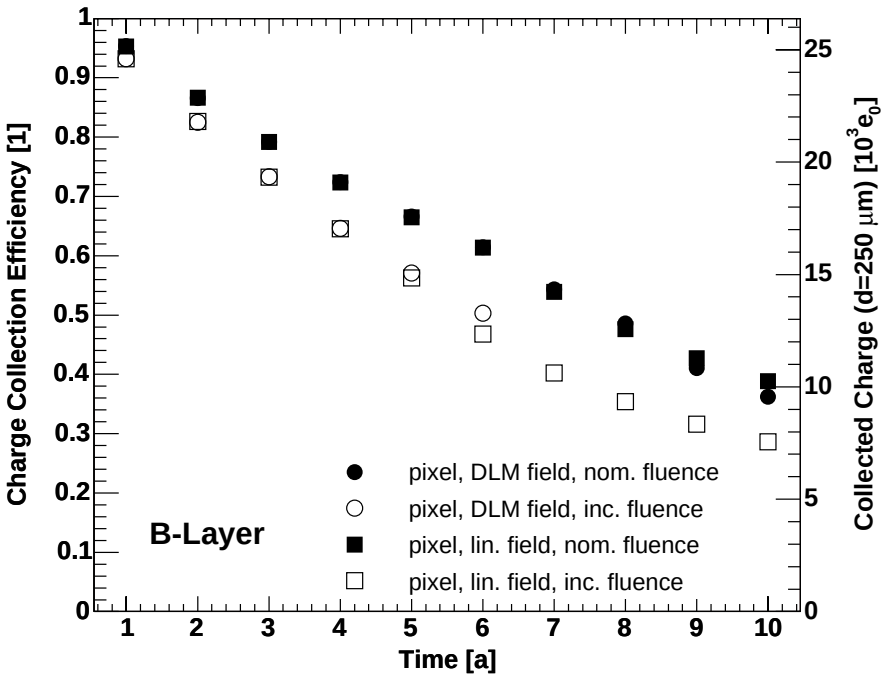

Fig. 11.22: Charge collection efficiency for the B layer vs. operation time with nominal and increased (+50%) fluence. For comparison the results from simulation with both models for electric field are given. The charge axis corresponds to 95 keV deposited energy (mean value of Landau).

for the electric field agree for almost every year. For increased fluence the deep level model fails in calculating the field after six years.
The good agreement between the two models for the electric field confirms that it is justified to approximate the electric field by a linear dependence on the substrate depth. However, it has to be remembered that this approximation works best for mips in pixel sensors. For pad-detector or close-to-surface charge injection—especially for p-side illumination—the results for CCE should differ much more. Considering the differences between measured and simulated CCEs for pad-detectors (sec. 10.3) a maximum systematic error of 0.1 for simulated CCEs should be assumed also for the CCE calculation of the pixel sensors. Table 11.7 compiles the CCE results.

11.6.2 Consequences of Trapping Time Annealing

The investigation of the annealing at elevated temperature in sec. 8.1.3 showed that the trapping probability $1/\tau_e$ for electrons decreases and reaches saturation. Its final value is about 20% lower than the initial value. For holes the trapping probability $1/\tau_h$ increases by up to 54%. In order to derive an estimation of the maximum influence of this annealing the simulation for layer 1 has been redone with γ_e decreased by 20% and γ_h increased by 50%. This resulted in an increase

year	CCE Q/Q_0 [1]								
	Layer 1				B-layer				S-LHC
	DLM		lin.		DLM		lin.		lin.
1	0.98	(0.97)	0.98	(0.97)	0.95	(0.93)	0.95	(0.93)	0.86
2	0.94	(0.92)	0.95	(0.92)	0.87	(0.83)	0.87	(0.83)	0.71
3	0.90	(0.86)	0.90	(0.86)	0.79	(0.73)	0.79	(0.73)	0.51
4	0.86	(0.82)	0.86	(0.82)	0.72	(0.65)	0.72	(0.65)	0.35
5	0.83	(0.78)	0.81	(0.78)	0.67	(0.57)	0.67	(0.56)	0.27
6	0.80	(0.74)	0.80	(0.74)	0.61	(0.50)	0.61	(0.47)	0.22
7	0.78	(0.71)	0.78	(0.71)	0.54	—	0.54	(0.40)	0.19
8	0.75	(0.68)	0.75	(0.68)	0.49	—	0.48	(0.35)	0.16
9	0.73	(0.64)	0.73	(0.61)	0.41	—	0.43	(0.32)	0.15
10	0.71	(0.61)	0.71	(0.56)	0.36	—	0.39	(0.29)	0.13

Table 11.7: Results for charge collection efficiencies for layer 1 and B-layer assuming the ATLAS standard scenario with 250 μm thick sensors. Values in parenthesis are valid for fluences increased by 50%. Column "DLM" contains results from calculation with deep level model, column "lin." contains results from linear field model.

of charge collection efficiency of 3–4% after ten years: the worsening effect of increased hole trapping is more than cancelled out by the lessened trapping of electrons since they contribute significantly more to the signal than the holes.

11.6.3 Detection Probability

If a particle passage through the sensor is detected is not determined only by the charge collection efficiency as it has been calculaed in this chapter. A particle is detected if the collected charge exceeds after its passage a certain threshold which is defined by the read-out electronics. Since the deposited charge fluctuates statistically only a detection probability P_{det} can be given.

The amount of charge which is deposited within a pixel-cell also depends on wether the particle track crosses one or more neighbouring pixel-cells. If several cells are hit the deposited charge is split into several smaller charges which could be too small to exceed the trigger level. The fraction of such tracks influences P_{det} as well. However, their exact fraction can be determined only by simulation studies of the ATLAS detector. For these reasons, in the following the determination of P_{det} is restricted to the case of tracks which hit only one pixel-cell.

From eq. (3.4) follows that a mip deposits on average $\Delta E_{\text{av}} = 95\,\text{keV}$ by passing through 250 μm of silicon. This leads to the creation of $\approx 26\,400$ electron-hole-pairs. The variation of the energy loss is described by eq. (3.5). Numerical evaluation of this equation yields a corresponding most probable energy loss ΔE_{mp} of 89.3 keV. Fig. 11.23(a) shows a plot of the Landau distribution. For its calculation $\beta = 1$ has been assumed.

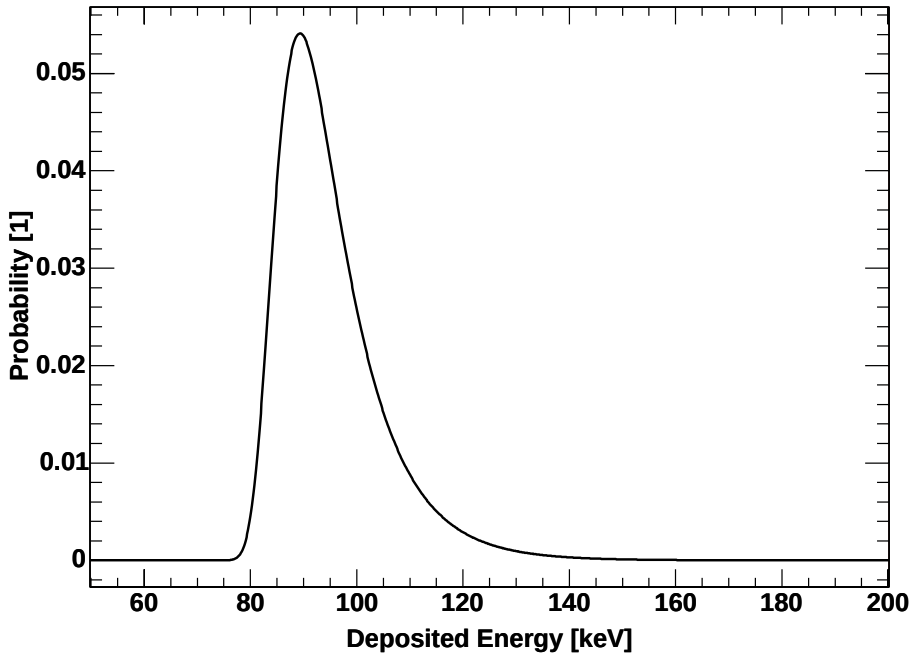

(a) Landau distribution.

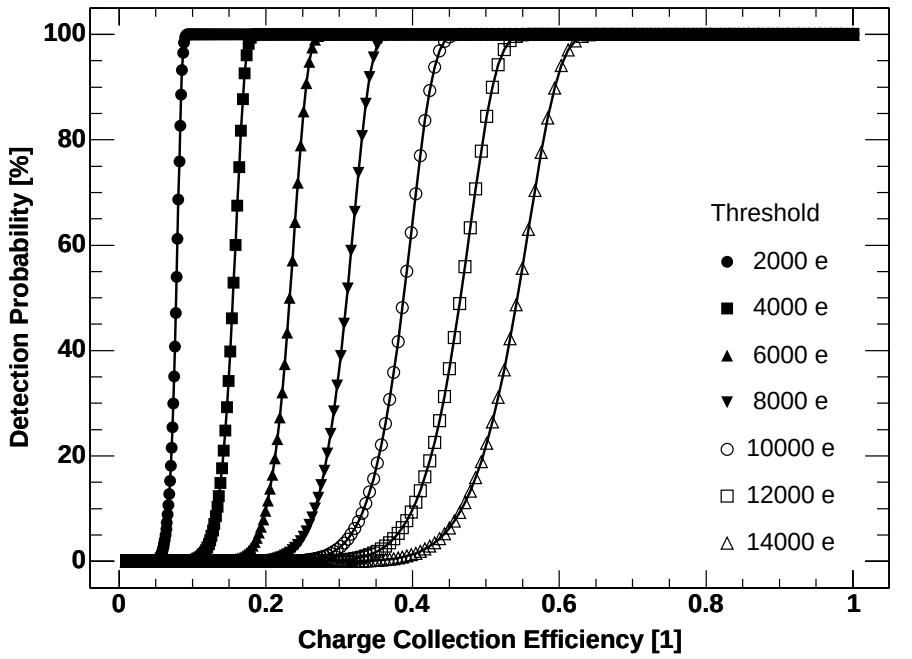

(b) Detection probability.

Fig. 11.23: (a) Landau distribution for 250 μm thick silicon sensor. The mean energy loss is 95 keV, the most probable energy loss is 89.3 keV. (b) Detection probability for mips depending on the sensor's charge collection efficiency for several trigger thresholds given in electron charges. See text for details.

In this simplified consideration the particle is detected if its deposited energy multiplied with the charge collection efficiency is above a certain trigger threshold E_{trig}. The trigger threshold is normally given in electron charges but it can be converted to an energy by considering that it takes 3.6 eV to create an electron-hole-pair. E_{trig} is calculated by

$$E_{\mathrm{trig}} = Q_{\mathrm{trig}} \cdot 3.6\,\mathrm{eV}/e_0\ . \tag{11.8}$$

Q_{trig} is the minimum required charge to trigger the read-out electronics and is given in electron charges e_0. The detection probability P_{det} for a given E_{trig} is given by

$$P_{\mathrm{det}} = \int_{E_{\mathrm{trig}}}^{\infty} L(\lambda(\Delta E))\,d\Delta E \Bigg/ \int_{0}^{\infty} L(\lambda(\Delta E))\,d\Delta E\ . \tag{11.9}$$

This equation shows that P_{det} falls with increasing trigger threshold E_{trig}. Fig. 11.23(b) shows plots of P_{det} vs. charge collection efficiency of the sensor for several trigger thresholds given in electron charges.
In unirradiated modules of the ATLAS pixel detector the threshold will be set to $2\,000\,e_0$. In irradiated modules ($\Phi_{\mathrm{eq}} = 10 \cdot 10^{14}\,n_{\mathrm{eq}}/\mathrm{cm}^2$) the threshold will be raised to $6\,000\,e_0$ in order to improve the signal-to-noise ratio. The sensor noise increases with irradiation due to higher leakage currents.
As can be seen in Fig. 11.23(b) P_{det} for a threshold of $6\,000\,e_0$ starts to drop if the CCE is below ≈ 0.30. Comparing this result with the numbers in Table 11.7 it can be concluded that the sensors in layer 1 will collect enough charge even after ten years of operation with increased fluence. Since its minimum CCE of 0.56 is well above the critical value of 0.30 this sensor will work well even with charge-sharing between neighbouring pixel-cells. The same conclusions apply for B-layer after five years of operation. After ten years of operation at increased fluence the CCE in B-layer will be still sufficient if charge-sharing plays no large role. Considering charge-sharing particle detection becomes less reliable since the CCE drops to the critical value of 0.30.
It has to be stated that the charge collection efficiencies and collected amounts of charge derived in this chapter are valid only for $250\,\mu$m thick pixel-detectors. The transfer to other thicknesses is not trivial since alongside different deposited charge—whose mean value is proportional to the sensor's thickness—the Ramo potential and field configuration change as well. This problem will be discussed shortly in the next section.

11.7 Super-LHC

Super LHC (SLHC) is an upgraded LHC which has a ten times higher luminosity. This will also lead to a radiation load being ten times higher. The sensors for trackers will have to stand up to $10^{16}\,n_{\mathrm{eq}}/\mathrm{cm}^2$ in this scenario. The data for charge

trapping taken in this thesis are used to make an estimation of the expected charge collection efficiency after ten times higher fluences than in LHC. For this purpose the ATLAS standard scenario for layer 1 is used with fluences being ten times higher. The field is described by the linear approximation. Fig. 11.24 shows the results for CCE. Numerical results are listed in Table 11.7. After ten years the

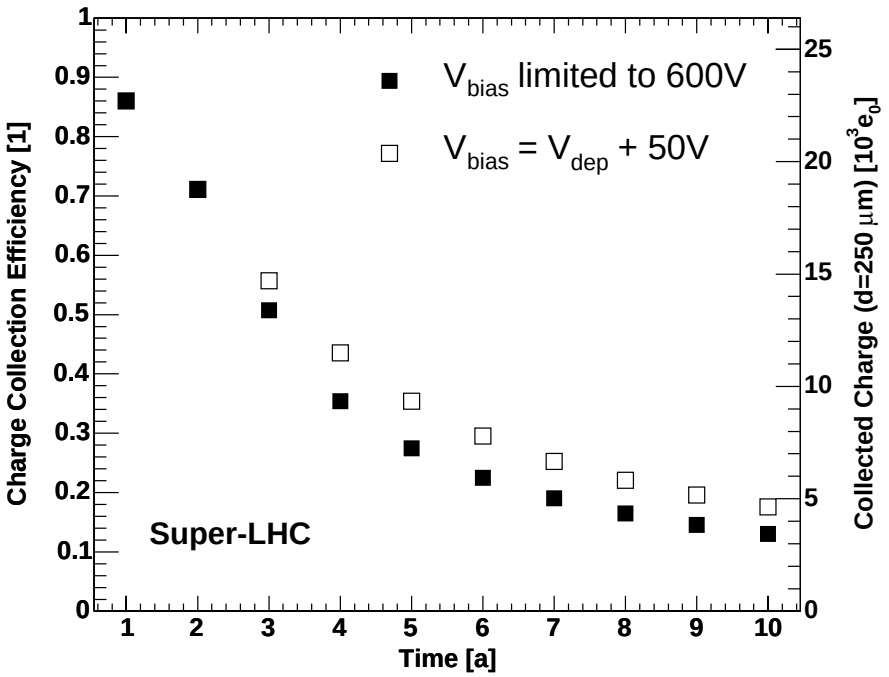

Fig. 11.24: Charge collection efficiency for layer 1 vs. operation time with fluences expected for the Super-LHC scenario. Close symbols show the results for V_{bias} limited to 600 V, open symbols show result for fully depleted pixel sensor ($V_{\mathrm{bias}} = V_{\mathrm{dep}} + 50\,\mathrm{V}$). The charge axis corresponds to 95 keV deposited energy (mean value of Landau).

charge collection efficiency drops to $\approx$ 13%. The bias voltage is assumed to be still limited to 600 V. The final value for V_{dep} is ≈ 4400 V, so the depletion depth of the sensor is only 92 μm. However, operation with $V_{\mathrm{bias}} = V_{\mathrm{dep}} + 50\,\mathrm{V}$ does not improve the CCE much since the region adjacent to the n-side is depleted anyway and 90% of the signal caused by a charge-carrier drifting from p- to n-side are induced on the last 100 μm (see sec. 11.5.2).
Therefore, it is useful to consider using thinner sensors with a thickness of only 200 μm. They have the advantage of introducing less detector material into the ATLAS detector and thereby reduce multiple scattering. Calculations show that roughly the same charge would be collected in 200 μm thick pixel-sensors after ten years of operation; the higher CCE of the thinner devices due to shorter drift-paths and larger depleted fraction of bulk is cancelled out by less deposited charge.

Details of the calculation are given in app. D.
Thus it can be concluded that using thinner sensors at very high fluences is not disadvantagous with respect to collected charge.

Part V

Conclusions

Chapter 12

Conclusions

THIS chapter draws the conclusions from measurements and simulations presented in the previous chapters. It starts with a short summary of the aim of this work. The second section compiles the steps done in order to reach that aim. This description is followed by a summary of the measurement results and a discussion of their relevance for the ATLAS pixel detector. Finally, the conclusions which have been drawn for the ATLAS pixel detector are presented.

12.1 Aim of this Work

The Pixel Detector will be the innermost sub-detector of ATLAS which will be one of the experiments at the LHC collider. The task of this sub-detector is particle tracking in an environment that is characterised by a high interaction rate, high track density and heavy radiation load of up to $10 \cdot 10^{14}\, n_{\mathrm{eq}}/\mathrm{cm}^2$.
The design of the sensors for the pixel detector considers the high track density by a high granularity and density of its pixel cells. The high density of pixel cells sets the requirements for the necessary two-dimensional connection technique—bump-bonding—between sensor and read-out electronics. In a specialised part of this work test-structures for process qualification of the bump-bond technique and long-term tests of the connection reliability have been designed.
The high radiation load affects the charge collection properties of the sensors. This has to be taken into account by the choice of the pixel sensor design and the used substrate material.

The sensors are fabricated from oxygenated silicon. The radiation hardness of this material with respect to effective doping concentration was proven to be superior to standard material by the RD48 collaboration. The research of RD48 included the dependence on fluence and annealing time of the effective doping concentration and leakage current in a fluence range up to $10 \cdot 10^{14}\, n_{\mathrm{eq}}/\mathrm{cm}^2$.
The aim of this thesis is to investigate how the ATLAS pixel detector will work in the given environmental conditions for its planned life-time of ten years. The

starting points for this investigation are the chosen sensor design and the results obtained by other groups before.
In this thesis the existing data on irradiated silicon for effective doping concentration and leakage current are completed by own measurements of the effective trapping times and the electric field configuration in irradiated pad-detectors in the relevant fluence range.
The obtained results are applied in simulations of the ATLAS operation. The simulations explore several aspects of the operational conditions and calculate the expected detection probability for minimum ionising particles during the life-time of the ATLAS experiment.

12.2 Charge Collection in Pad-Detectors

12.2.1 Sample Set

The sample set which has been used for measurements consisted of pad-detectors which were fabricated on wafers from oxygenated silicon. The ATLAS pixel sensors have been fabricated from the same material.
After a pre-characterisation with IV- and CV-measurements the samples were irradiated either with 24 GeV-protons or with reactor neutrons. Equivalent fluences of the irradiations were in the range $(0.22\text{–}8.9)\cdot 10^{14}\ n_{\mathrm{eq}}/\mathrm{cm}^2$ for protons and $(1.0\text{–}6.0)\cdot 10^{14}\ n_{\mathrm{eq}}/\mathrm{cm}^2$ for neutrons. Determination of effective doping concentrations and its annealing behaviour showed an expected behaviour of the material.
Therefore, the sample set used in this work can be considered to be a representative sample of the material used for fabrication of ATLAS sensors.

12.2.2 Measurement of Charge Trapping Times

Fluence Dependence

Charge trapping can be described by the effective trapping probability $1/\tau_{e,h}$. The trapping probability has been determined separately for holes and electrons by measuring the pulse-shapes after close-to-surface charge injection with a red laser (TCT). Investigation of the fluence dependence showed a linear dependence on the equivalent fluence Φ_{eq}; the trapping probabilities can be parameterised in the form $1/\tau_{e,h} = \gamma_{e,h}\cdot\Phi_{\mathrm{eq}}$. This behaviour is in agreement with results from other publications ([Kb02] and [Li03]/[RD50]) and can be explained by an introduction of trapping centres which is proportional to fluence. The numerical results for $\gamma_{e,h}$ are:

	e-trapping $\gamma_e\ [10^{-16}\ \mathrm{cm/ns}]$	h-trapping $\gamma_h\ [10^{-16}\ \mathrm{cm/ns}]$
protons	4.97 ± 0.14	5.25 ± 0.17
neutrons	3.53 ± 0.24	5.10 ± 0.39

These numbers show that electron trapping does not scale with the NIEL hypothesis since protons introduce more trapping centres than neutrons at the same equivalent fluence. This indicates that several kinds of electron-traps exist and that one kind is caused by point-defects since point-defects are more abundant after proton-irradiation.
Compared to [Kb02] and [Li03]/[RD50] the values for trapping probabilities measured within this work are considered to be the most appropriate ones to describe charge trapping in the ATLAS pixel sensors since they cover the largest fluence range and are measured on the same material as is used for the ATLAS pixel sensors.

Annealing

A study of accelerated annealing (at 60°C) showed a saturation of the trapping probabilities. The trapping probability for electrons decreased and saturated at values being lower by $\approx 20\%$. Hole trapping was increased by $20 - 55\%$. These results agree with observations reported in [Kb01].
This annealing behaviour is advantagous for the ATLAS operation since the trapping of electrons—which are more important for the signal formation in n-on-n-pixel sensors than holes—decreases. In such sensors the decrease of $1/\tau_e$ overcompensates the increasing hole trapping as has been shown by simulation studies (see below). Since the annealing leads to a saturation—stability of the plateau has been observed for several hours at 60°C—a larger annealing effect during the long-term ATLAS operation is not expected.

12.2.3 Electric Field in Irradiated Pad-Detectors

The second large topic of the TCT measurement was the investigation of the electric field in irradiated silicon-detectors.
From charge collection curves which have been compensated for charge trapping it can be concluded that the pad-detectors reached their maximum sensitive volume already at bias voltages below the nominal full depletion voltage obtained from CV-measurements. This effect increases with fluence. This observation was confirmed by measurements of the electric fields. The electric fields were obtained from TCT measurements by a newly developed deconvolution method.
The main goal of the study of electric fields was to develop a parameterisation of the field that can be used in simulations of charge drift in highly irradiated (Φ_{eq}above $\approx 1 \cdot 10^{14}\, n_{\mathrm{eq}}/\mathrm{cm}^2$) silicon-detectors. In order to derive such a parameterisation a model considering one deep acceptor and one deep donor level has been used. Additionally, shallow levels with a fluence depending concentration were considered within this model.
The measured electric fields in pad-detectors can be described well by the deep level model when using a constant deep acceptor concentration and a deep donor concentration that increases linearly with fluence. This shows that the observed

double peak structure of the electric field in irradiated silicon-sensors can be described by an inhomogeneous space-charge which is caused by partially occupied deep level states.
The deep level concentrations are obtained from fits of a parameterisation to electric fields that have been measured at several fluences. The parameterisation is derived from a simplified model. Therefore, these concentrations should not be considered as giving a correct description on a microscopic level and their application should be restricted to the calculation of electric fields in silicon-detectors (pn-junctions) which have been irradiated with equivalent fluence above $\approx 1 \cdot 10^{14}\, n_{\mathrm{eq}}/\mathrm{cm}^2$.

12.2.4 Simulation of Pad-Detectors

The results for charge trapping times and electric field configuration have been used to develop software (EDCALC, CDCALC and RACALC) for the simulation of charge drift in irradiated pad-detectors.
Comparisons between measured and simulated pulse-shapes showed that the signal-formation in irradiated pad-detectors is well described by the developed software. The electric field parameterisation based on the deep level model describes the pulse-shape in irradiated pad-detectors better than a linear approximation of the electric field.
The algorithm for calculating the field configuration works well if the bias voltage is at least 50 V above the depletion voltage obtained from CV-measurements and the minimum field strength in the detector is larger than 1 keV. For lower bias voltages the measured fields are only badly described.
For the conditions given above the software was able to reproduce the measured charge collection efficiencies for electrons after p-side illumination with a systematic deviation of maximum 0.1. For holes the agreement between simulation and measurement is significantly better. This can be explained by the form of the field configuration and the choice of illuminated side of the detector: electrons move through the problematic low-field region *before* inducing the major part of their signals while holes reach the low-field region *after* having generated most of their signal. Therefore, for the calculation of CCEs in mip-detection—where the charge-carriers are injected homogeneously—a smaller systematic error is expected since the low field region has less weight in the total signal.

12.2.5 Relevance for ATLAS

The measurement results obtained in this work have been measured on samples which were fabricated from the same material as the ATLAS sensors and were irradiated with fluences which are expected during ATLAS operation.
In combination with earlier results from other groups the results form a data set that can be used to calculate all parameters which are relevant for charge collection. These are depletion voltage, leakage current, trapping times and electric field.

The developed simulation tools were qualified by showing that they can reproduce the observations made on pad-detectors.
Therefore, the data and simulation methods are considered to be appropriate to make predictions for the ATLAS pixel detectors.

12.3 Application for ATLAS

12.3.1 Test Beam Modules

The first application of the developed software was the calculation of the depletion voltages for irradiated modules which have been used for measurements in a testbeam.
The software was successful in reproducing the observed depletion voltage for the modules.

12.3.2 ATLAS Standard Scenario

Depletion voltages and leakage currents were calculated for the so-called ATLAS standard scenario which represents the expected profiles of temperature and irradiation during the ATLAS operation. Considering the limitation of applicable bias voltage to 600 V, it will be possible to operate the sensors of layer 1 fully depleted even after ten years of operation with nominal fluence. If the fluences are increased by 50% in order to take into account the uncertainty of the total pp-cross-section at LHC energies the depletion voltage will be 800 V. The corresponding values for the B-layer after five years are 435 V and 620 V. After ten years the depletion voltage for the B-layer will reach 1080 V (1540 V for increased fluence). As a consequence it will not be possible to operate these sensors fully depleted during the whole operation-time of ten years.
Calculations of the leakage current showed that it will stay below the limit which is required by the read-out electronics. Power consumption of a sensor tile will not exceed 1.5 W for layer 1 after ten years and 2 W for B-layer after five years. However, towards high fluences the leakage current will be reduced by partial depletion. Therefore, also the power consumption is limited. Considering this effect, the power consumption will stay below 1.5 W even for B-layer after ten years of operation.

12.3.3 Collected Charge and Detection Probability

Examination of the Ramo-field showed that the major part of the signal is generated by charges drifting in the bulk close to the n-side (90% on the last 100 μm and 50% on the last 20 μm). This has two consequences: the signal is dominated by electron drift and the drift path fraction which is closer to the p-side is less significant. Due to the latter reason a reliable calculation of the electric field close to the n-side is more important than towards the p-side. Therefore, all calculations

of CCE were also done with a linear description of the field. Comparison between the two descriptions—linear and deep level model— showed no large difference in the important bulk region towards the n-side. Consequently, the calculated CCEs did not depend strongly on the chosen field model for bias voltages well above depletion voltage. For partial depletion only the linear model was used. It might underestimate CCE since the linear model contains no depletion zone at the p-side for bias voltages being below V_{dep}. However, as stated above, this region is of less importance.
For the sensors in layer 1 the simulation predicts a charge collection efficiency of 71% after ten years of operation. The B-layer will still have a charge collection efficiency of at least 36% after this time. If the expected fluences are increased by 50% these numbers drop to 56% and 29%, respectively.
A simulation which used for the trapping times the saturation values after accelerated annealing at 60°C showed that the annealing of the trapping times can be neglected for ATLAS predictions.
Minimum ionising particles deposit on average 95 keV ($\hat{=}26\,400\,e_0$) in 250 μm thick silicon sensors. Considering a corresponding Landau distribution with a most probable energy loss of 89.3 keV the detection probability for given trigger threshold and charge collection efficiency was derived. Using a minimum CCE of 29% the detection probability will be almost 100% if the trigger threshold is not higher than 6 000 electron charges.
If charge-sharing between pixel-cells should become important layer 1 will still work reliable for ten years and B-layer will do so for five years as well. However, after ten years of operation detection with charge-sharing will become difficult in the B-layer. The exact detection probabilities can be determined only within simulations of the complete ATLAS pixel detector since there the role of charge-sharing can be investigated more thoroughly.

12.3.4 Will the ATLAS Pixel Sensor Work?

The predictions for depletion voltages which have been computed within this thesis state that the allowed range of bias voltage will be sufficient to fully deplete the sensors during most of their planned operation-time.
Charge collection studies showed that the sensors will deliver enough charge to the front-end electronics even in partial depletion. During the planned operation-times of the pixel detector layers the collected charge will be large enough to enable reliable particle detection even if the charge is divided between two pixel-cells.
Therefore, from point of charge-collection a proper functionality of the ATLAS pixel sensor is expected.

12.4 Super-LHC

The measurement results obtained within this work have also been used to extrapolate the results up to a fluence of $78 \cdot 10^{14}\, n_{\mathrm{eq}}/\mathrm{cm}^2$ as it would be expected for

layer 1 in a Super-LHC scenario with luminosities being increased by a factor 10. This calculation predicted a charge collection efficiency of 13% for a 250 μm thick pixel-sensor which is biased with 600 V. Fully depleted ($V_{\mathrm{dep}} \approx 4\,400$ V) this sensor would reach a CCE of $\approx 19\%$. Full depletion improves the CCE only little since the additionally depleted sensor volume is opposite to the collecting electrode on the n-side and the trapping is too strong at these fluences to collect efficiently charges from this region.

12.5 Outlook

In this thesis it has been shown that TCT-measurements are a useful tool to explore the properties of silicon detectors. This method could be developed further to position-resolved TCT. With such an improved method the electric field in detectors could be measured at several positions. This would allow to investigate the influence of edge-effects in pad-detectors. A very interesting application for position-resolved TCT would be the measurement of charge-collection at different positions in a pixel-cell. If applied to other detector materials—like CdZnTe—the homogeneity of the material can be investigated.
During the operation phase of the ATLAS experiment the simulation has to be updated in order to take into account the real history of temperature and irradiation.

Part VI

Reference Material

Appendix A

Constants and Silicon Material Properties

APPENDIX A contains tables of physical constants, material properties of silicon and abbreviations used for this thesis.

A.1 Physical Constants

Symbol	Meaning	Value
c	speed of light	$299\,792\,458\,\mathrm{ms}^{-1}$
e_0	elementary charge	$1.602 \cdot 10^{-19}\,\mathrm{C}$
ε_0	permittivity of free space	$8.854 \cdot 10^{-12}\,\mathrm{F/m}$
$\hbar = h/2\pi$	Planck constant	$1.054 \cdot 10^{-34}\,\mathrm{Js}$ $= 6.582 \cdot 10^{-16}\,\mathrm{eV\,s}$
k	Boltzmann constant	$1.381 \cdot 10^{-23}\,\mathrm{J/K}$ $= 8.617 \cdot 10^{-5}\,\mathrm{eV/K}$
N_0	Avogadro constant	$6.022 \cdot 10^{23}\,\mathrm{mol}^{-1}$
m_0	electron mass	$511\,\mathrm{keV}$ $= 9.109 \cdot 10^{-31}\,\mathrm{kg}$
r_0	classical electron radius	$2.817 \cdot 10^{-13}\,\mathrm{cm}$

Table A.1: Physical constants with their values as used for this thesis. The numbers have been taken from [PG02] and rounded to a sufficient precision.

A.2 Material Properties of Silicon

Symbol	Property	Value
Z	atomic number	14
A	atomic mass	$28.09\,\mathrm{g/mol}$
ρ_m	mass density	$2.33\,\mathrm{g/cm^3}$
$\varepsilon_{\mathrm{Si}}$	dielectric constant	11.75
E_G	band gap ($T = 300\,\mathrm{K}$)	$1.12\,\mathrm{eV}$
	density of state effective masses	
m_e	electrons	$1.18\ m_0$
m_h	holes	$0.81\ m_0$
	effective density of state	
N_C	conduction band	$3.22 \cdot 10^{19}\,\mathrm{cm^{-3}}$
N_V	valence band	$1.83 \cdot 10^{19}\,\mathrm{cm^{-3}}$
	therm. velocities ($T = 300\,\mathrm{K}$)	
$v_{th,e}$	electrons	$2.3 \cdot 10^7\,\mathrm{cm/s}$
$v_{th,h}$	holes	$1.65 \cdot 10^7\,\mathrm{cm/s}$
	mobilities ($T = 300\,\mathrm{K}$)	
μ_e	electrons	$1450\,\mathrm{cm^2/Vs}$
μ_h	holes	$505\,\mathrm{cm^2/Vs}$

Table A.2: Material properties of silicon [DN82], [PG02] and [Lu99].

A.3 Abbreviations

Abbreviation	Meaning
CCE	charge collection efficiency
CCM	charge correction method
CV	capacitance-voltage (characteristic)
DLM	deep level model
DUT	device under test
ECC	exponentiated charge crossing
IP	interaction point
IV	current-voltage (characteristic)
mip	minimum ionizing particle
SCR	space charge region
SCSI	space charge sign inversion
TCT	Transient Current Technique

Table A.3: Abbreviations used in this work.

Appendix B

Measurements of Depletion Voltage

THIS appendix contains some additional information of more technical character which are connected with the determination of the depletion voltage. Sec. B.1 shows a short investigation of the dependence of the depletion voltage extracted from CV-measurements on the measurement frequency. The last section shows a possibility to obtain V_{dep} from measurements with a β-source.

B.1 Measurement Frequency

One free parameter of the CV-measurement is the frequency f_m of the sinusoidal voltage which is superimposed to the DC bias voltage by the LCR-meter. The influence of f_m on the result for V_{dep} has been investigated by measurements on an unirradiated diode (sample $\emptyset$) and on the irradiated sample C ($\Phi_{\mathrm{eq}} = 5.0 \cdot 10^{14}\, n_{\mathrm{eq}}/\,\mathrm{cm}^2$, 30 min annealing at 60°C before measurement). Fig. B.1 shows plots of the obtained CV-curves.
Measurements on the unirradiated diode yield no dependence of shape on the measurement frequency. The extracted depletion voltage is (within errors) independent from f_m over four orders of magnitude as the plot in Fig. B.2 shows. For irradiated diodes the picture is completely different: the shape of CV-curves depends strongly on the measurement frequency as can be seen in the bottom plot in Fig. B.1. Also the range of possible measurement frequencies is limited, for too low or high frequencies the kink in the CV-curve is not clearly visible, making a reliable analysis impossible. However, the strong dependence of the extracted depletion voltage on f_m is the worst problem, see Fig. B.2. The depletion voltages $V_{\mathrm{dep},300}$ shown in this figure have been calculated from the measured V_{dep} by $V_{\mathrm{dep},300} = V_{\mathrm{dep}} \cdot (300\,\mu\mathrm{m}/d)^2$, where d is the thickness of the sample. This is done in order to make the depletion voltages which are measured on samples with different thicknesses comparable.
By the definition given in in chapter 3 V_{dep} is related to the complete depleting of

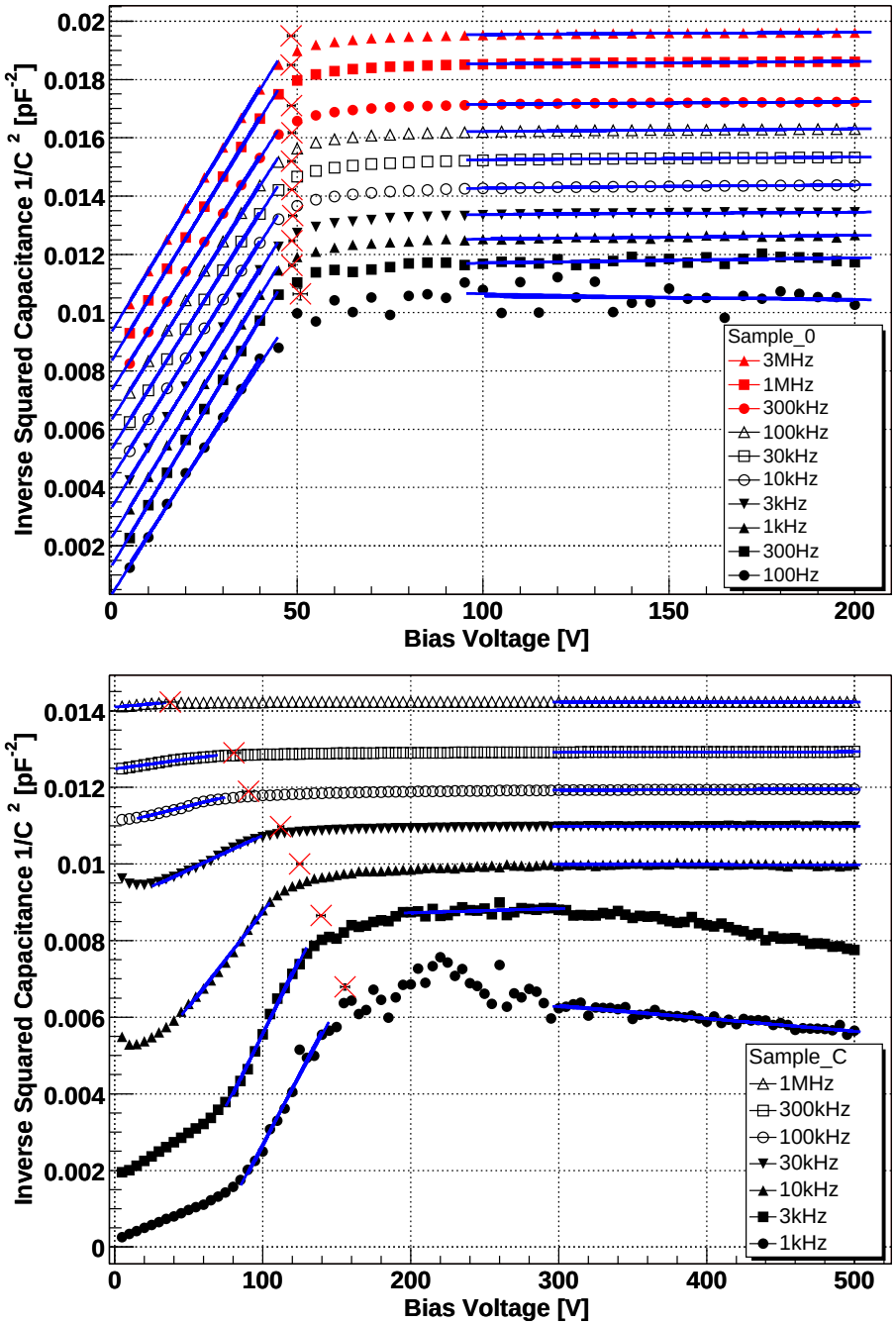

Fig. B.1: CV-curves measured with different measurement frequencies on sample ∅(unirradiated, upper figure) and sample C ($\Phi_{eq} = 5.0 \cdot 10^{14}\, n_{eq}/\,cm^2$, 30 min annealing at 60°C, lower figure). All measurements were done at -6°C. The curves are shifted vertically by $0.001\,pF^{-2}$ per curve to improve legibility of the plot, lowest curve is not shifted.

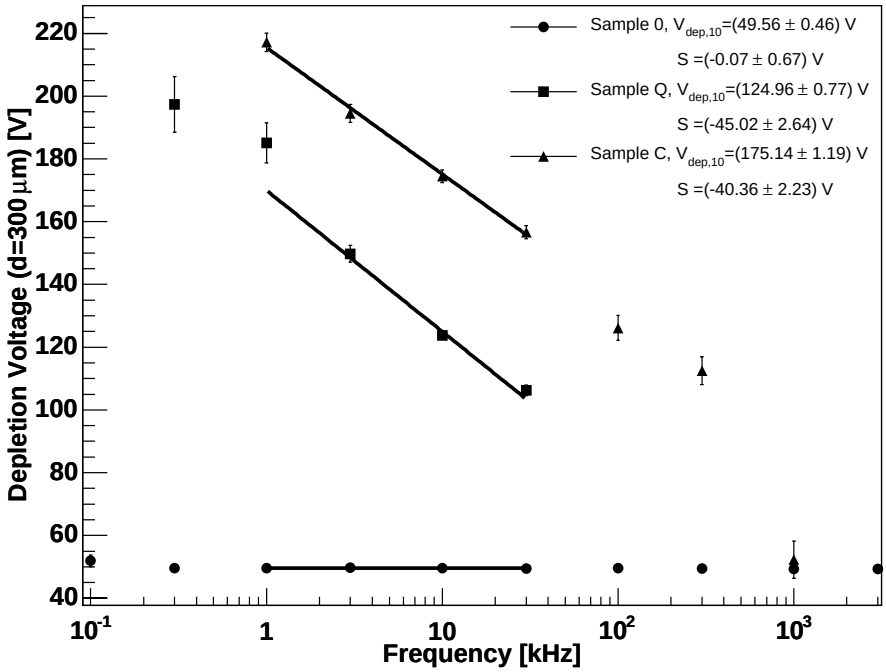

Fig. B.2: Depletion voltages extracted from the CV-curves shown in Fig. B.1 vs. measurement frequency f_m. Additionally, measurements on sample Q are included in the plot. The displayed depletion voltages are given for a detector thickness of 300 μm.

the diode's bulk. As long as the AC voltage which is added by the LCR-meter is small compared to the bias voltage the depth of the depletion zone does not change significantly and V_{dep} should not depend on the measurement frequency. Therefore, the observed dependence on f_m is clearly an artefact of the measurement technique.
In order to parameterise the dependence on the frequency the function

$$V_{\mathrm{dep}} = V_{\mathrm{dep},10} + S \cdot \log_{10}(f_m/10\,\mathrm{kHz}) \tag{B.1}$$

is fitted to the data points. $V_{\mathrm{dep},10}$ is the depletion voltage measured with $f_m = 10\,\mathrm{kHz}$, S gives the change per factor 10 in f_m. This function describes the data quite well if the chosen frequency range is not too large.
This parameterisation does not consider a physical explanation of the frequency dependence. However, it may be used as a tool to compare data measured at different frequencies as already proposed by other authors [Ca02].
A further open question is the behaviour of this dependence during the annealing process. Fig. B.3 displays measurements of V_{dep} during accelerated annealing at 60°C of sample Q ($\Phi_{\mathrm{eq}} = 2.04 \cdot 10^{14}\, n_{\mathrm{eq}}/\,\mathrm{cm}^2$). CV-measurements with several frequencies were performed after 30, 45, 60 and 180 min of accelerated annealing. The fits of eq. (B.1) show only a slight variation of S from $(-44.1 \pm 2.6)\,\mathrm{V}$ after 30 min to $(-52.6 \pm 4.1)\,\mathrm{V}$ after 180 min. The parameter $V_{\mathrm{dep},10}$ changes of course

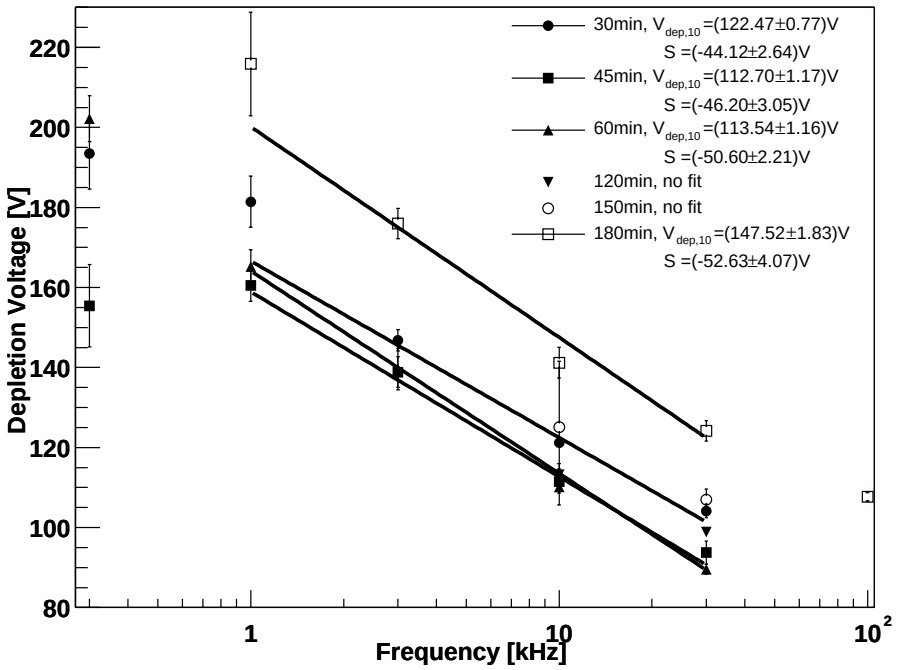

Fig. B.3: Depletion voltages with different measurement frequencies on sample Q ($\Phi_{\mathrm{eq}} = 2.04 \cdot 10^{14}\, n_{\mathrm{eq}}/\,\mathrm{cm}^2$) during accelerated annealing at 60°C.

strongly due to annealing as it represents the depletion voltage at a fixed frequency.

B.2 Measurements with a β-Source

B.2.1 Measurement

The measurements presented in this section have been done on an unirradiated pad-detector which was connected to a charge-sensitive pre-amplifier. The pre-amplifier output signal was amplified by a spectroscopy amplifier and analysed with a multi-channel-analyser. Charge deposition in the pad-detector was done with a ^{90}Sr-source. A scintillator with photo-multiplier tube behind the pad-detector supplied a trigger signal. The trigger was necessary in order to reduce the noise and to suppress signals which are caused by low-energetic β-particles.
Fig. B.4 shows the spectrum of deposited energy of penetrating electrons from the ^{90}Sr source. The measurement was done with sample C11_04, which has been used only for test purposes.
The data are fitted with a gaussian and a Landau distribution according to eq. (3.5). Generally, the data are much better described by the Landau distribution as can be seen on the much lower value for χ^2/ndf (423/459 for Landau distribution compared to 7168/459 for gaussian). Especially the tail towards high energy loss is better described.

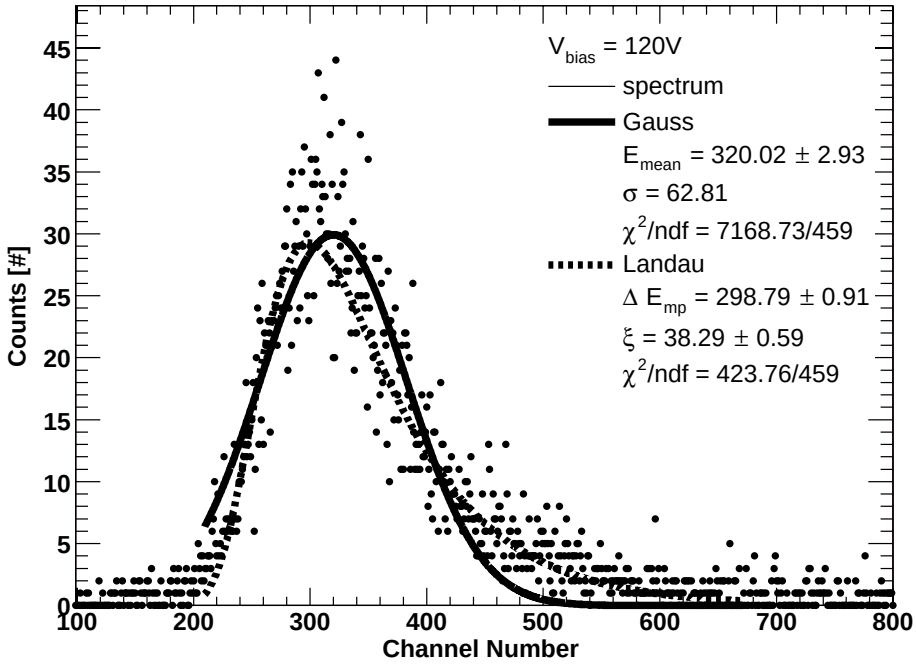

Fig. B.4: Energy loss distribution measured with a ^{90}Sr source on a pad-detector.

The peak positions E_{mean} from the gaussian fits and the most probable energy depositions ΔE_{mp} (see sec. 3.1.4) from the Landau fits are plotted vs. $\sqrt{V_{\text{bias}}}$ (see Fig. B.5). Straight lines below and above the kink can be fitted to these plots. Their intersection point gives the depletion voltage. The same fitting procedure can be applied to ξ vs. $\sqrt{V_{\text{bias}}}$. Since ξ is proportional to the thickness of the absorber (cf. eq. (3.6))—i.e. the depleted thickness in case of a pn-junction—it can also be used to determine V_{dep}.
The results for V_{dep} from the three methods are:

derived from	V_{dep}
ΔE_{mp}	54.0±1.7
ξ	53.2±8.1
E_{mean}	52.4±1.9
capacitance	60.8±2.8

The result from a CV-measurement is given for comparison.

B.2.2 Discussion

The energy deposition spectra can be well described by the Moyal approximation to the Landau distribution. However, the region around the peak is worse fitted by this function. This may have several reasons: Firstly, Landau's theory is

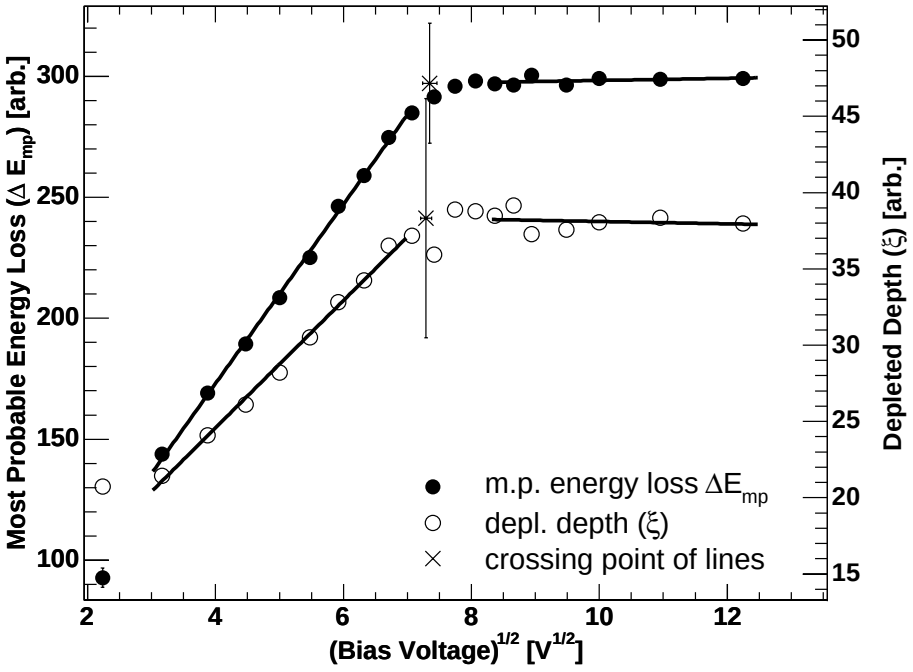

(a) Fit of Landau function.

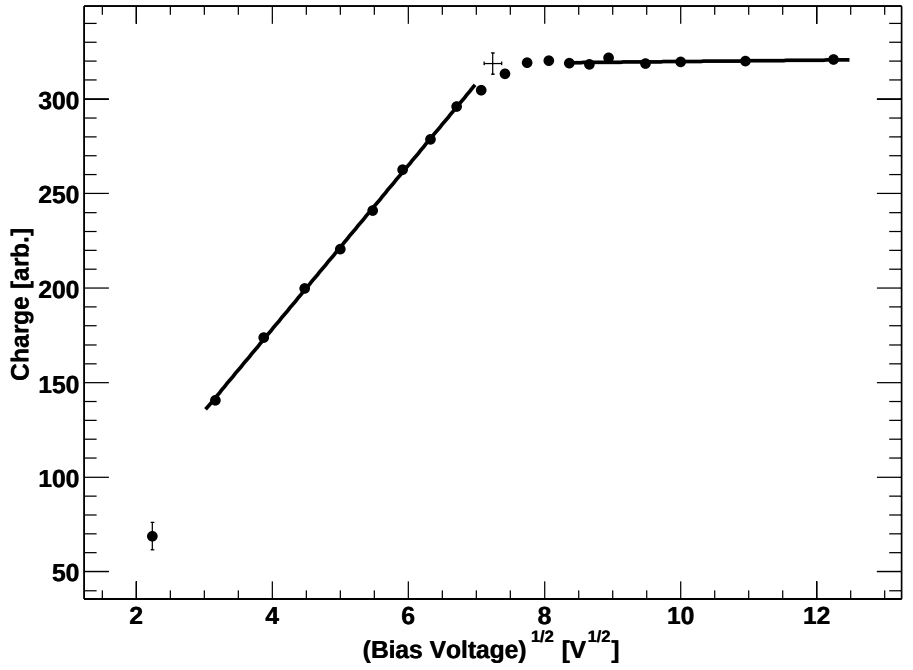

(b) Fit of Gaussian function.

Fig. B.5: (a): Most probable energy loss ΔE_{mp} vs. $\sqrt{V_{\mathrm{bias}}}$ and ξ-parameter vs. $\sqrt{V_{\mathrm{bias}}}$ from fits of Landau distributions to spectra. (b): Mean values of the peaks from gaussian fits to spectra.

applicable for very thin absorbers [Le94]. Taking into regard the low energies of the electrons, this condition may not be fulfilled. Usage of Vavilov's theory which is more suitable for thicker absorbers may yield better results. Especially this function has a narrower but higher peak compared to Landau's theory while the tail towards high energy transfers has the same height. But it is very difficult to use this theory for fitting. Therefore, usage of Landau's theory seems still to be suitable since the aim—measurement of depletion voltage—can be achieved with it.

The measurement of the thickness of the depletion zone with β-particles can be analysed in three ways, all of them giving consistent results. The result from the evaluation of ξ vs. $\sqrt{V_{\mathrm{bias}}}$ has a significantly larger error than the two other methods.

This measurement is quite complicated in its application due to little signal charges in the diode even by using unirradiated samples. In irradiated samples with increased leakage currents and therefore much higher noise the experimental set-up has to be carefully designed in order to suppress noise as much as possible.

Appendix C

Supplement to TCT-Measurements

THIS chapter contains some additional plots for the measurements presented in chapter 8.

C.1 Charge Collection Efficiency

Fig. C.1 and C.2 show additional charge collection curves to the analysis presented in sec. 8.2.

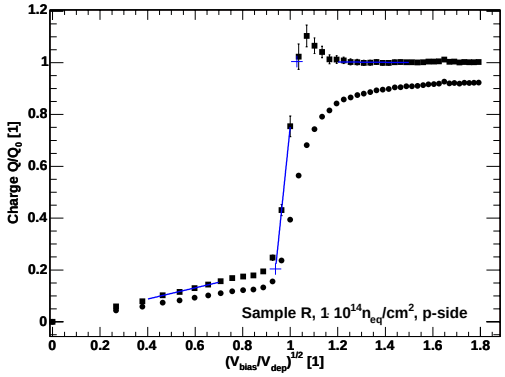

(a) Sample R, p-side

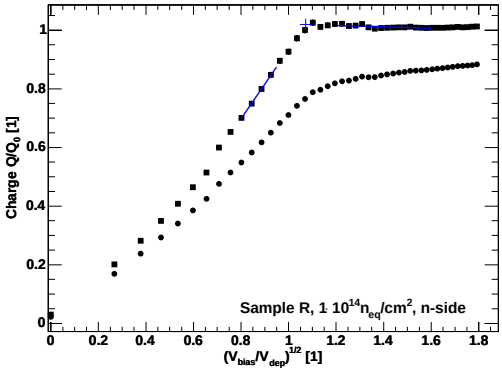

(b) Sample R, n-side

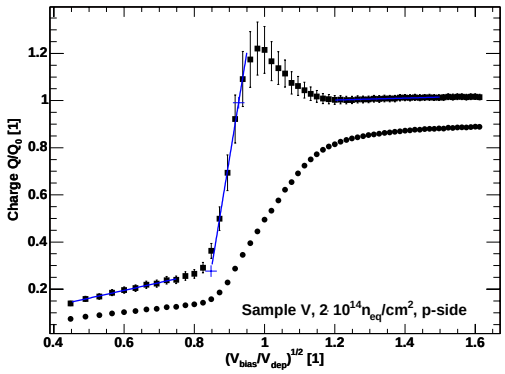

(c) Sample V, p-side

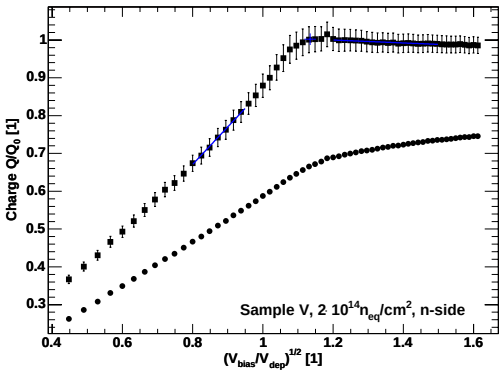

(d) Sample V, n-side

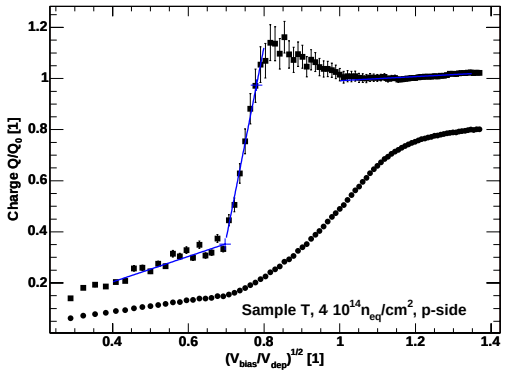

(e) Sample T, p-side

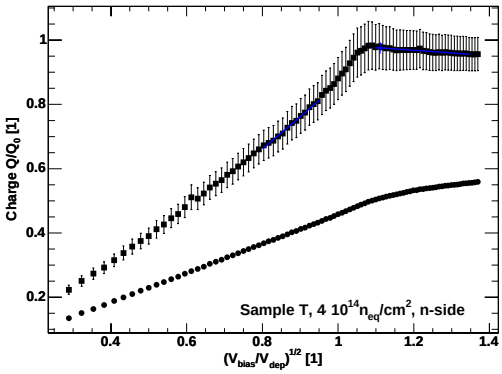

(f) Sample T, n-side

Fig. C.1: Measured (lower curves) and corrected (upper curves) charge collection efficiencies vs. $\sqrt{V_{\mathrm{bias}}/V_{\mathrm{dep}}}$ as measured with neutron-irradiated samples.

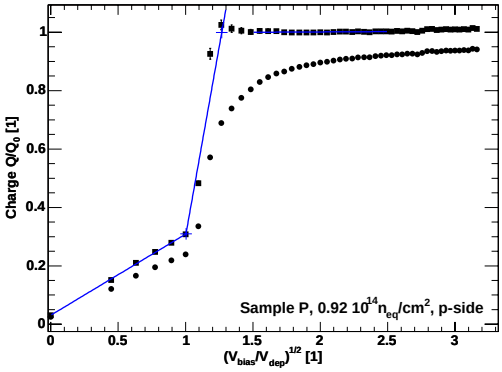

(a) Sample P, p-side

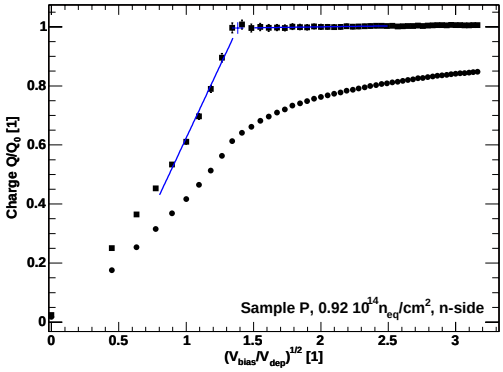

(b) Sample P, n-side

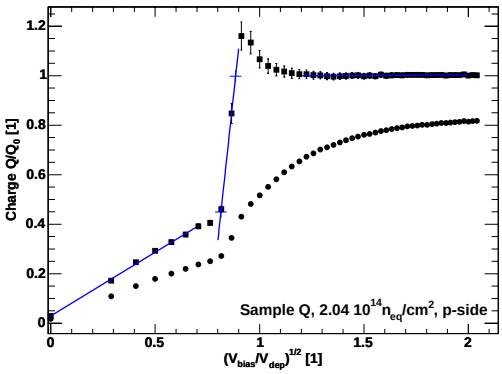

(c) Sample Q, p-side

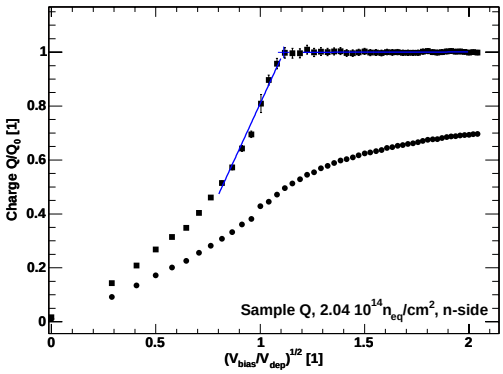

(d) Sample Q, n-side

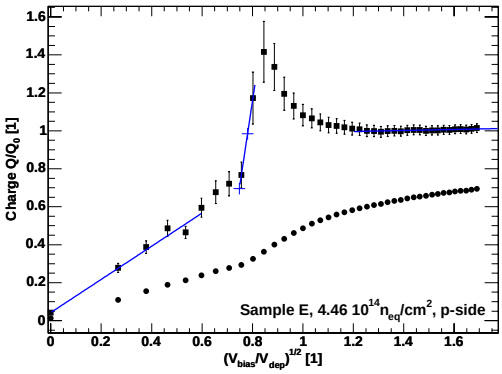

(e) Sample E, p-side

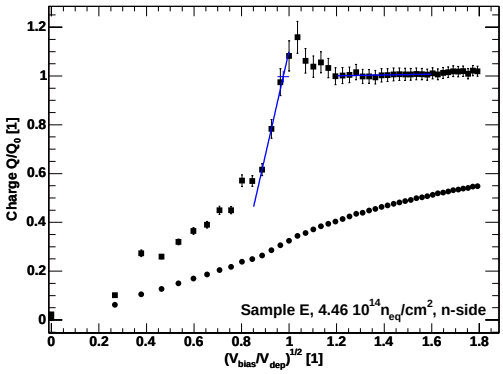

(f) Sample E, n-side

Fig. C.2: Measured (lower curves) and corrected (upper curves) charge collection efficiencies vs. $\sqrt{V_{\mathrm{bias}}/V_{\mathrm{dep}}}$ as measured with proton-irradiated samples.

C.2 Electric Field in Underdepleted Sensors

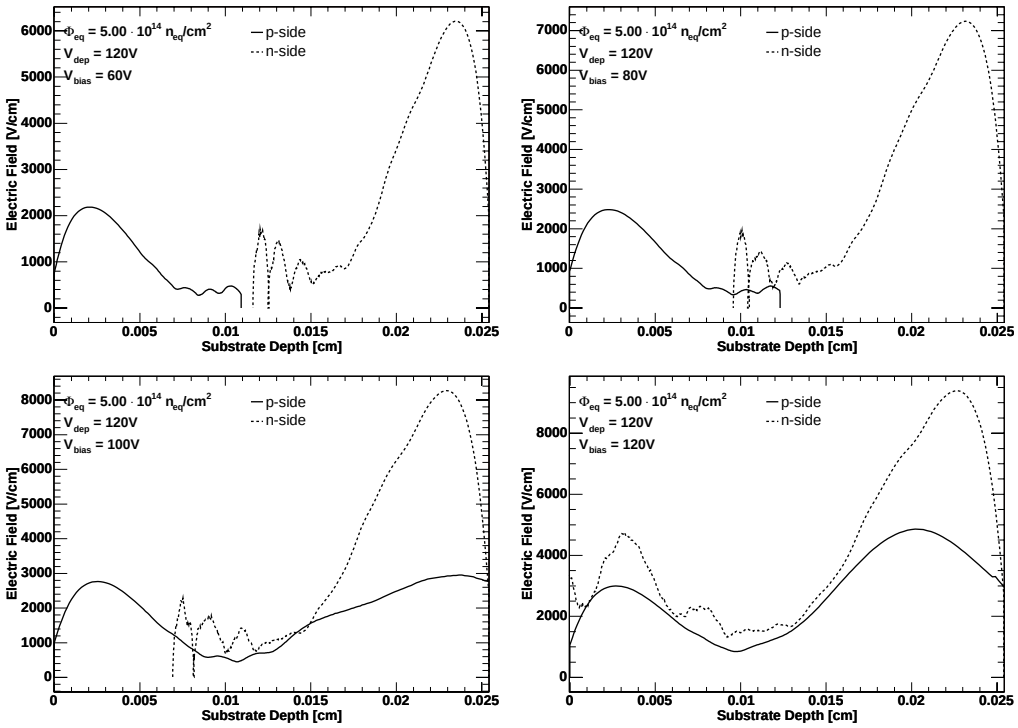

Fig. C.3: Deconvoluted electric fields for bias voltages below the depletion voltage. Measured on sample C, $\Phi_{\mathrm{eq}} = 5.00 \cdot 10^{14}\, n_{\mathrm{eq}}/\mathrm{cm}^2$. Solid lines show the result from p-side illumination, dashed lines from n-side illumination.

Appendix D

Thin Sensors for Super-LHC

FOR an upgrade of the ATLAS Pixel Detector usage of sensors with a thickness of 200 μm is investigated. This appendix contains results for 200 μm thick sensors which correspond to those given in chapter 11 for 250 μm thick sensors.

D.1 Ramo-Potential

Fig. D.1 shows the Ramo potential of an infinite strip detector with a thickness of 200 μm. In Fig. D.2 the x-component of the Ramo field for a drift path centered underneath a pixel is plotted. In a thinner detector the segmented n-side-region is stronger weighted than in a 250 μm thick sensor: considering a particle that drifts from p- to n-side 90% of the total signal is induced on the last 90 μm, 50% on the last 20 μm of the drift path.

D.2 CCE and Detection Probability

The expected charge collection efficiency and collected charge for a 200 μm thick pixel sensor is shown in Fig. D.3. The calculation has been done with a linear field approximation. Fig. D.4(a) shows the Landau distribution for a thin sensor. The mean energy loss of a mip ($\beta = 1$) in 200 μm silicon is 76 keV, the most probable energy loss is 71.5 keV. Fig. D.4(b) shows the corresponding detection probabilities.
The thinner sensors have a higher charge collection efficiency since the signal charges have shorter drift-paths and the sensors can be operated fully depleted up to higher fluences. The resulting charge collection efficiencies are 42% after five years and 22% after ten years. The corresponding numbers for 250 μm thick sensors are 35% and 18%, respectively. For these numbers full depletion ($V_{\text{bias}} = V_{\text{dep}} + 50\,\text{V}$ is assumed in calculation. However, the better CCEs are cancelled out by less deposited charge. The thinner sensor gives after five years a signal charge of 8 800 e_0 and after ten years 4 600 e_0. Sensors with a thickness of 250 μm deliver 9 400 e_0 and 4 600 e_0.

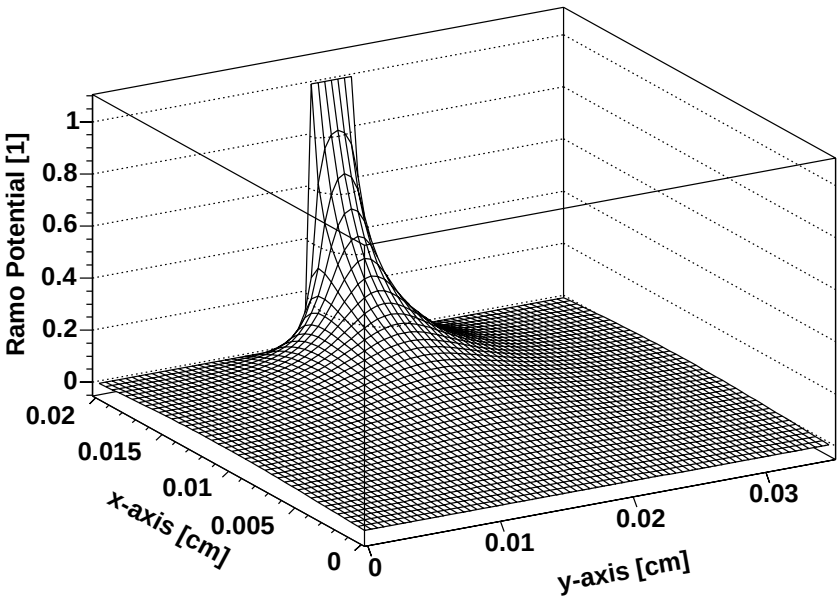

Fig. D.1: Numerical solution for the Ramo potential of an infinite strip-detector with thickness $d = 200\,\mu$m, pitch $50\,\mu$m and an implantation width of $30\,\mu$m. The sensor has been simulated with an extension in y covering seven strips on a 51×71 lattice. This plot corresponds to Fig. 9.4.

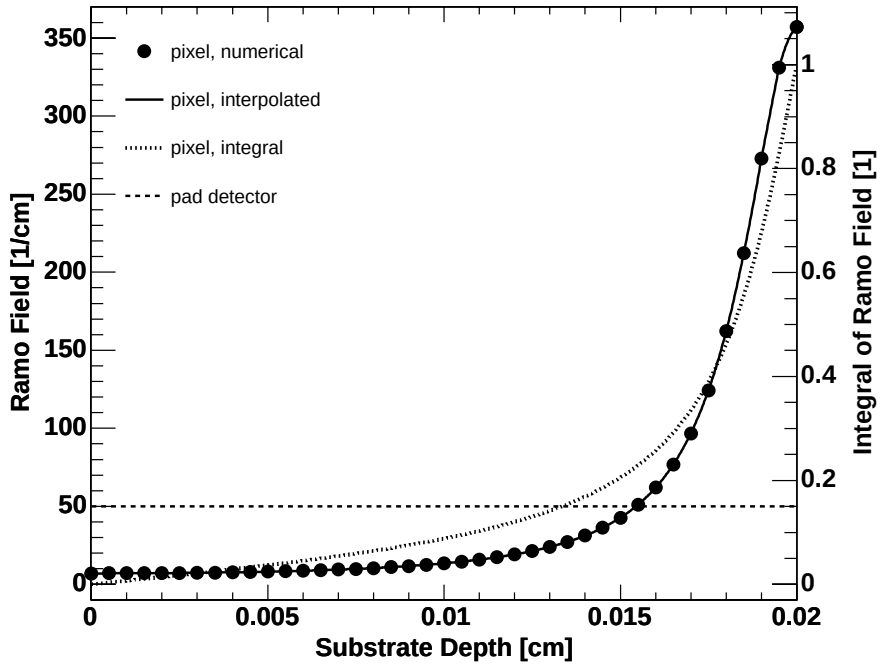

Fig. D.2: Ramo-Field in x-direction for pad-detector (dashed line) and pixel-detector (solid line). For the pixel detector the Ramo field is taken at the centre of the pixel ($y = y_c$). Markers indicate the numeric results obtained from RACALC with a $5\,\mu$m lattice, the solid line shows the parabolic interpolation. The dotted line gives the integral of the Ramo-field. Both detectors are $200\,\mu$m thick. This plot corresponds to Fig. 11.12.

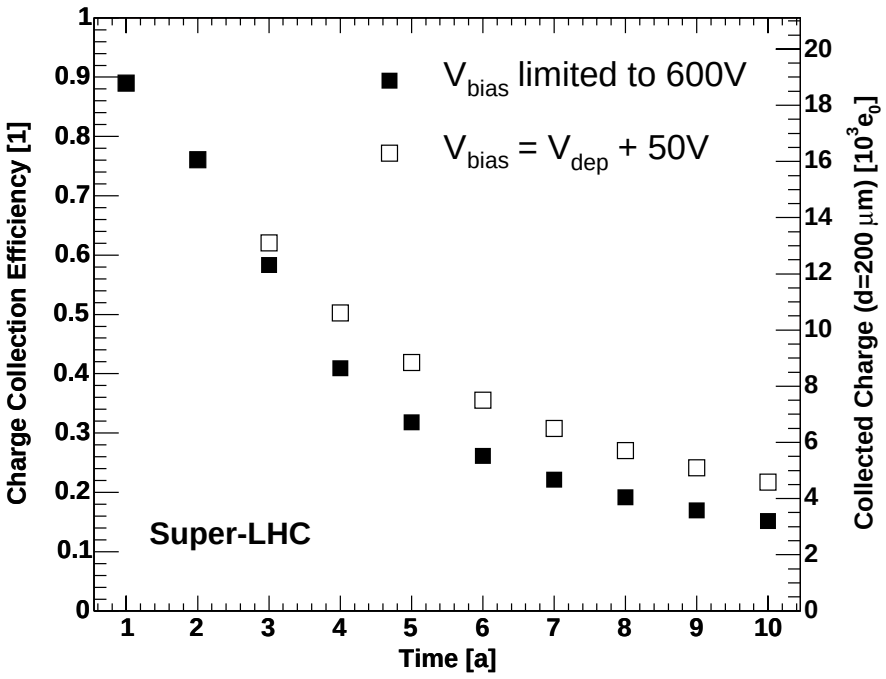

Fig. D.3: Charge collection efficiency for layer 1 vs. operation time with fluences expected for the Super-LHC scenario. Closed symbols show the results for V_{bias} limited to 600 V, open symbols show result for fully depleted pixel sensor ($V_{\text{bias}} = V_{\text{dep}} + 50\,\text{V}$). The thickness of the sensor is 200 μm. This plot corresponds to Fig. 11.24.

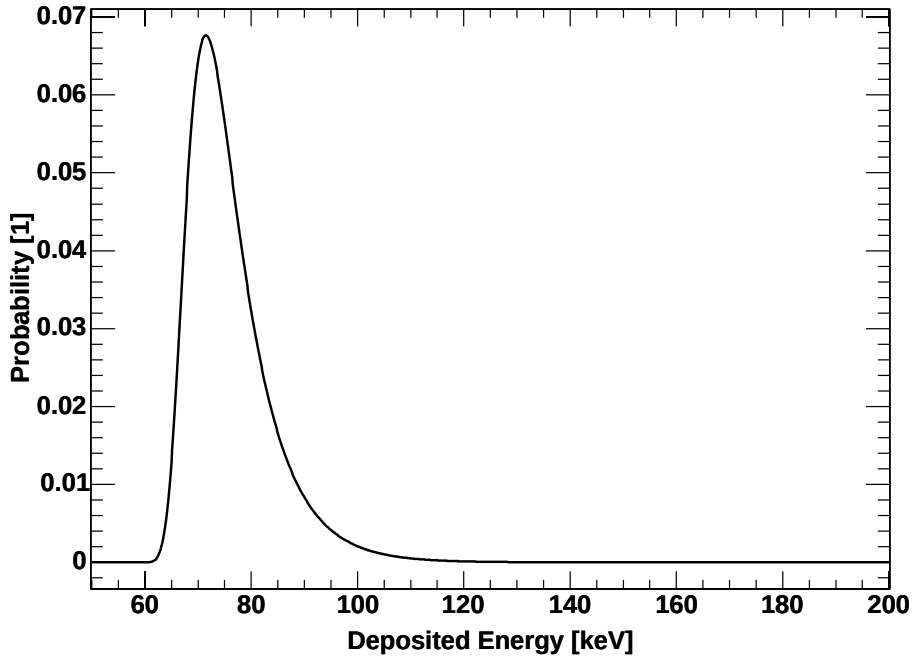

(a) Landau distribution.

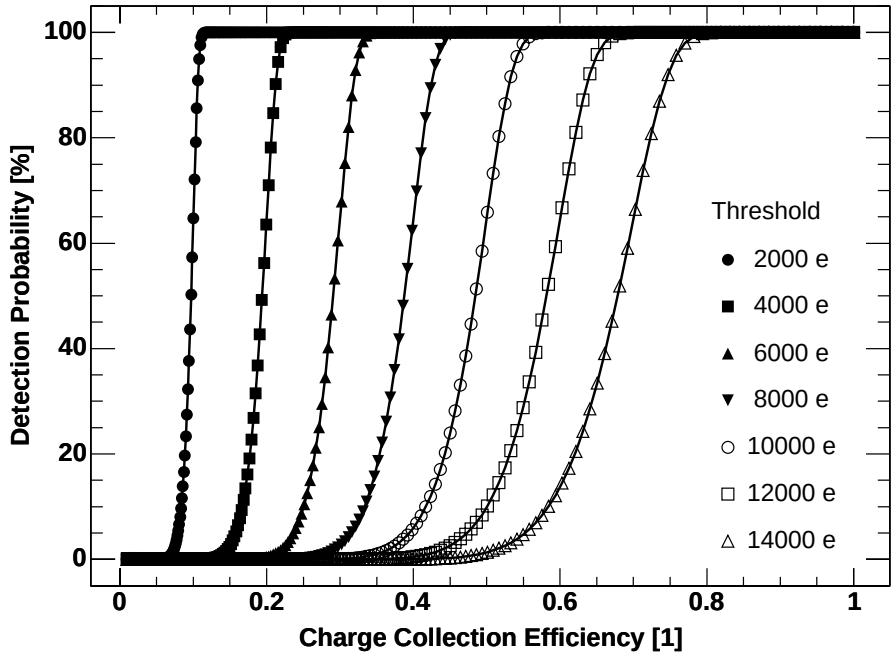

(b) Detection probability.

Fig. D.4: (a) Landau distribution for 200 μm thick silicon sensor. The mean energy loss is 76 keV, the most probable energy loss is 71.5 keV. (b) Detection probability for mips depending on the sensor's charge collection efficiency for several trigger thresholds given in electron charges. These plots correspond to Fig. 11.23.

List of Figures

List of Tables

References

[AT97] ATLAS Inner Detector Community, *Inner Detector Technical Design Report, Vol. I and II*, TDR 4 and 5, CERN/LHCC 97-16, Geneva, 30 April 1997

[AT98] ATLAS Pixel Detector Community, *Pixel Detector Technical Design Report*, TDR 11, CERN/LHCC 98-13, Geneva, 31 May 1998

[AT99] ATLAS Collaboration, *Detector and Physics Performance Technical Design Report, Vol. I and II* TDR 14 and 15, CERN/LHCC/99-14 and CERN/LHCC/97-15, Geneva, 1999.

[Bn96] Rene Brun and Fons Rademakers, *ROOT - An Object Oriented Data Analysis Framework*, Proceedings AIHENP'96 Workshop, Lausanne, Sep. 1996, Nucl. Instr. & Meth. in Phys. Res. A 389 (1997), p. 81–86, see also http://root.cern.ch/.

[Bo94] F.W. Bopp et al., Phys. Rev. D49 (1994) 3236, P. Aurenche et al., Phys. Rev. D45 (1992) 92

[Bo98] R. Bock et al., *The Particle Detector BriefBook*, Springer, 1998

[Br00] T.J. Brodbeck, A. Chilingarov, T. Sloan, E. Fretwurst, M. Kuhnke, G. Lindström, *A new method of carrier trapping time measurement*, Nucl. Instr. & Meth. in Phys. Res. A 455 (2000), p. 645–655

[Br02] T.J. Brodbeck et al., *Carrier mobilities in irradiated silicon*, Nucl. Instr. & Meth. in Phys. Res. A 477 (2002), p. 287–292

[Bu00] T. Butz, *Fouriertransformation für Fußgänger*, 2. Auflage, B.G. Teubner Stuttgart, 2000

[Ca02] D. Campbell, A. Chilingarov, T. Sloan, *Frequency and temperature dependence of the depletion voltage from CV measurements for irradiated Si detectors*, Nucl. Instr. & Meth. in Phys. Res. A 492 (2002), p. 402–410

[Ce01] M. Cervetto, C. Gemme, *Measurement of the depletion voltage of the irradiated sensor*, presentation given at Pixel Week, February 2001 at CERN, Geneva

[CPS] M. Glaser, information on irradiation facilities at the CERN Proton Synchrotron on WWW, http://irradiation.web.cern.ch/irradiation/Flux-3.htm

[CiS] CiS Institut für Mikrosensorik gGmbH, Konrad-Zuse-Str. 14, 99099 Erfurt, Germany, http://www.cismst.de

[Da00] Working group on daisy chain dummies within ATLAS Pixel Detector Community, members: Jean-Claude Clemens (CPPM Marseille), Maurice Garcia-Sciveres (LBL), Claudia Gemme (INFN Genoa), Kristina Hinrichs (University of Bonn), Olaf Krasel (University of Dortmund), Oegmundur Runolfsson (University of Bonn)

[Da55] W.C. Dash, R. Newman, *Intrinsic Optical Absorption in Single-Crystal Germanium and Silicon at 77 K and 300 K*, Phys. Rev., Vol. 99 (1955), No. 4, p. 1151

[DN82] DIN-Blatt Nr. 50439, Deutsches Institut für Normung e.V., Berlin 1982

[Do04] D. Dobos, diploma-thesis, University of Dortmund, 2004

[Er95] V. Eremin, Z. Li, I. Ilyashenko, Nucl. Instr. & Meth. in Phys. Res. A 360 (1995), p. 458

[Er02] V. Eremin, E. Verbitskaya, Z. Li, *The origin of double peak electric field distribution in heavily irradiated silicon detectors*, Nucl. Instr. & Meth. in Phys. Res. A 476 (2002), p. 556–564

[Fa94] A. Fasso et al., Proc. 4th Intl. Conf. On Calometry and their Applications, World Scientific, Singapore (1994) 493.

[Fl97] T. Fließbach, *Elektrodynamik*, 2. Auflage, Spektrum Akademischer Verlag, Heidelberg, Berlin, Oxford, 1997

[Ge00] C. Gemme, *Measurement of the depletion voltage of the irradiated sensors*, presentation given at Pixel Week December 2000 at CERN, Geneva

[Gl99] M. Glaser, L. Durieu, F. Lemeilleur, M. Tavlet, C. Leroy, P. Roy, *New irradiation zones at the CERN-PS*, Nucl. Intr. & Meth. A 426 (1999), p. 72–77

[Gl02] M. Glaser, M. Moll, *Proton and neutron irradiation facilities in the PS East Hall*, presentation given on the "EP technical coordinator meeting", 23.09.2002, available on http://www.cern.ch/irradiation/pub

[Go02] R. Goscinny, A. Uderzo, *Asterix chez les Helvetes, Editions Hachette*, 2002

[Gr93] C. Grupen, *Teilchendetektoren*, BI Wissenschaftsverlag, 1993

[HH] Universität Hamburg, Institut für Experimentalphysik, Luruper Chaussee 149, DESY Bldg. 67b, D-22761 Hamburg, http://sesam.desy.de/

[Hü01] F. Hügging, *Der ATLAS Pixelsensor, Der state-of-the-art Pixelsensor für teilchenphysikalische Anwendungen mit extrem hohen Strahlungsfeldern*, Ph.D. thesis, University of Dortmund, June 2001, UniDO PH-E4 01-05

[KN95] G. Pfennig et al., *Karlsruher Nuklidkarte*, Forschungszentrum Karlsruhe GmbH, 6. Auflage, 1995

[Ko02] R. Kohrs, *Charakterisierung von ATLAS-Pixelmodulen im Laserstrahl und hinsichtlich der "bump"- und "flip-chip"-Technologie*, Diplomarbeit, Universität Bonn, BONN-IB-2002-15, 2002

[Kr00a] O. Krasel, *Damage Projections for Pixel Sensors*, presentation given at Pixel Week, June 2000 at CERN, Geneva

[Kr00b] O. Krasel, *Effects of Flip Chipping to Irradiated Sensors*, presentation given at Pixel Week, September 2000 at CERN, Geneva

[Kr00c] O. Krasel, *Radius Dependence of the Radiation Damage*, presentation given at Pixel Week, September 2000 at CERN, Geneva

[Kr00d] O. Krasel, *Layout for New Dummy Modules*, presentation given at Pixel Week, December 2000 at CERN, Geneva, available from WWW: https://edms.cern.ch/file/249473/1/okrasel_daisy.ps

[Kr00e] O. Krasel, *Effects of Flip Chipping to Irradiated Sensors*, presentation given at Pixel Week December 2000 at CERN, Geneva

[Kb01] G. Kramberger, *Signal Development in irradiated silicon detectors*, Ph.D. thesis, University of Ljubljana, Ljubljana 2001

[Kb02] G. Kramberger, V. Cindro, I. Mandic, M. Mikuz, M. Zavrtanik, *Effective trapping time of electrons and holes in different silicon materials irradiated with neutrons, protons and pions*, Nucl. Instr. & Meth. Phys. Res. A481 (2002), p. 100–108

[Ki98] E.S. Krištof, *Characterization of Neutron Flux in the Exposure Channel F19 of the TRIGA Mark II Reactor in Ljubljana*, Proceedings of Nuclear Energy in Central Europe 98, Terme Čatež, Slovenia, September 7–10, (1998) 43.

[Le94] W. R. Leo, *Techniques for Nuclear and Particle Physics Experiments*, 2. Auflage, Springer-Verlag 1994

[Li03] G. Lindstroem, E. Fretwurst, D. Contarato, F. Hoenniger, G. Kramberger, M. Moll, E. Nossarzewska, I. Pintilie, R. Roeder, A. Schramm, J. Stahl, *Results on epi-diodes with superior radiation tolerance*, presented on the 3rd RD50 Workshop, CERN, Geneva, 2003

[Lo03] D. Louis, *C/C++*, Markt & Technik, 2003

[Lu99] G. Lutz, *Semiconductor Radiation Detectors*, Springer, 1999

[Me99] D. Menichelli, M. Bruzzi, Z. Li and V. Eremin, *Modeling of Observed Double Junction Effect*, Nucl. Instr. & Meth. in Phys. Res. A 426 (1999), p. 135–139

[Mi03] Marko Mikuž, private communication, 2003

[Mo99] M. Moll, *Radiation Damage in Silicon Particle Detectors*, DESY-THESIS-1999-040, December 1999

[Mo03] Michael Moll (CERN), private communication April 2003

[PG02] K. Hagiwara et al., *Review of Particle Physics*, K. Hagiwara et al., Phys. Rev. D66, 0100001 (2002)

[Pe91] D. H. Perkins, *Hochenergiephysik*, Addison-Wesley, (1991)

[Po97] Povh, Rith, Scholz, Zetsche, *Teilchen und Kerne*, Springer-Verlag, (1997)

[Ra39] S. Ramo, *Currents Induced by Electron Motion*, Proc. IRE 27 (1939) 584.

[RD2] The RD2 Collaboration, *CERN RD2 Status Report to the DRDC*, January 1992 CERN/DRDC/92-4 (1992)

[RD48] ROSE Collaboration (Research and development On Silicon for future Experiments), RD48 collaboration at CERN/Geneva, see also http://rd48.web.cern.ch/RD48/

[RD48b] The ROSE Collaboration (R&d On Silicon for future Experiments), *3rd RD48 Status Report*, CERN/LHCC 2000-09, 31. Dezember 1999

[RD48c] RD48 Collaboration: G. Lindström, M. Ahmed, S. Albergo, P. Allport, D. Anderson, L. Andricek et al., *Radiation Hard Silicon Detectors – developments by the RD48 (ROSE) collaboration*, Nucl. Instr. & Meth. in Phys. Res. A 466 (2001), pp. 308–326

[RD50] RD50 Collaboration: F. Campabadal et al., *RD50 Status Report 2002/2003, Radiation hard semiconductor devices for very high luminosity colliders*, CERN-LHCC-2003-058 and LHCC-RD-002, CERN, Geneva, 14.11.2003

[Rj03] S. Rajek, *Charakterisierung des Ladungssammlungsverhaltens von strahlungsgeschädigten Siliziumsensoren für teilchenphysikalische Anwendungen am LHC*, diploma thesis, University of Dortmund, 2003

[Se90] S. Selberherr, W. Hänsch, M. Seavey and J. Slotboom, *The evolution of the MINIMOS mobility model*, Solid-State Electronics Vol. 33, No. 11, pp. 1425–136, 1990

[Sz85] S.M. Sze, *Semiconductor Devices*, Physics and Technology, John Wiley & Sons, New York, 1985

[Wü01] J. Wüstenfeld, *Characterisation of Ionisation-Induced Surface Effects for the Optimisation of Silicon-Detectors for Particle Physics Applications*, Ph.D. thesis, Internal Report UniDo PH-E4 01-06, University of Dortmund, Dortmund, 2001

[Wu92] R. Wunstorf, *Systematische Untersuchungen zur Strahlenresistenz von Silizium-Detektoren für die Verwendung in Hochenergiephysik-Experimenten*, Ph.D. Thesis, Universität Hamburg, DESY FHIK-92-01 (1992)

[Zi85] J.F. Ziegler, J.P. Biersack, U. Littmark, *The Stopping and Range of Ions in Solids*, Pergamon Press, New York 1985

[Žo98] D. Žontar, *Study of Radiation Damage in Silicon Detectors for High Luminosity Experiments at LHC*, Ph.D. Thesis, Ljubljana (1998)

Acknowledgements

At this place I want to acknowledge the help and support I obtained during the last years in performing this work:

First of all, I am grateful to Prof. Dr. Claus Gößling for his confidence and support during the last four years. It was a pleasure to work in his group. I am indebted to PD Dr. Dr. Wolfgang Rhode as well for giving the second reference.

I would like to thank Dr. Alexandre Chilingarov, Dr. Reiner Klingenberg and Dr. Renate Wunstorf for their interest in my work and the many fruitful discussions. I also profited from many inspiring conversations with colleagues from the RD50 and the ATLAS collaboration.

I want to thank Dr. Michael Moll, Maurice Glaser, Petr Sicho, Prof. Dr. Marko Mikuž and Dr. Vladimir Cindro for performing the sample irradiations and Ralf Röder from CiS for supplying samples.

Andreas Borowski, Stephanie Münstermann, Silke Rajek and Holger Sprungk took part in my measurement program. I want to thank them for the persistent work and the measurements they performed. Theo Villett and Kai Warda gave great support in all technical problems.

It was always a pleasure to work with the other colleagues of the Lehrstuhl für Experimentelle Physik IV at the University of Dortmund: Daniel Dobos, Christoph Hoffmann, Dr. Fabian Hügging, Henning Kiel, Jonas Klaiber-Lodewigs, Dr. Jurek Kudlaty, Dr. Dieter Lüke, Martin Maß, Daniel Münstermann, Ingo Reisinger, Monika Schoknecht, Andrea Teichmann, Jörg Walbersloh, Jens Weber and Dr. Jens Wüstenfeld. I apologise for the huge number of tiny plots I showed in the group meetings.

Special thanks to Dr. Reiner Klingenberg, Sandra Oehl and Dr. Renate Wunstorf for carefully proof-reading the manuscript of this thesis.

Last but not least I want to thank my parents Rita and Ewald Krasel, my grandmother Elfriede Lackner and my partner Sandra Oehl for all the support and encouragement I obtained from them during these laborious years.